



# 1<sup>st</sup> International Conference on

## Evolving Materials and Nanotechnology for Sustainable Development (EMNSD-2020)

15-16 December 2020



### Organised By

**Department of Physics,  
Central Institute of Technology Kokrajhar,  
Deemed to be University (under MHRD, Govt. of India),  
Kokrajhar, BTR, Assam-783370, India.**

**Editors**

**Dr. Manasi Buzar Baruah  
Dr. Pranjal Kalita**

Website: [www.emnsdconference.in](http://www.emnsdconference.in)

INTERNATIONAL CONFERENCE ON  
EVOLVING MATERIALS AND NANOTECHNOLOGY FOR SUSTAINABLE  
DEVELOPMENTS, EMNSD-2020

15-16 DECEMBER 2020 (TUESDAY-WEDNESDAY)

(Online Mode)

*Organized by*

Department of Physics, Central Institute of Technology Kokrajhar  
(Deemed to be University, Ministry of Education, Govt. of India)  
Kokrajhar, BTR, Assam 783370, India.

Copyright@2021, by Central Institute of Technology Kokrajhar

*All rights reserved, No part of this proceeding publication may be reproduced mechanically, electronically or by any other means, including photocopying without written permission of the publisher.*

*Published by*

Dr. Manasi Buzar Baruah (Convenor), Assistant Professor, Department of Physics,  
Central Institute of Technology Kokrajhar  
(Deemed to be University, MoE, Govt. of India), Kokrajhar, BTR, Assam 783370, India.

First Edition: 15 April 2021; Price: 250 (INR)

ISBN No. 978-93-5426-643-0

*Edited by*

**Dr. Manasi Buzar Baruah**

**Assistant Professor, Department of Physics, CITK**

&

**Dr. Pranjal Kalita**

**Associate Professor, Department of Chemistry, CITK**

*Printed at*

Shyamalata Printers, Santinagar, Kokrajhar, Assam

**1<sup>st</sup> International Conference**  
**on**  
**Evolving Materials and Nanotechnology for Sustainable**  
**Development (EMNSD-2020)**  
**(Online Mode)**

**15-16 December 2020**



**Organised by**  
**Department of Physics,**  
**Central Institute of Technology Kokrajhar,**  
**Deemed to be University (Under MHRD, Govt. of India)**  
**Kokrajhar, BTR, Assam-783370, India.**

# A TRIBUTE TO PROFESSOR INDRANI BANERJEE

Professor Indrani Banerjee, Dean of School of Nanosciences at the Gujarat Central University, Gandhinagar, Gujarat, India, passed away on 11 April 2021 because of COVID-19 at the age of 48 years. The scientific fraternity including our institute Central Institute of Technology Kokrajhar along with the parent institute deeply mourn this sudden death. We pay our tribute to the great soul.

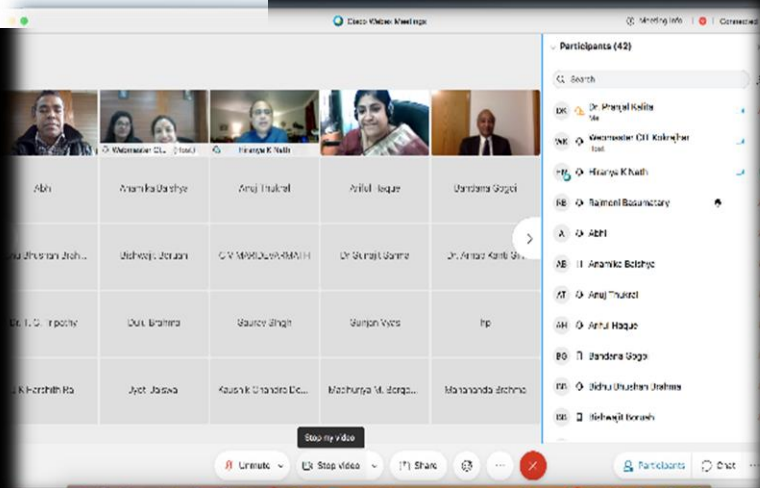
We were so fortunate to have Prof. Indrani Banerjee madam as one of the resource persons of the International Conference “*Evolving Materials and Nanotechnology for Sustainable Development*” (EMNSD, 15-16 December 2020).

Prof. Banerjee graced our event with spectacular lecture on ***Structure Function Relation of Microwave Synthesized Muga Silk Nanoparticles***, where all the participants as well as speakers and all the members of the program greatly benefited. We glad to interact with Prof. Banerjee madam on screen and enthuses about madam’s outstanding work.

A recipient of ‘Better Opportunities for Young Scientists in Chosen Areas of Science and Technology’ (Boyscast) fellowship and Commonwealth Academic Fellowship, UK, Prof Banerjee was a visiting scientist and postdoctoral research associate at Mechanical and Aerospace Engineering Department, University of California, Los Angeles, USA. She was also a visiting academician at Brunel University, London and a postdoctoral fellow at Bhabha Atomic Research Centre, Mumbai.

With a PhD (2007) from Bhabha Atomic Research Center, Pune University, Prof. Banerjee joined Birla Institute of Technology, Mesra as Assistant Professor in Physics, continued as Associate Professor in the same institute till 2017. Prof. Banerjee joined School of Nanoscience at Central University of Gujarat, Gandhinagar and continued there till her last day.

Prof. Banerjee was a great teacher and admirable researcher of the highest moral values, will be respectfully remembered by all who came in contact with madam as a person of highest integrity, honesty and sincerity.



## **Acknowledgement**

We would like to extend our extreme gratefulness to the Director, Prof. Debkumar Chakraborty, Central Institute of Technology Kokrajhar (CITK) for the approval of organising the International Conference EMNSD-2020 and his stimulating support. We are very much grateful to the registrar Ms. Chaitali Brahma, CITK for her strong cooperation for grant success of the program. We are grateful to our management for their support, motivation and encouragement without which this event could not have been organized. We are very much thankful to each and all members who directly or indirectly extended their helping hand with moral support. Saying thank you is not enough but the individual and collective contribution of all speakers and participants mean a lot for the grand success of EMNSD-2020 followed by publication of conference proceeding with ISBN in form of E-Book. Special thanks to Mr. Biswajit Paul, (Library Information Assistant) for his continuous support for the success.





# केन्द्रीय प्रौद्योगिकी संस्थान कोकराझार CENTRAL INSTITUTE OF TECHNOLOGY KOKRAJHAR

Deemed to be University, MHRD, Govt. of India

Kokrajhar, BTAD, Assam 783370

[www.cit.ac.in](http://www.cit.ac.in)

## MESSAGE FROM THE DESK OF DIRECTOR



It gives me immense pleasure to share with you that the Department of Physics, Central Institute of Technology Kokrajhar (Deemed to be University, MHRD, Govt. of India), Assam is organizing International Conference on “Evolving Materials and Nanotechnology for Sustainable Development (EMNSD)” 15- 16 December, 2020 in on line mode. The topic is quite relevant and significant which includes most prominent dimensions of the study in the field of materials and nanotechnologies. Taking this fact into consideration, the CITK is going to adopt a step to create a healthy academic horizon which is urgently needed for all-round development of the nation with global standard. I welcome all esteemed speakers and participants to deliver their interesting & valuable talks in the conference EMNSD 2020.

I acknowledge efforts put by all organizing members. I wish a grand success.

With Best Wishes

*Deb Kumar Chakrabarti*

**Prof. Deb Kumar Chakrabarti**

**Director (Officiating) CIT Kokraj**



# केन्द्रीय प्रौद्योगिकी संस्थान कोकराझार CENTRAL INSTITUTE OF TECHNOLOGY KOKRAJHAR

Deemed to be University, MHRD, Govt. of India

Kokrajhar, BTAD, Assam 783370

[www.cit.ac.in](http://www.cit.ac.in)

## MESSAGE FROM THE DESK OF REGISTRAR



Greetings from CITK...

I am happy to say that the Department of Physics of Central Institute of Technology Kokrajhar (Deemed to be University, MHRD, Govt of India) is going to organize the International Conference on “Evolving Materials and Nanotechnology for Sustainable Development (EMNSD)” 15- 16 December, 2020 in on line mode. This conference will bring the wave of knowledge from different fields across the world along with the platform to interact, discuss the challenges and exchange the expertise towards building a possible collaboration. With this message, I am honoured and delighted to welcome you to attend this conference. I welcome each and every participants of the conference to feel the learning environment of CIT Kokrajhar and to make the event grant success.

I appreciate the hard work of the entire team, as well bringing out a Book of Abstracts highlighting the recent research outcomes in the related field. I wish great success for the successful conduct of the delightful event EMNSD 2020 and hope this mission will be carried out with even more dynamism in the years ahead.

**Ms. Chaitali Brahma**

**Registrar, CIT Kokrajhar, Assam**

## FROM THE DESK OF HEAD OF THE DEPARTMENT



*It involves extraordinary delight to take note of that the Physics Department CITK will put together the first International conference Evolving Materials and Nanotechnology for Sustainable Development (EMNSD-2020). It involves incredible pride that the coordinator of the conference has been effective in making a gigantic effect on the target participant within short span of time. The conference has got a staggering response across the globe which is essentially stunning. It is an incredible accomplishment for the organiser to arrange the publication of Abstracts in the form of a book having ISBN status.*

*On behalf of the Department and also on my personal behalf I would like to thank the organisers of EEMNSD-2020 for their untiring efforts and constant endeavour to make the conference new heights.*

*I wish EMNSD-2020 a grand success!!*

*Dr. B N Parida*

*Assoc. Prof. & Head,*

*Department of Physics,*

*CIT Kokrajhar, Assam, India*



# International Conference on Evolving Materials and Nanotechnology for Sustainable Development

(Online Mode)



## FROM THE DESK OF CONVENOR

I am so honored and delighted to take the opportunity to convey my best of regards to you all who have given your valuable time towards fulfilment of the **International Conference on Evolving Materials and Nanotechnology for Sustainable Development (EMNSD-2020) on 15-16 December 2020 (Tuesday-Wednesday)** in online mode via Cisco WebEx. I would like to welcome you all respected persons to the glorious moment for our CIT Kokrajhar. We are so happy to receive to have very good response from Eminent Persons across the globe as well as the nation along with our native places.

The aim of the conference is to tie the thought of researchers working in academia and other professionals through their research presentations in current technological trends. EMNSD 2020 is providing an excellent forum for exchange of ideas, scientific interactions and potential for collaboration in materials science with nanotechnology.

We have received a very good number of participants for both oral and poster presentation from wide-ranging area of materials and nanotechnology based on the theme of Sustainable Development. We are very much delighted to publish all those as a conference abstract book and selected full papers in form of conference proceeding with ISBN. We hope, these publications will be valuable and memorable assets for the contributors, host institutes and other Academic and Research bodies.

On the behalf of organizing committee of EMNSD 2020. I would like to extend our gratefulness to Prof. Devkumar Chakrabarty, Director, CITK, for approval cum strong encouragement. I am also very much obliged to Ms. Chaitali Brahma, Registrar, CITK for the support and cooperation in all dimensions. I would like to extend my sincere gratitude to all members of advisory board and also appreciate Dr. Bichitra Nanda Parida, Head of Department of Physics, CITK for continues stimulating cooperation. The programme would not be up to the mark without the full contribution of members of organizing committee, staffs, research scholars, speakers, delegates, participants, students, and all who have joined their hands directly or indirectly to make the event grand success. So, I am very much thankful to them from bottom of heart.

I hope all of us will have a great time with peer groups in this conference and would receive many great tips to implement those in your works. On behalf of organising committee I would like to convey our best wishes to you all and appeal you to make our conference a great success.



**Dr. Manasi Buzar Baruah,**

*Convener, EMNSD-2020*  
*Assistant Professor, Department of Physics*  
*CIT Kokrajhar, Assam, India*  
*Email id: [emnsd20@cit.ac.in](mailto:emnsd20@cit.ac.in)*



### **Advisory Committee**

1. *Dr. Chris Holland, UK*
2. *Prof. Madan Bhattacharya, USA*
3. *Prof. Absar Ahmad, AMU, India*
4. *Dr. Avik Mukherjee, CITK, India*
5. *Prof. Hemanta Kumar Kalita, CITK, India*
6. *Prof. Monomoy Goswami, CITK, India*
7. *Prof. Tapan Kumar Maity, CITK, India*
8. *Dr. Indrani Banerjee, CUG, India*
9. *Dr. Bichitra Narayan Parida, CITK, India*
10. *Dr. Pranjal Kalita, CITK, India*

### **Organising Committee**

1. *Dr. Rajib Lochan Hota, Assoc. Prof., CIT Kokrajhar*
2. *Dr. Sandeep Kumar Srivastava, Assoc. Prof., CIT Kokrajhar*
3. *Mr. Mahananda Brahma, Asst. Prof., CIT Kokrajhar*
4. *Dr. Bhaskar Saha, Asst. Prof., CIT Kokrajhar*
5. *Mr. Sanjib Narzary, Asst. Prof., CIT Kokrajhar*
6. *Dr. Anamika Deka Kalita, Asst. Prof., CIT Kokrajhar*
7. *Dr. Sahalad Borgiary, Asst. Prof., CIT Kokrajhar*
8. *Dr. Gunajit Sarma, Asst. Prof., CIT Kokrajhar*
9. *Dr. Santosh Kumar, Asst. Prof., CIT Kokrajhar*
10. *Mr. Bikramjit Choudhury, Asst. Prof., CIT Kokrajhar*
11. *Mr. Jeet Dutta, Asst. Prof., CIT Kokrajhar*
12. *Dr. Kaushik Dev Sharma, Asst. Prof., CIT Kokrajhar*
13. *Mr. Ranjan Patowary, Asst. Prof., CIT Kokrajhar*
14. *Mr. Yendrembam Suresh Singh, Asst. Prof., CIT Kokrajhar*

### **Technical Committee**

1. *Mr. Biswajit Paul, LLA, CIT Kokrajhar*
2. *Mr. Bipin Brahma, Network Admn (i/c), CIT Kokrajhar*
3. *Mr. Nayan Moni Barman, JTS, Dept. of CSE*

**EMNSD 2020**

## CONTENTS

<b>Paper Code</b>	<b>Author</b>	<b>Title</b>	<b>Page Number</b>
EMNSD-2020/OP/01	Ariful Haque	Challenge and Success in Synthesis of Quadruple Perovskite A'A <sub>3</sub> B <sub>4</sub> O <sub>12</sub> at Ambient Pressure	1
EMNSD-2020/OP/04	A. Raja	All-Optical Binary to Quaternary Radix Converters Using Soa-Prs	9
EMNSD-2020/OP/05	Bandana Gogoi	A Study on Iron Oxide ( $\Gamma$ - Fe <sub>2</sub> O <sub>3</sub> ) Nanoparticles Synthesized Using Precipitation Method and its Possible Applications	15
EMNSD-2020/OP/06	Jayanta Kumar Majhi	Plasmon Resonances in Interacting Ni Nanoparticles Embedded in Dielectric	25
EMNSD-2020/OP/14	Kousik Mukherjee	Tera-Hertz Optical Asymmetric Demultiplexer (Toad) Using Quantum Dot Semiconductor Optical Amplifier	31
EMNSD-2020/OP/20	Arnab Kanti Giri	Direct Synthesis of Co <sub>3</sub> O <sub>4</sub> Nanomaterials by Carbonate Precursor	38
EMNSD-2021/OP/22	H C Medhi	Design of a Power Inverter Using Solar Cell as a Source of Charger	47
EMNSD-2020/OP/27	Sanjib Baglari	Structural and Optical Properties of Green Synthesized Copper Oxide Nanoparticles	54
EMNSD-2020/PP/03	Kousik Mukherjee	Frequency encoded All optical single bit memory unit using Tera Hertz Optical Asymmetric Demultiplexer(TOAD)	63
EMNSD-2020/PP/04	Junmoni Barman	Effect of Fe Substitution on the Magnetic Properties of MnCo <sub>2</sub> O <sub>4</sub>	69
EMNSD-2020/PP/05	Upama Das	Review On Metal Nanoparticles Embedded in Molybdenum Disulfide Nanosheets: Synthesis and Properties	80
EMNSD-2020/PP/14	A. Baro	High Power Analysis of a Junctionless Field Effect Transistor With High K Spacer and Low Work Function Gate Material	96

<b>EMNSD-2020/PP/15</b>	<b>Avijit Chowdhury</b>	A Review on Layered Graphene Oxide and Transition Metal Dichalcogenides Material: Synthesis and Application in Memory Devices	102
<b>EMNSD-2021/PP/17</b>	<b>Sonali Dutta</b>	Estimation of Radon Exhalation Rate in Soil Samples of Oil Field Area of Tinsukia District of Assam and its Possible Correlation with Radium Content in Soil Using Can Technique Method	116
<b>EMNSD-2021/PP/34</b>	<b>Absar Ahmad</b>	Effect of Endophytic Fungus <i>Fusarium oxysporum</i> on Crystallographic Properties of PdO: Nanoparticles Synthesis, Characterization and Evaluation of Anti-oxidant Activity	125

## Challenge and Success in Synthesis of Quadruple Perovskite $A'A_3B_4O_{12}$ at Ambient Pressure

Ariful Haque\*, Sudipa Bhattacharya and Md. Motin Seikh\*

Department of Chemistry, Visva-Bharati University, Santiniketan-731235, West Bengal, India

*Email: haqueariful.chem@gmail.com (A. Haque)*

### ABSTRACT

Here we have described the genesis of real challenge in synthesizing  $A'A_3B_4O_{12}$  quadruple perovskite at ambient pressure that largely hampers the exploration of this family of oxides. In this proceeding, we have reported two new compositions namely  $BiCu_3Ti_3CrO_{12}$  and  $LaCu_{2.5}Mn_{0.5}Ti_{2.5}Fe_{1.5}O_{12}$  synthesized at ambient pressure and compared their magnetic properties with our earlier reported results with the congener oxides. We observed highly contrasting magnetic feature by changing chemical compositions either in B-site  $BiCu_3Ti_3MO_{12}$  ( $M=Cr, Mn \& Fe$ ) or in A-site  $A'Cu_{2.5}Mn_{0.5}Ti_{2.5}Fe_{1.5}O_{12}$  ( $A'=La$  and  $Bi$ ). The ambient pressure synthesized compounds highlight the opportunity to explore the chemical effect on physical properties in this family of quadruple perovskite.

**Keywords:** Quadruple perovskite, Ambient pressure, Antiferromagnetic, Ferrimagnetic.

### INTRODUCTION:

The quadruple perovskites of general formula  $A'A_3B_4O_{12}$ , where both the A and B-sites can be occupied by transition metal ions, provide excellent opportunities to discover exotic functionality due to widening the landscape of electronic and magnetic interactions between the metal ions [1]. Unlike the simple  $ABO_3$  type perovskite oxides having only B-B interaction,  $A'A_3B_4O_{12}$  exhibits all A-A, B-B, and A-B types of interactions inducing complexity and the possibility of a new phenomenon. Interestingly, the A-site cations in  $A'A_3B_4O_{12}$  practically avail four coordinated square planar geometry. The remaining eight oxide ligands are at significantly larger distance, as the A-site cations in perovskite structure usually have twelve coordination numbers. This structural constraint restricts the metal ions to occupy the A-site only by the strongly Jahn-Teller active cations, such as  $Cu^{2+}$  or  $Mn^{3+}$ . Such fixation of metal ions in square

planar coordination usually requires high pressure for synthesis, and hampers exploring this series of oxides. Consequently, unlike simple perovskites, quadruple perovskites are much less studied. Developing a strategy for ambient pressure synthesis of quadruple perovskites will allow the investigation of such oxides overcoming the difficulty of high-pressure synthesis.

In this regard, the first ambient pressure synthesis of  $\text{CaCu}_3\text{Ti}_4\text{O}_{12}$  about five decades ago provides a clue to progress in this direction [2]. Accordingly, several compositions of  $(\text{Ln}/\text{Ca})\text{Cu}_{3-x}\text{Ti}_{4-y}\text{Mn}_{x+y}\text{O}_{12}$  was successfully synthesized at ambient pressure via solid state route under sealed tube [3,4].  $\text{CaCu}_3\text{Ti}_4\text{O}_{12}$  exhibits antiferromagnetic ordering below 25 K where A-site  $\text{Cu}^{2+}$  ions are coupled antiferromagnetically through  $\text{Cu}^{2+\uparrow}-\text{O}-\text{Ti}-\text{O}-\text{Cu}^{2+\downarrow}$  exchange pathway. The substitution of nonmagnetic Ti by a magnetic ion like Mn in the B-site gives rise to the dramatic evolution of electrical and magnetic properties. Here,  $\text{Cu}^{2+\uparrow}-\text{O}-\text{Ti}-\text{O}-\text{Cu}^{2+\downarrow}$  exchange path gets transformed to  $\text{Cu}^{2+\uparrow}-\text{O}-\text{Mn}\downarrow-\text{O}-\text{Cu}^{2+\uparrow}$  with two magnetic sublattice of parallel spins which are coupled antiferromagnetically eventually resulting in ferrimagnetic ground state [3]. However, the magnetic behavior of Fe doped  $\text{Bi}_{2/3}\text{Cu}_3\text{Ti}_4\text{O}_{12}$  is rather complex [5]. Unlike the Mn substituted samples, upon 10% Fe doping in  $\text{Bi}_{2/3}\text{Cu}_3\text{Ti}_4\text{O}_{12}$ , the AFM interaction becomes weaker, and a further increase in Fe does not show any clear magnetic transition. Instead, a strong competition between ferromagnetic and antiferromagnetic interaction has been suggested to prevail [5]. The compound  $\text{BiCu}_3\text{Ti}_3\text{FeO}_{12}$  shows spin glass behavior, whereas  $\text{BiCu}_3\text{Fe}_4\text{O}_{12}$  is probably an antiferromagnet [6]. However,  $\text{BiCu}_{2.5}\text{Mn}_{0.5}\text{Ti}_{2.5}\text{Fe}_{1.5}\text{O}_{12}$  has been realized to show strong competition between ferromagnetic and antiferromagnetic interactions leading to phase segregation [5]. This contrasting behavior of Mn and Fe doped samples must be related to the chemical nature of these two elements. To further substantiate such chemical effect on the magnetic property, we have performed ambient pressure synthesis of  $\text{BiCu}_3\text{Ti}_3\text{CrO}_{12}$  and  $\text{LaCu}_{2.5}\text{Mn}_{0.5}\text{Ti}_{2.5}\text{Fe}_{1.5}\text{O}_{12}$  and compared with  $\text{BiCu}_3\text{Ti}_3(\text{Mn}/\text{Fe})\text{O}_{12}$  and  $\text{BiCu}_{2.5}\text{Mn}_{0.5}\text{Ti}_{2.5}\text{Fe}_{1.5}\text{O}_{12}$ , respectively, to highlight the effect on both the A- and B-sites.

### EXPERIMENTAL DETAILS:

$\text{BiCu}_3\text{Ti}_3\text{CrO}_{12}$  and  $\text{LaCu}_{2.5}\text{Mn}_{0.5}\text{Ti}_{2.5}\text{Fe}_{1.5}\text{O}_{12}$  have been synthesized at ambient pressure by conventional citrate-gel method [7]. Stoichiometric amounts of required metal salts were dissolved in 80 mL of distilled water. Then 5 mL of concentrate nitric acid was poured into the reaction mixtures to prevent the hydrolysis of aquated metal ions. After that, the reaction mixture

was rotated by a magnetic stirrer to obtain a clear solution. Then citric acid was added to this solution in about four times the mole ratio of the metal ions. The resulting solution was rotated at 60 °C for 6 h by a magnetic stirrer and then evaporated at 100 °C to form the gel. Then the gel was dried into crude powder at 250 °C. The obtained crude was then treated in the air at 750 °C at a heating rate 5°C/minute for 16 h followed by 800 °C for 24 h with intermediate grindings to obtain the final products. The powder X-ray diffraction (PXRD) data were measured with a Bruker D8 Advance X-ray diffractometer using Cu K $\alpha$  radiation ( $\lambda=1.5418 \text{ \AA}$ ) working at 40 kV and 40 mA. The XRD patterns were collected in the  $2\theta$  range of 10°–80° using Lynxeye detector (1D mode) with a step size of 0.02° and a dwell time of 1 s per step. The d. c. magnetization measurements were carried using a superconducting quantum interference device (SQUID) magnetometer with a changeable temperature cryostat (Quantum Design, San Diego, USA). FE-SEM and EDX analyses were performed using a *Zeiss GeminiSEM 450* field emission scanning electron microscope at an accelerating voltage of 20 kV.

## RESULTS AND DISCUSSION:

The PXRD patterns of  $\text{BiCu}_3\text{Ti}_3\text{CrO}_{12}$  and  $\text{LaCu}_{2.5}\text{Mn}_{0.5}\text{Ti}_{2.5}\text{Fe}_{1.5}\text{O}_{12}$ , without any detectable impurity peak, have been shown in **Figure 1**, confirming the phase purity of the samples. Both the patterns refined using the Rietveld method can be properly indexed with cubic  $I-m3$  space group. The refinement parameters, cell constants, bond lengths, and bond angles are summarized in **Table -1**. The FE-SEM images of  $\text{BiCu}_3\text{Ti}_3\text{CrO}_{12}$  and  $\text{LaCu}_{2.5}\text{Mn}_{0.5}\text{Ti}_{2.5}\text{Fe}_{1.5}\text{O}_{12}$  (**Figure 2(a)-(b)**) reveal the larger agglomerated grains with irregular shape and size. The representative EDX spectra of the samples are shown in **Figure 2(c)-(d)**. The average cationic ratio appended on the spectrum obtained from the EDX spectra was recorded at different regions of the samples confirming the nominal composition of the compounds.

The temperature dependent magnetization of  $\text{BiCu}_3\text{Ti}_3\text{CrO}_{12}$  measured under an applied field of 1000 Oe between 5-300 K in zero-field cooled (ZFC) and field cooled (FC) protocols are shown in **Figure 3(a)**. Unlike the parent  $\text{Bi}_{2/3}\text{Cu}_3\text{Ti}_4\text{O}_{12}$ , which shows a single magnetic transition around 25 K,  $\text{BiCu}_3\text{Ti}_3\text{CrO}_{12}$  exhibits two anomalies around 22 K and 75 K, respectively. The first one corresponds to the parent phase. The second anomaly can be attributed to the local magnetic ordering around the dopant Cr center. These transitions are antiferromagnetic in nature, as suggested from the isothermal magnetization measured at 5 and 50 K (see inset in **Figure 3(a)**). There is a small jump in the magnetization near  $H=0$  followed

by the gradual increase in moments with the applied field. The jump in magnetization can be related to the small ferromagnetic components arising out of spin canting. The canted antiferromagnetic state has also been reported in  $\text{CaMn}_{6.5}\text{Cr}_{0.5}\text{O}_{12}$  [8]. The evolution of a new magnetic transition (75 K) in  $\text{BiCu}_3\text{Ti}_3\text{CrO}_{12}$  with the retention of low temperature ordering (22 K) is remarkably different from the  $\text{BiCu}_3\text{Ti}_3\text{FeO}_{12}$  and  $\text{BiCu}_3\text{Ti}_3\text{MnO}_{12}$  [5]. For these latter two compounds, the low temperature ordering at 25 K corresponding to the parent  $\text{BiCu}_3\text{Ti}_4\text{O}_{12}$  phase has completely been suppressed.  $\text{BiCu}_3\text{Ti}_3\text{FeO}_{12}$  enters into spin glass state, whereas  $\text{BiCu}_3\text{Ti}_3\text{MnO}_{12}$  becomes ferrimagnetic below 120 K with the several fold increase in magnetization (**Figure 3(c)**). To better visualize this remarkable change in magnetic properties in  $\text{BiCu}_3\text{Ti}_3\text{MO}_{12}$  with  $M = \text{Cr, Fe and Mn}$ , we have plotted the data of Fe and Mn congeners in **Figures 3(b) & (c)**. In  $\text{BiCu}_3\text{Ti}_3\text{MnO}_{12}$ , the Mn is able to flip the antiparallel spins of the A-site  $\text{Cu}^{2+}$  like domino effect and eventually results in ferrimagnetic states by aligning its spin opposite to  $\text{Cu}^{2+}$  spins [3,4]. In this regard, the influence of Cr is likely to be localized. This result highlights the prominent chemical effect of B-site of substitution in  $A'A_3B_4O_{12}$  quadruple perovskites.

To investigate the possibility of such a chemical effect for A'-site substitution, we have synthesized  $\text{LaCu}_{2.5}\text{Mn}_{0.5}\text{Ti}_{2.5}\text{Fe}_{1.5}\text{O}_{12}$  at ambient pressure and compared its magnetic property with our previously reported data on  $\text{BiCu}_{2.5}\text{Mn}_{0.5}\text{Ti}_{2.5}\text{Fe}_{1.5}\text{O}_{12}$  in Ref. 5. Accordingly, the magnetic data of  $A'\text{Cu}_{2.5}\text{Mn}_{0.5}\text{Ti}_{2.5}\text{Fe}_{1.5}\text{O}_{12}$  ( $A' = \text{La and Bi}$ ) are plotted in **Figure 4**. The isothermal magnetization measured at 5 K (see insets in **Figure 4**) revealed the comparable moments and similar features of  $M(H)$  curves for both the samples. The moments increase with the applied field without any signs of saturation even at  $\pm 5$  T, which indicates the possible antiferromagnetic background. But the noticeable contrast is clear from the  $M(T)$ -curves. For the  $\text{BiCu}_{2.5}\text{Mn}_{0.5}\text{Ti}_{2.5}\text{Fe}_{1.5}\text{O}_{12}$  sample, the transition is practically smeared up over a broad range of temperature, and only ZFC branch data shows humpy nature (**Figure 4(a)**). In contrast,  $\text{LaCu}_{2.5}\text{Mn}_{0.5}\text{Ti}_{2.5}\text{Fe}_{1.5}\text{O}_{12}$  shows a clear transition below 50 K with a peak around 20 K in both the ZFC and FC data (**Figure 4(b)**). This differential behavior can be attributed to the local lattice distortion in the case of  $\text{BiCu}_{2.5}\text{Mn}_{0.5}\text{Ti}_{2.5}\text{Fe}_{1.5}\text{O}_{12}$  which is instigated by the stereoactive  $6s^2$ -lone pair electrons of  $\text{Bi}^{3+}$  ions. We believe that  $\text{LaCu}_{2.5}\text{Mn}_{0.5}\text{Ti}_{2.5}\text{Fe}_{1.5}\text{O}_{12}$  is also susceptible to electronic phase separation like  $\text{BiCu}_{2.5}\text{Mn}_{0.5}\text{Ti}_{2.5}\text{Fe}_{1.5}\text{O}_{12}$  where the ferromagnetic and antiferromagnetic clusters coexist [5].

## CONCLUSION:

We have synthesized two new members of the quadruple perovskites family, namely  $\text{BiCu}_3\text{Ti}_3\text{CrO}_{12}$  and  $\text{LaCu}_{2.5}\text{Mn}_{0.5}\text{Ti}_{2.5}\text{Fe}_{1.5}\text{O}_{12}$  at ambient pressure. Both the samples are crystallized in cubic  $I-m\bar{3}$  space group. The samples are characterized by PXRD, FE-SEM and magnetization measurements. We have made a comprehensive analysis of magnetic data for two series  $\text{BiCu}_3\text{Ti}_3\text{MO}_{12}$  ( $M = \text{Cr, Fe and Mn}$ ) and  $A'\text{Cu}_{2.5}\text{Mn}_{0.5}\text{Ti}_{2.5}\text{Fe}_{1.5}\text{O}_{12}$  ( $A' = \text{La and Bi}$ ). We observed strong chemical effect on magnetic properties for substitution on either A'- or B-sites. We believe our findings will motivate the researchers to explore the possibility of ambient pressure synthesis of  $A'A_3B_4O_{12}$  quadruple perovskites and to examine their novel properties.

## ACKNOWLEDGEMENTS

The authors gratefully acknowledge financial support from the Science and Engineering Research Board (SERB), Government of India, by a grant No: EMR/2016/000083 to M.M. Seikh. Mr. Haque thanks DST, Govt. of India, for INSPIRE Fellowship (DST/INSPIRE Fellowship/2017/IF170240). The FE-SEM facility through DST sponsored PURSE program of Visva-Bharati is highly acknowledged.

## Reference:

- [1] Vasil'ev, A.N. and Volkova, O.S. New functional materials  $\text{AC}_3\text{B}_4\text{O}_{12}$  (Review), *Low Temp. Phys.* **33** (2007), 895–914.
- [2] Deschanvres, A., Raveau, B. and Tollemer. F. Substitution of copper for a divalent metal in perovskite-type titanates. *Bull. Soc. Chim. Fr.* **11**(1967), 4077-4078.
- [3] Seikh, Md. M., Caignaert, V., Pralong, V. and Raveau, B. Ferrimagnetism up to 200 K in Ti-rich double perovskites  $\text{ACu}_3\text{Ti}_{4-x}\text{Mn}_x\text{O}_{12}$ : Role of double exchange mechanism *Appl. Phys. Lett.* **103** (2013), 082401.
- [4] Seikh, Md. M., Caignaert, V., Sundaresan, A., De, Chandan. and Raveau, B. Ti-rich double perovskites  $\text{LnCu}_{3-y}\text{Ti}_{2-x}\text{Mn}_{2+x+y}\text{O}_{12}$ : ferrimagnetism and magnetoresistance up to room temperature *J. Mater. Chem. C.* **2** (2014), 6061.
- [5] Haque, A., Sukla, A., Dutta, U., Ghosh, D., Gayen, A., Mahata, P., Vasundhara, M. and Kundu, A .K. and Seikh, Md. M. Incompatible magnetic and dielectric properties of  $\text{BiCu}_{3-x}\text{Mn}_x\text{Ti}_{4-y}\text{M}_y\text{O}_{12}$  ( $x = 0 \& 0.5$ ;  $y = 1 \& 1.5$  and  $M = \text{Fe \& Mn}$ ) *Ceram. Int.* **46** (2020), 5907-5912.

[6] Long, Y., Saito, T., Tohyama, T., Oka, K., Azuma, M. and Shimakawa, Y. Intermetallic Charge Transfer in A-Site-Ordered Double Perovskite  $\text{BiCu}_3\text{Fe}_4\text{O}_{12}$  *Inorg. Chem.* **48** (2009), 8489–8492.

[7] Pal, K., Dey, A., Jana, R., Ray, P., Bera, P., Kumar, L., Mandal, T., K., Mohanty, P., Seikh Md. M. and Gayen, A., Citrate combustion synthesized Al-doped  $\text{CaCu}_3\text{Ti}_4\text{O}_{12}$  quadruple perovskite: synthesis, characterization and multifunctional properties *Phys. Chem. Chem. Phys.*, **22**, (2020), 3499–3511.

[8] Seikh, Md. M., Pralong, V. , Lebedev, O.I. and Raveau, B. Cubic structure and canted antiferromagnetism of  $\text{CaMn}_7\text{O}_{12}$  doped with trivalent cations (Fe, Al, Cr) *Solid State Commun.* **180** (2014) 52–55.

**Table-1:** The refinement parameters, cell constant, bond length and bond angles of  $\text{BiCu}_3\text{Ti}_3\text{CrO}_{12}$  and  $\text{LaCu}_{2.5}\text{Mn}_{0.5}\text{Ti}_{2.5}\text{Fe}_{1.5}\text{O}_{12}$ .

Parameters	$\text{BiCu}_3\text{Ti}_3\text{CrO}_{12}$	$\text{LaCu}_{2.5}\text{Mn}_{0.5}\text{Ti}_{2.5}\text{Fe}_{1.5}\text{O}_{12}$
Fitting parameters (S. G.: $I-m\bar{3}$ )	$a = 7.431(3) \text{ \AA}$ $R_b = 8.12$ $R_f = 7.95$ $\chi^2 = 3.21$	$a = 7.453(1) \text{ \AA}$ $R_b = 2.35$ $R_f = 1.58$ $\chi^2 = 5.42$
Bond length	$\text{Cu-O} : 1.898 \text{ \AA}$ $\text{Cr/Ti-O} : 1.999 \text{ \AA}$	$\text{Cu/Mn-O} : 1.973 \text{ \AA}$ $\text{Fe/Ti-O} : 1.978 \text{ \AA}$
Bond-angel	$\text{Cu-O-Cu} : 102^\circ$ $\text{Cu-O-Cr} : \sim 111^\circ$ $\text{Cr/Ti-O-Cr/Ti} : \sim 138^\circ$	$\text{Cu-O-Cu} : 103^\circ$ $\text{Cu/Mn-O-Fe/Ti} : \sim 109^\circ$ $\text{Fe/Ti-O-Fe/Ti} : \sim 141^\circ$

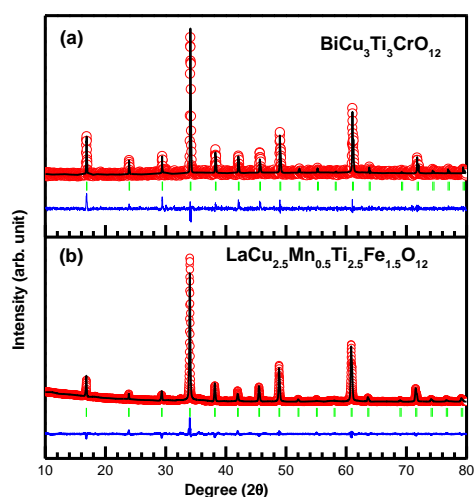


**Figure 1:** PXRD pattern of (a)  $\text{BiCu}_3\text{Ti}_3\text{CrO}_{12}$  and (b)  $\text{LaCu}_{2.5}\text{Mn}_{0.5}\text{Ti}_{2.5}\text{Fe}_{1.5}\text{O}_{12}$ . The open red circles, black lines, the bottom blue lines and green vertical bars represent the experimental data, calculated pattern, difference curve and Bragg position, respectively.

The  
and

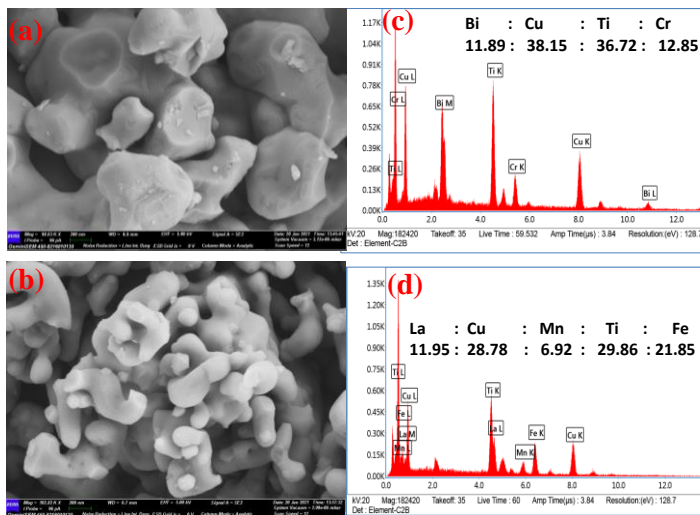


**Figure 2:** The FE-SEM images for (a)  $\text{BiCu}_3\text{Ti}_3\text{CrO}_{12}$  and (b)  $\text{LaCu}_{2.5}\text{Mn}_{0.5}\text{Ti}_{2.5}\text{Fe}_{1.5}\text{O}_{12}$ . representative EDX spectra elemental ratio of (c)  $\text{BiCu}_3\text{Ti}_3\text{CrO}_{12}$  and (d)  $\text{LaCu}_{2.5}\text{Mn}_{0.5}\text{Ti}_{2.5}\text{Fe}_{1.5}\text{O}_{12}$ .

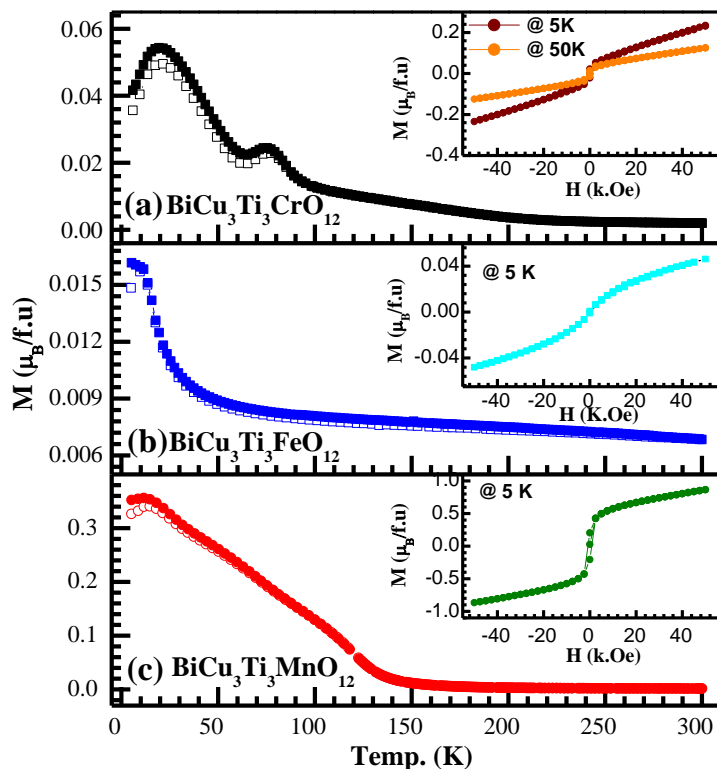


**Figure 3:** Temperature dependent magnetization of (a)  $\text{BiCu}_3\text{Ti}_3\text{CrO}_{12}$ , (b)  $\text{BiCu}_3\text{Ti}_3\text{FeO}_{12}$  and (c)  $\text{BiCu}_3\text{Ti}_3\text{MnO}_{12}$ . The open and filled symbols correspond to ZFC and FC data set, respectively. Inset shows the corresponding isothermal magnetization plots. Magnetic data of (b)  $\text{BiCu}_3\text{Ti}_3\text{FeO}_{12}$  and (c)  $\text{BiCu}_3\text{Ti}_3\text{MnO}_{12}$  are adapted from Ref. [5].

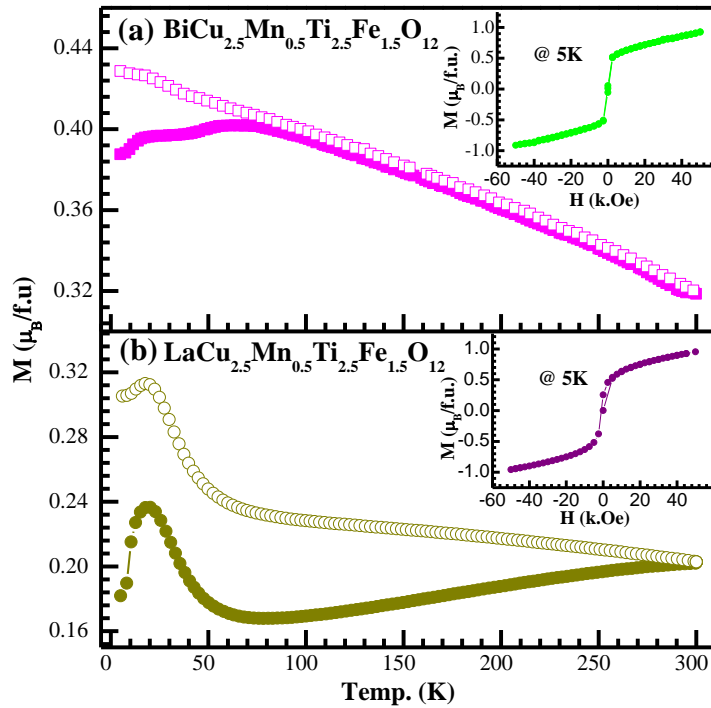


**Figure 4:** Temperature dependent magnetization of (a)  $\text{BiCu}_{2.5}\text{Mn}_{0.5}\text{Ti}_{2.5}\text{Fe}_{1.5}\text{O}_{12}$  and (b)  $\text{LaCu}_{2.5}\text{Mn}_{0.5}\text{Ti}_{2.5}\text{Fe}_{1.5}\text{O}_{12}$ . The open and filled symbols correspond to ZFC and FC data set, respectively. Inset shows the corresponding isothermal magnetization plot. Magnetic data of (a)  $\text{BiCu}_{2.5}\text{Mn}_{0.5}\text{Ti}_{2.5}\text{Fe}_{1.5}\text{O}_{12}$  is taken from reference [5].

## All-Optical Binary to Quaternary Radix Converters Using Soa-Prs

A. Raja\*<sup>1,2</sup>, K. Mukherjee<sup>2,3</sup> and J. N. Roy<sup>1,3</sup>

<sup>1</sup>Department of Physics, Kazi Nazrul University, Asansol, INDIA.

<sup>2</sup>Department of Physics, B.B.College, Asansol, INDIA.

<sup>3</sup>COSOD, Kazi Nazrul University, Asansol, INDIA.

Email: [ashifphysics@gmail.com](mailto:ashifphysics@gmail.com)

### ABSTRACT

In this paper, we have designed a quaternary logic-based all-optical “binary to quaternary” radix converter. The semiconductor optical amplifier-based polarization rotation switches (SOA-PRS) have been used as the basic switching element in the design. The design is very simple, needs only two SOA. The circuit performance has been analyzed and some performance-related matrices like the Quality factor (QF) and Extinction Ratio (ER) have been calculated. The circuit can operate at an ultra-high speed (100 Gb/s). The SOA-based designs are always simple, compact, and less power-consuming than other switches and structures. The SOA-PRS works in the principle of non-linear polarization rotation (NPR) or cross-polarization modulation (XpolM) effect in SOA.

**Keywords:** Semiconductor Optical Amplifier, Cross-polarization Modulation, Radix Converter

### INTRODUCTION:

The optical circuits already established their superiority over the electrical and electronic information processing circuits after the invention of optical fibers and optical amplifiers. In the last decade, multivalued circuits are becoming one of the interesting fields of research [1, 2]. Multivalued circuits are always better than binary circuits for dealing with a wide range of data using minimum hardware complexity. Some works based on the multivalued ternary and quaternary optical circuits have been designed and analyzed by few research groups [3, 4]. Most of these works are based on interferometric switches where the signal interferes in external optical couplers and the mode of interference depends on the optical path traversed by the signals. So the signal handling is difficult. On the other hand, the SOA-PRS switches or NPR switches works based on XpolM and all the interaction between the signal happens within the cavity of the switches internally [5-7]. So the signal handling is easy and the switch is less power consuming (optical power <1mW, injection current <200mA)[8, 9]. In this communication, we have designed a quaternary logic-based all-optical “binary to quaternary” radix converter [4] using SOA-PRS. The SOA’s are very famous for operational speed, wide gain bandwidth, moderate noise, and fast gain recovery [10-12]. The design of the radix converter is simple and compact made of only two SOA’s.

The circuit can operate at an ultra-high speed (~100 Gb/s). The circuit operation is expressed with a quaternary polarization encoding scheme (where 0, 1, 2 & 3 represents no light, horizontally polarized light, vertically polarized light, and mixed polarized light respectively) [9].

## THEORY

The switching operation of the SOA-PRS is based on the intensity-dependent birefringence and gain saturation effect in SOA. The phenomenon is known as XpolM and is also known as NPR [8, 9]. In this effect, the intensity and state of polarization of the weak probe signal are affected by the higher intensity control signal. The mathematical model is described in the papers of H.J.S. Dorren et al [5] and S. Zhang et al [6]. We have already implemented SOA-PRS switches to designed some binary [8] and multivalued [9] circuits in our previous communications. The numerical values of the parameters used for the best performance of the switch are also described there. The simulation works have been done, solving the “rate equations” of the SOA using the MATLAB computational program. Non-inverting ports are used to show the polarization rotation effects of the circuit. The output signal coming out from the non-inverting port (Y1, Y2) will be high when the input control signal is present (high) and vice versa.

The output signal intensity ( $I_Y$ ) of the circuit can be expressed as the sum of the output signal intensity of SOA-PRS1 ( $I_{Y1}$ ), SOA-PRS 2 ( $I_{Y2}$ ) and is given by,

$$I_Y = I_{Y1} + I_{Y2}$$

$$= a(I_1 + I_2 + 2\sqrt{I_1 I_2} \cos \phi)_{SOA-PRS1} + b(I_1 + I_2 + 2\sqrt{I_1 I_2} \cos \phi)_{SOA-PRS2} \quad (1)$$

Where, a, b represents the coefficients corresponding to the binary numbers A and B respectively.  $I_1, I_2$  are the intensity corresponding to the transverse electric and magnetic components of the output probe signal.  $\phi$  is the phase difference between the TE and TM components imposed by the control signal.

**Circuit operation:** The circuit of our all-optical binary to quaternary radix converter is shown in Fig.1. A and B inputs represent the Most Significant Bit (MSB) and Least Significant Bit (LSB) of the binary number. Y is the output representing the quaternary number.

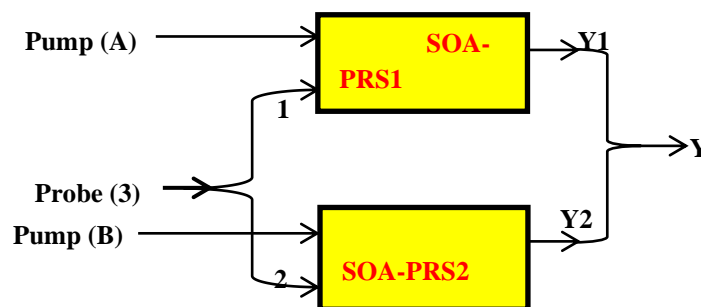


**Figure 1.** Design of the Radix Converter

**Case 1:** When binary number 0 enters the circuit, we have  $A=B=0$ . In this case, both the pump signal of SOA-PRS 1 and SOA-PRS 2 is absent. So the non-inverting output ports emit no signal ( $Y1=Y2=0$ ). Then the final output is  $Y=0+0=0$  (no light). Then we have quaternary number 0 for the binary input 0.

**Case 2:** When binary number 1 enters the circuit, we have  $A=0, B=1$ . In this case, the pump signal for the SOA-PRS 1 is absent, and that for the SOA-PRS 2 is present. The non-inverting output of SOA-PRS 1 will emit no signal. The vertically polarized probe signal of SOA-PRS 2 will be rotated to a horizontally polarized signal. So  $Y1=0$  and  $Y2=1$ . Then the final output will be  $Y=0+1=1$  (horizontally polarized light). So we get quaternary number 1 for the binary input 1.

**Case 3:** When binary number 10 enters the circuit, we have  $A=1, B=0$ . In this case, the pump signal for the SOA-PRS 1 is present, and that for the SOA-PRS 2 is absent. The horizontally polarized probe signal of SOA-PRS 1 will be rotated to a vertically polarized signal. The non-inverting output of SOA-PRS 2 will emit no signal. So  $Y1=2$  and  $Y2=0$ . Then the final output will be  $Y=2+0=2$  (vertically polarized light). Then we have quaternary number 2 for the binary input 10.

**Case 4:** When binary number 11 enters the circuit, we have  $A=B=1$ . In this case pump signals for both the SOA-PRS 1 and SOA-PRS 2 are present. The horizontally polarized probe signal of SOA-PRS 1 will be rotated to a vertically polarized signal. The vertically polarized probe signal of SOA-PRS 2 will be rotated to a horizontally polarized signal. So  $Y1=2$  and  $Y2=1$ . Then the final output will be  $Y=2+1=3$  (mixed polarized light). So we have quaternary number 3 for the binary input 11.

The truth table for the operation of the circuit is shown in table 1.

**Table 1.** The truth table of the Radix Converter

Binary Input		Y1	Y2	Quaternary Output
Pump(A)	Pump(B)			Y=Y1+Y2
MSB	LSB			
0	0	0	0	0
0	1	0	1	1
1	0	2	0	2
1	1	2	1	3

## RESULTS & DISCUSSION

The QF [8] of the proposed radix converter can be calculated using Eq. (2).

$$QF = [(P_m^1 - P_m^0)/(\sigma^1 + \sigma^0)] \quad (2)$$

Where,  $P_m^1$ : average power of the high state,  $P_m^0$ : average power of the low state,  $\sigma^1$ : standard deviation of high state,  $\sigma^0$ : standard deviation of low state.

The variation of the QF of the circuit with the change in control power is shown in Fig.2.

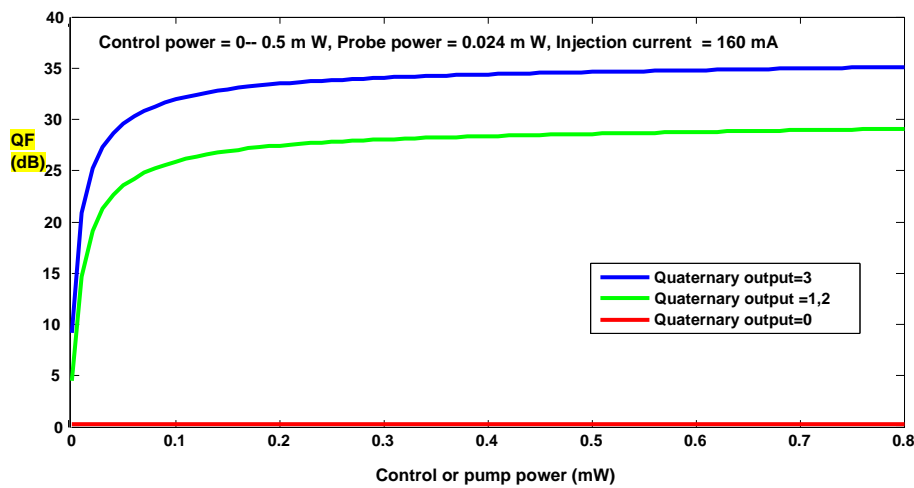


**Figure 2.** The QF versus control power graph

The ER [8] can be calculated using Eq. (3)

$$ER = 10\log(P_{min}^1/P_{max}^0) \quad (3)$$

Where,  $P_{min}^1$  and  $P_{max}^0$  are the maximum and minimum levels of output power respectively.

The variation of the ER of the circuit with the change in control power is shown in Fig.3.

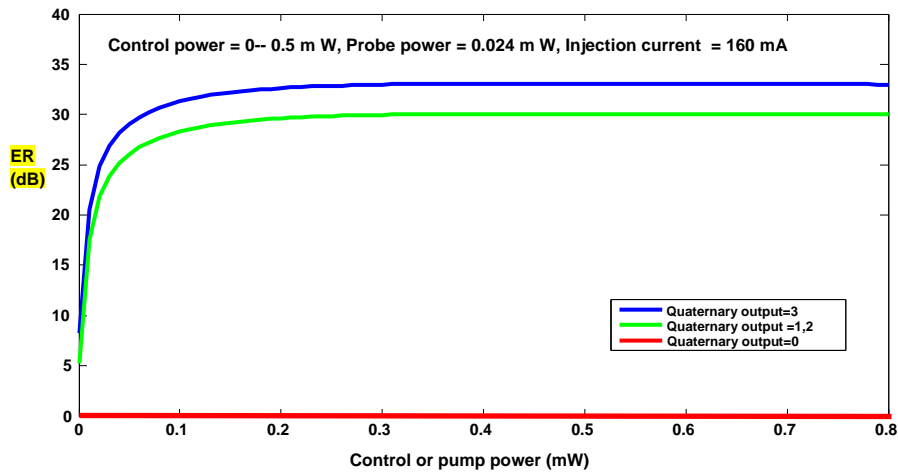


**Figure 3.** The ER versus control power graph

The QF and ER of the radix converter both increase with the increase in control power. In absence of the control signal, we get nothing but a small amount of power due to the amplified spontaneous emission (ASE) noise effect [8, 9]. Then we have a very small amount of QF and ER and are shown in Fig.2 and Fig.3 using the red line.

The pseudo-eye diagram of the binary to quaternary radix converter circuit is shown in Fig.4.

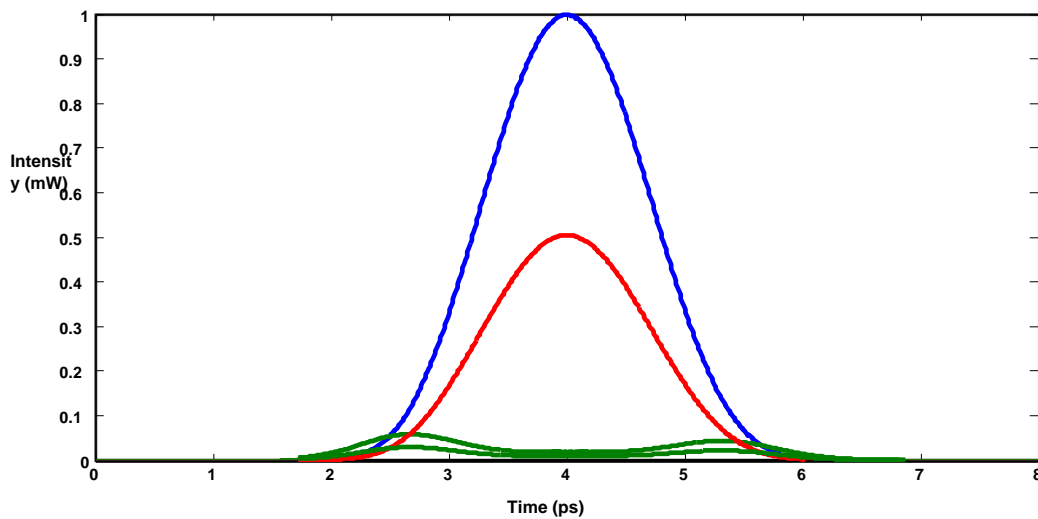


**Figure 4.** Pseudo Eye Diagram for the Radix converter

The Relative Eye Opening (REO) [8] of the circuit can be measured using Eq.(4)

$$REO = \left( \frac{P_{min}^1 - P_{max}^0}{P_{min}^1} \right) \sim 86\% \quad (4)$$

## CONCLUSION

In this paper, all-optical polarization encoded binary to quaternary radix converter is designed to exploit the XpolM effect of SOA. Some performance-related matrices like QF and ER have also been calculated. The main advantage of this scheme is having a good QF ( $>10\text{dB}$ ) and less bit error rate ( $<10^{-20}$ ). The NPR switches work efficiently in the low input (pump) power region ( $\leq 0.5\text{mW}$ ). High power levels reduce the conversion efficiency in the SOA because of the gain saturation effect. Any change in polarization of input signals can be controlled using some additional polarization controllers (PC). This technique can also be used to design some higher-order multi-valued all-optical circuits [9]. For better speed, Quantum Dot SOA can be used in the designs [13].

### References:

- [1] Hurst, S.L. Multiple-valued logic – its status and its future, *IEEE Transactions on Computers* **C-33** (1984) 1160-1179.
- [2] Park, S.J., Yoon, B.H., Yoon, K.S., Kim, H.S., Design of Quaternary Logic Gate Using Double Pass-transistor Logic with neuron MOS Down Literal Circuit, *Proceedings of the 34 the International Symposium on Multiple-valued logic*, (ISMVL'04, University of Toronto, Toronto, 2004), 198-203.  
<https://doi.org/0.1109/ISMVL.2004.1319941>
- [3] Roy, J.N., Chattopadhyay, T. All-Optical Quaternary Logic-Based Information Processing: Challenges and Opportunities, In: Ruiz, R., Michell, J.A.(eds.), Design and Architectures for Digital Signal Processing, IntechOpen.(2013), <https://doi.org/10.5772/51559>
- [4] Chattopadhyay, T., Roy, J.N. All-optical conversion scheme: binary to quaternary and quaternary to binary number. *Optics and Laser Technology* **41** (2009) 289-294.
- [5] Dorren, H.J.S., Lenstra, D., Liu, Y., Hill, M.T., Khoe, G.D. Nonlinear polarization rotation in semiconductor optical amplifiers: Theory and applications to all-optical flip flop memories. *IEEE. J. Quant. Elect.* **39** (2003) 141-148.
- [6] Zhang, S., Liu, Y., Zhang, Q., Li, H., Liu, Y. All-optical sampling based on nonlinear polarization rotation in semiconductor optical amplifiers. *Journal of optoelectronics and biomedical materials* **1** (2009) 383-388, <https://doi.org/10.1007/s10825-019-01393-5>
- [7] Guo, L.Q., Connelly, M.J. Signal induced birefringence and dichorism in a tensile-strained bulk semiconductor optical amplifier and its application to wavelength conversion. *Journal of Lightwave Technology* **23** (2005) 4037-4045.
- [8] Raja, A., Mukherjee, K., Roy, J.N. Design, analysis, and application of all-optical multifunctional logic using semiconductor optical amplifier-based polarization rotation switch. *Journal of Computational Electronics* (2020) <https://doi.org/10.1007/s10825-020-01607-1>
- [9] Raja, A., Mukherjee, K., Roy, J.N., Maji, K. Analysis of all-optical polarization-encoded quaternary Galois field adder processing soliton pulses. *Journal of Optics* (2020) <https://doi.org/10.1007/s12596-020-00594-7>
- [10] Zoiros, K.E. Special issue on applications of semiconductor optical amplifiers. *Applied Sciences*. **8** (2018) 1185.
- [11] Said, Y., Rezig, H. SOAs nonlinearities and their applications for next generation of optical networks, *Advances in Optical Amplifiers*, <https://www.intechopen.com>
- [12] Cleary, C.S., Power, M.J., Schneider, S., Webb, R.P., Manning, R.J. Fast gain recovery rates with strong wavelength dependence in a non-linear SOA, *Optics Express* **18** (2010) 25726.
- [13] Komatsu, K., Hosaya, G., Yashima, H., All-optical logic NOR gate using a single quantum dot SOA assisted an optical filter, *Opt. Quant. Electr.* **50** (2018) 131.

## A Study on Iron Oxide ( $\Gamma$ - $\text{Fe}_2\text{O}_3$ ) Nanoparticles Synthesized Using Precipitation Method and its Possible Applications

Bandana Gogoi\*<sup>1</sup> and Upamanyu Das<sup>2</sup>

<sup>1,2</sup>Department of Physics, Rajiv Gandhi University, Doimukh, AP, INDIA.

<sup>1</sup> Department of Physics, D.N.Govt. College, Itanagar, A.P, INDIA.

Email: [bandana.gogoi12@gmail.com](mailto:bandana.gogoi12@gmail.com)

### ABSTRACT

The recent nanotechnological impact has been observed greatly in society as well as in environment. Magnetic Nanomaterials showing unique novel magnetic behaviour show great potential applications. Iron oxide nanomaterials have drawn considerable attention and interest have been developed for unique properties they show at extremely small size like high surface to volume ratio, surface modification property, excellent magnetic property with better biocompatibility. Therefore more efforts have been devoted for the synthesis of ecofriendly, biocompatible Iron Oxide NPs. Magnetite ( $\text{Fe}_3\text{O}_4$ ) and Maghemite ( $\gamma$ -  $\text{Fe}_2\text{O}_3$ ) and Hematite ( $\alpha$ - $\text{Fe}_2\text{O}_3$ ) are promising member of Iron oxide family. Promising qualities of these nanoparticles can be applicable in the field of specific technical and biomedical applications. Nanostructuring can result a new magnetic state called superparamagnetism. In this study an experimental setup is designed to observe the size effect in magnetic properties of the material with the preparation of Magnetite ( $\text{Fe}_3\text{O}_4$ ) and Maghemite ( $\gamma$ -  $\text{Fe}_2\text{O}_3$ ) as magnetic sample and observed that ensemble of particles together show superparamagnetism at elevated temperatures. The morphology of the particles has also been studied. Theoretical analysis on superparamagnetism where there is an unusual change in shape of hysteresis loop showing state of zero magnetization has also been discussed.

**Keywords:** Nanomagnetism, Superparamagnetic, Nanoparticle, Ferromagnetism.

### INTRODUCTION:

Various studies have been done on different metal oxide particles. Among the different metal oxide studies, iron oxides ( $\text{Fe}_x\text{O}_y$ ) NPs can offer unique advantages over others. The promising contributions towards many technological applications like targeted drug delivery, magnetic resonance imaging (MRI), bio sensing, bio separation etc increases the attention of researchers towards this engineered material. The inexpensive production, biocompatibility and safety to environment and other living being, made great contribution to develop interest to investigate this noble material [1-5]. Among the other properties Iron oxide NPs are physically and chemically stable that can be manipulated under the influence of an external magnetic field. Due to the reduction in size, magnetic ordering inside the particle changes, at the same

time surface property also changes remarkably [6]. Magnetic behaviour shown by many NPs can be attributed to many factors like chemical composition, structural distribution, amount of defectiveness and type of defectiveness present in crystal lattice. The size, shape and morphology of the particle and its interaction with the surrounding matrix and neighbouring particles provide major contribution in deciding magnetic nature of the particles. Among various magnetic metal oxides iron oxides ( $\text{Fe}_x\text{O}_y$ ) NPs are considered to be technologically more important, eco-friendly and comparatively less hazardous.

Iron oxides are found to be exists in nature in many forms. Magnetite ( $\text{Fe}_3\text{O}_4$ ) and Maghemite ( $\gamma\text{-Fe}_2\text{O}_3$ ) and Hematite ( $\alpha\text{-Fe}_2\text{O}_3$ ) are most commonly found iron oxide forms in nature [11]. Among these commonly available iron oxides Magnetite and Maghemite has got more attention and investigation on its application in the field of biomedical. Both Magnetite ( $\text{Fe}_3\text{O}_4$ ) and Maghemite ( $\gamma\text{-Fe}_2\text{O}_3$ ) shows their biocompatibility and low toxic nature towards human health and other living world.

Magnetite ( $\text{Fe}_3\text{O}_4$ ) and Maghemite ( $\gamma\text{-Fe}_2\text{O}_3$ ) generally found to contain single domain of about 5–20 nm in diameter and therefore possess large surface area as compared to volume. The quantum size effects at nanodimension also lead to some dramatic change in magnetic behaviour of the iron oxide material resulting in superparamagnetic behaviour and quantum tunnelling of magnetisation as well. The  $\text{Fe}_3\text{O}_4$  nanocrystal shows spinal structure where  $\text{Fe}^{3+}$  ions are distributed randomly between octahedral and tetrahedral sites.  $\text{Fe}^{2+}$  ion occupies solely the octahedral sites having six oxide ions as the nearest neighbours [7]. Basically they are ferromagnetic and show the properties of spontaneous magnetisation in bulk state.

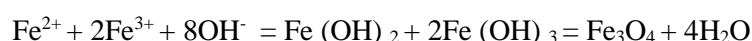
Synthetic route is one of the various factors that can affect the magnetic properties of a material. A synthetic route can affect strongly in determining the magnetic properties of Iron Oxide NPs also. Further it is reported by Margulies et al. that magnetic behaviour of magnetite nanoparticle changes with crystal morphology. The coercivity of the magnetite NPs are observed to be changed as sphere < cubes < octahedral [8,9]. The routes followed during preparation and the coating medium used may play key role in determining the size distribution, morphology, magnetic behaviour and surface chemistry of the magnetic nanoparticles. Hence the preparation method is one of the responsible factors for determining the intrinsic properties as well as the applications of iron oxide nanomaterials. A large variety of synthetic routes have been reported in the literature for the preparation of iron oxides ( $\text{Fe}_x\text{O}_y$ ) NPs which includes chemical co-precipitation method, hydrolysis, thermal decomposition, sol-gel method, microemulsion, sonochemical etc. [3,4,10]. These routes may be distinguished as aqueous routes and non -aqueous routes. Aqueous routes could draw more attention in the sense of their low cost high productivity side and are highly sustainable. Chemical co-precipitation method is the most commonly used versatile method for the production of  $\text{Fe}_3\text{O}_4$  or  $\gamma\text{-Fe}_2\text{O}_3$  NPs. This method critically affects the physical and chemical behaviour of nanoscopic iron oxide particles and generates wide variety of particles with wide size distributions.

Moreover it is observed that Fe<sub>3</sub>O<sub>4</sub>/γ-Fe<sub>2</sub>O<sub>3</sub> NPs without coating or naked are highly reactive and shows high tendency of aggregation. This high tendency towards aggregation can result poor magnetism, reactivity and mobility of NPs produced. Hence to avoid aggregation, chemical stability of the NPs is highly desirable and surface modification is very much necessary. To achieve chemically stable and less aggressive NPs the following methods may be adopted to stabilize nanoparticles as desired (a) Surface coating of NPs by using appropriate polymer stabilizers/surfactants (eg; carboxylates, phosphates) (b) By deposition of a layer of inorganic metals (e.g., gold) or nonmetals (e.g., graphite), or oxides (e.g. SiO<sub>2</sub>) (c) By the generation polymeric shells that avoid cluster growth after nucleation (composite particles, nanocapsule). (d) Forming lipid-like coatings (e.g., liposomes/ lipid NPs) around the magnetic core. Surface coating can result with improved quality of the nanoparticles in terms of chemical stability in the solvent. Particles with Surface coating reduce the particles aggregation remarkably hence this approach is very much popular in the field of biotechnology and medical science applications. [11, 12]. In the present work, our basic objective is to design ecofriendly co-precipitation method to synthesize magnetic iron oxide NPs with low cost additives and to analyse the results by studying morphological as well as enhanced magnetic properties due to size effect.

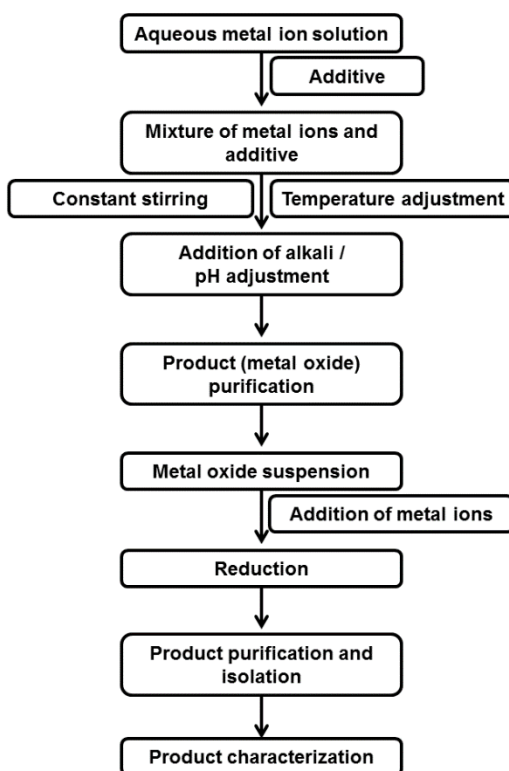
## 1. MATERIALS AND METHODS

### 1.1 Synthesis method

wet chemical method has been designed to synthesize the magnetic iron oxide NPs, as template based wet chemistry methods is reported to be the most appropriate, efficient and low cost method for the preparation of metal oxide NPs. The conventionally used co-precipitation method comprises the mixing of ferric and ferrous ions in 1: 2 molar ratios in high concentration of basic solutions at room temperature or at high temperature. The size and shape of the iron oxide NPs produced depends on the type of salt used, ion ratio of ferric and ferrous salt, temperature of the reaction, value of pH, stirring rate and speed of dropping of basic solution to the mixture of salts [13,14,15]. The reaction mechanism may be represented as



A schematic synthesis procedure opted in this present study is presented by **Scheme 1**.



**Scheme 1.** Schematic representation of co-precipitation synthetic route

### 1.2 Sample preparation

Fe<sub>3</sub>O<sub>4</sub> nanoparticles were prepared in the lab using the conventional co-precipitation method. Sample preparation has been done using anhydrous iron chloride (FeCl<sub>3</sub>, 98% purity) and Iron Sulphate heptahydrate (FeSO<sub>4</sub> 7H<sub>2</sub>O, 98.5% purity) from Merck and. NaOH as the basic solution. Methyl cellulose is used to give polymer coating to stabilize the nanoparticles and to avoid aggregation. Ferric and ferrous ions were mixed in the ratio 1:2 molar units in basic solution at different elevated temperatures. The reaction took place under the constant stirring of three hours duration using magnetic stirrer. A wide variety of factors has been adjusted to tune the size and morphology as well as to set the magnetic behaviour and surface properties of the produced iron oxide NPs. The temperatures were set at 50<sup>0</sup> C, 60<sup>0</sup>C, 70<sup>0</sup> C etc; The size and shape of nanoparticles were monitored controlling the pH value, adjusting the strength and nature of ion and salt and ion ratio of Fe (II) /Fe (III). The black precipitations produced after reaction were collected and were isolated to do the further treatment. The produced products were washed and centrifuged at 10000- 15000 rpm for three times and were dried. This conventional procedure is cheap and suitable for large scale production.

### 1.3 Characterisation of samples

#### 1.3.1 TEM image study

The products obtained were prepared for analytical treatment. The TEM images of the samples have been taken to study the morphology and the size distribution of nanoparticles. TEM image shows that the particles are almost uniform and cubical in shape and are poorly mono-disperse.

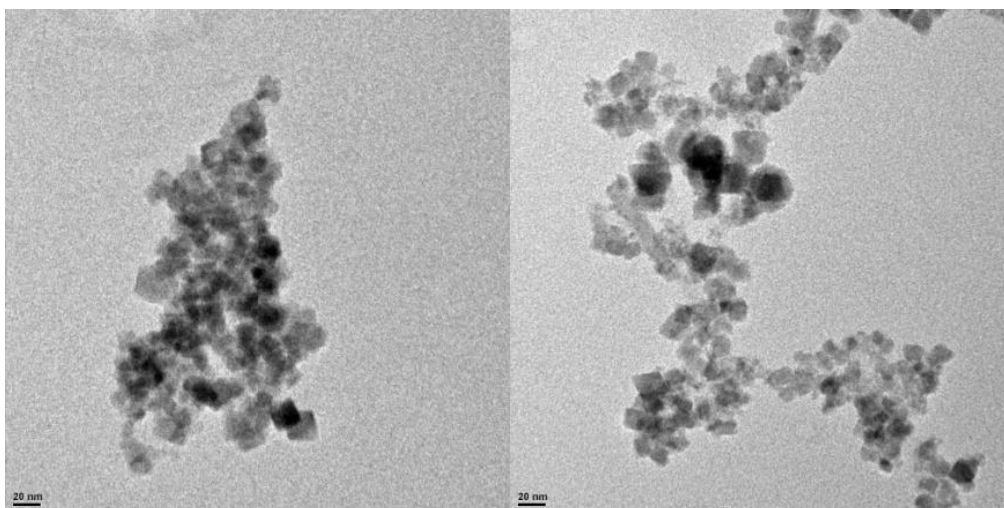


**Figure 1.** TEM image of IONP at 50<sup>o</sup> C.

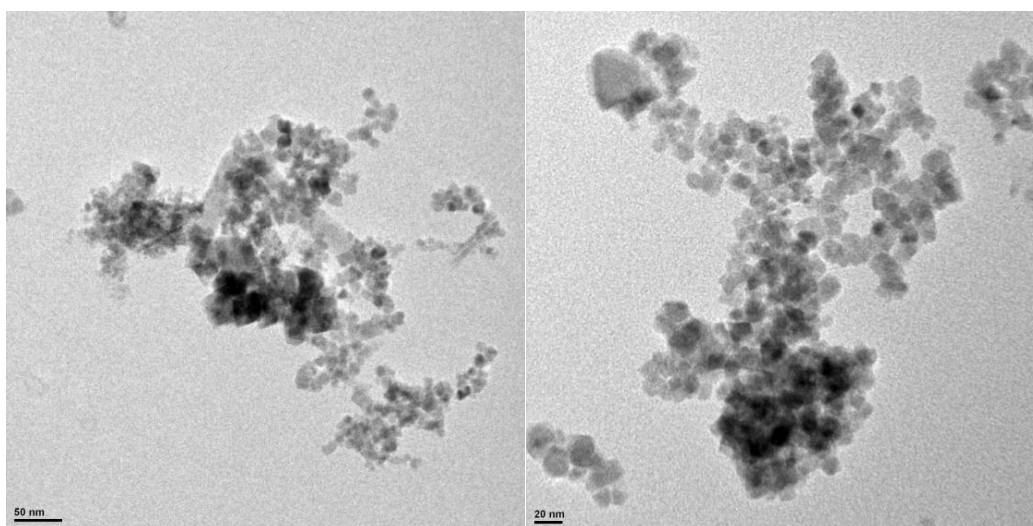


**Figure 2.** TEM image of IONP at 60<sup>o</sup> C.

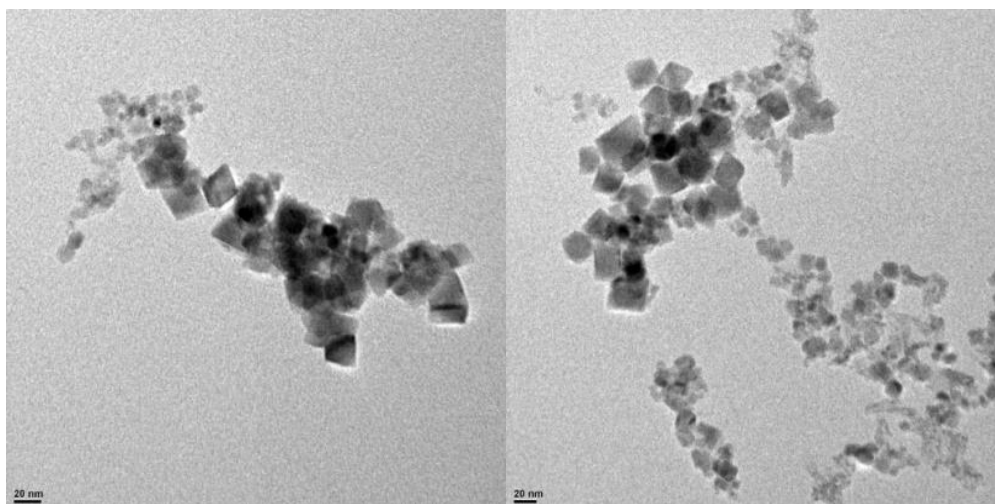


**Figure 3.** TEM image of IONP at 70<sup>0</sup> C

Figure 1, figure 2 and figure 3 show the TEM images at temperatures 50<sup>0</sup> C, 60<sup>0</sup> C and 70<sup>0</sup> C respectively. The ensemble shows well separated particle variation and cubical shape structure.

### 1.3.2 VSM study

In order to study the magnetic behaviour of Fe<sub>3</sub>O<sub>4</sub> NPs, the magnetization measurement of NPs were done with VSM. VSM is being the commonly used versatile method of measuring magnetic properties which determines the magnetic moment by vibrating the sample perpendicular to the uniform magnetic field in between a set of coils. The results have been analysed to study the Hysteresis loop of the sample.

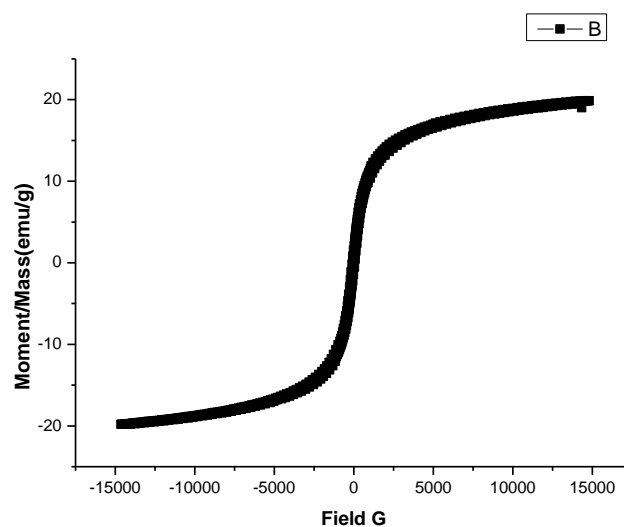


**Figure 4.** Hysteresis Curve of IONP at 60<sup>0</sup> C

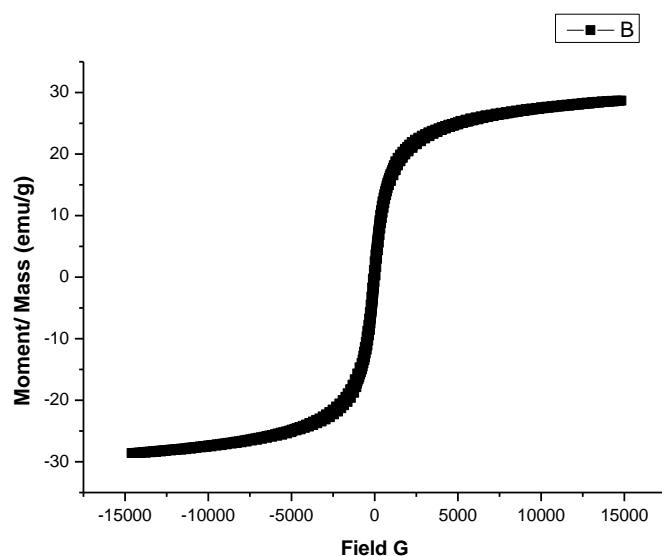


**Figure 5.** Hysteresis Curve of IONP at 70<sup>0</sup> C

Figure 4 and figure 5 show the Hysteresis curves of Fe<sub>3</sub>O<sub>4</sub> NPs at 60<sup>0</sup> C and 70<sup>0</sup> C. A plot has been drawn with Magnetic field Vs Magnetic moment and the Hysteresis curves of Fe<sub>3</sub>O<sub>4</sub> NPs were prepared. The resulted hysteresis loops are seen to be appeared like S shape or sigmoid shape. The thin curve shows no remanence and negligible coercivity.

## 2. RESULTS & DISCUSSION

TEM analysis shows that sizes of the particles are uneven and indicates agglomeration. Agglomeration is observed in all the prepared samples, but with rise in temperature magnetite particles becomes more uniform in size distribution. Although alglomeration is very difficult to avoid in magnetite nanoparticle, high centrifuge rate and surface coating by polymer can help to some extent.

VSM analysis results show that hysteresis loops obtained possess no particular area but they shows a curve passing through origin. This is a kind of typical paramagnetic behavior. This particular behaviour of hysteresis curve indicates the superparamagnetic properties of cubical shape Fe<sub>3</sub>O<sub>4</sub> NPs. It shows a very sharp and steep rise in magnetisation in the initial state following a gradual and smooth change of magnetisation with increasing magnetic field and finally reaching the saturation.

The term superparamagnetism refers to the physical description of non- interacting magnetic particle ensemble when particle size is reduced below a critical dimension in ferromagnetic or ferrimagnetic materials. Below critical size nanoparticles show unstable magnetization. This particular behaviour is due to quantum size effects and increased surface area of nano sized particles. At nano size, spin wave energy becomes comparable to thermal energy, hence spin-spin interaction becomes more prominent over

thermal energy hence energy barrier potential becomes in sufficient to control spin exchange. The exchange coupling that exist between the magnetic dipoles at room temperature or elevated temperature can result in random orientations of magnetic spins inside the particles which can result in zero remnant magnetisation and zero coercivity. This particular phenomenon is observed in magnetic nanoparticles if the thermal energy  $k_B T$  is of the same order of magnitude of anisotropy energy of the particles. This condition effectively leads to zero measured magnetic moment of the sample. The magnetization inverts spontaneously, as thermal energy  $k_B T$  is comparable to the anisotropy energy. Nanoscopic magnetic particles showing the phenomenon of superparamagnetism, thermal fluctuations play an important role in the magnetization process. This behaviour seems to be similar to paramagnetic behaviour but with a much steeper increase of susceptibility (higher susceptibility). The saturation magnetization which represents the spin alignments of the magnetic sample decreases with particle size [16-20].

The prepared sample of  $Fe_3O_4$  NPs shows superparamagnetism by flipping the magnetic moments resulting paramagnetic behavior. This is one of the important aspects of magnetic properties of  $Fe_3O_4$  NPs, at nanodimension. The saturation magnetisation  $M_s$  value for magnetic iron oxide NPs prepared have been observed to be around 20-30 emu/g which is smaller than the bulk saturation magnetisation value i.e. around 100 emu/g.

### 3. CONCLUSION

Transition metals are the most abundantly studied magnetic material because they are more relevant to the application in various fields. Scientific interest has been developed to study the basic and fundamental properties of Magnetic iron oxides in a more profound way. In the present work cubical shape  $Fe_3O_4 / \gamma-Fe_2O_3$  NPs were prepared using precipitation method. Particle system displays superparamagnetic behaviour at elevated temperature with the reduction of particle size at nanolevel. Saturation Magnetization value observed to be decreases compared to bulk value. Magnetite or Maghemite particles truly show the size effect when dimension is reduced to nearly atomic scale. Near future it is going to prove its great potentiality in the field of medical science.

### REFERENCES

- [1] Ai, H., Flask, C., Weinberg, B., Shuai, X. T., Page, I M. D., Farrel, D., Duerk, J. and Gao, J. Magnetite-loaded polymeric micelles as ultrasensitive magnetic- resonance probes. *Adv. Mater.* **17** (2005), 1949.
- [2] Song, H. T., Choi, J. S., Huh. Y. M., Kim, S., Jun, Y. W., Suh, J. S. and Cheon, J. Surface Modulation of Magnetic Nanocrystals in the Development of Highly Efficient Magnetic Resonance Probes for

- Intracellular Labeling. *J. Am. Chem. Soc.* **127** (2005), 9992.
- [3] Lee, N. and Hyeon, T. Designed synthesis of uniformly sized iron oxide nanoparticles for efficient magnetic resonance imaging contrast agents. *Chem. Soc. Rev.* **41** (2012), 2575.
- [4] Majewski, P. and Thierry, B. Functionalized Magnetite Nanoparticles – Synthesis, Properties, and Bio- Applications. *Crit. Rev. Solid St. Mater. Sci.* **32** (2007), 203.
- [5] Lübbe, A. S., Bergemann, C., Huhnt, W., Fricke, T., Riess, H., Brock, J. W. and Huhn, D. Preclinical experiences with magnetic drug targeting: tolerance and efficacy. *Can. Res.* **56** (1996), 4694.
- [6] Issa, B., Obaidat, I. M., Albiss, B. A. and Haik, Y. Magnetic Nanoparticles: Surface Effects and Properties Related to Biomedicine Applications. *Int. J. Mol. Sci.* **14** (2013) 21266.
- [7] Liu, X., Kaminski, M. D., Guan, Y., Chen, H., Liu, H. and Rosengart, A. J. Preparation and characterization of hydrophobic superparamagnetic magnetite gel. *J. Magn. Magn. Mater.* **306** (2006), 248.
- [8] Sena, S. P., Lindley, R. A., Blythe, H. J., Sauer, C., Al-Kafarji, M. and Gehring, G. A. Investigation of magnetite thin films produced by pulsed laser. *J. Magn. Magn. Mater.* **176** (1997), 111.
- [9] Qiu, H., Pan, L., Li, L., Zhu, H., Zhao, X., Xu, M., Qin, L. and Xiao, J. Q. Microstructure and Magnetic Properties of Magnetite Thin films Prepared by Reactive Sputtering. *J. Appl. Phys.* **102** (2007), 113913.
- [10] Laurent, S., Forge, D., Port, M., Roch, A., Robic, C., Vande, r Elst. L. and Muller, R. N. Magnetic iron oxide nanoparticles: synthesis, stabilization, vectorization, physicochemical characterizations, and biological applications. *Chem. Rev.* **108** (2008), 2064.
- [11] Cornell, R. M., Schwertmann, U. *The Iron Oxides: Structure, Properties, Reactions, Occurrences and Uses*, (Weinheim ed: Wiley-VCH, 2003)
- [12] Boyer, C., Whittaker, M.R., Bulmus, V., Liu, J. and Davis, T. P. The design and utility of polymer-stabilised iron-oxide nanoparticles for nanomedicine applications. *NPG Asia Mater.* **2** (2010), 23.
- [13] Safari, J., Zarnegar, Z., Heydarian, M. Magnetic Fe<sub>3</sub>O<sub>4</sub> Nanoparticles as Efficient and Reusable Catalyst for the Green Synthesis of 2-Amino-4H-chromene in Aqueous Media. *Bull. Chem. Soc. Jpn.* **85** (2012), 1332.
- [14] Okuda, M., Takeguchi, M., O Ruairc, O., Tagaya, M., Zhu, Y., Hashimoto, A., Hanagata, N., Schmitt, W. and Ikoma, T. Structural analysis of hydroxyapatite coating on magnetite nanoparticles using energy filter imaging and electron tomography. *J. Elec. Micro.* **59** (2009). 173.
- [15] Fadli, A., Komalansari, Adnan, A., Iwantono, Rahimah and Addabsi, A.S. Synthesis of Magnetite Nanoparticles via Co- precipitation Method. *IOP Conf. Series: Mat. Sci. and Eng.* **622**(2019), 012013
- [16] Guimaraes, A. P. *Principles of nano magnetism*, NanoScience and technology , ISBN 978-3-642-01481-9
- [17] Goll, D., Berkowitz, A.E. and Bertram, H. N. Critical sizes for ferromagnetic spherical hollow nanoparticles. *Phys. Rev. B* **70** (2004), 184432

[18] Bean, C. P., Livingston, J.D. Superparamagnetism. *J. Appl. Phys.* **30** (1959), S120

[19] Schmid, G. ed., *Nanoparticles: From Theory to Application*, Wiley-VCH Verlag GmbH & Co. KGaA, 2004.

[20] Yang, C., Hou, Y. L. and Gao, S. Nanomagnetism: Principles, nanostructures, and biomedical applications. *Chinese Phys. B* **23** (2014), 057505

## Plasmon Resonances in Interacting Ni Nanoparticles Embedded in Dielectric

Jayanta Kumar Majhi

Post Graduate Department of Physics, Banwarilal Bhalotia College, Asansol, India.

Email: [devmajhi794@gmail.com](mailto:devmajhi794@gmail.com)

### ABSTRACT

The optical absorption (OA) properties of interacting Ni nanoparticles (NPs) of radius 10 nm embedded in dielectric have been studied theoretically, using modified Maxwell-Garnett (MG) model. The OA spectra for non-interacting NPs exhibit two broad absorption bands corresponding to 3.69 eV and 6.06 eV in lower and higher energy region. These absorption bands come from surface plasmon resonance (SPR) in Ni NPs. Here, we have considered interacting Ni NPs and the interaction is represented by a parameter  $K$ . For our calculation we have varied the value of  $K$  from 0 to 50. Interestingly, the plasmon resonance peak shift towards lower energy with increase of  $K$ . This can be explained on the basis of driven damped harmonic oscillator model. It is well known that Ni is a strong ferromagnetic material. Therefore, the simultaneous existence of ferromagnetic and plasmonic properties make the Ni NPs more superior and can be used as optical nano-antennas for magnetic manipulation and also in different optoelectronic and photonic devices.

**Keywords:** Ni nanoparticles, surface plasmon resonance, interparticle interaction, redshift

### INTRODUCTION:

The studies of optical absorption (OA) properties of interacting metal nanoparticles (NPs) and their assemblies attracted a lot of attention due to their transport and guiding ability to the electromagnetic wave in nano-optics [1]. The most of the research work have been focused on the surface plasmon resonance (SPR) in noble metal NPs and their assemblies. For interacting noble metal NPs, the plasmon mode has been demonstrated for interparticle separation much less than the wavelength of exciting electromagnetic radiation [2-4]. Although, several works have been done in this direction, but the less attention has been paid to transition metal like Ni, Co and Fe. Due to much higher SPR energies, the Ni NPs could also be of technological interest for UV photonic applications than those of noble metals. However, the application of SPR in Ni NPs is

not limited to UV regime rather; it finds applications in photonics, non-linear optics, optoelectronics [5], biosensors [6] and others. The SPR is very important phenomenon of the optical properties of metal. The theory of SPR depends on the Drude free electron model of metal. For free electron like metals this model is highly applicable, although, some departures from the model can be found in case of few metals for their SPR energies lying very close to the d-band and hence the interaction between them cannot be neglected [7].

Recently, multiple SPR absorption bands corresponding to non-interacting Zn [8, 9] and Ni NPs [10, 11] embedded in dielectric (silica) has been reported [12]. In both the cases the OA bands were recognized as SPR [8, 10, 11, 12]. A considerable peak shift with interaction in case of noble metals has also been observed [13].

In this article, the interparticle interaction is taken into account to calculate the OA spectra of Ni NPs using the modified MG model [14]. Here, we have varied the parameter  $K$  from 0 to 50 for a particle of radius 10 nm. Interestingly the both SPR peaks show redshift with increase of the parameter  $K$  and arise due to the SPR of the surface electrons in Ni NPs. This property of interacting transition metal NPs can be used to tune the plasmon resonance from UV to visible region of electromagnetic spectrum.

## CALCULATION METHOD

The SPR properties of the small spherical metal particles have been generally studied using Mie theory in the “quasi-static limit”. In this limit, extinction can be regarded as absorption. But in a relatively denser medium one uses the MG type effective medium theory [14]. The details of the theory can be found in the reference [15]. In the calculation the concept of effective dielectric function has been used and we have considered the interacting Ni NPs. The interaction is regarded as a parameter designated by  $K$  whose values were taken from 0 to 50 with a fixed particle size ( $R = 10$  nm). The volume fraction ( $f = 0.1$ ) and dielectric function (DF) of the surrounding medium were kept fixed.

## RESULTS & DISCUSSION

In Fig. 1(a) we have shown the calculated OA spectra of spherical non-interacting Ni NPs, of radius 10 nm embedded in silica glass. The spectra show two broad absorption bands at around 3.69 and 6.06 eV which are believed to be appeared due to surface plasmon resonance [1]. The OA spectra corresponding to interacting Ni NPs also exhibit the two SPR absorption peaks as shown in the Fig. 1(b). The SPR peaks are found to become prominent and shift towards lower energy side with increase in the values of the parameter  $K$ . The observation of the shift of plasmon absorption peak clearly indicates that there is a substantial redshift in both the bands with increase of  $K$ .

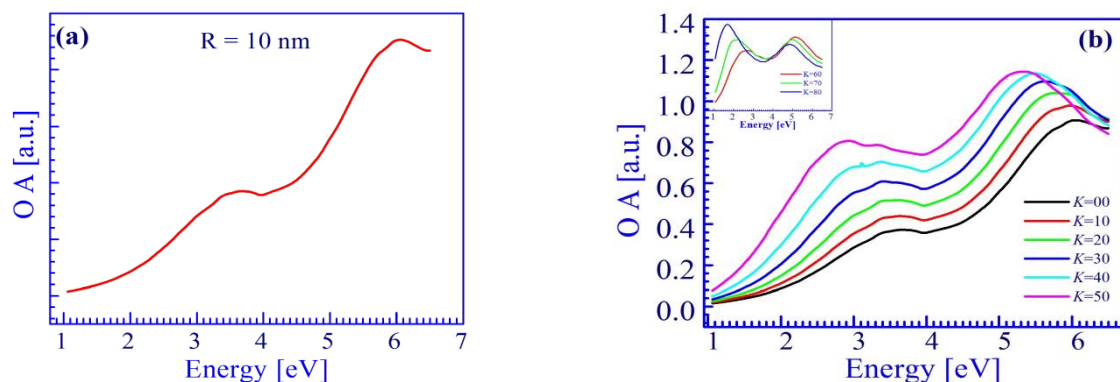


Fig. 1: The OA spectra as function of energy for (a) non- interacting and (b) interacting Ni NPs of radius 10 nm embedded in silica. Inset shows the spectra for some other particle size.

Further, the intensity of the absorption peaks has been found to increase with increase in the interaction with corresponding reduction in its full width at half maximum (FWHM). The existence of such SPR bands has also been observed experimentally in Ni NPs embedded in silica matrix with peak positions around 3.3 eV and 6.0 eV respectively [10]. Although, there are some differences between the experimental and theoretical results due to inconsistency in the available literature data for the dielectric constants of Ni. The effect of this interaction on the SPR absorption for Ni is as strong as that of SPR absorption in noble metal NPs [14]. For transition metal NPs the size dependent SPR energy is determined using the following condition [5, 10, 16] given by the equation

$$[\{\varepsilon_1(\omega) + 2\varepsilon_m(\omega)\}^2 + \varepsilon_2^2(\omega)] = \text{Minimum}, \quad (1)$$

where  $\varepsilon_1$  and  $\varepsilon_2$  are the real and imaginary parts of the DF of the metal NPs, and  $\varepsilon_m$  is the dielectric constant of the medium. All the parameters are frequency dependent. In most of the cases, for simplicity the following condition is used to find the SPR criterion [12],

$$\{\varepsilon_1(\omega) + 2\varepsilon_m(\omega)\} = 0 \quad (2)$$

instead of Eq.(1). Although, it is derived and found by neglecting  $\varepsilon_2(\omega)$  from Eq.(1). We can make such assumption for small values of  $\varepsilon_2(\omega)$  but for larger values Eq. (2) cannot be used. The actual mechanism of SPR absorption of Ni has been explained clearly in the ref.[13] and one can confirm that both the bands appeared due to SPR [12]. For interacting Ni NPs the SPR frequency can be estimated by considering the point dipole approximation. However, the SPR energy may be changed with the size but such change for interacting NPs is weaker in comparison to the change due to dipole-dipole interaction. When the particles come close to each other, the electromagnetic interaction comes into play and the electric field get distorted [17]. The amount of distortion depends on the separation between the particles and hence the interaction. Such changes lead to splitting of the SPR energy due to two types of polarization modes namely transverse and longitudinal [18]. The higher energy peak is associated with the transverse polarization while the lower energy peak is with the longitudinal polarization mode [19]. The SPR peak energy decreases linearly with the increase of  $K$  as shown in Fig. 2(a)-(b).

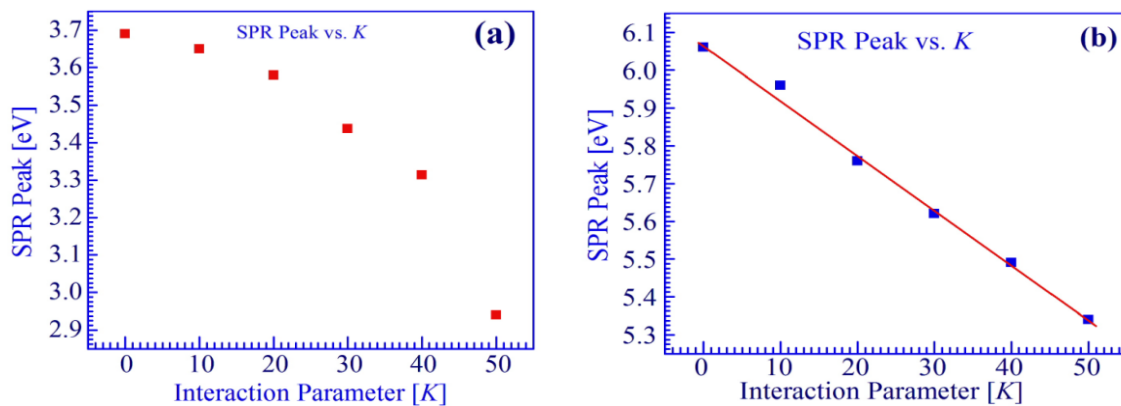


Fig. 2 The variation of the (a) lower and (b) higher energy SPR Peak with the parameter  $K$

Thus the range of tunability of the SPR absorption is greatly enhanced by considering interaction between the particles. Although, in case of the lower energy peak, the variation is nonlinear but more or less the trend of the shift is the same i.e. both the peak show redshift. It is also seen that the shift of both the SPR peak for interacting particles is more pronounced than the corresponding **shift of SPR peak** for non-interacting **nanoparticles (i.e.  $K=0$ )**, that means the effect of interparticle interaction on the SPR absorption is more than that of the effect of particle size on the SPR in case of Ni NPs. Actually the plasmon peak shift is associated with the materials intrinsic plasmon damping which can be explained on the basis of driven damped harmonic oscillator model in which the oscillator amplitude is associated with near field amplitude and the energy dissipation is associated with far field extinction [19]. Although, the damping is not only the reason of the spectral shift, rather in nanostructure the size effect and larger value of the imaginary part of the dielectric function also play an important role [19].

## CONCLUSION

The OA spectra of interacting Ni NPs of radius 10 nm embedded in silica have been calculated theoretically using modified MG model. The calculated spectra exhibit two absorption bands, one in the higher energy side and other in the lower energy region. The positions of both the absorption band have been found to shift towards lower energy side with increase in the value of  $K$ . Such observation is mainly due to the dipole-dipole interaction. The higher energy peak is stronger than that of the lower energy peak. In addition due to the large spectral shift between the lower and higher energy peaks, and simultaneous ferromagnetic and plasmonic properties, the Ni NPs is suitable material for use of plasmonic antenna and in nanophotonic devices etc.

## REFERENCES

- [1] J.K Majhi, P.K. Kuiri, AIP Conf. Proce.,1665, 050015 (2015)
- [2] S. A. Maier, P. G. Kik, H. A. Atwater, S. Meltzer, E. Harel, B. E. Koel and A. A. G. Requicha, Nat. Mater., 2, 229 (2003)
- [3] J. R. Krenn, et al., Phys. Rev. Lett., 82, 2590 (1999)
- [4] S. A. Maier, P. G. Kik and H. A. Atwater, Appl. Phys. Lett., 81, 1714 (2002)
- [5] M. L. Brongersma, J. W. Hartman and H. A. Atwater, Phys. Rev. B: Condens. Mater. Phys., 62, 16356 (2000)

- [6] A. L. Stepanov, Rev. Adv. Mater. Sci. 26, 1 (2010).
- [7] M. O. Cağlayan, N. Atar, and Z. Üstündağ, J. Comput. Theor. Nanosci 10, 1248 (2013)
- [8] Y. Takeda et al. Nucl. Instrum. Methods B 257, 47 (2007)
- [9] H. Amekura et al., Nanotechnology, 18, 395707 (2007)
- [10] P. K. Kuri, J.K. Majhi, Plasmonics, 1, 11 (2017)
- [11] H. Amekura, Y. Takeda and N. Kishimoto, Nucl. Instrum. Methods B 222, 96 (2004)
- [12] T. Isobe et al., J. Non-Cryst. Solids, 189, 173 (1995)
- [13] J. K. Majhi, P. K. Kuri, AIP Conference Proceedings: Vol 1665, No 1
- [14] J. K. Majhi , S. K Mondal and P. K Kuri, Energy Environ. Focus, 2017
- [15] J.K.Majhi , A.C. Mandal , and P.K.Kuri J. Comput. Theor. Nanosci 12 (2015) 2997
- [16] M.A. Gracia, J. Llopis, and S E Paje, Chem. Phys. Lett. 315, 313 (1999)
- [17] H. Hövel, S. Fritz, A. Hilger, U. Kreibig, and M. Vollmer, Phys. Rev. B 48, 18178, (1993)
- [18] J. Wang et al Nanoscale, 2, 681 (2010)
- [19] Y. Xia and N. J. Halas, MRS Bull., 30, 338 (2005)

## **Tera-Hertz Optical Asymmetric Demultiplexer (Toad) Using Quantum Dot Semiconductor Optical Amplifier**

**Kousik Mukherjee**

Physics Department, B B College, Asansol, West Bengal India  
Centre of Organic Spintronics and Optoelectronic Devices, Kazi Nazrul University, Asansol, West Bengal India

### **ABSTRACT**

TOAD is an important all-optical switch having various applications in all-optical logic gates and processors. It also finds applications in designing different types of processors for optical networking like code converters, parity checkers, generators etc. Most of the TOAD based designed so far reported used Semiconductor Optical Amplifier (SOA) for designing the TOAD, but in this communication, conventional SOA is replaced by quantum dot SOA or QDSOA. This enables the device to operate with a high speed as demanded by modern-day optoelectronic communication systems. QDSOA has a higher operating speed due to its lower gain recovery time compared to conventional SOA. This paper investigates TOAD based on QDSOA as an optical switch..

**Keywords:** TOAD; Quantum dot SOA; Optical Switch; Extinction ratio

### **INTRODUCTION:**

Tera-Hertz Optical Asymmetric Demultiplexer (TOAD) is an important device for all-optical signal processing [1-5]. These TOADs use single Semiconductor Optical Amplifier (SOA) for its operation. Another variant of TOAD is found in the works [6-10] is called dual control dual SOA TOAD or DCTOAD. The application of DCDSTOAD makes the system hardware less complex. However, most of these TOADs use conventional SOAs with bulk semiconductor materials. Semiconductor optical amplifiers also use quantum dots in place of bulk materials to show improvements in the performance of the devices [11]. Quantum dot SOA (QDSOA) has advantages over its bulk counterparts as they show higher saturation power, larger gain bandwidth, pattern effect free nonlinearities like cross gain modulation (XGM), cross-phase modulation (XPM), and four-wave mixing. Moreover, QDSOAs have a slower population and polarization relaxations are the reason for these improved nonlinearities. Therefore, QDSOA

based devices will show improved performance [12]. The work [12] describes a 4bit digital to analog converter (DAC) using quantum dot SOA based TOAD (QDSTOAD). This motivates to use QDSOA in TOAD and see the effects as optical switch. In Figure 1, self-assembled InGaAs quantum dots on GaAs substrate is used to design the QDSOA, in which the wetting layer is grown with Stranski- Kranstanow mode[11].

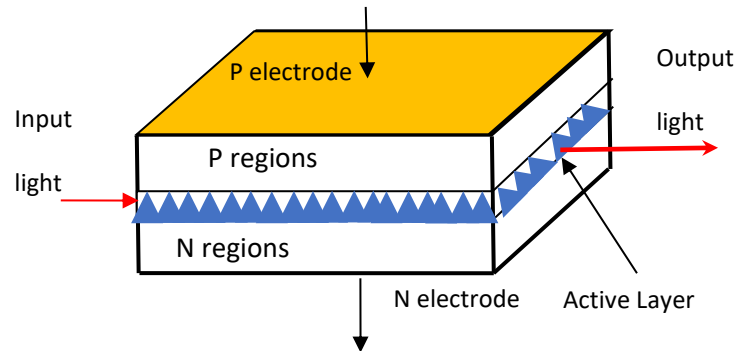


Figure 1. Quantum dot SOA

TOAD based on QDSOA is shown in figure 2. It consists of a fiber loop with a QDSOA placed asymmetrically acts as a nonlinear element. The control power changes the gain and phase of the data signal which after circulating the loop from opposite direction interfere and gives two outputs at destructive and constructive ports.

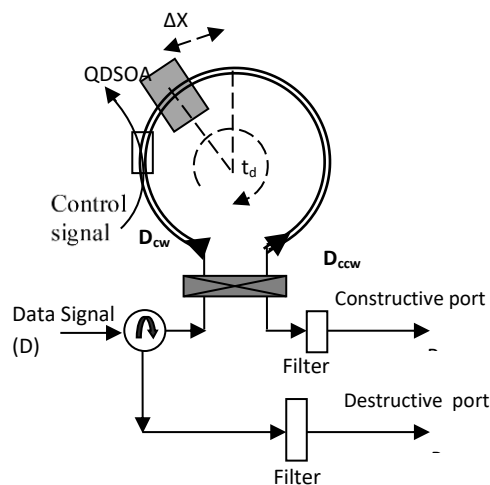


Fig 2. TOAD based on QDSOA

The outputs of constructive port and destructive ports are given by

$$P_{T,R} = 0.25P_{in}[G_0 + G(t) \pm 2\sqrt{G_0G(t)} \cos(\Delta\theta)] \quad (1),$$

where  $G_0$  is the unsaturated gain and  $G(t)$  is the time-dependent gain and  $\Delta\theta$  is the phase difference between interfering co and counter-propagating data signals  $D_{cw}$  and  $D_{ccw}$  as shown in figure 2.

### MATHEMATICAL MODELING:

To investigate dynamics of the QDSOA, rate equation model described in [12, 13] is considered. The following equations (2) to (5) are numerically solved to calculate extinction ratio(ER):

$$\frac{\partial N}{\partial t} = \frac{J}{eL_w} - \frac{N(1-h)}{\tau_{w2}} + \frac{N_Q}{\tau_{2w}L_w} - \frac{N}{\tau_{wR}} \quad (2)$$

$$\frac{\partial h}{\partial t} = -\frac{h}{\tau_{2w}} - \frac{N(1-h)L_w}{\tau_{w2}N_Q} + \frac{(1-f)h}{\tau_{21}} - \frac{f(1-h)}{\tau_{12}} \quad (3)$$

$$\frac{\partial f}{\partial t} = \frac{(1-f)h}{\tau_{21}} - \frac{f(1-h)}{\tau_{12}} + \frac{f^2}{\tau_{1R}} - \frac{L_w g_{max}(2f-1)P}{N_Q A_{eff} h \nu} \quad (4)$$

Here  $N, h,$  and  $f$  are the occupation probabilities of wetting layer, excited state, and ground-state respectively. Signal propagation along the length ( $z$ -direction) of the QDSOA is given by[13],

$$\frac{\partial P}{\partial z} = \frac{[g_{max}(2f-1) - \alpha_{int}]P}{A_{eff} h \nu} \quad (5)$$

Where  $P$  is the total input power injected into the QDSOA.

### SIMULATION RESULTS AND OPERATION:

Table 1 shows the parameters for the simulation used in this paper. These parameters (except the universal constants) are optimized for the performance of the device TOAD. The extinction ratio is defined as  $ER = 10\log_{10}(P_1^{\min}/P_0^{\max})$ , where  $P_1^{\min}$ , and  $P_0^{\max}$  are minimum power of output '1' and a maximum power of output bit '0' respectively.

---

Table 2. Parameters used for simulations[12]

---

Spontaneous lifetime(radiative) in the WL( $\tau_{wR}$ ) = 0.2 ns
Relaxation time of electron from the WL to ES( $\tau_{w2}$ ) = 3 ps
Relaxation time of electron from ES to GS( $\tau_{21}$ ) = 0.16 ps
Group velocity( $V_g$ ) = $8.3 \times 10^7$ m/s
Escape time of electron from ES to WL( $\tau_{2w}$ ) = 1 ns,
Escape time of electron from GS to ES( $\tau_{12}$ ) = 1.2 ps
Radiative lifetime(spontaneous) in Quantum Dot( $\tau_{1R}$ ) = 0.4 ns
Material gain coefficient, $g_{\max} = 14 \text{ cm}^{-1}$
internal loss $\alpha_{\text{int}} = 2 \text{ cm}^{-1}$
Injection current density, $J = 1 \text{ kA/cm}^2$
$L_w = 250 \text{ nm}$
Transparent current density, $N_Q = 5.0 \times 10^{10}$
Effective area, $A_{\text{eff}} = 0.75 \text{ } \mu\text{m}^2$ .

---

We have first optimized the QDSTOAD for the control power. It is found that an ER value of 3.86dB, and 28.5dB are calculated for 1.5mW of control power for transmitted port and reflected port respectively (Figures 3 and 4). This shows that the reflected port has better ER than the transmitted port and has better switching operation.

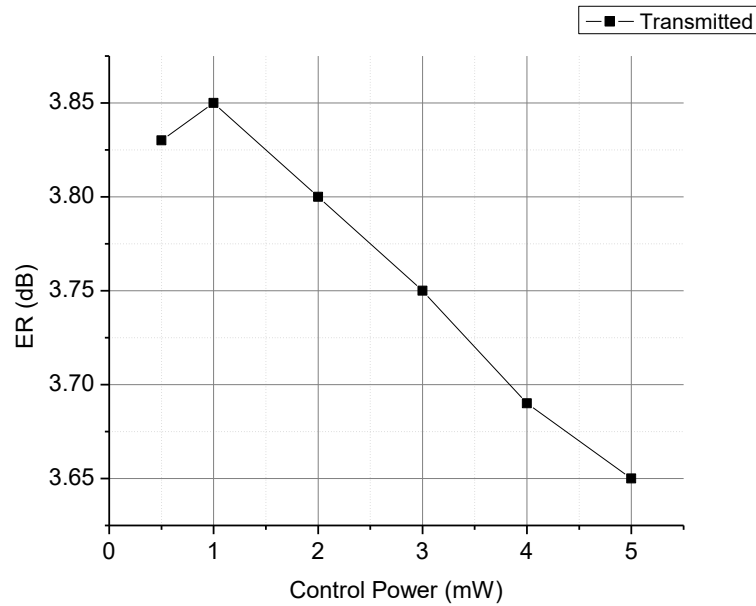


Figure 3. Variation of ER of transmitted port with control power

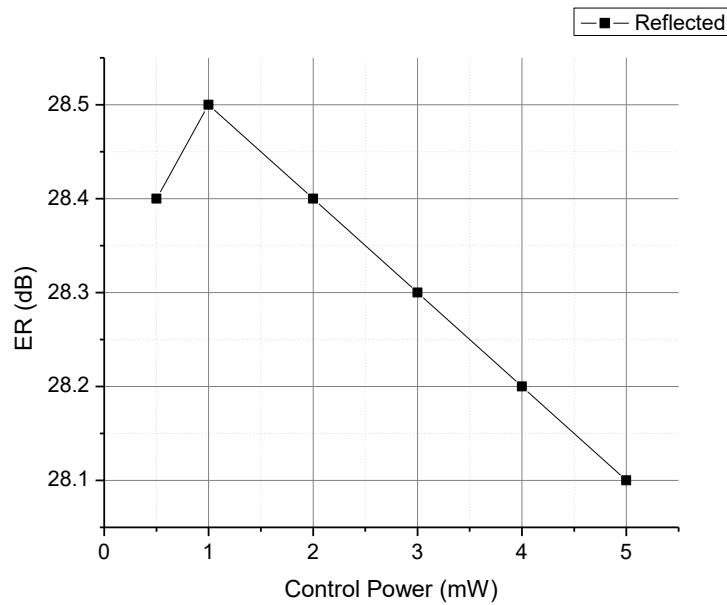


Figure 4. Variation of ER of reflected port with control power

Figure 5 optimizes ER for line-width enhancement factor (LEF) and it is found that a maximum ER of 3.86dB is for LEF equals to 5 for the transmitted port. However, ER values decrease with LEF for the reflected port as clear from figure 5.

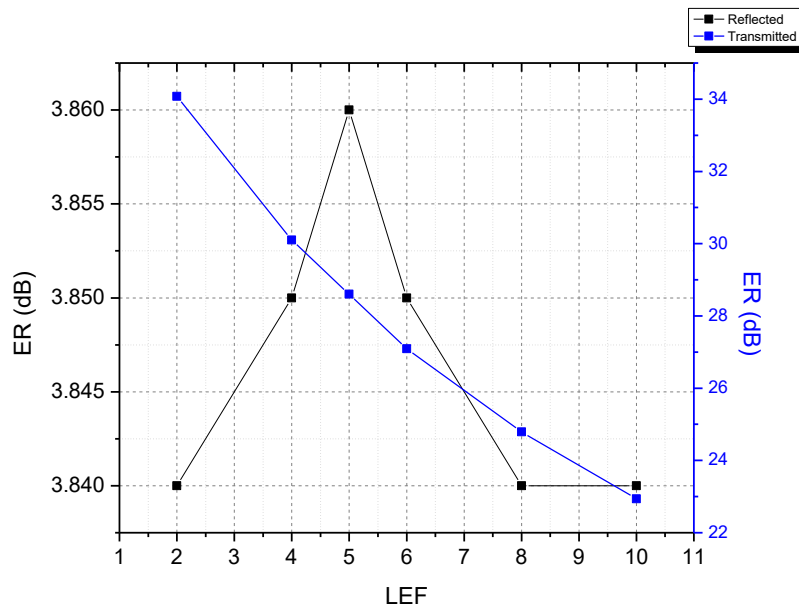


Figure 5. Variation of ER with LEF

**CONCLUSIONS:** In this paper, QDSOA based TOAD is designed and investigated theoretically using numerical modeling and ER is calculated for both the ports. The reflected port shows ER value as high as 28.5dB. In the future, the TOAD needs further investigation in terms of different parameters like amplitude modulation(AM), contrast ratio(CR), Quality factor(Q), etc.

## REFERENCES

- [1] K. Mukherjee, "Terahertz Optical Asymmetric Demultiplexer (TOAD) based frequency encoded all-optical NOT gate", Proceedings of the international conference on laser, materials, & communication, pp 242 – 244, Burdwan, India, December 7 to 9, 2011, ISBN 983 - 93 - 80813 - 14 - 1.
- [2] A. K. Mondal, All-Optical DFT using TOAD based Cross-Bar switches, JCSC, online ready, <https://doi.org/10.1142/S0218126619501561>.
- [3] A. Bhattacharya, D. Gayen, T. Chattopadhyay, Design of 2-to-4 All-Optical Decoder with the Help of Terahertz Optical Asymmetric Demultiplexer, International Journal of Modern Nonlinear Theory and Application, Vol.5 No.1, 2016.
- [4] K. Mukherjee, "Terahertz Optical Asymmetric Demultiplexer (TOAD) based frequency encoded all optical NOT gate", Proceedings of the international conference on laser,

- materials, & communication, pp 242 – 244, Burdwan, India, December 7 to 9, 2011, ISBN 983 - 93 - 80813 - 14 - 1.
- [5] K. Maji, K. Mukherjee, A. Raja, Frequency encoded all optical universal logic gate using tera hertz optical demultiplexer, *Int. Journal of Optics and Photonics*, 4,3,1-7(2018).
- [6] K. Maji, K. Mukherjee, Analysis of Soliton based XOR Gate using Dual-Control Terahertz Optical Asymmetric Demultiplexer (DCTOAD), *Journ. Optics and Photonics Technl.* 4,4,1-5(2019)
- [7] K. Maji and K. Mukherjee, "Performance analysis of optical logic XOR gate using dual-control Tera Hertz Optical Asymmetric Demultiplexer (DCTOAD)," *2019 Devices for Integrated Circuit (DevIC)*, Kalyani, India, 2019, pp. 58-60, doi: 10.1109/DEVIC.2019.8783496.
- [8] K. Maji, K. Mukherjee and M. K. Mandal, "Analysis of All Optical Dual Control Dual SOA TOAD Based 2's Complement Generator," *2020 IEEE VLSI DEVICE CIRCUIT AND SYSTEM (VLSI DCS)*, Kolkata, India, 2020, pp. 119-123, doi: 10.1109/VLSIDCS47293.2020.9179909.
- [9] K. Mukherjee, K. Maji, M. K. Mandal, Design and analysis of all- optical dual control dual SOA Tera Hertz asymmetric demultiplexer based half adder. *Opt Quant Electron* 52, 402 (2020). <https://doi.org/10.1007/s11082-020-02522-2>
- [10] K. Maji, K. Mukherjee, A. Raja, (2020). Design and performance analysis of all optical 4-bit parity generator and checker using dual-control dual SOA terahertz optical asymmetric demultiplexer (DCDS-TOAD), *Journal of Optical Communications* (published online ahead of print 2020), 000010151520190098. doi: <https://doi.org/10.1515/joc-2019-0098>
- [11] M. Sugawara, H. Ebe, N. Hatori, and M. Ishida, Theory of optical signal amplification and processing by quantum-dot semiconductor optical amplifiers, *PHYSICAL REVIEW B* 69, 235332, 2004.
- [12] K. Mukherjee, S. Dutta, S. Roy, et al. All-Optical digital to analog converter using Tera Hertz Optical Asymmetric Demultiplexer based on quantum dot semiconductor optical amplifier. *Opt Quant Electron* 53, 242 (2021). <https://doi.org/10.1007/s11082-021-02900-4>
- H. Baghban, R. Maram et al, Quantum dot semiconductor optical amplifiers: optical pumping versus electrical pumping, *Journal of Optics*, 13,035406,2011

## Direct Synthesis of Co<sub>3</sub>O<sub>4</sub> Nanomaterials By Carbonate Precursor

Arnab Kanti Giri\*<sup>1</sup> and Jong-Sung Yu<sup>2</sup>

<sup>1</sup>Department of Chemistry, Karim City College, Jamshedpur, Jharkhand, India

<sup>2</sup>Department of Energy Science and Engineering, Daegu Gyeongbuk Institute of Science and Technology, South Korea.

**Email:** *giri.arnabkanti54@gmail.com*

### ABSTRACT

Herein, the monodisperse Co<sub>3</sub>O<sub>4</sub> with various morphology is reported. Within this demonstration, a series of Co<sub>3</sub>O<sub>4</sub> with different morphology was synthesized using cobalt ammonium carbonate as precursor by hydrothermal method. In the present work we successfully synthesize pure phase of Co<sub>3</sub>O<sub>4</sub> microcube by direct (one step) hydrothermal process by carbonate-based precursor. The materials were characterized by XRD, SEM, TEM, EDX, TGA analysis. The kinetics have been studied for the formation mechanism of the materials. The materials were used for the post synthesis of core-shell type materials for different task specific applications.

**Keywords:** Co<sub>3</sub>O<sub>4</sub>, Nanostructure, Cube, Hydrothermal

### INTRODUCTION:

Co<sub>3</sub>O<sub>4</sub> has been widely considered as an efficient electrocatalyst [1-4]. Co<sub>3</sub>O<sub>4</sub> with spinel crystal structure is beneficial for the electron transport between Co<sup>2+</sup> and Co<sup>3+</sup> ions and considered an effective catalyst for OER processes [5-8]. But due to its low electrical conductivity and dissolution, short active site density and agglomeration nature during electrocatalytic processes, the electrocatalytic activity is not superior [8]. To overcome this problem research on faceted Co<sub>3</sub>O<sub>4</sub> nanostructure materials has been explored extensively [9-13]. Among the various faceted Co<sub>3</sub>O<sub>4</sub>, cubelike structure is one of the major morphology due its exposed {100} facet [14-17]. There are few reports for the synthesis of cubes like template assisted synthesis [14, 15], solution based hydrothermal process [16-17]. In some cases, the reaction time is longer by using urea as a reagent [16]. In these literatures strong base like NaOH was used [17]. For the synthesis of metal oxides using carbonates yields metal carbonate as an intermediate which upon heating produce the metal oxide. So, an additional step is required to synthesize the metal oxides. Direct synthesis of Co<sub>3</sub>O<sub>4</sub> nanoparticles without calcination process is a promising technique for the

development of  $\text{Co}_3\text{O}_4$ -based functional nanomaterials [17]. So, direct synthesis of faceted  $\text{Co}_3\text{O}_4$  nanostructures is the main focus of the present work.

In the present work, we report the direct hydrothermal synthesis of pure phase of  $\text{Co}_3\text{O}_4$  nanomaterials by carbonates. Elimination of strong hydroxide base or any organic or inorganic template for the synthesis of  $\text{Co}_3\text{O}_4$  cubes.  $\text{Co}_3\text{O}_4$  is used as a template for core shell void  $\text{Co}_3\text{O}_4@ \text{CoS}_2$ . The OER performances of the synthesized materials are quite good and expected to be a good energy material.

## MATERIALS & METHODS

### Chemicals.

Cobalt (II) Chloride, Hexahydrate was procured from Oriental Chemical Industry, South Korea; ammonium carbonate was purchased from Samchun Chemicals, South Korea. Potassium ethyl xanthogenate was purchased from Sigma Aldrich. All the chemicals were used as-obtained without any further purification. Water with a resistivity of  $18 \text{ M}\Omega \text{ cm}^{-1}$ , obtained from a Millipore water purifier, was used for all the performed experiment.

### Synthesis of Cube like $\text{Co}_3\text{O}_4$

11 g of Cobalt (II) Chloride, Hexahydrate dissolved in 500 mL of water. 40 ml of the solution was taken and 1.8 g of solid ammonium carbonate was added with continuous stirring (500 rpm). Within 2–3 min the solution became clear. Then, 160 ml of water was added to the clear solution and stirred (500 rpm) for 5 min. 50 ml of the resultant solution was diluted to 200 ml and then 50 ml transferred to Teflon lined stainless steel autoclave and kept in a pre-heated oven at  $200^\circ\text{C}$  for 2h. The resultant black materials were collected through centrifugation and washed with water for several times. The materials were dried at  $70\text{--}80^\circ\text{C}$  for 6 h.

### Synthesis of Cube like $\text{Co}_3\text{O}_4@ \text{CoS}_2$

In typical procedure, 0.5 gm  $\text{Co}_3\text{O}_4$  was dispersed in 40 ml water. Then 1 gm of Potassium ethyl xanthogenate was added to the solution and stirred for 5 min and transferred to Teflon lined stainless steel autoclave and kept in a pre-heated oven at  $200^\circ\text{C}$  for 4h. The resultant black materials were collected through centrifugation and washed with water for several times. The materials were dried at  $70\text{--}80^\circ\text{C}$  for 6 h. This synthesized  $\text{Co}_3\text{O}_4@ \text{CoS}_2$  treated with different temperatures in  $\text{N}_2$ ,  $\text{N}_2/\text{H}_2$  atmosphere.

## RESULTS & DISCUSSION

### Synthesis and characterization

From the XRD data it is confirmed that the pure  $\text{Co}_3\text{O}_4$  phase is obtained after hydrothermal treatment (**Fig. 1a**). JCPDS card No. 43-1003) and confirmed the formation of phase pure  $\text{Co}_3\text{O}_4$ . **Fig. 1b** represents the phase of  $\text{Co}_3\text{O}_4$  and  $\text{CoS}_2$ . The XRD pattern of the  $\text{Co}_3\text{O}_4$  nanoparticles present diffraction peaks at  $19^\circ$  (111),  $31^\circ$  (220),  $37^\circ$  (311),  $39^\circ$  (222),  $45^\circ$  (400),  $55^\circ$  (422),  $60^\circ$  (511) and  $65^\circ$  (440), which are indexed to the cubic phase of  $\text{Co}_3\text{O}_4$  spinel structure. The XRD pattern (**Fig. 1b**) of the  $\text{CoS}_2$  at  $27^\circ$  (111),  $32^\circ$  (200),  $39^\circ$  (211),  $46^\circ$  (220), which are index to  $\text{CoS}_2$  phase [18].

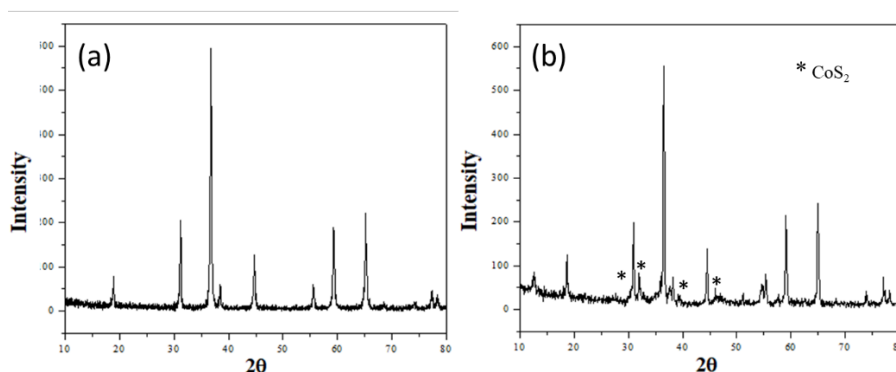


**Fig. 1** (a) XRD pattern of  $\text{Co}_3\text{O}_4$  and (b)  $\text{Co}_3\text{O}_4@\text{CoS}_2$

In the TG analysis (**Fig. 2**), a very little weight loss ( $\sim 1\%$ ) is observed. No distinct weight loss indicates the pure  $\text{Co}_3\text{O}_4$  phase in asynthesize product.

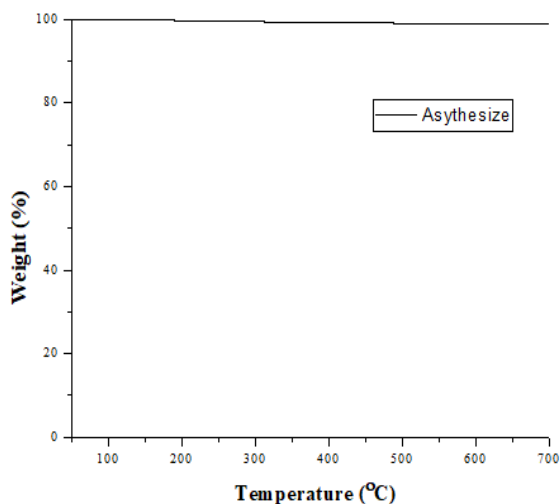


**Fig. 2** TGA analysis of asynthesized  $\text{Co}_3\text{O}_4$ .

Low-magnified SEM image (**Fig. 3a**) of  $\text{Co}_3\text{O}_4$  shows a cube like structure. From the SEM analysis it is also confirmed that the synthesized materials are monodisperse ( $\sim 95\%$ ). The

individual cubes are around 200-300 nm. TEM images of the hydrozincite also confirmed the cube like structure of  $\text{Co}_3\text{O}_4$  nanoparticles (**Fig. 3b**). All the TEM observations also support the SEM observations. The EDX mapping shows the Co and O (Red and Blue colour) in cubes and indicates the pure phase of  $\text{Co}_3\text{O}_4$  (**Fig. 4**).

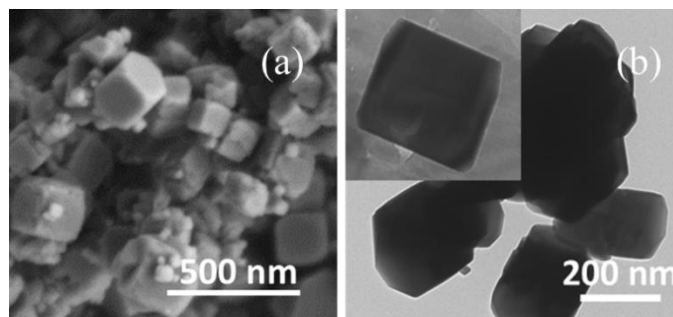


**Fig. 3** (a) SEM images and (b) TEM images of asynthesized Cube like  $\text{Co}_3\text{O}_4$ .

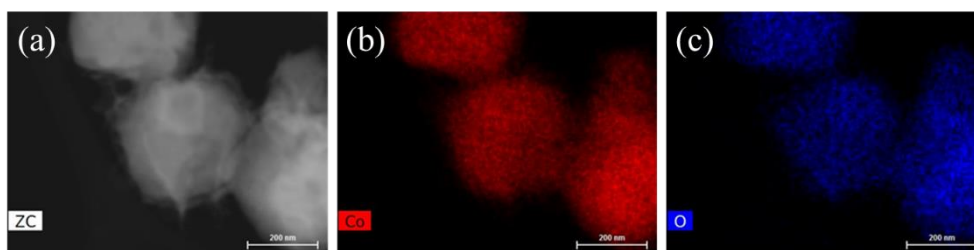


**Fig. 4** (a), (b) & (c) EDX mapping of Cube like  $\text{Co}_3\text{O}_4$  structure.

### Formation mechanism:

The formation mechanism of  $\text{Co}_3\text{O}_4$  is interesting and still a scope of research. Major focus was given to understand the core-shell formation mechanism. But the formation mechanism of  $\text{Co}_3\text{O}_4@\text{CoS}_2$  is well understood by the controlled experiments (**Table 1**). From the TEM analysis it is observed that when the  $\text{Co}_3\text{O}_4$ :Xanthate ratio is increased then the coating occurs effectively (**Fig. 5**). **Fig. 6** represents the mechanism of Void core-shell formation [19, 20]. In our case kirkendall diffusion is the most probable mechanism as per the experimental observation.

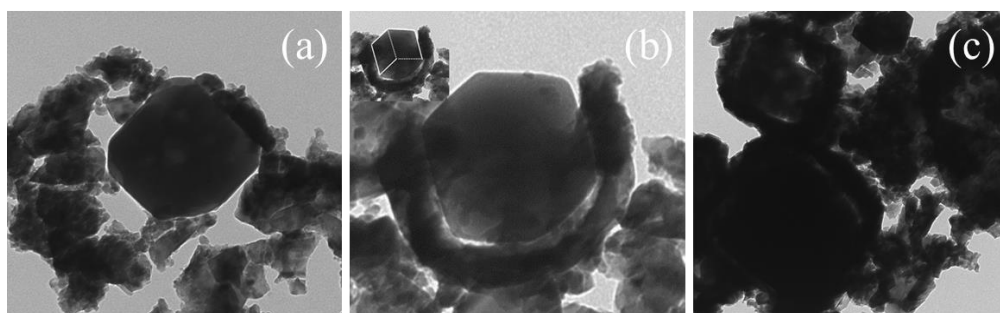


**Fig. 5** Controlled experiments (a) No coating, (b) partial coating and (c) full coating of CoS<sub>2</sub> on Co<sub>3</sub>O<sub>4</sub>.

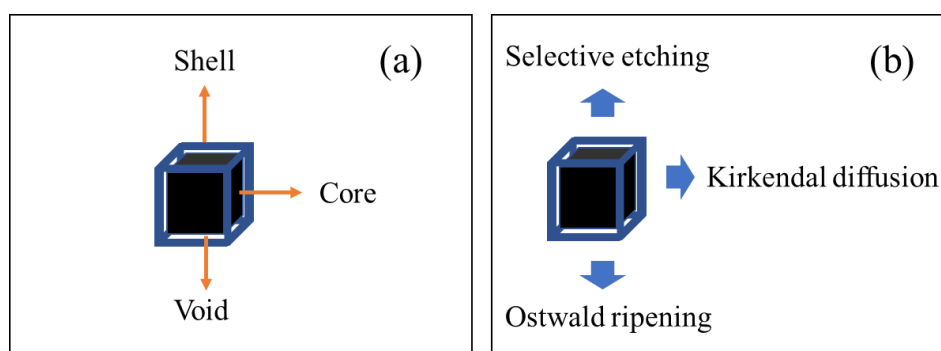


**Fig. 6** (a) & (b) Schematic representation of Void core-shell mechanism

From the controlled experiments the following equation can be predicted. The previous literatures also support the following reaction [20, 21]. Initially, xanthate decomposed to carbon disulphide (**Eq. 1**), CS<sub>2</sub> in presence of water and CS<sub>2</sub> reacts with Co<sub>3</sub>O<sub>4</sub> to form core-shell structure (**Eq. 2**).



**Table 1** Phase and morphology controlled by Potassium ethyl xanthate

Co <sub>3</sub> O <sub>4</sub> :X	Phase	Morphology
X= Potassium ethyl xanthate (mol ratio)		
1:0.5	Co <sub>3</sub> O <sub>4</sub> @CoS <sub>2</sub>	No coating
1:1	Co <sub>3</sub> O <sub>4</sub> @CoS <sub>2</sub>	Partial coating
1:1.5	Co <sub>3</sub> O <sub>4</sub> @CoS <sub>2</sub>	Full coating

### OER Performances:

The OER performances of Co<sub>3</sub>O<sub>4</sub> and Co<sub>3</sub>O<sub>4</sub>@CoS<sub>2</sub> was performed. The Co<sub>3</sub>O<sub>4</sub>@CoS<sub>2</sub>-H-500 C showed best performances among other synthesized catalyst. (**Fig. 7**) Co<sub>3</sub>O<sub>4</sub>@CoS<sub>2</sub>-H-500 C shoed the OER performances at 1.75 V (Vs. RHE) at 0.1 M KOH. This catalyst showed the lower overvoltage among the synthesized catalysts. The effect of calcination temperature with different gaseous environment on OER performances can be explained by increased crystallinity for better electron transport. But from the data it is shown that the OER performances of Co<sub>3</sub>O<sub>4</sub>@CoS<sub>2</sub> is better than Co<sub>3</sub>O<sub>4</sub>. This is due to the fast electron transfer between heterojunction of core-shell structure.

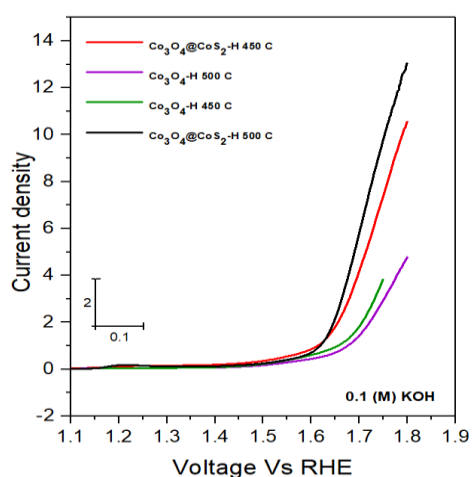


**Fig. 7** OER performances of Co<sub>3</sub>O<sub>4</sub> and Co<sub>3</sub>O<sub>4</sub>@CoS<sub>2</sub>.

## CONCLUSION

Monodisperse nanostructured  $\text{Co}_3\text{O}_4$  with different morphology was synthesized using cobalt ammonium carbonate as precursor by hydrothermal method. In the present work we successfully synthesize pure phase of  $\text{Co}_3\text{O}_4$  microcube by direct (one step) hydrothermal process by carbonate-based precursor. The materials were used for the post synthesis of core-shell type materials for different task specific applications. The kinetics have been studied for the formation mechanism of the materials and xanthate concentration play an important role for formation of void in core shell structure. The synthesis of this material requires simple laboratory instruments. The  $\text{Co}_3\text{O}_4@\text{CoS}_2$  core-shell material showed quite good OER performances and expected to be a useful energy material.

## ACKNOWLEDGEMENT

Author acknowledges to Prof. Jong-Sung Yu for financial support for this work. I acknowledge to DGIST, South Korea for all the characterizations of the materials. Author also acknowledges to Tong-Hyun Kang for the OER characterisations. Author also acknowledged to Dr. Asit Baran Panda, Principal Scientist, CSIR-LML, Jamshedpur, Jharkhand for the initial support of this work. Author acknowledges to Karim City College, Jamshedpur and Kolhan University, Chaibasa. Author is thankful to EMNSD 2020, organized by CIT, Kokrajhar, for giving the opportunity to present my work in this platform.

## REFERENCES

- [1] Akshatha, S., Sreenivasa, S., Parashuram, L., Udaya kumar, V., Alharthi, F. A., Rao, T. M. C. and Kumar, S. Microwave assisted green synthesis of p-type  $\text{Co}_3\text{O}_4$ @Mesoporous carbon spheres for simultaneous degradation of dyes and photocatalytic hydrogen evolution reaction. *Materials Science in Semiconductor Processing* **121** (2021), 105432.
- [2] Du, J., Li, C. and Tang, Q. Oxygen vacancies enriched  $\text{Co}_3\text{O}_4$  nanoflowers with single layer porous structures for water splitting. *Electrochimica Acta* **331** (2020), 135456.
- [3] Jayaseelan, S. S., Bhuvanendran, N., Xu, Q. and Su, H.  $\text{Co}_3\text{O}_4$  nanoparticles decorated Polypyrrole/carbon nanocomposite as efficient bi-functional electrocatalyst for electrochemical water splitting. *International Journal of Hydrogen Energy* **45** (2020), 4587.
- [4] Jiang, J., Chen, Y., Cong, H., Tang, J., Sun, Y., Hu, X., Wang, L., Han, S. and Lin, H. Highly efficient hydrogen evolution reaction of  $\text{Co}_3\text{O}_4$  supports on N-doped carbon nanotubes in an alkaline solution. *Ionics* **26** (2020), 3437.
- [5] Zhang, S. L., Guan, B. Y., Lu, X. F., Xi, S., Du, Y. and Lou X. W. (David) Metal Atom-Doped  $\text{Co}_3\text{O}_4$  Hierarchical Nanoplates for Electrocatalytic Oxygen Evolution. *Adv. Mater.* **32** (2020), 2002235.

- [6] Zheng, H., Xie, D., Li, H., Wu, S., Qin, B., Cui, Z., Zhang, X. and Zhang, J. 2D Metal Organic Framework Derived  $\text{Co}_3\text{O}_4$  for the Oxygen Evolution Reaction and High-Performance Lithium-Ion Batteries. *chemnanomat* **6** (2020), 1770-1775.
- [7] Araújo, M. P., Nunes, M., Rocha, I. M., Pereira, M. F. R. and Freire, C.  $\text{Co}_3\text{O}_4$  Nanoparticles Anchored on Selectively Oxidized Graphene Flakes as Bifunctional Electrocatalysts for Oxygen Reactions. *ChemistrySelect* **3** (2018), 10064.
- [8] Ahmed, M. S., Choi, B. & Kim, Y. Development of Highly Active Bifunctional Electrocatalyst Using  $\text{Co}_3\text{O}_4$  on Carbon Nanotubes for Oxygen Reduction and Oxygen Evolution. *SCIENTIFIC REPORTS* **8** (2018), 2543.
- [9] Jain, P., Gupta, S. and Vinod, C. P. Role of exposed crystal facets in the atmospheric pressure CO hydrogenation on CoO nanostructures. *Nano-Structures & Nano-Objects* **23** (2020), 100504.
- [10] Zhang, C., Zheng, F., Zhang, Z., Xiang, D., Cheng, C., Zhuang, Z., Li, P., Lia, X. and Chen, W. Fabrication of hollow pompon-like  $\text{Co}_3\text{O}_4$  nanostructures with rich defects and high-index facet exposure for enhanced oxygen evolution catalysis. *J. Mater. Chem. A* **7** (2019), 9059.
- [11] Yu, X., Meng, Q., Luo, T., Jia, Y., Sun, B., Li, Q., Liu, J. & Huang, X. Facet-dependent electrochemical properties of  $\text{Co}_3\text{O}_4$  nanocrystals toward heavy metal ions. *Scientific Reports* **3** (2013), 2886.
- [12] Wei, R., Zhou, X., Zhou, T., Hu, J. and Ho, J. C.  $\text{Co}_3\text{O}_4$  Nanosheets with In-Plane Pores and Highly Active {112} Exposed Facets for High Performance Lithium Storage, *J. Phys. Chem. C* **121** (2017) 19002.
- [13] Sun, H., Ang, H. M., Tadea, M. O. and Wang, S.  $\text{Co}_3\text{O}_4$  nanocrystals with predominantly exposed facets: synthesis, environmental and energy applications. *J. Mater. Chem. A* **1** (2013), 14427.
- [14] Geng, H., Guo, Y., Ding, X., Wang, H., Zhang, Y., Wu, X., Jiang, J., Zheng, J., Yanga, Y. and Gu, H. Porous cubes constructed by cobalt oxide nanocrystals with graphene sheet coatings for enhanced lithium storage properties. *Nanoscale* **8** (2016), 7688.
- [15] Lü, Y., Zhan, W., He, Y., Wang, Y., Kong, X., Kuang, Q., Xie, Z. and Zheng, L., MOF-Templated Synthesis of Porous  $\text{Co}_3\text{O}_4$  Concave Nanocubes with High Specific Surface Area and Their Gas Sensing Properties. *ACS Applied Material Interfaces* **6** (2014), 4186.
- [16] Cao, F., Wang, D., Deng, R., Tang, J., Song, S., Lei, Y., Wang, S., Su, S., Yangab, X. and Zhang, H. Porous  $\text{Co}_3\text{O}_4$  microcubes: hydrothermal synthesis, catalytic and magnetic properties. *Crystengcomm* **13** (2011), 2123.
- [17] Kanie, K., Tsujikawa, Y. and Atsushi, M. Direct Hydrothermal Synthesis of Size-Controlled  $\text{Co}_3\text{O}_4$  Nanocubes under Highly Condensed Conditions. *Materials Transaction* **58** (2017), 1014.
- [18] Chen, W., Wang, H., Li, Y., Liu, Y., Sun, J., Lee, S., Lee, J. and Cui, Y. In Situ Electrochemical Oxidation Tuning of Transition Metal Disulfides to Oxides for Enhanced Water Oxidation. *ACS Cent. Sci.* **1** (2015), 244.
- [19] Chee, W., Tan, S. F., Baraissov, Z., Bosman, M. and Mirsaidov, U. Direct observation of the nanoscale Kirkendall effect during galvanic replacement reactions. *Nature Communications* **8** (2017), 1224.

- [20] Giri, A. K., Charan, C., Ghosh, S. C., Shahi, V. K. and Panda, A. B. Phase and composition selective superior cholesterol sensing performance of ZnO@ZnS nano-heterostructure and ZnS nanotubes. *Sensors and Actuators B: Chemical* **229** (2016), 14.
- [21] GENISEL, M. F. Synthesis of Ti, Cr, Mn, Fe, Co, Ni, Cu, Zn Sulfides By Solid-Gas Reactions, Investigation Of Structural And Conducting Properties. The Graduate School of Natural And Applied Sciences Of Middle East Technical University, M.Sc. Thesis, 2005.

## Design of a Power Inverter Using Solar Cell as a Source of Charger

\*H C Medhi

Department of Electronics, St. Edmund's College, Shillong-793003, Meghalaya, India

\*Email: [hemenmedhi1984@gmail.com](mailto:hemenmedhi1984@gmail.com)

### ABSTRACT:

The increasing demand and depletion of fossil fuels in India lead us to shift our focus to renewable sources which are not only the future unlimited source of energy but also ecofriendly and viable for environment. Solar energy is a form of renewable energy and is a very efficient method of saving electricity which does the same functioning as the electricity but the main difference is that the major source is solar energy. This paper focuses on the design of solar modules serve as a source of charger through solar charge controller to the battery and inverter for converting the direct current into an alternating current for house hold application. It has more advantages because it needs less maintenance, no use of fuel, light in weight, rugged, noiseless and does not require an alternating current for charging.

**Keywords:** Solar cell, Inverter Circuit, MOSFET

### INTRODUCTION:

It is evident that solar energy is renewable source of all. It is a process in which solar energy is converted into electrical energy using solar panel. Solar energy is the radiant energy. The earth receives 174 watts of solar radiation at the upper atmosphere 30% reflected back to space and rest is observed by clouds, ocean, and mass. Human harness solar energy in many different ways space heating and cooling, lighting, hot water, cooking etc. the solar energy are only limited by human ingenuity.

Solar technologies are characterized as either passive or active depending on the way the energy captured converts and distributed [1]. Active solar techniques use photovoltaic panel which we are going to use this type of solar panel in circuit, as we all know that solar energy is a renewable source of energy and is inexhaustible. Using sun's energy we can charge a 12V battery through

charger circuit, we can even charge our cell phones with the help of mobile charger circuit and a CFL bulb can be glown with the designed inverter circuit.

## 1. EXPERIMENTAL WORK

The block diagram demonstrates about solar inverter which converts the solar energy in to electrical energy for house hold application. Hence it is renewable source of energy and more efficient. Through this process we can consume solar energy for our daily life requirement. As its energy in the form of electrical energy is used to charge the mobiles and batteries too.

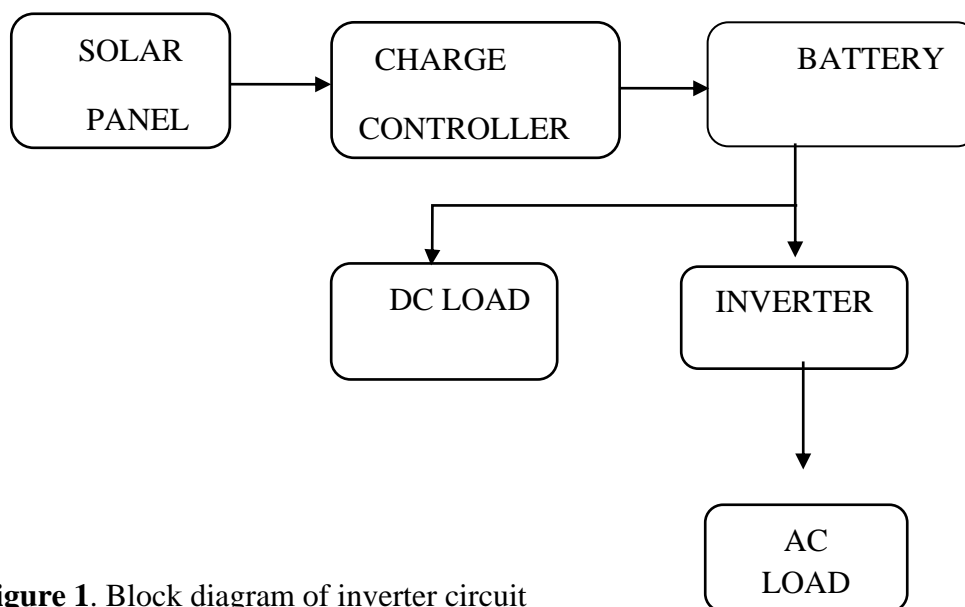


**Figure 1.** Block diagram of inverter circuit

### i. SOLAR PANEL

Collection of solar cells is known as solar panel. Combinations of small solar cells together can be used for generating power that can be used over a large area. The electricity produced by a solar cell depends upon the mount of light that hits a cell. The principle on which solar panel works is photo voltaic effect is a physical and chemical phenomenon in which voltage or current created in a material when sunlight falls on it [2, 3].

### ii. SOLAR CHARGER CIRCUIT

When solar radiation falls on solar plate then it absorbs sun rays as a source for generating electricity. These sun rays are the light energy (photon) directly coming from the sun. In this

circuit a diode of series In 4001 is placed which is used to give a unidirectional flow of current in the circuit i.e., current could only flow from solar panel to battery and not from battery to solar panel. After the battery an IC of series LM317 is used as voltage controlling device [4].

### **iii. BATTERY**

A battery is a device that stores the charge for further application. In this circuit the main function is to store power and during storage of AC power supplied it acts as a beneficial source of power via inverter to AC load. Lead acid battery or Ni – Cd battery banks can be charged with the help of solar charger circuit. For this at stationary locations series of solar Cells are installed. These solar cells can be directly connected to battery banks to store energy for off peak hours. They can also be used in peak hours for saving energy during day time. The range of charging voltage produced from solar panel depends upon the intensity of the Sun. Thus to protect the solar charger circuit [5] from over charging or over voltages a voltage regulator must be used along with the solar charger circuit.

### **iv. AC LOAD**

It is the output of the inverter circuit. The inverter circuit converts the DC source into 220V AC which is consumable for appliances.

### **v. DC LOAD**

It is the output power which we can directly obtain from the battery. It is efficient in supplying the power to gadgets operating on low DC voltage.

## **4. Inverter**

Inverter is a device that converts Direct current (or DC) to Alternating Current (or AC) using transformers, switching circuits and control circuits. Home inverters or home UPS takes the DC power from the batteries and converts it into AC power used by the load connected at home. Similarly, an off grid solar inverter operates. In case of grid connected, solar inverter the DC power is generated from the solar panels and AC power is given to the grid. In case of “grid connected” solar inverter when the power is coming from the grid, the UPS and Inverter system charges the batteries using the power coming from the grid. When the power coming from the grid is off, then the inverter takes the DC power from the batteries and converts it into AC to

appliances. An automatic switch is used to sense whether the power is coming from the grid and if not then it switches the UPS into battery mode.

#### **i. IC CD4047**

It is a CMOS low power mono stable / a stable multivibrator with logic techniques incorporated to permit positive or negative – edge triggered 14 - lead hermetic dual – in-line ceramic packages. It can operate in only one mode at a time. It requires an external capacitor (between pin 1 & 3) and an external resistor (between pin 2&3) to determine the output pulse width in the mono stable mode, and the output frequency in the a stable mode. Its various features are wide supply voltage range: 3V to 15 V, high noise immunity, true and complemented buffered out puts, low power compatibility, low power consumption and only one external R and C is required.

#### **ii. MOSFET IRFZ44**

MOSFET IRFZ44 [6] is an N-channel enhancement mode standard level field –effect power transistor in a plastic envelope using trench technology which is used for both amplifying and switching purpose. MOSFETS are the most common transistors used because of its main advantage that it requires lesser amount of current to turn on while it delivers much higher amount of current to load. The device features very low on-state resistance and has integral zener diodes giving ESD protection up to 2KV, maximum  $V_{DS}$  (Drain source voltage) as 55 V and can handle continuous drain current up to 49A.

#### **iii. TRANSFORMER (12-0-12)**

A transformer is a static device that transfers electrical energy from one circuit to another through electromagnetic induction at constant frequency. Transformers are used in circuits to increase or decrease the voltages value. In this paper the transformer used is of 12-0-12 Volt and 5A. It has 230V primary windings and centre tapped secondary winding.

#### **iv. RESISTORS**

In this circuit the resistors of different ratings are used. Those are resistors of 100ohm, 1 K ohm and 100 K ohm variable resistor.

**v. CAPACITOR (0.22uf)**

In this circuit the capacitor used is of 0.22 $\mu$ F.

**5. WORKING OF INVERTER CIRCUIT**

DC supply to the inverter circuit is provided by 12V battery. In this a combination of 'R' & 'C' is used which works as an oscillating circuit. This circuit endows the frequency of oscillation. Through this oscillation circuit capacitor gets fully charged and thus triggers the IC when it reaches at threshold voltage. Once the capacitor is completely charged, it starts discharging through the resistor and the common line. At pin 4, 5, 6 & 14 of IC positive supply comes and at pin 7,8,9 & 12 of IC negative supply comes . IC used in the circuit is such that one time we get out put at IC pin number 10 and second time we get out put at IC pin number 11. Thus due to the output of IC, MOSFET get triggered.

When we get output at IC pin number 10 at that time MOSFET 1 gets triggered. It act as a closed switch. Thus the primary circuit of transformer will get completed due to which voltages would be induced in the secondary of the transformer. When MOSFET 1 acts as closed switch at that time the direction of flow of current in the primary winding would be clockwise and at the same time the direction of flow of current in the primary winding would be clockwise and at the same time the direction of flow of current in the secondary would be anti-clockwise. The output obtained from secondary winding of transformer would be square wave. This wave would be positive in nature.

When we get out put at IC pin number 11 at that time MOSFET 2 gets triggered [7]. It will now act as a closed switch. Thus the primary circuit of transformer will get completed due to which voltages would be induced in the secondary of the transformer. When MOSFET 2 acts as closed switch at that time the direction of flow current in the primary winding would be anticlockwise and at same time the direction of flow of current in the secondary would be clockwise. The output obtained from secondary winding of transformer would be square wave. This wave would be negative in nature. Thus the net output obtained would be complete square wave.

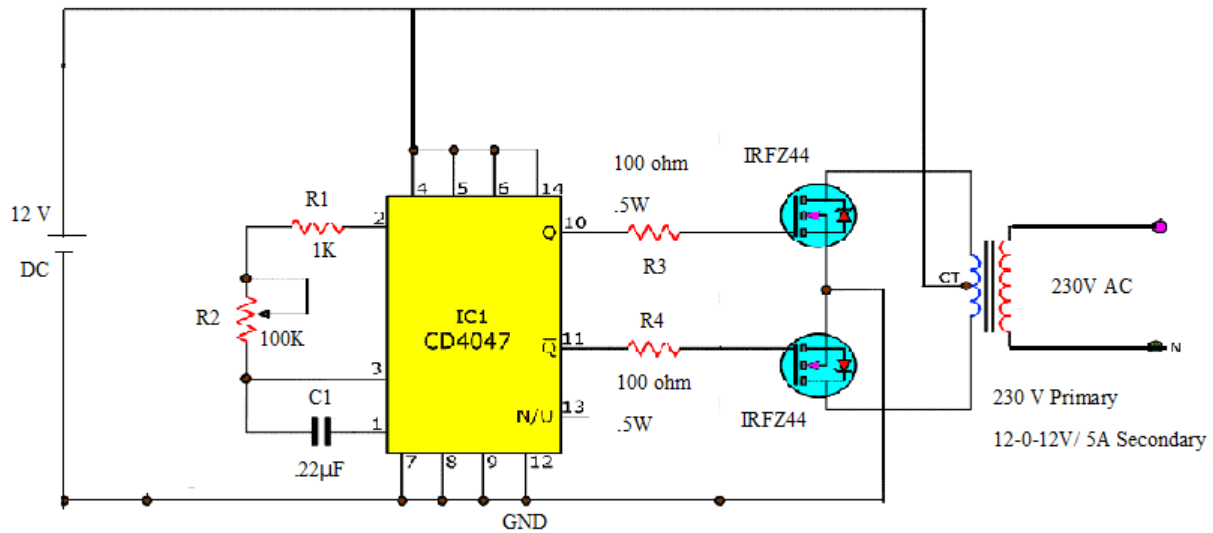


**Figure 2.** Circuit diagram of inverter

## 6. PROTECTIVE FUNCTIONS OF THE SOLAR INVERTER

### i. OVERLOAD PROTECTION

When the power consumption of the appliance /appliances exceeds the total power of the solar inverter, it will then revert to the protection state within 20 seconds until you reduce the load.

### ii. SHORT CIRCUIT PROTECTION

If an appliance short circuits, the solar inverter will revert to the protection state until the appliance is removed.

### iii. THERMAL PROTECTION

As inverter is semiconductor-based equipment, sensitive to overheating and operate best at cooler temperatures. If the temperature of the solar inverter gets too hot it will protect with automatic temperature controlled section developed by front end electronics.

### iv. REVERSE POLARITY PROTECTION

If connected incorrectly no current will pass through the solar inverter. For that purpose a diode (IN5408) is connected to the positive terminal of the inverter.

## 7. CONCLUSION

A solar panel using inverter with charger and charge controller had successfully been designed and developed. Solar charger was used to store DC power which was generated by photovoltaic effect of solar panel. To protect from over charging of the battery simple auto cut off circuit is designed and tested. The output of charger circuit is fed to auto cut off circuit using relay which is completely automatic which protects the battery from over charging. Inverter circuit is used to convert DC power into AC power which is used to drive the loads. Level indicator circuit helps to determine the amount of charge left in the circuit which can easily be implemented in real life to increase the efficiency of solar inverter. Using microcontroller instead of relay the system of solar inverter circuit will be made more attractive and reliable.

## REFERENCES

- [1] Bindhiya Manger , Deepak Rasaily, Tashi Rapden Bhutiya, Mingma Lepcha, Reepika Gurung, "Design of Inverter with Solar Charge", International Journal of Engineering Trends and Technology (IJETT) –volume-33, pp 389-391, Number8-March 2018.
- [2] Nishit Kapadia, Amit patel, Dinesh Kapadia, " Simulation and design of low cost single phase solar inverter" , International journal of Emerging Technology and Advanced Engineering , ISSN-2250-2459, Volume 2, pp 158-159, February 2012
- [3] Vikash Kulkarani , Rajesh Nehete, " Simulation and analysis of photovoltaic (PV) based solar inverter system " , International Journal of Soft computing and Engineering ISSN: 2231-2307, Volume 3, pp 114, January 2014
- [4] Paul Hersch, Kenneth Zweibei, Basic photovoltaic principles and methods , United states of America , pp 7-8, February 1982
- [5] Manisha Ghodke , Sujata Naduvinamni, Anusha Kanchagar, Chitra patil ,Akshata Miskin , " Design and development of stabilized regulated fixed and variable DC power supply unit with short circuit protection " , Proceeding of NCRIET & Indian J. Series , ISSN: 2250-0138, PP 3-4,2015
- [6] [www.alldatasheet.com](http://www.alldatasheet.com)
- [7] Rajesh Singh Shekhawatt, RuchikaSingh Rao,Kajal Kumari and Vinod Kumar,"Solar Panel Using Inverter with Level Indicator" , International Journal of Innovative and Emerging Research and Engineering ,Volume-3, Issue 3,2016

## Structural and Optical Properties of Green Synthesized Copper Oxide Nanoparticles

Sanjib Baglari<sup>a</sup>, Riu Riu Wary<sup>b</sup>, Pranjal Kalita<sup>c</sup>, Manasi Buzar Baruah<sup>b\*</sup>

<sup>a</sup>Department of Physics, Birjhora Mahavidyalaya, Bongaigaon, Assam:783380, India

<sup>b</sup>Department of Physics, Central Institute of Technology, Kokrajhar, Assam:783370, India

<sup>c</sup>Department of Chemistry, Central Institute of Technology, Kokrajhar, Assam:783370, India

\*Corresponding author: Email: [mbaruah@cit.ac.in](mailto:mbaruah@cit.ac.in)

### ABSTRACT

Discarded fruit peels create various environmental pollutions, the reuse of such waste peels reduces pollution, waste as and it also sustains environmental balance. In this communication, we have reported the synthesis of copper oxide nanoparticles using aqueous extract of citrus maxima peel and copper nitrate as precursor. The prepared CuO NPs were characterized by XRD, SEM, EDS, FTIR, PL and UV-visible spectroscopy. The obtained result revealed that the synthesized CuO nanoparticles were spherical in shape with monoclinic crystal structure. UV-visible diffuse reflectance spectroscopy was used to estimate the direct and indirect band gap energy of CuO nanoparticles. Photoluminescence (PL) was carried out to investigate materials imperfection and recombination mechanism.

### INTRODUCTION:

In recent year, the green synthesis becomes an alternative method for material fabrications because of various environmental issues. The method utilizes green chemistry for the synthesis of nanoscale materials for various potential applications and attracted the attention of researcher in contrast to the traditional method which produces harmful waste product for the environment. In general, the traditional method employed organic solvent, harsh reducing agent, flammable, toxic and corrosive chemical compounds and required sophisticated instruments and time consuming. However, green technology utilizes the only environmentally available natural product and reduces the usages of chemical reagents with improvement in crystal quality along with the efficiency of method.

Nanomaterials have various applications in the field of science and technology and biomedical applications because of its unique and remarkable properties as compare to the bulk counterparts [1]. Due to the large surface area and high surface energy of nanoparticles, metal oxide nanoparticles are used broadly in the form of nanoscale [2-4]. Electronic, magnetic, antibacterial, catalysis, sensing and optical properties made the nanomaterials superior in nanoscale. Among various type of nanomaterials, Copper Oxide (CuO) is another p-type semiconductor with narrow indirect band gap energy  $\sim 1.2$  eV [5,82] with

excellent superconducting properties and widely used in the field of catalysis [7], gas sensor [8], dye-sensitized solar cell [4] etc. due to its low cost, non-toxicity and thermal stability.

The various method has been employed for the synthesis of CuO nanoparticles (NPs) such as microwave-assisted [9], Hydrothermal [10], sol-gel [11], thermal decomposition [12], and chemical precipitation [13]. Recently, different kind of plant, peel and root extract has been used for the synthesis of NPs as a stabilizing or capping agent [14,15]. Plant extract contains various biological compounds such as flavonoids, alkaloids, phenolic compounds, quinol, amino acid, and chlorophyll pigments which acts as a reducing agent and itself act as a stabilizing agent to reduce metal ions to nanoparticles and eliminates the use of any other stabilizing agent [14]. Different kind of plants and peels extract like *Calotropis gigantean* [4], *Punica granatum* [16], *Thymus vulgaris* [17], *Cassia auriculata* [18] has been used for the synthesis of CuO NPs. Along with plant extract, fruit peels extract was also useable for green synthesis of NPs. *Citrus maxima* is a fruit of citrus family, its peel contains polysaccharide, essential oil, pectin, and flavonoids, and so on [19,20]. Iron NPs were synthesized using an aqueous solution of citrus maxima peel as a reducing agent [21]. A thorough literature review suggested that none have reported aqueous solution of citrus maxima peel for the synthesis of CuO NPs using copper nitrate precursors. However, these peels are discarded in an environment which causes environmental issues. Re-use of such waste products avoids pollutions in an environment. Concerning all these, current work reports the use of citrus maxima peel extract as a reducing and stabilizing agent for the production of CuO NPs using copper nitrate precursor and structural, morphological and optical properties were carried out.

## **MATERIALS AND METHODS:**

### **Synthesis of CuO nanoparticles**

Fresh *Citrus maxima* fruit was peeled and washed several times with distilled water and then cut into pieces and air-dried. 50 gm of said peel pieces were then boiled in 150 ml distilled water at 70-80°C for 1 hour. A light yellow solution was formed which was cooled at room temperature and filtered several times using Whatmann No. 1 filter paper. 30 ml extract was taken from the stock solution and stirred. Afterward, 1 gm of copper nitrate trihydrate [Cu(NO<sub>3</sub>)<sub>2</sub>.3H<sub>2</sub>O] was added into the extract and then the solution was heated slowly until the temperatures reaches to 80°C. The solution was heated until it changed to brown colored paste and then cooled. The paste was transferred to the ceramic crucible and sintered at 400°C for 1 hour. Black powder was collected and ground in mortar pestles and stored in vacuum desiccators for further characterizations.

### **Characterization of CuO NPs**

Different techniques were used for the characterization of the materials. The phase purity of the material was characterized by powder X-Ray diffraction (PANALytical E'XPRT, Netherlands) with CuK $\alpha$  as a incident beam ( $\lambda=1.54 \text{ \AA}$ ) in the range of 30-80<sup>0</sup> at scanning rate of 1<sup>0</sup>/min. The morphology, particle size and elemental composition were analyzed using Scanning Electron Microscopy (SEM) and Energy Dispersive X-Ray Spectroscopy (EDS). Optical properties and band energy were evaluated using UV-Vis

NIR spectroscopy with diffuse reflectance. Function group of the material was studied by Fourier Transform Infrared (FTIR) Spectrometer, Shimadzu FTIR 8201. The room temperature photoluminescence (PL) was carried out using spectrophotometer, RF 6000 for the identification of defect state.

## RESULTS AND DISCUSSION

The crystal structure, crystallite size was examined using powder X-Ray diffraction spectroscopy. Figure 1. shows the powder XRD diffraction pattern of the synthesized sample. All the diffraction peaks of XRD patterns are well matched with JCPDS Card No. : 45-0937 of CuO with a monoclinic crystal structure. The sharp and intense peaks indicate the high crystallinity of CuO NPs. No other diffraction peaks from Cu<sub>2</sub>O, Cu(OH)<sub>2</sub> and impurity were observed which confirms the pure monoclinic phase formation of grown product. From the figure-1 it is clear that (-110) and (110) have a stronger intense peak than others, indicates that the strong preferential orientation in the (-110) and (110) direction. The average crystallite size (D) of the CuO NPs was determined using Debye-Scherrer's formula -

$$D = \frac{k\lambda}{\beta_{hkl}\cos\theta} \quad (1)$$

where  $k$  and  $\lambda$  represents shape factor (0.9) and wavelength of incident radiation (1.5406Å).  $\beta_{hkl}$  and  $\theta$  are full width half maxima (FWHM) and scattering angle. The average crystallite size was 18.32 nm.

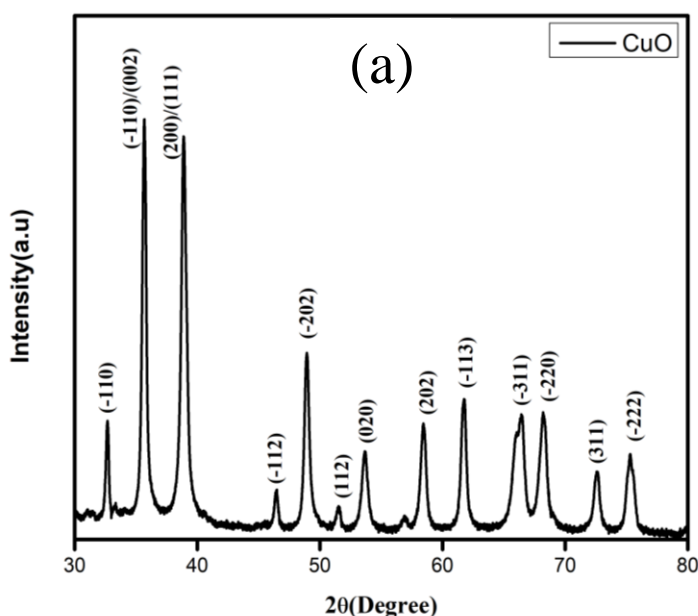


Figure 1. (a) XRD pattern of sample of CuO NPs

Fourier transform- infrared (FTIR) spectroscopy was used to analyze the functional group present in the material and the spectrum is shown in Figure 2. The presence of broad band in the region of 3540-2800 cm<sup>-1</sup> may be due to the stretching vibration of O-H and C-H [21,23]. The peak positioned at 2358.07 cm<sup>-1</sup> indicates the presence of CO<sub>2</sub> molecules. The band at 1639 cm<sup>-1</sup> indicates the stretching vibration of C=O in aldehydes and ketones which confirms the presence of phenolic acid and terpenoid on the surface of NPs. In addition to it, the stretching vibration of C-N at 1206 cm<sup>-1</sup> indicates the presence of aliphatic amines [21]. The absorption band at around 1389.79 cm<sup>-1</sup> can be attributed to the C-C stretching of the aromatic ring. The sharp and intense peak at around 531.39 cm<sup>-1</sup> is due to the characteristic stretching

vibration of Cu-O along the [101] direction on the monoclinic crystal structure of CuO, which confirms the formation of CuO. Moreover, the absence of band at  $610\text{ cm}^{-1}$  indicates that there is no phase formation of  $\text{Cu}_2\text{O}$  and confirms the phase purity of CuO [24]. FTIR spectroscopy suggested the presence of phenolic acid, terpenoid, aliphatic amines, and aromatic ring on the surface of CuO NPs which were thought to act as capping or stabilizing agents for the formation of CuO NPs.

The Scanning electron microscopy (SEM) and energy dispersive x-ray spectroscopy (EDS) of CuO NPs were carried out to evaluate morphology and elemental composition and it is shown in Figure 3 (a-b). The SEM image reveals the distinguishable spherical morphology of CuO NPs with an average size of about 33.44 nm and it is in good agreement with the size computed from XRD patterns. It is clear from the SEM image that CuO NPs synthesized using citrus maxima peel aqueous extract produce uniform spherical morphology. The peaks of Cu and O in EDX spectrum display that NPs are composed of Cu and O only and the absence of extra peak indicates the purity of synthesized CuO NPs and this result supports the XRD spectra of CuO NPs. However, an extra peak is observed from the substrate used. CuO NPs are constituted with 75.04 and 24.96 wt% of Cu and O respectively. The overall result suggested the pure phase formation of CuO NPs using aqueous citrus maxima peel extract.

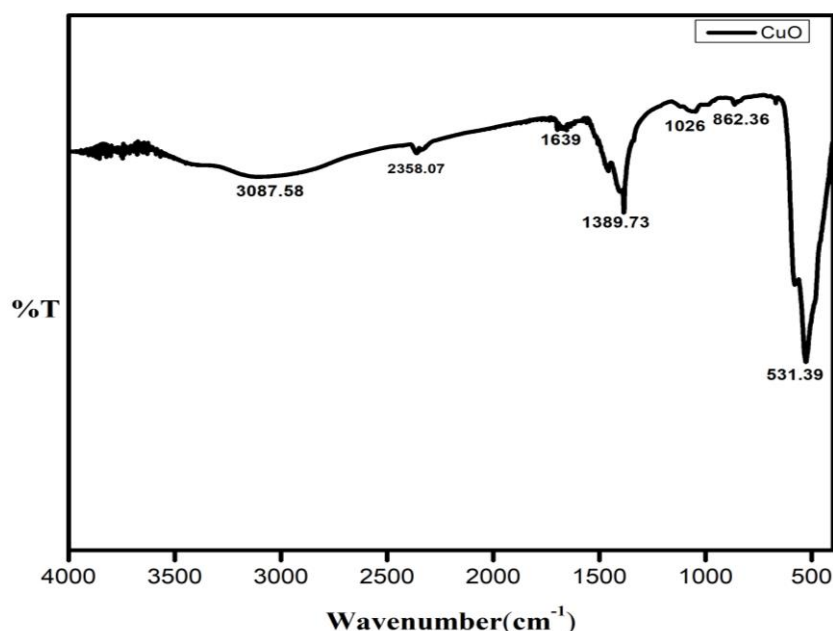


Figure 2. FTIR spectra of CuO NPs synthesized using aqueous peel extract.

UV-Vis NIR spectroscopy in diffuse reflectance mode was carried to analyze the spectral response of the sample as shown in Figure 4(a). Kubelka-Munk formula [22] was employed to estimate the band gap energy of the material.  $F(R)$  was derived from  $F(R) = \frac{(1-R)^2}{2R}$ , here  $F(R)$  is equivalent to the absorbance coefficient, and  $R$  is the absolute reflectance. From the spectrum, it was clear that sample exhibit absorption peak at 256 nm associated with  $\text{Cu}^{2+}$  ion in the zeolite structure. Also, the absorption band at 427 nm attributed to the  $\text{Cu}^{2+}$  was also observed which is related to the electron transmission of d orbitals [25,26]. This confirms the presence of copper (II) ion in the material. Moreover, peak around 550 nm belongs to  $\text{Cu}_2\text{O}$  resulting from the decomposition of CuO [27]. The optical band-gap of indirect and direct band-gap was calculated using Tauc's plot by plotting  $[F(R) \times h\nu]^{0.5}$  and  $[F(R) \times h\nu]^2$  versus photon energy (Figure 4(b)&4(c)) and the energy was observed by extrapolating liner portion to the energy axis and the observed value was 1.4 eV and 3.17 eV respectively and the result is in accordance

to other reported literature [5]. The higher direct band gap energy to that of indirect indicates the crystallinity of the materials [28]. However, the observed indirect band gap energy is greater than the bulk counterparts of CuO (~1.2 eV) which could be attributed to the quantum confinement effect for the small individual crystal size observed in SEM analyses. When the size of the materials decreases to the nanoscale, the wavelength of light becomes large with respect to the size of the materials and the low coordination atoms with lower atomic interaction increases on the surface of the materials. As the size of the particle becomes smaller than Bohr radius the electrons are become more confined in the particle. Due to this confinement effect the band gap energy increases [29].

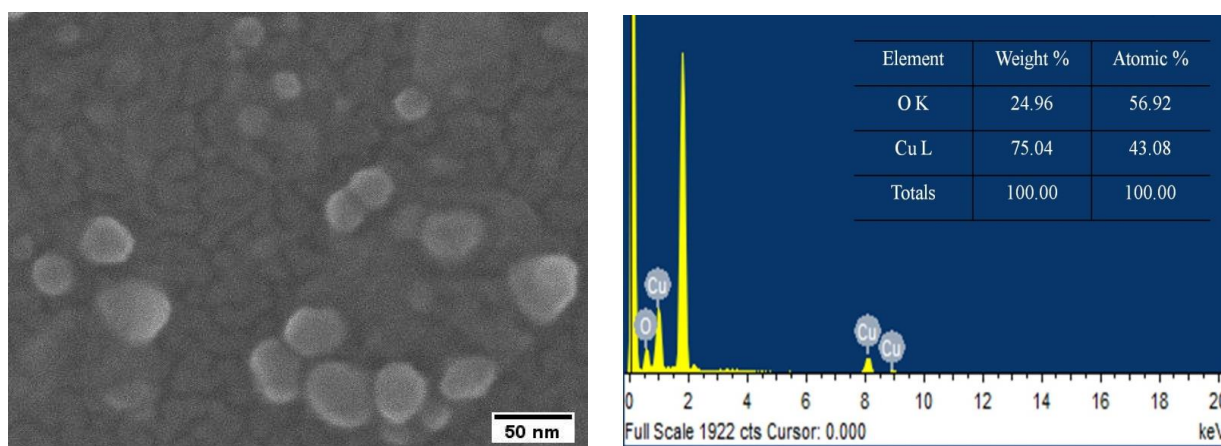


Figure 3 (a) SEM micrograph of CuO and (b) Elemental composition spectra of the sample

Figure 5. corresponds to room temperature photoluminescence (PL) spectra of CuO NPs. The spectra consist of four peaks located at 380, 402, 426, and 524 nm. A strong UV emission band known as near band edge (NBE) emission is observed at 380 nm attributed to the recombination of electron-hole pair in free excitons [30]. Violet and blue emission at 402 and 426 nm was also observed in the visible region attributed to the oxygen vacancy and interstitial oxygen [22] and this result is consistent with the luminescence band of CuO reported by other literature [31,32]. In addition to it, the broad small hump which is known to be green emission band around 528 nm could be associated with singly ionized oxygen vacancy originated from the recombination of electrons with holes [33,34]. However, the origin of luminescence in CuO is still in contradiction and only few reports are available. S. Dagher et al. reported different NBE emission peak depending upon the size of colloidal CuO nanoparticles [35]. The different PL emission peaks suggests that depending upon the morphology, particle size, CuO exhibit different emission peaks.

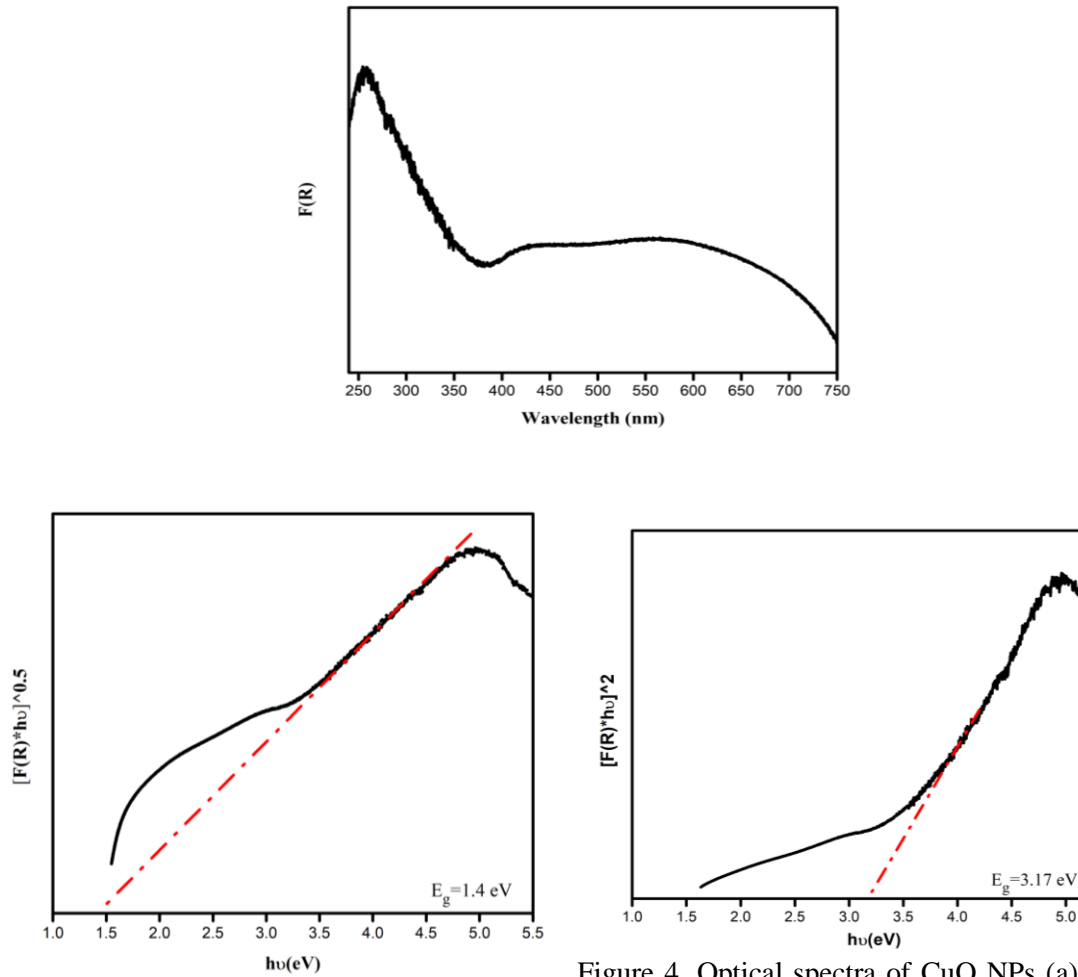


Figure 4. Optical spectra of CuO NPs (a) . Tauc's plot of CuO NPs (b) Indirect transition and (c) direct transition.

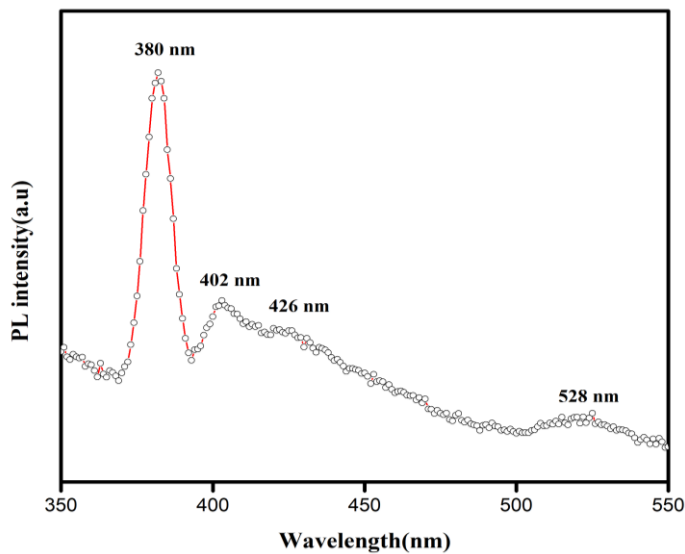


Figure 5. Photoluminescence spectra of CuO NPs.

**CONCLUSIONS:**

In this work, we have reported the synthesis of CuO through environmentally friendly method using aqueous extract of citrus maxima. XRD result showed the pure monoclinic phase of the materials supported by FTIR and EDS analysis. FTIR result indicated the presence of phenolic acid, terpenoid, aliphatic amines and aromatic ring which acts as reducing or capping agent. SEM result showed spherical morphology of particles with an average particle size of 33.44 nm. The indirect optical band gap energy was evaluated from Tauc's plot and found to be 1.4 eV which suggested that the materials will be useful for photocatalytic applications. PL spectra showed both UV and Visible emission peaks with dominant NBE emission peak at about 380 nm. The green synthesis method using aqueous peel extract will contribute to environmental issues and create economic benefits. Finally, while recognizing our limitation of analysis, the work presented in this paper leave avenues for further study of present materials. In view of application, we propose further study may be carried out in future for application of the synthesized materials.

**ACKNOWLEDGEMENT:**

The authors would like to thank IISER, Mohali, NIT Silchar for providing material characterization facilities to carry out this work.

**REFERENCES:**

- [1]. N. Verma and N. Kumar, Synthesis and biomedical applications of Copper Oxide Nanoparticles: An expanding horizon, ACS Biomater. Sci. Eng. 5 (2019) 1170-1188.
- [2]. S. Prakash, N. Elavarasan, A. Venkatesan, K. Subashini, M. Sowndharya, V. Sujatha, Green synthesis of copper oxide nanoparticles and its effective applications in Biginelli reaction, BTB photodegradation and antibacterial activity, Advanced Powder Technology 29 (2018) 3315-3326.
- [3]. H. Siddiqui, M.S. Qureshi, F.Z. Haque, Valuation of CuO nanoflakes for its suitability as an absorbing material in solar cells fabrication, Optik, 127 (2016) 3713-3717.
- [4]. J.K. Sharma, M.S. Akhtar, S. Ameen, P. Srivastava, G. Singh, Green synthesis of CuO nanoparticles with leaf extract of Calotropis gigantean and its dye-sensitized solar cell applications, Journal of Alloys and Compounds 632 (2015) 321-325.
- [5]. N. Sreeju, A. Rufus, D. Philip, Nanostructured copper (II) oxide and its noval reduction to stable copper nanoparticles, Journal of Physics and Chemistry of Solid, 124 (2019) 250-260.
- [6]. F. Bayansal, B. Sahin, M. Yuksel, N. Biyikli, H.A. Cetinkara, H.S. Guder, Influence of coumarin as an additive on CuO nanostructures prepared by successive ions layer adsorption and reaction (SILAR) method, Journal of Alloys and Compounds, 566 (2013) 78-82.
- [7]. X. Chen, D. Chu, L. Wang One-step and green synthesis of novel hierarchical hydrangea flower-like CuO nanostructures with enhanced photocatalytic activity, Physics E: Low-dimensional systems and Nanostructures 106 (2019) 194-199.
- [8]. M. Chawla, V. Sharma, J.K. Randhawa, Facile one pot synthesis of CuO nanostructures and their effect on nanenzymatic glucose Biosensing, Electrocatalysis 8 (2017) 27-35.
- [9]. P. Sutradhar, M. Saha, D. Maiti, Microwave synthesis of copper oxide nanoparticles using tea leaf and coffee powder extract and its antibacterial activity, J Nanostruct Chem 4 (2014) 86.

- [10].V.A. F. Samson, K. M. Racik, S. Prathap, J. Madhavan, M. V. A. Raj, Investigation of structural, optical and dielectric studies of Copper Oxide nanoparticles, *Materials Today:Proceedings* 8 (2019) 386-392.
- [11].T. Pandiyarajan, R. Udayabhaskar, S. Vignesh, R. A. James, B. Karthikeyan, Synthesis and concentration dependent antibacterial activities of CuO nanoflakes, *Material Science and Engineering C*, 33 (2013) 2020-2024.
- [12].D.Das, B. C. Nath, P. Phukon, S. K. Dolui, Synthesis and evaluation of antioxidant and antibacterial behavior of CuO nanoparticles, *Colloids and Surface B: Biointerfaces* 101 (2013) 430-433.
- [13].C.C. Lin, J. S. Liao, Production of CuO nanoparticles using a simple precipitation method in a rotating packed bed with blade packing, *journal of Alloys and Compounds*, 775 (2019) 419-426.
- [14].A.K. Mittal, Y. Chisti, U. C. Banerjee, Synthesis of nanoparticles using plant extracts, *Biotechnology Advances*, 31 (2013) 346-356.
- [15].L. Chen, I. Batjikh, J. Hurh, Y. Han, Y. Huo, H. Ali, J. F. Li, E. j. Rupa, J. C. Ahn, R. Mathiyalangan, D. C. Yang, Green synthesis of zinc oxide nanoparticles from root extract of *Scutellaria baicalensis* and its photocatalytic degradation activity using methylene blue, *Optik*, 184 (2019) 324-329.
- [16].A.Y. Ghidan, T. M. Al-Antary, A. M. Awwad, Green synthesis o CuO nanoparticles using punica granatum peels extract: effect on green peach aphid, *Environmental Nanotechnology, Monitoring & Management*, 6 (2016) 95-98.
- [17].M. Nasrollahzadeh, S.M. Sajadi, A. R. Vartooni, S. M. Hussin, Green synthesis of CuO nanoparticles using aqueous extract of *thymus vulgaris* L.leaves and their catalytic performance for N-arylation of indoles and amines, *Journal of Colloid and Interface Science* 466 (2016) 113-119.
- [18].G. Sharmila, M. Thirumarimurugan, Phytofabrication, characteristic and antibacterial activity of cassia auriculata leaf extract derived CuO nanoparticles, *J Inorg Organomet Polym*, 27 (2017) 668-673.
- [19].S.M. Njoroge, H. Koaze, P. N. Karanja and M. Sawamura, Volatile constituents of redblush grapefruit (*citrus paradisi*) and Pummelo (*Citrus grandis*) peel essential oils from Kenya, *J. Agric. Food. Chem.* 53 (2005) 9790-9794.
- [20].G.N. Kim, J.G.Shin, H. D. Jang, Antioxidant and antidiabetic activity of dangyuja (*citrus grandis* osbeck) extract treated with *aspergillus saitoi*, *Food Chemistry* 17 (2009) 35-41.
- [21].Y. Wei, Z. Fang, L. Zheng, L. Tan, E. P. Tsang, Green synthesis of Fe nanoparticles using *Citrus maxima* peels aqueous extracts, *Material Letters*, 186 (2016) 384-386.
- [22].H. Siddidui, M. S. Qureshi, F. Z. Haque, Surfactant assisted wet chemical synthesis of copper oxide (CuO) nanostructures and their spectroscopic analysis, *Optik*, 127 (2016) 2740-2747.
- [23].N.R. Dhineshababu, V. Rajendran, N. Nithyavathy, R. Vetumperumal, Study of structural and optical properties of cupric oxide nanoparticles, *Appl. Nanosci.*
- [24].T. Velusamy, A. Liguori, M. M-Montero, D. B. Padmanaban, D. Carolan, M.Gherardi, V. Colombo, P. Maguire, V. Svrcek, D. Mariotti, Ultra-small CuO nanoparticles with tailored energy-band diagram synthesized by a hybrid plasma-liquid process, *Plasma Processes and Polymers*, 14 (2014) e1600224.
- [25].T. Tenkyong, N. Bachan, J. Raja, P.N. Kumar and J. M. Shyla, Investigation of sol-gel processed CuO/SiO<sub>2</sub> nanocomposite as a potential photoanode material, *Materials Science-Poland*, 33 ( 2015) 826-834.
- [26].H.A. ElBatal, A.M. Abdelghany, F.H. ElBatal, Kh.M. ElBadry, F.A. Moustaffa, UV-Visible and infrared absorption spectra of gamma irradiated CuO-doped lithium phosphate, lead phosphate and zinc phosphate glasses: A comparative study, *Physics B*, 406 (2011) 3694-3703

- [27].Y. Zhang, S. Wang, X. Li, L. Chen, y. Qian, Z. Zhang, CuO shuttle like nanocrystals synthesized by oriented attachment, *Journal of Crystal Growth* 291 (2006) 196-201.
- [28].N.R. Dhineshababu, V. Rajendran, N. Nithyavathy & R. Vetumperumal, Study of structural and optical properties of cupric oxide nanoparticles, *Applied Nanoscience*, 6 (2016) 933-939.
- [29].S. Eustis and M. A. El-Sayed, Why gold nanoparticles are more precious than pretty gold: Nobel metal surface plasmon resonance and its enhancement of the radiative and nonradiative properties of nanocrystals of different shapes, *Chem. Soc. Rev.*, 35 (2006) 209-217.
- [30].P. Chand, A. Gaur, A. Kumar, U. M. Gaur, Structural and optical study of Li doped CuO thin films on Si (100) substrate deposited by pulsed laser depositions, *Applied Surface Science*, 307 (2014) 280-286.
- [31].K. Mageshwari, R. Sathyamoorthy, Flower-shaped CuO Nanostructures: Synthesis, characterization and antimicrobial activity, *Journal of Material Science & Technology*, 29 (2013) 909-914.
- [32].R. Sathyamoorthy, K. Mageshwari, Synthesis and hierarchical CuO microspheres: Photocatalytic and antibacterial activities, *Physics E*, 47 (2013) 157-161.
- [33].L. V. Devi, T. Selvalakshmi, S. Sellaiyan, A. Uedono, K. Sivaji, S. Sankar, Effect of La doping on the lattice defects and photoluminescence properties of CuO, *Journal of Alloys and Compounds*, 709 (2017) 496-504
- [34].P. Vinothkumar, C. Manoharan, B. Shamugapriya & M. Bououdina, Effect of reaction time on structural, morphological, optical and photocatalytic properties of copper oxide (CuO) nanostructures, *Journal of Material Science: Material in electronics* 30 (2019) 6249-6262.
- [35].S. Dagher, Y. Haik, A. I. Ayesh, N. Tit, Synthesis and optical properties of colloidal CuO nanoparticles, *journal of Luminescence*, 151 (2014) 149-154.

## Frequency encoded All optical single bit memory unit using Tera Hertz Optical Asymmetric Demultiplexer(TOAD)

Kajal Maji<sup>1,2</sup>, Kousik Mukherjee\*<sup>2</sup>, Mrinal Kanti Mandal<sup>1</sup>

<sup>1</sup>Department of Physics, National Institute of Technology Durgapur, Durgapur, India

<sup>2</sup>Department of Physics, Banwarilal Bhalotia College, Asansol, India

Email: [kajalmaji200@gmail.com](mailto:kajalmaji200@gmail.com)

### Abstract:

The frequency encoded all-optical single bit memory unit operation is described using Tera Hertz Optical Asymmetric Demultiplexer (TOAD) based interferometric switch. Terahertz Optical Asymmetric Demultiplexer (TOAD) is a fundamental optical switch in an optical communication system. In the frequency encoding scheme, the states of information '0' and '1' are denoted by signals of frequency  $\nu_1$  and  $\nu_2$ , respectively. This single-bit memory unit's output shows in the form of a truth table in terms of wavelengths.

**Keywords:** TOAD; Frequency encoding; SOA; Memory unit.

### 1. Introduction:

All-optical signal processing has emerged as an alternative to an electronic system[1]. The demand of high-speed logic gates and processing units boosted the research in semiconductor optical amplifier based devices to implement different types of all-optical processors [2-7]. This includes all-optical logic gates, two's complement generator, comparator, and many others. Tera hertz optical asymmetric demultiplexer or TOAD is an all-optical switch uses SOA in such a way that the speed is increased considerably compared to simple SOA and many proposals for all-optical logic gates and processors have been designed using TOAD and its variant dual control TOAD(DCTOAD)[7-13]. Frequency encoding for states of information has many advantages[1-4,7,10], and hence TOAD based designs with frequency encoding are very much attractive for future optical technologies. In this communication, a frequency encoded single bit memory unit using TOAD is designed and analyzed and shows improved performance compared to our earlier work described in[1]. In this communication, frequency encoded memory using TOAD is developed and interpreted for the first time as far as the author's knowledge goes.

## 2. TOAD based optical switch:

Tera Hertz Optical Asymmetric Demultiplexer (TOAD) is an interferometric switch. It consists of a loop mirror with one Semiconductor Optical Amplifier (SOA), circulator,  $2 \times 2$  coupler, and filters. It has one control input, one data signal input, and two outputs one is called output port 1, and the other is output port 2. When there is no control signal present only data signal enters into the TOAD, the data signal breaks into two components: one is the clockwise component, and the other is the counterclockwise component, which propagate around the loop and reach the SOA at different times. These components experience the same unsaturated SOA gain and recombine at the coupler. As no phase difference is introduced between them, the data signal comes from the output port 2. If the control signal is present, due to the gain saturation of the SOA and refractive index change, the two components will experience a different phase shift. If the phase difference is  $\pi$ , they recombine in the coupler, and the data signal will exit through output port 1. TOAD-based optical switch as shown in figure 1.

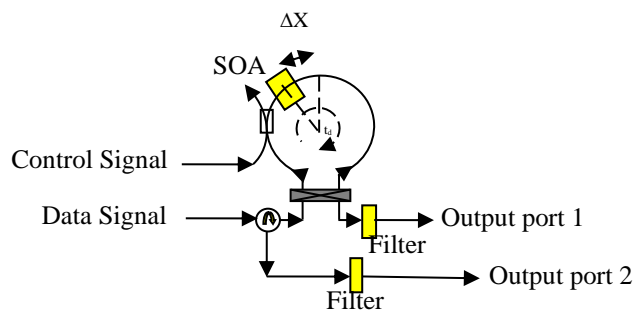


Figure 1. TOAD based optical switch

## 3. Frequency encoded single bit memory unit:

Frequency encoded TOAD-based single bit memory unit as shown in figure 2. It consists of four TOAD-based switches, filters ( $\nu_1$  pass and  $\nu_2$  pass), beam splitters (BS), and mirrors. It has one input A and two outputs  $Y_1$  and  $Y_2$ .

### 3.1 Working Principle of single bit memory unit:

We have used the data signal, and the control signal has different frequencies.

**Case 1:** When the input A is a signal of frequency  $\nu_1$ , i.e., '0', it passes through the  $\nu_1$  pass filter. So the TOAD  $T_1$  output generates a signal of frequency  $\nu_2$ , i.e., '1'. So the output of  $Y_1$  is  $\nu_2$ , i.e., '1'. A part of this output frequency  $\nu_2$ , i.e., '1', is applied in the input of TOAD  $T_4$  through the  $\nu_2$  pass filter and generates a signal of frequency  $\nu_1$ , i.e., '0'. So the output of  $Y_2$  is  $\nu_1$ , i.e., '0'. Now let

us explain what happens when the input is made off. In this condition, TOAD  $T_1$  still receives a signal of frequency  $\nu_1$  from the output  $Y_2$  and generates an output signal of frequency  $\nu_2$ , i.e., '1'. So the output of  $Y_1$  is  $\nu_2$ , i.e., '1'. A part of this output of frequency  $\nu_2$ , i.e., '1' is applied in the input of TOAD  $T_4$  through the  $\nu_2$  pass filter and generates a signal of frequency  $\nu_1$ , i.e.'0' as  $Y_2$  as output. So the previous condition is verified when the input is made off. Thus the device has a memory. So the memory unit is stored a high state signal even if the input signal made off because of feedback. When storing the new information into the memory, first erase the previously stored memory. This is called clearing memory. To clear the memory data signal frequency remains made off. There are no output exits from any TOAD  $T_1$  and TOAD  $T_4$ , i.e., there is nothing at the outputs  $Y_1$  and  $Y_2$ . This is the memory unit' clear state, and now the memory unit is ready to store new information.

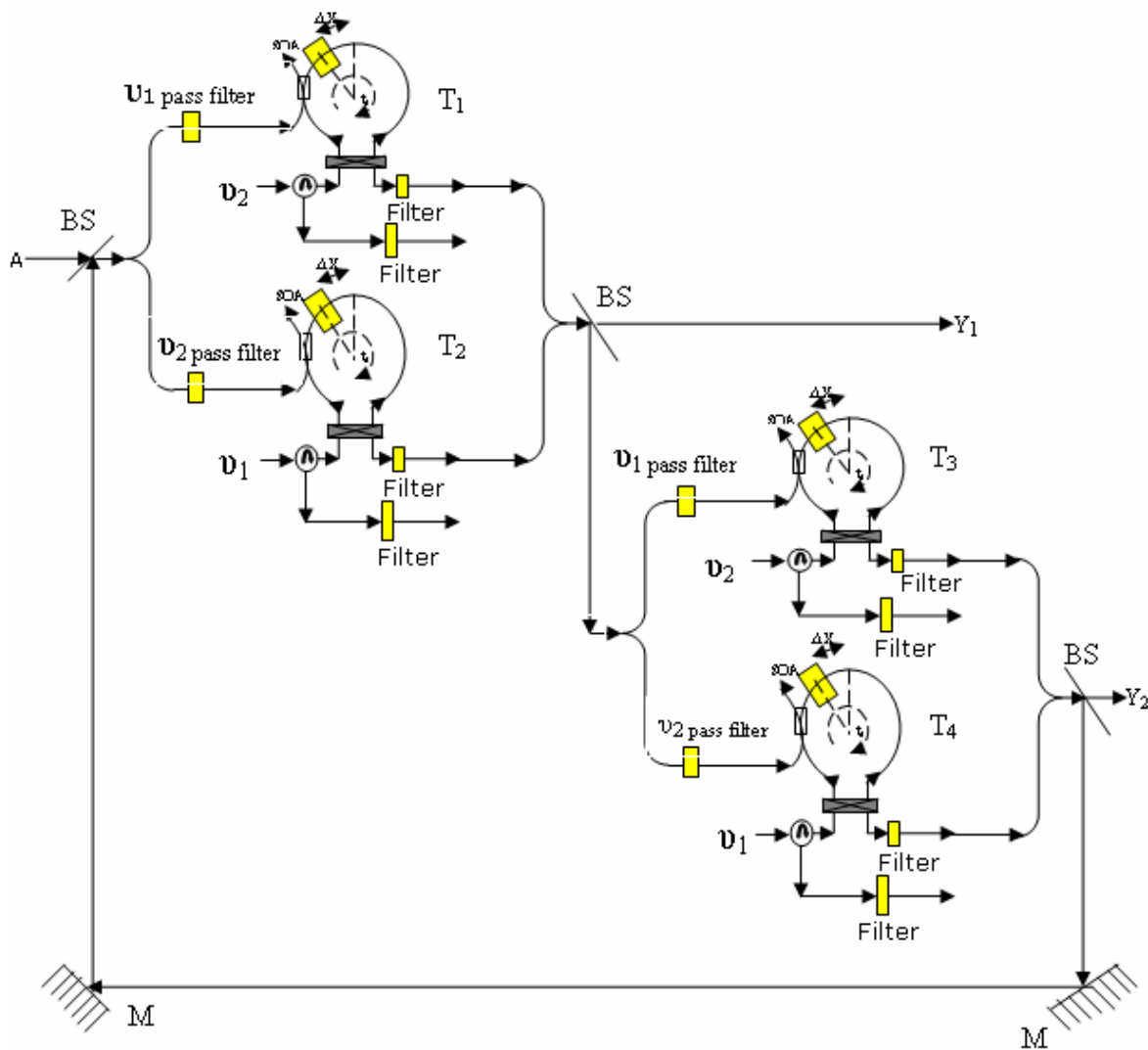


Figure2. Frequency encoded single bit memory unit circuit using TOAD

**Case2:** When the input A is a signal of frequency  $\nu_2$ , i.e., '1', it passes through the  $\nu_2$  pass filter. So the TOAD  $T_2$  output generates a signal of frequency  $\nu_1$ , i.e. '0'. So the output of  $Y_1$  is  $\nu_1$ , i.e., '0'. A part of this output frequency  $\nu_1$ , i.e. '0', is applied in the input of TOAD  $T_3$  through the  $\nu_1$  pass filter and generates a signal of frequency  $\nu_2$ , i.e., '1'. So the output of  $Y_2$  is  $\nu_2$ , i.e., '1'. Now let us explain what happens when the input is made off. In this condition, TOAD  $T_2$  still receives a signal of frequency  $\nu_2$  from the output  $Y_2$  and generates an output signal of frequency  $\nu_1$ , i.e., '0'. So the output of  $Y_1$  is  $\nu_1$ , i.e., '0'. A part of this output of frequency  $\nu_1$ , i.e. '0', is applied in the input of TOAD  $T_3$  through the  $\nu_1$  pass filter and generates a signal of frequency  $\nu_2$ , i.e., '1' as output  $Y_2$ . So the previous condition is verified when the input is made off. Thus the device has a memory. So the memory unit is stored low state signal even if the input signal is made off because of feedback. When storing the new information into the memory, first erase the previously stored memory again. To clear the memory data signal frequency is made off again. So the figure 2 can store single bit optical information in terms of frequency. This single-bit memory unit's output is shown in the truth table1.

Table1. Truth table of single bit memory unit

Input	Output	
A	$Y_1$	$Y_2$
$\nu_1(0)$	$\nu_2(1)$	$\nu_1(0)$
$\lambda_1=1550 \text{ nm}$	$\lambda_2=1560 \text{ nm}$	$\lambda_1=1550 \text{ nm}$
$\nu_2(1)$	$\nu_1(0)$	$\nu_2(1)$
$\lambda_2=1560 \text{ nm}$	$\lambda_1=1550 \text{ nm}$	$\lambda_2=1560 \text{ nm}$

#### 4. Simulation and Result:

Simulated input and output of the TOAD based single bit memory unit are shown in figure 3 and figure 4. Figure 3 shows the optical power spectrum when the input A is a signal frequency  $\nu_1$  and outputs  $Y_1 = \nu_2$  and  $Y_2 = \nu_1$ . Figure 4 shows the optical power spectrum when the input A is a signal frequency  $\nu_2$  and outputs  $Y_1 = \nu_1$  and  $Y_2 = \nu_2$ . We have used control signal and data signal pulse as gaussian pulse[3], and we choose the two wavelengths  $\lambda_1=1550 \text{ nm}$  for the frequency  $\nu_1$  and  $\lambda_2=1560 \text{ nm}$  for the frequency  $\nu_2$ . In [4], SOA parameters are use for this simulation.

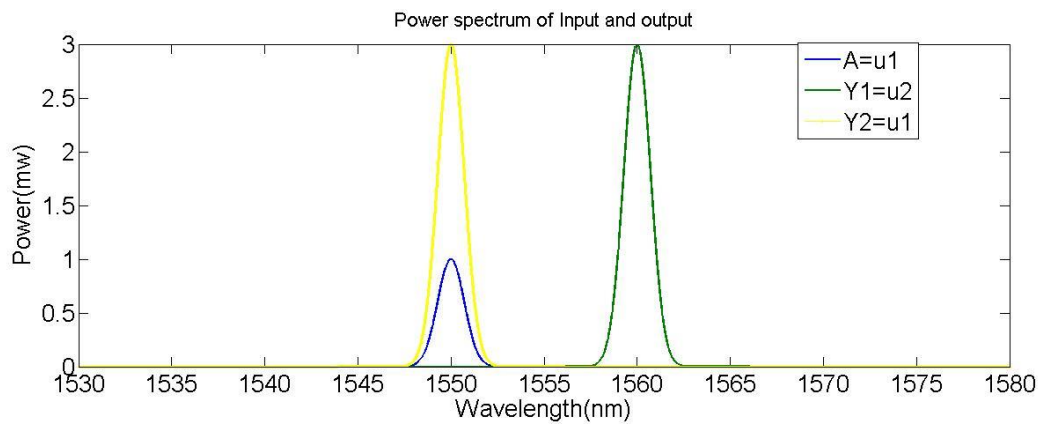


Figure3. Simulated optical power spectrum of the TOAD based single bit memory unit when input A is a signal frequency  $\nu_1(\lambda_1=1550 \text{ nm})$  and outputs  $Y_1= \nu_2(\lambda_2=1560 \text{ nm})$  and  $Y_2= \nu_1(\lambda_1=1550 \text{ nm})$ .

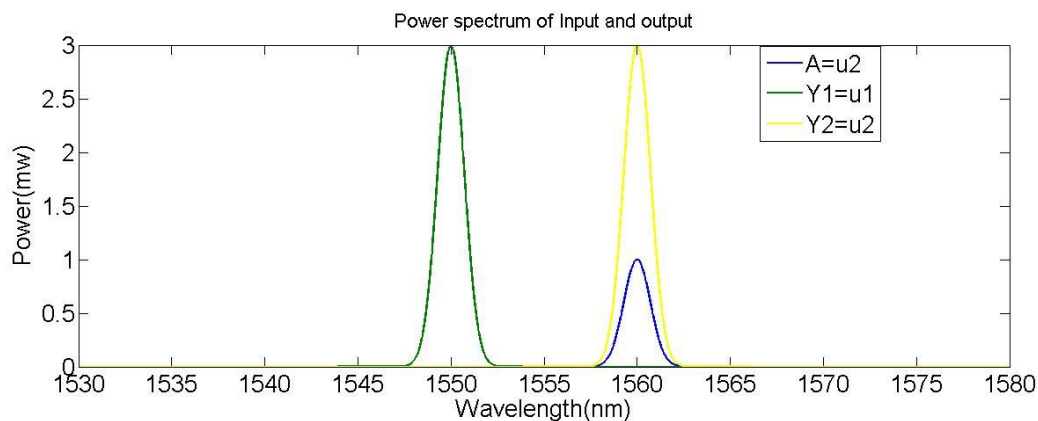


Figure4. Simulated optical power spectrum of the TOAD based single bit memory unit when input A is a signal frequency  $\nu_2(\lambda_2=1560 \text{ nm})$  and outputs  $Y_1= \nu_1(\lambda_1=1550 \text{ nm})$  and  $Y_2= \nu_2(\lambda_2=1560 \text{ nm})$ .

### Conclusion:

Frequency encoded all-optical single bit memory unit using TOAD is successfully analyzed and characterized. This single-bit memory unit's operation is based on frequency conversion and simulated by MATLAB. We have shown the output optical spectrums of the single-bit memory unit. The output of a single-bit memory unit shows the possibility of various applications in optical and electrical communication systems.

### References:

1. K Mukherjee, AK Meikap, D Kumbhakar “Frequency encoded all optical single bit memory unit using difference frequency generation alone” *Optical and Quantum Electronics*, 43,

- pages101–107(2012)
2. S Dutta, S Mukhopadhyay “An all optical approach of frequency encoded NOT based Latch using semiconductor optical amplifier” *Journal of optics*, 39, pages39–45(2010)
  3. K.Maji,K.Mukherjee and A.Raja “An alternative method for implementation of frequency-encoded logic gates using a terahertz optical asymmetric demultiplexer (TOAD)” *Journal of computational electronics* 18, pages1423–1434(2019)
  4. K.Maji,K.Mukherjee and A.Raja “Frequency Encoded all-Optical Universal Logic Gates using Terahertz Optical Asymmetric Demultiplexer” *Int. J. of Phot. and Opt. Tech.*, vol. 4, no. 3, pp. 1-7, (2018)
  5. Xiang Zhang, Sunil Thapa & Niloy Dutta “All-optical XOR gates based on dual semiconductor optical amplifiers” *Cogent Physics*, 6:1, 1660495, 2019
  6. K. Mukherjee, K. Maji, A. Raja, All optical four bit two’s complement generator and single bit comparator using reflective semiconductor optical amplifier, *IJNBM*, 9.1/2.2020.
  7. K. Mukherjee, “Terahertz Optical Asymmetric Demultiplexer (TOAD) based frequency encoded all optical NOT gate”, *Proceedings of the international conference on laser, materials, & communication*, pp 242 – 244, Burdwan, India, December 7 to 9, 2011, ISBN 983 - 93 - 80813 - 14 - 1.
  8. A. K. Mondal, All-Optical DFT using TOAD based Cross-Bar switches, *JCSC*, online ready, <https://doi.org/10.1142/S0218126619501561>.
  9. A. Bhattacharya, D. Gayen, T. Chattopadhyay, “Design of 2-to-4 All-Optical Decoder with the Help of Terahertz Optical Asymmetric Demultiplexer”, *International Journal of Modern Nonlinear Theory and Application*, Vol.5 No.1, 2016.
  10. K. Maji, K. Mukherjee, A. Raja, Frequency encoded all optical universal logic gate using tera hertz optical demultiplexer, *Int. Journal of Optics and Photonics*, 4,3,1-7(2018).
  11. K. Maji and K. Mukherjee, "Performance analysis of optical logic XOR gate using dual-control Tera Hertz Optical Asymmetric Demultiplexer (DCTOAD)," *2019 Devices for Integrated Circuit (DevIC)*, Kalyani, India, 2019, pp. 58-60, doi: 10.1109/DEVIC.2019.8783496.
  12. K. Mukherjee, K. Maji, M. K. Mandal, “Design and analysis of all- optical dual control dual SOA Tera Hertz asymmetric demultiplexer based half adder.” *Opt Quant Electron* 52, 402 (2020). <https://doi.org/10.1007/s11082-020-02522-2>
  13. K. Maji, K.Mukherjee, A.Raja “Design and performance analysis of all optical 4-bit parity generator and checker using dual-control dual SOA terahertz optical asymmetric demultiplexer (DCDS-TOAD)”, *Journal of Optical Communications* (published online ahead of print 2020), 000010151520190098. doi: <https://doi.org/10.1515/joc-2019-0098>

**Effect of Fe Substitution on the Magnetic Properties Of  $MnCo_2O_4$** Junmoni Barman\*<sup>1</sup> and S. Ravi<sup>2</sup><sup>1</sup> Department of Physics, Rajiv Gandhi University, Arunachal Pradesh-791112, India<sup>2</sup> Department of Physics, Indian Institute of Technology Guwahati, Guwahati-781039, Assam, India**Email:** [barmanjunmoni@gmail.com](mailto:barmanjunmoni@gmail.com)**ABSTRACT**

Single phase samples of  $Mn(Co_{1-x}Fe_x)_2O_4$  ( $x = 0 - 0.5$ ) were synthesized by using sol-gel route. Rietveld refinement of the room temperature X-ray diffraction patterns reveal cubic spinel structure of the samples with  $Fd\bar{3}m$  space group. The lattice parameter is found to increase systematically with increase in the Fe concentration. Magnetization measurements show ferrimagnetic transition in all the samples and the transition temperature is found to increase with increase in Fe concentration, *i.e.* from 176 K for  $x = 0$  to 446 K for  $x = 0.5$ . From the Curie-Weiss fit of the susceptibility data in the paramagnetic region, the possible cationic distribution in this compound is found to be of the type  $Co^{2+}[Co_{1-2x}^{3+}Fe_{2x}^{3+}Mn^{3+}]O_4$  with  $Co^{3+}$  in low spin state. The saturation magnetization and the theoretical as well as the experimental effective magnetic moment are found to increase with increasing Fe concentration. Both parent and Fe doped samples show an unusual hysteresis behavior below a certain temperature. This unusual hysteresis behavior is attributed to the domain wall pinning effect which is found to decrease with increasing Fe concentration.

**Keywords:** Spinel Cobaltite;  $MCo_2O_4$ ; Ferrimagnetic**INTRODUCTION:**

Spinel compounds with general chemical formula  $AB_2O_4$ , containing two or more types of cations in tetrahedral A and octahedral B sites, have been studied for decades owing to their interesting electric, magnetic, optical and catalytic properties [1-10]. Out of several spinel compounds, transition metal cobaltite  $MCo_2O_4$  ( $M = Mn, Ni, Zn, Cu, Mg$  etc.) have attracted significant interest for fundamental research and also for technological applications in many areas such as colossal magnetoresistance (CMR), magnetic sensors, fuel cell electrodes, electrical

catalysts, microwave absorption, *etc.* [3-10]. Among these cobaltite, spinel  $\text{MnCo}_2\text{O}_4$  has been studied widely due to its promising applications as a magnetic material and its unusual hysteresis behavior [9-12].  $\text{MnCo}_2\text{O}_4$  is in general described as an inverse spinel oxide with  $\text{Fd}\bar{3}m$  space group in which the manganese cations show preference for octahedral sites [3]. However, the cationic distribution of  $\text{MnCo}_2\text{O}_4$  is still not well established. Several cationic distribution have been proposed for stoichiometric  $\text{MnCo}_2\text{O}_4$  and non-stoichiometric  $\text{Mn}_x\text{Co}_{3-x}\text{O}_{4+\delta}$  on the basis of (i) electrical conductivity:  $\text{Co}^{2+}[\text{Co}^{2+}\text{Mn}^{4+}]_2\text{O}_4$  or  $\text{Co}^{3+}[\text{Co}^{3+}\text{Mn}^{2+}]_2\text{O}_4$  [3, 13], and (ii) neutron diffraction and magnetic measurements:  $\text{Co}^{2+}[\text{Co}_{2-x}^{3+}\text{Mn}_x^{3+}]_2\text{O}_4$  [3, 13,14] and  $\text{Co}^{2+}[\text{Co}^{2+}\text{Mn}^{4+}]_2\text{O}_4$  [3, 13]. Bulk  $\text{MnCo}_2\text{O}_4$  is a long range ferrimagnetic (FIM) oxide with the transition temperature,  $T_C \approx 185$  K [9-11]. Also a peak at  $T_P \approx 177$  K is observed in the temperature dependent zero field cooled magnetization curve due to Hopkinson effect [10]. An unusual magnetic hysteresis behavior at temperatures below 130 K is observed by Joy and Date [9, 10]. In this temperature range, the initial magnetization curve lies outside the main loop while for  $T > 130$  K, normal hysteresis loops are observed. This unusual behavior of magnetic hysteresis loop is explained in terms of irreversible domain wall movements. An evolution of such unusual magnetic properties is studied by Borges *et al.* [11] for different crystallite size of  $\text{MnCo}_2\text{O}_4$ . Philip and Kutty have reported a change in the temperature coefficient of resistivity of  $\text{MnCo}_2\text{O}_4$  from negative to positive value below 100 K and this temperature is compared to the  $T_C$  of the material [7]. According to them the conduction in  $\text{MnCo}_2\text{O}_4$  is mainly due to hole hopping between  $\text{Mn}^{3+}$  and  $\text{Mn}^{4+}$ . In this present work, we have substituted  $\text{Fe}^{3+}$  ions with relatively larger magnetic moment, in place of  $\text{Co}^{3+}$  ions and carried out the study of structural and their interesting magnetic properties.

## MATERIALS & METHODS

$\text{Mn}(\text{Co}_{1-x}\text{Fe}_x)_2\text{O}_4$  ( $x = 0 - 0.5$ ) samples were synthesized by using sol-gel method. Stoichiometric ratio of  $\text{C}_4\text{H}_6\text{MnO}_4 \cdot 4\text{H}_2\text{O}$ ,  $\text{Co}(\text{NO}_3)_2 \cdot 6\text{H}_2\text{O}$  and  $\text{Fe}(\text{NO}_3)_3 \cdot 9\text{H}_2\text{O}$  of 99 % were weighed, dissolved in distilled water and mixed in a beaker. Citric acid and ethylene glycol were added to the solution and then the solution was heated slowly to evaporate the solvent, leaving a precipitate. The precipitate was grinded and calcined at 600 °C and 800 °C for 12 hours followed by final sintering in pellet form at 1000 °C for 24 hours. Powder X-ray diffraction pattern at room temperature was recorded by using Rigaku make X-ray diffractometer of model TTRAX III with  $\text{Cu-K}\alpha$  radiation.

Magnetization measurement both as a function of temperature and magnetic field were performed by using Lakeshore make Vibrating Sample Magnetometer (VSM) of model no. 7410.

## RESULTS & DISCUSSION

The X-ray diffraction (XRD) patterns obtained for all the samples at room temperature are found to be in single phase form. The XRD patterns were analyzed by Rietveld refinement technique by using Fullprof program. Refinement shows that all the samples crystallize in cubic spinel structure with  $Fd\bar{3}m$  space group. Figure 1 shows the XRD pattern of  $x = 0$  and 0.5 samples along with the Rietveld refinement data. For  $x = 0$  sample the lattice parameter is found to be  $a = 8.2753 \text{ \AA}$  which is comparable to those reported in literatures [11, 12]. The lattice parameter is found to increase systematically with increase in Fe concentration. It can be easily explained in terms of  $\text{Fe}^{3+}$  ions having larger ionic radius ( $0.645 \text{ \AA}$ ) replacing the  $\text{Co}^{3+}$  ions ( $0.61 \text{ \AA}$ ) in the octahedral site. Thus the doped  $\text{Fe}^{3+}$  ions indeed get substituted in Co site. The lattice parameters and the reliability factors related to Rietveld refinement of the samples are listed in table I. The occupancy value of Fe is found to be comparable to the nominal starting composition.

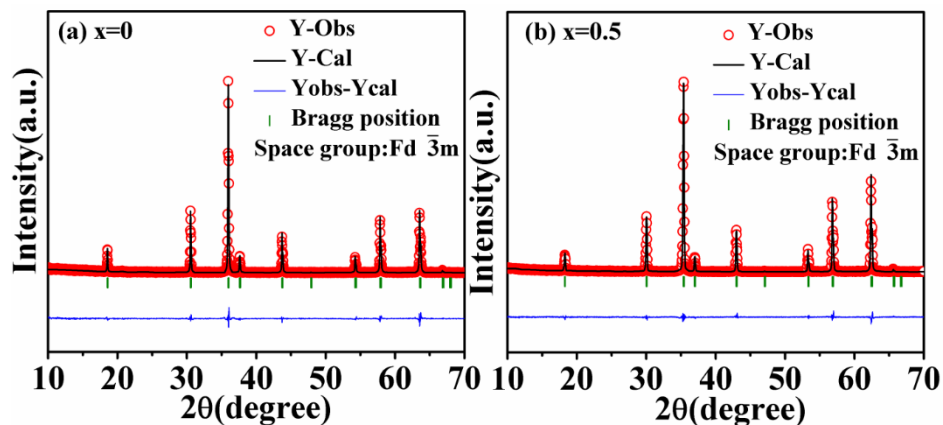


**Figure 1.** XRD patterns along with Rietveld refinement data for (a)  $x = 0$  and (b)  $x = 0.5$ . Y-Obs and Y-Cal represent the experimental and refined data respectively.

Magnetization as a function of temperature is measured for all the samples under zero field cooled (ZFC) and field cooled (FC) conditions for the applied field  $H = 500 \text{ Oe}$ . ZFC and FC curves for  $x = 0, 0.2, 0.3$  and  $0.5$  samples are shown in Figure. 2. Sharp magnetic transitions at the Curie temperature highlights the FIM behavior of the samples. The transition temperature determined from  $dM/dT$  versus  $T$  plot is found to be  $T_C = 175 \text{ K}$  for  $x = 0$  sample and is comparable to that reported in literatures [11, 12]. The FIM  $T_C$  is found to increase with increase

in Fe concentration. This increase in  $T_C$  is due to the substitution of  $\text{Fe}^{3+}$  ions with higher magnetic moment ( $5 \mu_B$ ) in place of the  $\text{Co}^{3+}$  ions in low spin state as such substitution strengthens the superexchange interactions between A and B site ions [14]. The overall shape of the ZFC curve is almost similar for all the samples. Strong irreversibility of magnetization is observed between ZFC and the FC curve at  $T < T_C$  due to the presence of large magnetocrystalline anisotropy. Such irreversibility is similar to the earlier reports for  $\text{MnCo}_2\text{O}_4$  [10] and also to some ferromagnetic (FM) and FIM oxides [15, 16]. Moreover, for each samples a maximum magnetization ( $T_P$ ) is observed just below the transition temperature in the  $M$ - $T$  plot under ZFC condition and then it drops off to a very low value. This peak is observed due to Hopkinson effect. It is a competition effect between the applied magnetic field and the magnetocrystalline anisotropy which changes with temperature. The domain wall pinning effect is also responsible for the shape of the ZFC curve. When the sample is heated in a small applied magnetic field the mobility of the domain walls may be increased i.e. the pinning of the domain wall is reduced as the temperature increases and the walls may be displaced easily along the direction of the applied field and this leads to a slight increase in the magnetization. When the sample is heated further, the magnetocrystalline anisotropy is reduced and this reduction may make the magnetization of the grains to orient easily in the direction of the magnetic field leading to an increase in magnetization. On the other hand, with increasing temperature the thermal agitation increases which leads to a decrease in magnetization. However, in the temperature range just below  $T_C$ , the easy magnetization rotation may dominant over the thermal agitation which leads to overall increase in magnetization. After this temperature the sample become demagnetized and the magnetization falls off to zero at  $T_C$ . Therefore, a peak is observed in the ZFC curve just below the  $T_C$  [17]. With increase in Fe concentration, along with  $T_C$ , the  $T_P$  value also increases and become enlarged. However, the  $T_P$  value decreases with increase in the applied magnetic field as shown in Figure 3 for  $x = 0$  and  $x = 0.1$ . Since the magnetocrystalline anisotropy decreases with increase in temperature and applied field, in case of high applied field it may be much easier to rotate the spins in the field direction relatively at low temperature. This is the reason of shifting of  $T_P$  towards low temperature with increase in the applied field.

In order to determine the valence state of Co, Mn and Fe and their distribution in tetrahedral and the octahedral sites, we have compared the experimental effective magnetic moment,  $\mu_{eff}$  with the theoretical effective magnetic moment,  $\mu_{th}$ . For this purpose, the susceptibility data in the paramagnetic region were fitted to the Curie-Weiss (CW) law  $\chi = C / (T - \theta_C)$ . The values of

effective magnetic moment,  $\mu_{eff}$  determined from the above fit are found to be  $6.29 \mu_B$  for  $x = 0$  sample and this value increases with increase in  $Fe^{3+}$  ( $3d^5$ ) concentration as expected. The Curie-Weiss fit for four of the samples are shown in the inset of Figure 2. The estimated theoretical values of magnetic moment  $\mu_{th}$  are determined by considering spin only contribution of  $Mn^{3+}$  and  $Co^{2+}$  and considering  $Co^{3+}$  in low spin state ( $S = 0$ ) and also considering the cationic distribution of the type  $Co^{2+}[Co_{1-2x}^{3+}Fe_{2x}^{3+}Mn^{3+}]O_4$ . The values of  $\mu_{th}$  are found to be comparable to the experimental values. Thus the cationic distribution obtained here is in accordance with that given by Wickham and Croft [14]. However, a slightly smaller value of  $\mu_{eff}$  than  $\mu_{th}$  for  $x = 0.4$  and  $0.5$  samples are due to the possibility that some of the  $Mn^{3+}$  ions in the samples may be in higher valence state, say  $Mn^{4+}$ . However, we have not determined the actual valence state of the ions. Also the  $\mu_{eff}$  increases with increasing Fe concentration as expected.

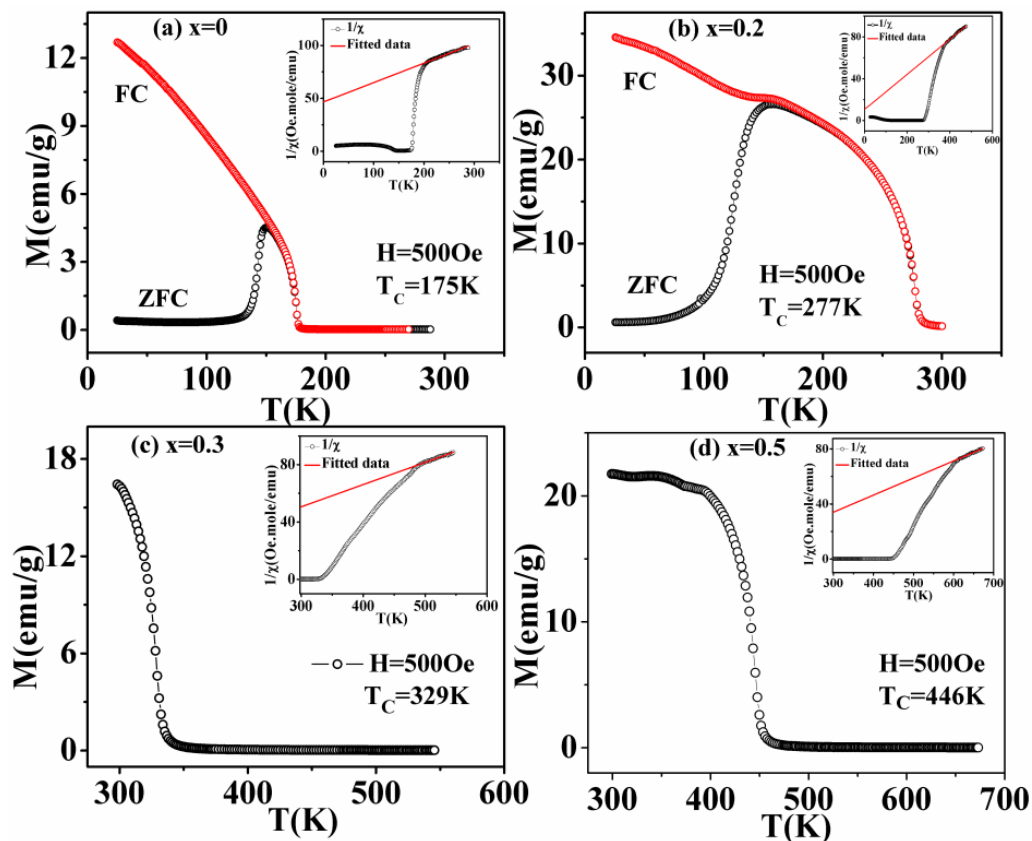


**Figure 2.** Temperature dependence of ZFC and FC magnetization for (a)  $x = 0$  and (b)  $x = 0.2$  and that of (c)  $x = 0.3$  and (d)  $x = 0.5$  samples at high temperatures. Insets show the Curie-Weiss fit for the respective samples.

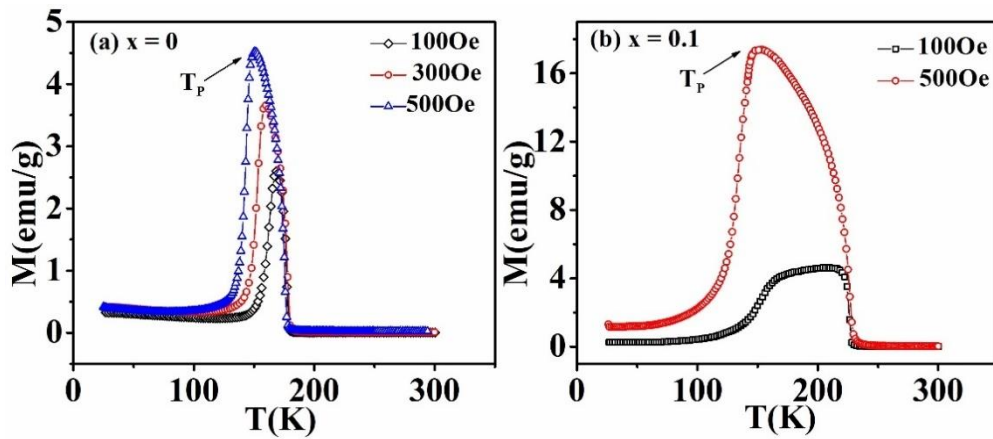


**Figure 3.** Temperature dependence of ZFC magnetization at different fields for (a)  $x = 0$  and (b)  $x = 0.1$  samples.

**Table 1.** The lattice parameter  $a$ , goodness of fit  $\chi^2$ ,  $R_P$ ,  $R_{Brag}$ ,  $R_F$ ,  $T_C$ ,  $\mu_{eff}$ ,  $\mu_{th}$  and  $M_s$  of  $Mn(Co_{1-x}Fe_x)_2O_4$ .

$x$	$a$ (Å)	$\chi^2$	$R_P$	$R_{Brag}(\%)$	$R_F(\%)$	$T_C$	$\mu_{eff}$	$\mu_{th}$	$M_s$
0	8.2753	3.84	9.68	3.63	3.32	175	6.29	6.25	0.34
0.1	8.3110	3.88	10.80	2.54	2.36	226	6.79	6.78	1.24
0.2	8.3450	4.82	8.99	3.66	3.81	277	7.18	7.28	1.93
0.3	8.3737	3.74	8.06	2.95	3.02	329	7.67	7.74	2.33
0.4	8.3927	4.35	7.41	2.67	2.75	388	7.87	8.18	2.73
0.5	8.4125	3.72	7.50	3.07	2.90	446	8.02	8.60	3.45

Typical  $M-H$  loops recorded at 25 K for all the samples are shown in Figure 4(a). The Fe doped sample shows enhanced saturation magnetization,  $M_s$  compared to the parent compound and it gradually increases with increasing Fe concentration as expected. The values of  $M_s$  obtained after subtracting the linear contribution are listed in table I. The coercivity,  $H_C$  decreases first with Fe concentration up to  $x = 0.2$  but starts increasing again as shown in Figure 4(b).

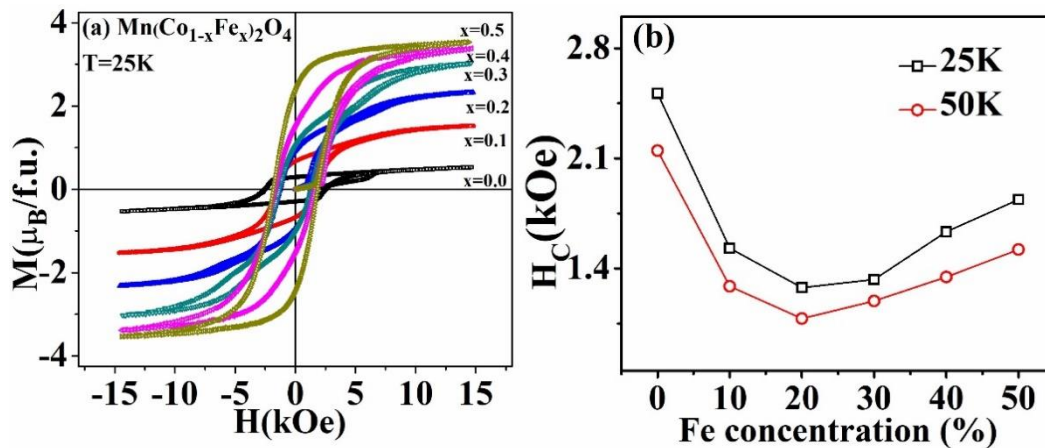


**Figure 4.** (a)  $M$ - $H$  loops of  $Mn(Co_{1-x}Fe_x)_2O_4$  at 25 K and (b) variation of  $H_C$  with Fe concentration at 25 K and 50 K.

The  $M$ - $H$  loops recorded for both parent and Fe doped samples show unusual hysteresis behavior below a certain temperature. The initial magnetization curve lies outside the main hysteresis loop. In order to clearly display this phenomenon, the  $M$ - $H$  loops for  $x = 0, 0.2$  and  $0.5$  at some certain temperatures are shown in expanded scale in Figure 5. It is found that for  $x = 0$  and  $x = 0.2$  samples up to 125 K such unusual behavior is observed but at 150 K the initial curve lies completely inside the loop. However, for  $x = 0.5$  sample the unusual hysteresis behavior is observed only at 25 K and after that normal hysteresis behavior is observed. For  $x = 0.1, 0.3$  and  $0.4$  this unusual hysteresis behavior is observed up to 125 K, 100 K and 75 K respectively (not shown). Thus with increase in Fe concentration this behavior is gradually shifted towards lower temperatures and may be disappeared if the Fe concentration is increased above 50 %. Such unusual hysteresis behavior is earlier observed for  $MnCo_2O_4$  [9, 10] and for some other compounds also [18-21]. Since the shape of the initial curve at low applied field is controlled by the domain wall motion, such unusual behavior is associated with irreversible domain wall motion which indicates the presence of domain wall pinning effect. In this case may be the domains are in minimum energy states by increasing the number of domains and thus bringing the domain walls to interact with pinning sites. Therefore, to move or to unpin the domain walls a higher magnetic field is required and because of this at small applied fields the domain walls move slowly and the initial magnetization curve lies outside the hysteresis loop. As the field is increased sufficiently, the pinning of the domain wall is overcome by the applied field and a normal initial curve is observed at higher field.

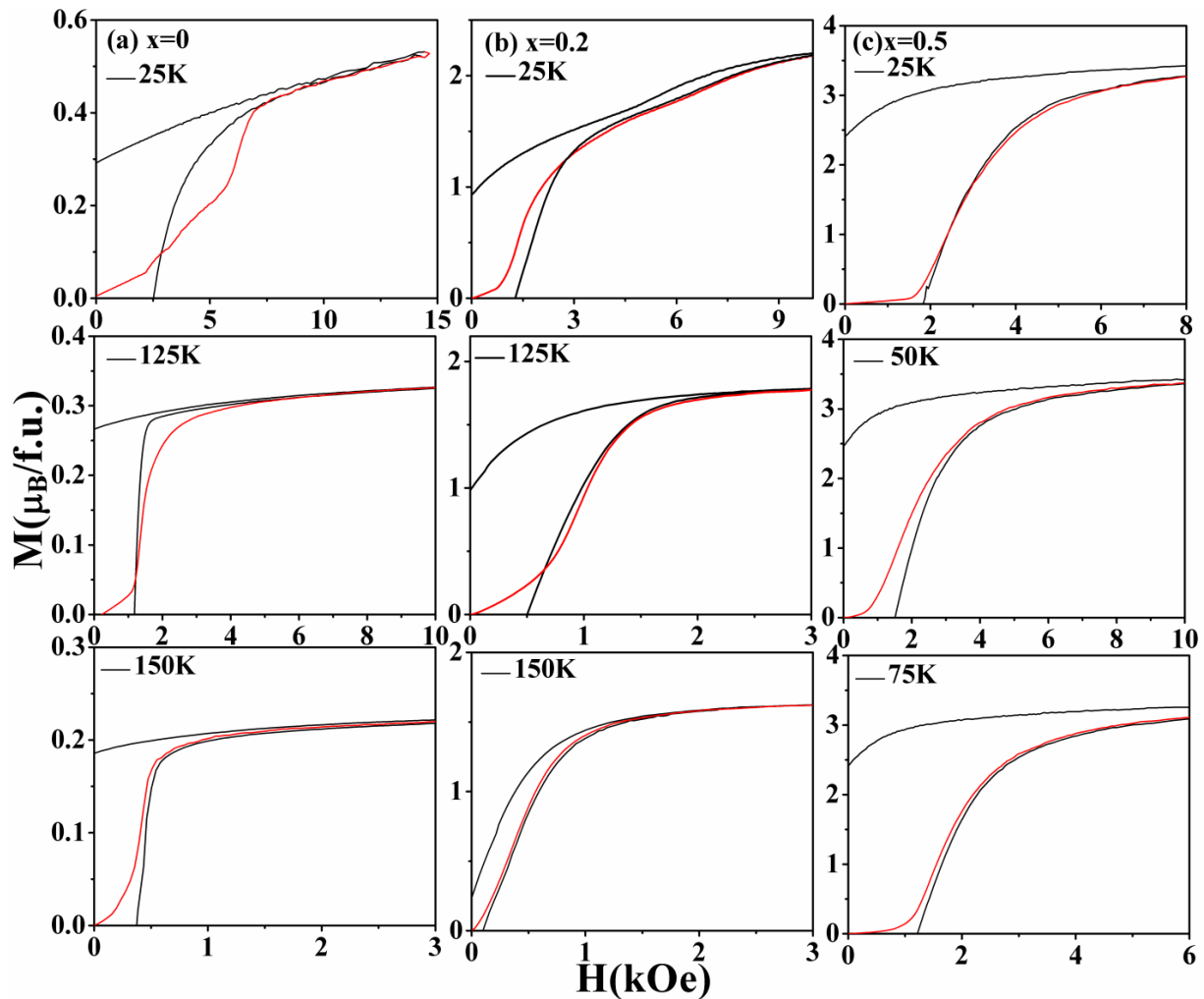


**Figure 5.** Initial magnetization (red line) and part of the hysteresis loop (black line) of (a)  $x = 0$ , (b)  $x = 0.2$  and (c)  $x = 0.5$ .

However, the initial curve lies outside the loop only up to a certain temperature as mentioned above. Since the samples are cooled through the  $T_C$  for both the ZFC curve and the hysteresis loop measurements, the ZFC curve and the initial magnetization curve can be compared to understand this behavior. Figure 6 shows the ZFC magnetization curves (solid lines) recorded at 500 Oe and the initial magnetization values (open circles) at the corresponding field strength at different temperatures for  $x = 0, 0.1, 0.2$  and  $0.5$  samples. Both are found to be identical as expected. Upon ZFC, the domain walls are pinned into random orientations and thus when a low field is applied, there is a competition between the random local magnetization orientation of the individual domain and the applied magnetic field, and the former one dominates at low temperature resulting in a magnetization lower than the expected. As discussed earlier, when the temperature increases the pinned domain walls become activated and slow motion of the domain

walls takes place resulting in a slow increase in magnetization. When temperature is further increased this pinning effect is completely overcome by the magnetic field energy and the increasing thermal activation energy, and the magnetization value reaches a maximum in the ZFC curve. This temperature is found to be about 150 K for  $x = 0, 0.1$  and  $0.2$  samples which corresponds to the temperature at which the initial curve lies completely inside the hysteresis loop and below this temperature it lies outside. For  $x = 0.5$  sample, though the complete peak in the ZFC curve is not observed but the increase in the magnetization occurs from about 30 K which means that the domain wall pinning effect become weaker at lower temperatures compared to the others and this is the reason for the initial curve to lie inside the hysteresis loop even at 50 K for this sample. Similar behavior is observed for the  $x = 0.3$  and  $0.4$  samples which are not shown here. Similar unusual hysteresis behavior at low applied field and temperature is also likely to occur if competing antiferromagnetic interactions are present in the samples. Although the presence of such antiferromagnetic interactions at low temperature was not reported yet on  $\text{MnCo}_2\text{O}_4$  based samples, further investigation is required to eliminate it in the present samples.

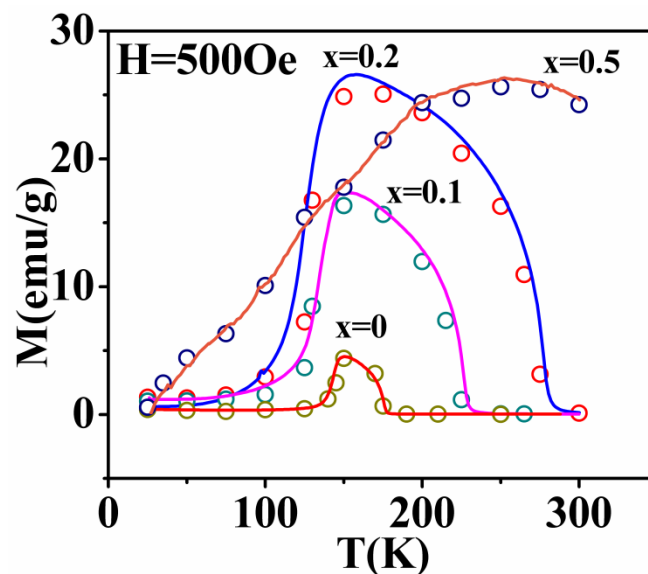


**Figure 6.** ZFC magnetization curve (Solid lines) for  $x = 0, 0.1, 0.2$  and  $0.5$  at  $H = 500$  Oe. The open circles correspond to magnetization values at 500 Oe taken from  $M-H$  loop at different temperatures.

## CONCLUSION

Mn(Co<sub>1-x</sub>Fe<sub>x</sub>)<sub>2</sub>O<sub>4</sub> ( $x = 0 - 0.5$ ) samples were prepared by sol-gel route and all the samples were found to be crystallized in cubic spinel structure with  $Fd\bar{3}m$  space group. The lattice parameter is found to increase systematically with increase in the Fe concentration. All the samples show FIM behavior and the  $T_C$  is found to increase with increase in Fe concentration. From the Curie-Weiss fit of the susceptibility data in paramagnetic region, the possible cationic distribution in this compound is found to be of the type  $Co^{2+}[Co_{1-2x}^{3+}Fe_{2x}^{3+}Mn^{3+}]O_4$  with  $Co^{3+}$  in low spin state. The  $M-H$  loops recorded for both parent and Fe doped samples show unusual hysteresis behavior below a certain temperature which can be compared with the ZFC curve of each sample. Both the shape of ZFC curve and the unusual hysteresis behavior is attributed to the domain wall pinning effect which is found to decrease with increasing Fe concentration. However, further investigation is needed to confirm the absence of any competing antiferromagnetic interaction at low temperature.

## ACKNOWLEDGEMENT

We acknowledge CIF, IIT Guwahati for high temperature VSM facility and DST-FIST for XRD facility.

## REFERENCES

- [1] Nissinen, T., Valo, T., Gasik, M., Rantanen, J. and Lampinen, M. Microwave synthesis of catalyst spinel MnCo<sub>2</sub>O<sub>4</sub> for alkaline fuel cell. *J. Power Sources* **106** (2002), 109-115.
- [2] Hinklin, T. R., Azurdia, J., Kim, M., Marchal, J. C., Kumar, S. and Laine, R. M. Finding spinel in all the wrong places. *Adv. Mater.* **20** (2008), 1373-1375.
- [3] Rios, E., Gauiter, J. L., poillerat, G. and Chartier, P. Mixed valency spinel oxides of transition metals and electrocatalysis: case of the Mn<sub>x</sub>Co<sub>3-x</sub>O<sub>4</sub> system. *Electrochim. Acta* **44** (1998), 1491-1497.
- [4] Nissinen, T., Kiros, Y., Gasik, M. and Lampinen, M. Comparison of preparation routes of spinel catalyst for alkaline fuel cells. *Mater. Res. Bull.* **39** (2004), 1195-1208.
- [5] Zhu, J. and Gao, Q. Mesoporous MCo<sub>2</sub>O<sub>4</sub> (M = Cu, Mn and Ni) spinels: Structural replication, characterization and catalytic application in CO oxidation. *Microporous Mesoporous Mater.* **124** (2009), 144-152.
- [6] Duan, L., Gao, F., Wang, L., Jin, S. and Wu, H. Hydrothermal synthesis and characterization of MnCo<sub>2</sub>O<sub>4</sub> in the low-temperature hydrothermal process: Their magnetism and electrochemical properties. *J. Adv. Ceram.* **2** (2013), 266-273.
- [7] Philip, J. and Kutty, T. R. N. Colossal magnetoresistance of oxide spinels, Co<sub>x</sub>Mn<sub>3-x</sub>O<sub>4</sub>. *Mater. Lett.* **39** (1999), 311-317.

- [8] Bhowmik, R. N. and Ranganathan, R. Magnetic order and electrical conductivity scaling of the spinel oxide  $Mn_{0.5}Ru_{0.5}Co_2O_4$ . *Phys. Rev. B* **74** (2006), 214417.
- [9] Joy, P. A. and Date, S. K. Comparison of the zero-field-cooled magnetization behavior of some ferromagnetic and ferrimagnetic systems. *J. Magn. Magn. Mater.* **218** (2000), 229-237.
- [10] Joy, P. A. and Date, S. K. Unusual magnetic hysteresis behavior of oxide spinel  $MnCo_2O_4$ . *J. Magn. Magn. Mater.* **210** (2000), 31-34.
- [11] Borges, F. M. M., Melo, D. M. A., Camara, M. S. A., Martinelli, A. E., Soares, J. M., Araujo, J. H. de and Cabral, F. A. O. Magnetic behavior of nanocrystalline  $MnCo_2O_4$  spinels. *J. Magn. Magn. Mater.* **302** (2006), 273-277.
- [12] Bazuev, G. V. and Korolyov, A. V. Magnetic behavior of  $MnCo_2O_{4+\delta}$  spinel obtained by thermal decomposition of binary oxalates. *J. Magn. Magn. Mater.* **320** (2008), 2262-2268.
- [13] Rios, E., Lara, P., Serafini, D., Restovic, A. and Gautier, J. L. Synthesis and characterization of manganese-cobalt solid solutions prepared at low temperature. *J. Chil. Chem. Soc.* **55** (2010), 261-265.
- [14] Wickham, D. G. and Croft, W. J. Crystallographic and magnetic properties of several spinels containing trivalent manganese. *J. Phys. Chem. Solids* **7** (1958), 351-360.
- [15] Kumar, P. S. A., Joy, P. A. and Date, S. K. On the irreversible magnetic behavior of the anisotropic ferromagnetic system  $SrRuO_3$ . *Physica B* **269** (1999), 356-361.
- [16] Kumar, P. S. A., Joy, P. A. and Date, S. K. Comparison of the irreversible thermomagnetic behaviour of some ferro-and ferrimagnetic systems. *Bull. Mater. Sci.* **23** (2000), 97-101.
- [17] Kwon, H. W. and Shon, S. W. Study of the Hopkinson Effect in the HDDR-treated Nd-Fe-B-type Material. *J. Magnetism* **6** (2001), 61-65.
- [18] Altuncevahtir, B. and Koymen, A. R. Peculiar behavior of the initial magnetization in CoNi thin films. *J. App. Phys.* **95** (2004), 8051.
- [19] Zysler, R. D., Fiorani, D. and Testa, A. M. Investigation of magnetic properties of interacting  $Fe_2O_3$  nanoparticles. *J. Magn. Magn. Mater.* **224** (2001), 5-11.
- [20] Senoussi, S. Irreversible effects in  $Au_{81}Fe_{19}$  and  $Ni_{79}Mn_{21}$  below the de Almeida-Thouless temperature. *J. Physique* **45** (1984), 315-322.
- [21] Sarkar, T., Duffort, V., Pralong, V., Caignaert, V. and Raveau, B. Oxygen hyperstoichiometric hexagonal ferrite  $CaBaFe_4O_{7+\delta}$  ( $\delta \approx 0.14$ ): Coexistence of ferrimagnetism and spin glass behavior. *Phys. Rev. B* **83** (2011), 094409..

## Review On Metal Nanoparticles Embedded in Molybdenum Disulfide Nanosheets: Synthesis and Properties

Upama Das\*<sup>1</sup>, Dr.Sulochana Deb<sup>2</sup>

<sup>1,2</sup>Department of Physics, Gauhati University, Guwahati-781014, Assam, India

Email: upama.das96@gmail.com

### ABSTRACT

Study of transition metal dichalcogenides (TDMCs) has become very crucial due to their wide range of applications in various fields such as sensors, supercapacitors, biological imaging, etc. Molybdenum Disulfide (MoS<sub>2</sub>) nanosheet is a 2D TMDCs semiconductor, which is considered to be an ideal substrate as it gets easily hybridized in presence of functional group and results in formation of MoS<sub>2</sub>-based nanocomposites. Amongst the different types of MoS<sub>2</sub>-based nanocomposites, Metal-MoS<sub>2</sub> nanocomposite are unique due to their unusual and extraordinary properties. In this review, we will be focussing on the various techniques of synthesis and properties displayed by Ag-MoS<sub>2</sub>, Au-MoS<sub>2</sub>, Pd-MoS<sub>2</sub> and Pt-MoS<sub>2</sub> nanocomposites.

**Keywords:** Molybdenum Disulfide, Metal-Molybdenum Disulfide, Surface plasmon resonance (SPR).

### 1. INTRODUCTION:

The study of Molybdenum Disulfide (MoS<sub>2</sub>) plays an important role due to their wide range of applications in lubricants, catalysis, sensors, supercapacitors, etc, [1-8]. MoS<sub>2</sub> nanosheets are 2D semiconductor which possess great chemical and thermal stability, large active surface area, high reactivity, and exhibit increased adsorption capacity [9-11]. Multi-layered MoS<sub>2</sub> nanosheets have indirect bandgap whereas monolayered MoS<sub>2</sub> nanosheets possess direct bandgap structure due to hybridization between the d orbitals of Mo atoms and p<sub>z</sub> orbitals of S [12]. Various methods such as spin coating, metal organic chemical vapour deposition, sputtering technique, etc. are used for the synthesis of the MoS<sub>2</sub> nanosheets [13-20]. Deposition of metal nanoparticles such as silver NPs, gold NPs, palladium NPs and platinum NPs on the surface of the MoS<sub>2</sub> nanosheets enhances its properties due to the surface plasmon resonance (SPR) effect displayed by these NPs [21,22].

### 2. SYNTHESIS OF METAL-MOLYBDENUM DISULFIDE NANOCOMPOSITE

Embedding metal nanoparticles on the surface of MoS<sub>2</sub> nanosheets results in enhancement of properties displayed by the nanocomposite along with it the intrinsic properties of the nanosheet are also maintained [1].

Here, we have reviewed some of the popularly used techniques by the researchers present in literature for the synthesis of the Metal-MoS<sub>2</sub> nanocomposite.

### 2.1. Self-Assembly / Hierarchical Assembly method

For the preparation of Gold-Molybdenum Disulfide (Au-MoS<sub>2</sub>) nanocomposite, Onur Parlak et al. dispersed MoS<sub>2</sub> nanosheets in phosphate buffer solution (PBS) and added AuNPs solution to it [20,23,24]. For synthesis of Silver-Molybdenum Disulfide (Ag-MoS<sub>2</sub>) nanocomposite, Xiao-Dong Zhu et al. dissolved silver nitrate (AgNO<sub>3</sub>), mercaptosuccinic acid (MSA) and sodium borohydride (NaBH<sub>4</sub>) solution together and to it MoS<sub>2</sub> powder, Ag-MSA NPs and dehydrated copper dichloride (CuCl<sub>2</sub>) was added [25-27].

### 2.2. Chemical synthesis method

Shao Su et al. prepared Au-MoS<sub>2</sub> nanocomposite, for which MoS<sub>2</sub> powder was dissolved in n-butyllithium solution in presence of argon (Ar), to it carboxymethyl cellulose (CMC) and HAuCl<sub>4</sub>·3H<sub>2</sub>O was added and the solution was heated in a microwave reactor [28]. A. J. Cheah et al. prepared Ag-MoS<sub>2</sub> nanocomposite, for which 2.0 mmol Na<sub>2</sub>MoO<sub>5</sub> and 10.0 mmol L-cysteine (HO<sub>2</sub>CCHCH<sub>2</sub>SH) were mixed together and kept in an autoclave, and then to it hydrazine and the AgNO<sub>3</sub> solution were added dropwise [29].

### 2.3. Hydrothermal Method

M. Sookhakian et al. prepared Ag-MoS<sub>2</sub> nanocomposite for which ammonium heptamolybdate ((NH<sub>4</sub>)<sub>6</sub>Mo<sub>7</sub>O<sub>24</sub>) and thioacetamide (C<sub>2</sub>H<sub>5</sub>NS) were dissolved together and transferred to an autoclave. And then finally, silver-ammonia (Ag(NH<sub>3</sub>)<sub>2</sub>OH) solution was added to it [30].

### 2.4. Laser beam and Microwave assisted method

Chorng Haur Sow et al. prepared Au-MoS<sub>2</sub> nanocomposite by the laser assisted method for which initially a beam of laser was focused on the MoS<sub>2</sub> nanosheets which converted it into micropatterns containing active nucleation sites and then the nanosheets were dipped into auric chloride (AuCl<sub>3</sub>) solution [31]. Lihui Yuwen et al. also prepared Au-MoS<sub>2</sub> nanocomposite by microwave assisted method for which MoS<sub>2</sub> nanosheet solution was dissolved in a mixture of

ascorbic acid (AA) aqueous solution, CMC aqueous solution and  $\text{HAuCl}_4$  aqueous solution under microwave irradiation [32,33].

### 3. PROPERTIES OF METAL-MOLYBDENUM DISULFIDE NANOCOMPOSITES

#### 3.1. Structural studies by X-Ray Diffraction method (XRD)

Structural properties of Ag-MoS<sub>2</sub> were determined by X. Wu et al. by using powder XRD method as shown in figure.3.1.(I). From the XRD data they have obtained it can be observed that the diffraction peaks at (002), (100), (103), and (110) refers to the MoS<sub>2</sub> nanosheets and additional diffraction peaks obtained at (111), (200), (220) and (311) are for the nanocomposite due to the contribution of the characteristic peaks of the AgNPs [34]. The XRD patterns of Au-MoS<sub>2</sub> nanocomposite obtained by Prianka Sharma et al. shown in figure 3.1.(II), displays diffraction peaks at (111), (200) and (220), which suggests that AuNPs on the surface of MoS<sub>2</sub> nanosheets are face centred cubic. Further, it can also be found that the intensity of the diffraction peaks obtained due to AuNPs increases with increase in concentration of AuNPs but it also decreases the diffraction peaks which are obtained due to MoS<sub>2</sub> as the AuNPs creates an obstruction for MoS<sub>2</sub> nanosheets and as a result it hinders its exposure area [35-37]. Eunjik Lee et al. characterised Pd-MoS<sub>2</sub> nanocomposite with XRD as shown in figure 3.1.(III). The peak of PdNPs at (111) indicates expansion of the lattice due to uptake of hydrogen and epitaxial relationship between Pd on MoS<sub>2</sub> which provides extra stability to the structure [38-44]. Lihui Yuwen et al. studied the XRD plots for Au-MoS<sub>2</sub>, Ag-MoS<sub>2</sub>, Pd-MoS<sub>2</sub> and Pt-MoS<sub>2</sub> nanocomposite. The XRD pattern obtained by them as shown in figure 3.1.(IV), reveals emergence of strong diffraction peaks at 38.5, 38.1, 40.3, and 40.0 upon deposition of AuNPs, AgNPs, PdNPs and Pt NPs, respectively on the surface nanosheets for the (111) cubic lattice planes of the NPs. The diffraction peak for MoS<sub>2</sub> becomes weaker as a result of surface modification of the nanosheets by metal NPs as they decrease the ordered restacking process of the MoS<sub>2</sub> nanosheets [33].

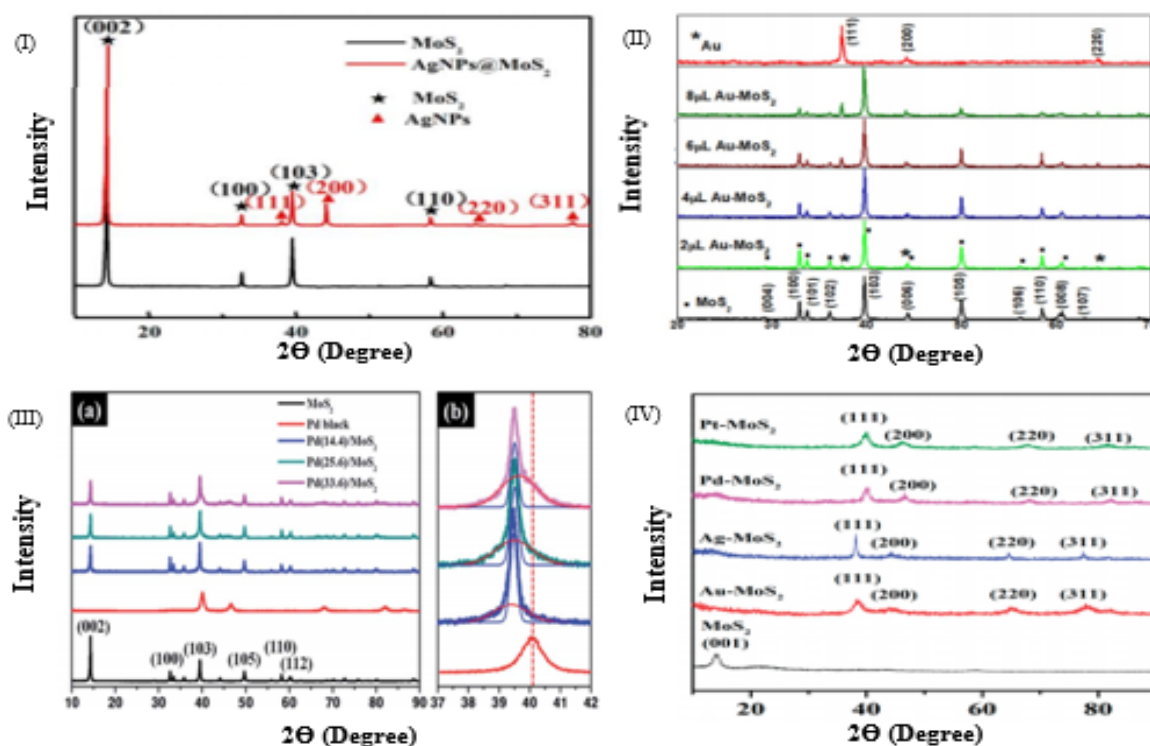


**Figure 3.1.** XRD patterns of (I)  $\text{MoS}_2$  nanosheets and  $\text{Ag-MoS}_2$  nanocomposite [34], (II)  $\text{MoS}_2$  and  $\text{Au-MoS}_2$  nanocomposite with different concentration of AuNPs [35], (III) (a)  $\text{MoS}_2$  and  $\text{Pd-MoS}_2$  nanocomposite and (b) magnified view of deconvolution between Pd (111) indicated by red lines and  $\text{MoS}_2$  (103) peaks by blue lines [38], (IV)  $\text{MoS}_2$ ,  $\text{Au-MoS}_2$ ,  $\text{Ag-MoS}_2$ ,  $\text{Pd-MoS}_2$  and  $\text{Pt-MoS}_2$  nanocomposite [33].

## 3.2. Morphological Properties

### 3.2.1. Morphological studies by using Transmission Electron Microscopy (TEM)

The TEM images for  $\text{Ag-MoS}_2$  nanocomposite obtained by A. J. Cheah et al. shown in figure 3.2.1.(I) displays slight structural change in the  $\text{MoS}_2$  nanosheets upon deposition of AgNPs as a result of partial removal of the  $\text{S}^{2-}$  ions by the use of the reducing agent, further the AgNPs also did not diffuse into the lattice of  $\text{MoS}_2$  hence, no alloy was formed [29,45,46]. The TEM analysis for  $\text{Au-MoS}_2$  nanocomposite was performed by Shao Su et al. as shown in figure 3.2.1.(II) depicts slight amount of change in the structure of nanosheets upon deposition of the AuNPs as the presence of NPs results in high density of energetic defects near the edges of  $\text{MoS}_2$  nanosheets [47-49]. The TEM images for  $\text{Pd-MoS}_2$  studied by Eunjik Lee et al. as shown in figure 3.2.1.(III) displays only horizontal interconnection between the PdNPs on the surface of nanosheet for low concentration of PdNPs, but when there is increase in concentration of PdNPs, one PdNPs gets

stacked over another, due to increase in electron density caused by thickening of the PdNPs layers on surface of MoS<sub>2</sub> nanosheets [38]. The TEM images obtained by Sagar H. Patil et al. as shown in figure 3.2.1.(IV), depicts that the spacing between lattice fringes of PtNPs was 0.22 nm which corresponds to the face centred cubic (111) planes of Pt NPs [50,51].

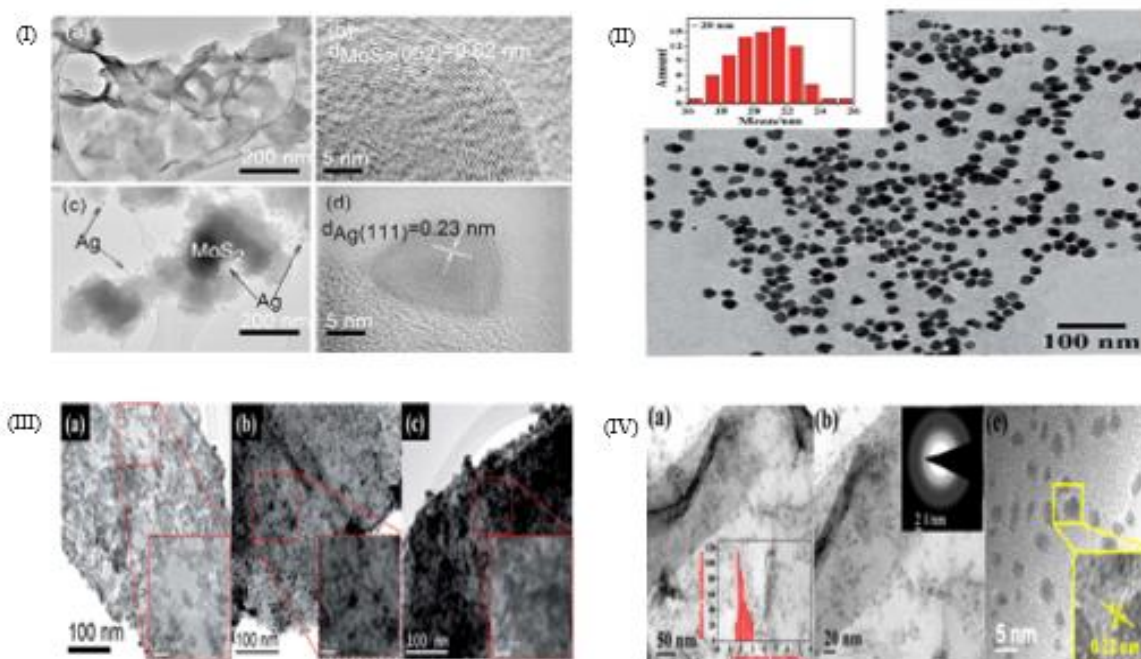


**Figure 3.2.1.** TEM image of (I)(a) MoS<sub>2</sub> nanosheets, (b) MoS<sub>2</sub> nanosheet depicting defect-rich active edges, (c) 20 wt% Ag-MoS<sub>2</sub> nanocomposite, (d) AgNPs embedded on the MoS<sub>2</sub> nanosheet [29], (II) Au-MoS<sub>2</sub> nanocomposite [47], (III) (a) Pd (14.4)-MoS<sub>2</sub>, (b) Pd (25.6)-MoS<sub>2</sub> and (c) Pd (33.6)-MoS<sub>2</sub>. (Insets: enlarged images of marked area) [38], (IV) (a) PtNPs on MoS<sub>2</sub> nanosheets (Inset: histogram of Pt particle size distribution), (b) higher magnification of the nanocomposite, (Inset: electron diffraction pattern for Pt-MoS<sub>2</sub>), (c) HRTEM image of Pt-MoS<sub>2</sub> (Inset: lattice fringe distance corresponding to (111) plane of Pt) [51].

### 3.2.2. Morphological studies by Scanning Electron Microscopy (SEM)

Ameena Nazneen et al. used the SEM analysis to study the morphology of Ag-MoS<sub>2</sub> nanocomposite as shown in figure 3.2.2.(I), the images depict that on depositing AgNPs on the surface of MoS<sub>2</sub> nanosheet the sheet-like MoS<sub>2</sub> nanostructures change to particle like form, it occurred due to the presence of the AgNPs which increases the number of active sites and structural defects on the surface of MoS<sub>2</sub> nanosheet [52]. According to the SEM data of Au-MoS<sub>2</sub>

obtained by Haofan Sun et al. as shown in figure 3.2.2.(II), the MoS<sub>2</sub> nanosheets were very thin and were highly exfoliated and the AuNPs were homogeneously dispersed on the surface the nanosheets [53]. Cihan Kuru et al. studied the morphological properties of Pd-MoS<sub>2</sub> as shown in figure 3.2.2.(III) it reveals that Pd-MoS<sub>2</sub> nanocomposite forms a continuous film in a self-assembled manner and the MoS<sub>2</sub> nanosheets were highly exfoliated as they appeared to be transparent [54]. From SEM images obtained by Sha Li et al. for Pt-MoS<sub>2</sub> nanocomposite shown in figure 3.2.2.(IV) reveals that PtNPs helps in maintaining the high edge defects in MoS<sub>2</sub> nanosheet and it also benefits by providing a real surface area to the active edges to the nanosheets [55].

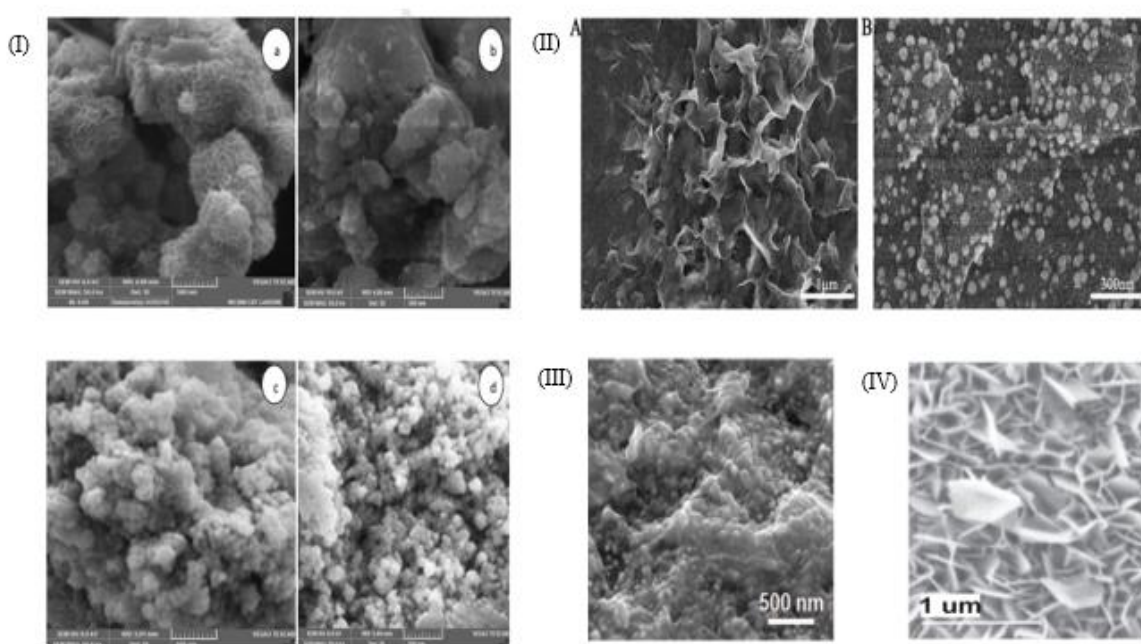


**Figure 3.2.2.** SEM images of (I) (a) pure MoS<sub>2</sub>, (b) 1% Ag-MoS<sub>2</sub>, (c) 2% Ag-MoS<sub>2</sub> and (d) 3% Ag-MoS<sub>2</sub> nanocomposites [52], (II) (A) MoS<sub>2</sub> and (B) Au-MoS<sub>2</sub> nanocomposites [53], (III) High magnification SEM image of Pd-MoS<sub>2</sub> nanocomposite [54], (IV) Pt decorated on MoS<sub>2</sub> nanosheets (Pt-MoS<sub>2</sub>) [55].

### 3.3. Optical Properties

#### 3.3.1. Optical studies by UV-Vis Spectroscopy

A.J. Cheah et al. used the UV-Vis spectroscopy to study the optical characteristics of the Ag-MoS<sub>2</sub> nanocomposite. The spectral data obtained by them is shown in figure 3.3.1.(I) which displays a broad absorption spectrum with peak centred at about 635 nm for MoS<sub>2</sub> nanosheets as

a result of excitation from the occupied to unoccupied 4d orbital of Mo, the absorption peak of Ag-MoS<sub>2</sub> nanocomposites also shows slight amount of blue shift and the presence of AgNPs on the surface of the nanosheet enhances the absorbance peak of the nanocomposites. At 400 nm and 438 nm, two small bumps or peaks were formed due to the localized surface plasmon resonance (SPR) of the AgNPs which occurs as a result of collective oscillation of the electrons in the conduction band, when the AgNPs interact with the incoming visible-light [29,56-60]. Shao Su et al. obtained two absorption peaks as shown in figure 3.3.1.(II), one intense peak was observed at around 260 nm and another at 320 nm for MoS<sub>2</sub>, on addition of AuNPs the absorption peak which was earlier at 260 nm got blue shifted to 210 nm and another new peak was formed at around 550nm, which corresponds to the characteristic SPR peak for AuNPs. As the concentration of HAuCl<sub>4</sub> was increased, initially the absorption peak got red shifted but later on further increase in concentration of HAuCl<sub>4</sub> a blue shift of the absorption peak was observed which is due to plasmon coupling and refractive index effects displayed by the AuNPs [28,61-64]. Lihui Yuwen et al. studied the optical properties of Ag-MoS<sub>2</sub>, Au-MoS<sub>2</sub>, Pd-MoS<sub>2</sub> and Pt-MoS<sub>2</sub> as shown in figure 3.3.1.(III). In case of Au-MoS<sub>2</sub> nanocomposite, along with slight shift in position of absorption peak significant enhancement of the absorbance peak at 500 nm to 1200 nm can also be observed, which is due to the of coupling of the SPR of the AuNPs. For Ag-MoS<sub>2</sub> a wide absorption peak was formed beyond 400 nm which corresponds to the SPR peak of the AgNPs. For both Pd-MoS<sub>2</sub> and Pt-MoS<sub>2</sub> no new peaks were observed but the absorbance peak starting from 300 nm to 1200 nm increased to a great extent, which is due to a wide absorption range but no distinct absorption peaks in the UV-Vis or in the near infrared region for the case of PdNPs and PtNPs [33,65-67].

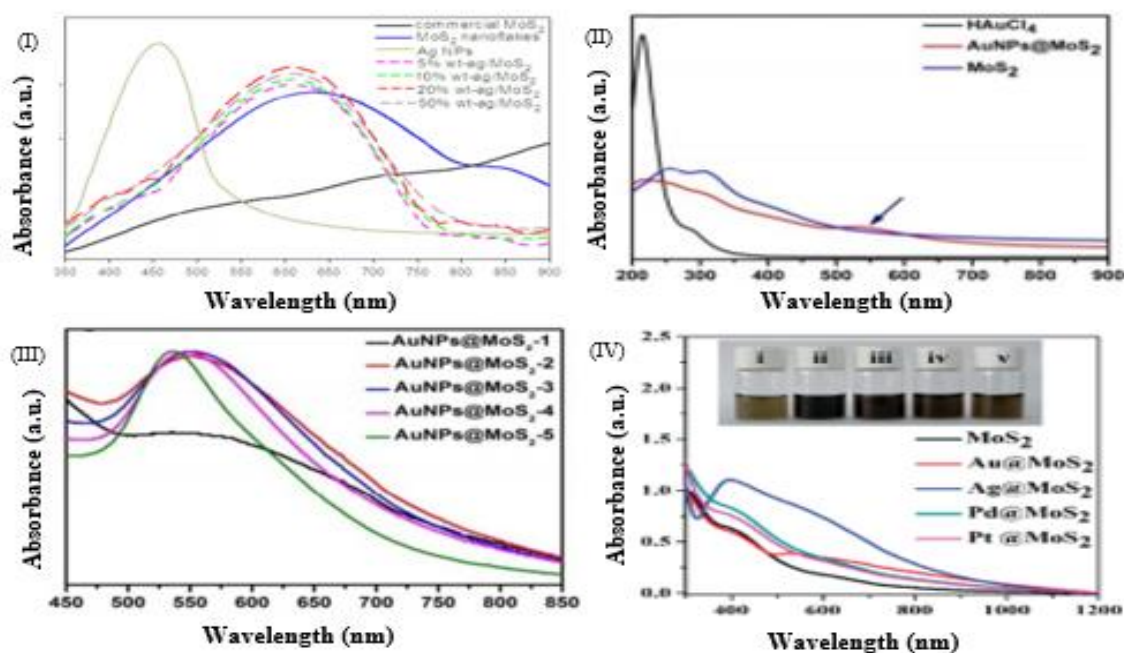


**Figure 3.3.1** UV-vis absorption spectra of (I) Bulk  $\text{MoS}_2$ ,  $\text{MoS}_2$  nanosheets and Ag- $\text{MoS}_2$  nanocomposite [29], (II)  $\text{MoS}_2$  nanosheets and Au- $\text{MoS}_2$  nanocomposite, (III) Different concentrations of Au- $\text{MoS}_2$  nanocomposite [28], (IV)  $\text{MoS}_2$ , Au- $\text{MoS}_2$ , Ag- $\text{MoS}_2$ , Pd- $\text{MoS}_2$ , and Pt- $\text{MoS}_2$  nanocomposite [33].

### 3.3.2. Optical studies by Raman Analysis

X. Wu et al. used the Raman analysis to study the optical properties of Ag- $\text{MoS}_2$  nanocomposite as shown in figure 3.3.2.(I). From the figure, it can be observed that the characteristic peak of the 20wt.% Ag- $\text{MoS}_2$  nanocomposites was stronger compared to the low concentrations of the NPs on the nanocomposite samples, as higher concentration of AgNPs is responsible for large local intense electromagnetic fields due to surface plasmon resonance effect which is significantly localized at the nanoscale junctions [34,68]. Ameena Nazneen et al. investigated the molecular vibrations in Ag- $\text{MoS}_2$  nanocomposite. They observed that the active modes of the Raman bands of  $\text{MoS}_2$  nanosheet are located at the peaks of  $280\text{ cm}^{-1}$  ( $E_{1g}$ ) and  $381\text{ cm}^{-1}$  ( $E_{2g}$ ). The band formed at  $381\text{ cm}^{-1}$  was formed as a result of antipodal vibration of two S atoms with a Mo atom. For low concentration of AgNPs, a low frequency vibrational mode ( $A_{1g}$ ) was observed at  $366\text{ cm}^{-1}$ , which occurs due to the distortion in structure due to the addition of AgNPs into the  $\text{MoS}_2$  lattice. On further increasing the concentration of AgNPs, the low-frequency vibrational mode ( $A_{1g}$ ) got shifted to  $315\text{ cm}^{-1}$ . For higher concentration of AgNPs, many low-frequency vibrational modes appeared at  $354\text{ cm}^{-1}$  ( $A_{1g}$ ),  $364\text{ cm}^{-1}$  ( $A_{1g}$ ),  $343\text{ cm}^{-1}$  ( $A_{1g}$ ),  $333\text{ cm}^{-1}$  ( $A_{1g}$ ), and  $323\text{ cm}^{-1}$  ( $A_{1g}$ ).

Upon comparing these peaks with that of the MoS<sub>2</sub> nanosheets it can be justified that on increasing the concentration of AgNPs, slight shifts and variation in the peaks at 280 cm<sup>-1</sup> and 380 cm<sup>-1</sup> were observed, which depict increase in structural defects [52,69-77]. Prianka Sharma et al. investigated the vibrational modes of Au-MoS<sub>2</sub> nanocomposite as shown in figure 3.3.2.(II). When AuNPs was added to the nanocomposite to form Au-MoS<sub>2</sub>, a red shift of the E<sup>1</sup><sub>2g</sub> and A<sub>1g</sub> modes can be observed and the new frequency difference between E<sup>1</sup><sub>2g</sub> and A<sub>1g</sub> modes came out to be about 25 cm<sup>-1</sup>. This shifting of the peak occurs as the lattice sites gets strained due to presence of AuNPs on the MoS<sub>2</sub> nanosheets. Increasing the concentration of AuNPs enhances the intensity peaks of the Raman spectra due to localized surface plasmon resonance (LSPR) displayed by AuNPs. Presence of AuNPs increases the electric field near the surface of AuNPs and thus, a peak of sharp intensity was obtained. This phenomenon is termed as Surface Enhanced Raman Scattering (SERS) [35,78,79]. L. Z. Hao et al. studied the properties of Pd-MoS<sub>2</sub> nanocomposite as shown in figure 3.3.2.(III). It was observed that the MoS<sub>2</sub> film exhibits two characteristic Raman peaks one of E<sup>1</sup><sub>2g</sub> mode at 376 cm<sup>-1</sup> due to the S and Mo atoms as they were oscillating in the antiphase parallel to the crystal plane and another of the A<sub>1g</sub> mode at 410 cm<sup>-1</sup> due to the S atoms oscillating in the antiphase out-of-plane. When the PdNPs were decorated on the surface of the MoS<sub>2</sub> nanosheet, red shift of about 6.0 cm<sup>-1</sup> of the A<sub>1g</sub> peak was observed whereas, there was no change in position of the E<sup>1</sup><sub>2g</sub> peak, due to which the separation between the E<sup>1</sup><sub>2g</sub> and A<sub>1g</sub> peaks decreases, which is due to the fact that for Pd-MoS<sub>2</sub> the A<sub>1g</sub> phonons couple more tightly with electrons than E<sup>1</sup><sub>2g</sub> phonons, which causes a significant change in the electronic structure and semiconductor characteristics of the nanocomposite [41,80].

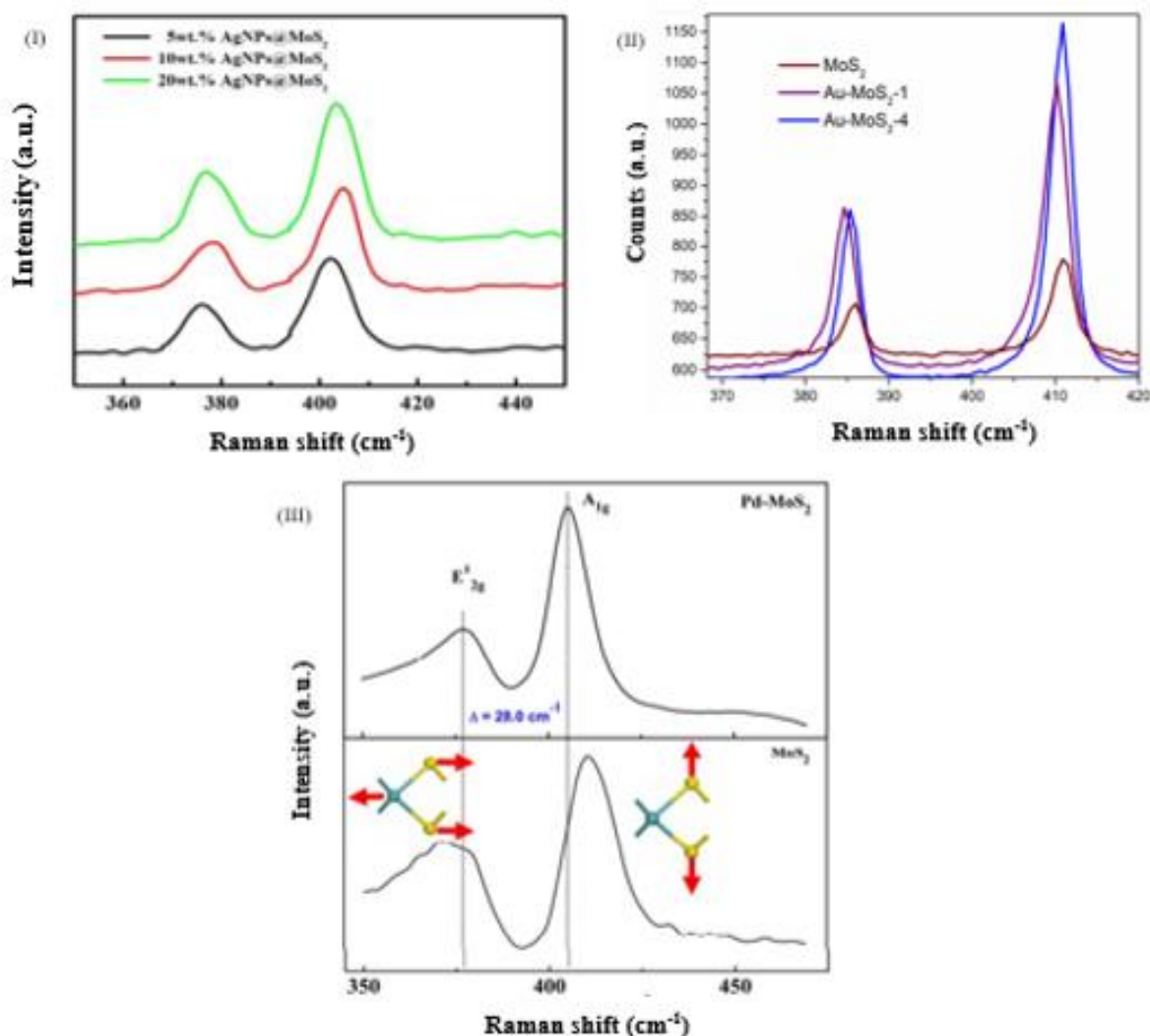


**Figure 3.3.2.** Raman characterization of (I) 5wt.%, 10wt.%, and 20wt.% Ag-MoS<sub>2</sub> nanocomposites [34], (II) MoS<sub>2</sub> and Au-MoS<sub>2</sub> nanocomposites, [35], (III) Pd-MoS<sub>2</sub> film (top) and MoS<sub>2</sub> film (bottom) (inset: oscillation of E'<sub>2g</sub> (left) and A<sub>1g</sub> (right) modes) [41].

## CONCLUSION

Among the different types of Metal-MoS<sub>2</sub> nanocomposites, the Ag-MoS<sub>2</sub> nanocomposites are most useful due to their tuneable optical (PL) properties, excellent electrical conductivity and extraordinary magnetic properties. The type of the band gap displayed by the MoS<sub>2</sub> nanosheets depends on the number of layers of the nanosheet. Occurrence of blue or red shift in the absorption peak of MoS<sub>2</sub> depends upon the size of metal NPs deposited on the surface of MoS<sub>2</sub> nanosheets. In case of Au-MoS<sub>2</sub>, the peak obtained at 210 nm got blue shifted due to the small size of the nanoparticles embedded on the nanosheets. For both Ag-MoS<sub>2</sub> and Au-MoS<sub>2</sub> nanocomposite another characteristic peak at 430nm and 550 nm, respectively was observed due

to the SPR phenomenon displayed by these noble metals NPs, but for Pd-MoS<sub>2</sub> and Pt-MoS<sub>2</sub> no new peaks were formed but a huge increase in the existing absorbance peak was observed, as both PdNPs and PtNPs do not display any distinct absorption peaks due to SPR phenomenon in the UV-Vis or in the near infrared region. The XRD diffraction peaks suggest that the Metal-Molybdenum Disulphide nanocomposites are hetero crystalline in structure. The intensity of the peaks for Raman spectra has also been enhanced by embedding the NPs on the surface of the nanosheets due to the increase in structural defects which resulted in formation of new peaks. In case of Pd-MoS<sub>2</sub> the A<sub>1g</sub> phonons couple more tightly with electrons than E<sub>2g</sub><sup>1</sup> phonons which results in significant change in the electronic structure and semiconductor characteristics of the nanocomposite. Analysing the morphological properties, it was found that certain nanocomposite which were prepared by using the chemical reduction process displayed structural defect due to the partial removal of the S<sup>2-</sup> ions by the use of reducing agent.

## REFERENCES

- [1] Shao Su, Yongqiang Xu, Qian Sun, Xiaodan Gu, Lixing Weng and Lianhui Wang, Noble Metal Nanostructure-decorated Molybdenum Disulfide Nanocomposites: Synthesis and Applications, *J. Mater.Chem. B*, 6, (2018), 5323-5334.
- [2] M. Chhowalla, H. S. Shin, G. Eda, L.-J. Li, K. P. Loh and H. Zhang, The Chemistry of 2D Layered Transition Metal Dichalcogenide Nanosheets, *Nat. Chem.*, 5, (2013), 263–275.
- [3] M. Naguib, V. N. Mochalin, M. W. Barsoum and Y. Gogotsi, MXenes: A new family of two-dimensional materials, *Adv. Mater.*, 26, (2014), 992–1005.
- [4] K. Watanabe, T. Taniguchi and H. Kanda, Direct-bandgap properties and evidence for ultraviolet lasing of hexagonal boron nitride single crystal, *Nat. Mater.*, 3, (2004), 404-409.
- [5] L. Li, Y. Yu, G. J. Ye, Q. Ge, X. Ou, H. Wu, D. Feng, X. H. Chen and Y. Zhang, Black phosphorus field-effect transistors, *Nat. Nanotechnol.*, 9, (2014), 372–377.
- [6] S. L. James, Metal-organic frameworks, *Chem. Soc. Rev.*, 32, (2003), 276–288.
- [7] P.P. Hankare, A.A. Patil, P.A. Chate, K.M. Garadkar, D.J. Sathe, A.H. Manikshete, I.S. Mulla, Characterization of MoSe<sub>2</sub> thin film deposited at room temperature from solution phase, *J. Cryst. Growth*, 311, (2008), 15-19.
- [8] K.M. Garadkara, A.A. Patila, P.P. Hankarea, P.A. Chateb, D.J. Sathea and S.D. Delekar, MoS<sub>2</sub>: Preparation and their characterization, *Journal of Alloys and Compounds*, 487, (2009), 786–789.
- [9] Molybdenum and Molybdenum Compounds, *Ullmann's Encyclopedia of Chemical Technology.*, Wiley-VCH, Weinheim Vol, 23, (2012).

- [10] Radisavljevic, B., Radenovic, A, Brivio, J. Giacometti, V., Kis, A., Single-layer MoS<sub>2</sub> transistors, *Nat. Nanotechnol.* 6, (2011), 147-150.
- [11] S. V. Prabhakar Vattikuti and Chan Byon, Synthesis and Characterization of Molybdenum Disulfide Nanoflowers and Nanosheets: Nanotribology, *Journal of Nanomaterials*, 710462, (2015), 11.
- [12] Nan Wang, Fang Wei, Yuhang Qi, Hongxiang Li, Xin Lu, Guoqiangzhao and Qun Xu, Synthesis of Strongly Fluorescent Molybdenum Disulfide Nanosheets for Cell-Targeted Labeling, *ACS Applied Materials and Interfaces*, 6, (2014), 19888-19894.
- [13] C. Amory, J.C. Bernede, N. Hamdadou, A study of textured non-stoichiometric MoTe<sub>2</sub> thin films used as substrates for textured stoichiometric MoS thin films, *Vacuum*, 72, (2004), 351.
- [14] J. Putz, M.A. Aegerter, Liquid Film Deposition of Chalcogenide Thin Films, *Thin Solid Films*, 351, (1999), 119.
- [15] A. Jäger-Waldau, M. Lux-Steiner, R. Jäger-Waldau, R. Burkhardt, E. Bucher, Composition and morphology of MoSe<sub>2</sub> thin films, *Thin Solid Films* 189, (1990), 339-345.
- [16] A.A. van Zomeren, J.H. Koegler, J. Schoonman, P.J. van der Put, Charge transport phenomena in thin-film cathodes, *Solid State Ionics*, 53, (1992), 333-338.
- [17] P.D. Fleischauer, Fundamental aspects of the electronic structure, materials properties and lubrication performance of sputtered MoS<sub>2</sub> films, *Thin Solid Films* 154, (1987), 309-322.
- [18] S.M. Delphine, M. Jayachandran, C. Sanjeeviraja, Pulsed electrodeposition and characterization of molybdenum diselenide thin film, *Mater. Res. Bull.* 40, (2005), 135-147.
- [19] J. Ouerfelli, S.K. Srivastava, J.C. Bernede, S. Belgacema, Effect of microwaves on synthesis of MoS<sub>2</sub> and WS<sub>2</sub>, *Vacuum* 83, (2009), 308-312.
- [20] J. Chao, Y. Zhang, D. Zhu, B. Liu, C. Cui, S. Su, C. Fan and L. Wang, Hetero-assembly of gold nanoparticles on a DNA origami template, *Sci. China: Chem.*, 59, (2016), 730-734.
- [21] Rasmagin, S.I., Apresyan, L.A., Analysis of the Optical Properties of Silver Nanoparticles, *Opt. Spectrosc.* 128, (2020), 327-330.
- [22] Markus Diantoro, Thathit Suprayogi, Ulwiyatus Sa'adah, Nandang Mufti, Abdulloh Fuad, ArifHidayat and Hadi Nur, Modification of Electrical Properties of Silver Nanoparticle, (InTechOpen, London, 2016), 233-248.
- [23] O. Parlak, A. I'ncel, L. Uzun, A. P. Turner and A. Tiwari, Structuring Au nanoparticles on two-dimensional MoS<sub>2</sub> nanosheets for electrochemical glucose biosensors, *Biosens. Bioelectron.*, (2017), 89, 545-550.
- [24] Chenyang Zhao, Youfang Zhang, Lunfeng Chen, Chaoyi Yan, Peixin Zhang, Jia Ming Ang, and Xuehong Lu, Self-Assembly-Assisted Facile Synthesis of MoS<sub>2</sub>-Based Hybrid Tubular Nanostructures for Efficient Bifunctional Electrocatalysis, *ACS Appl. Mater. Interfaces*, 10, 28, (2018), 23731-23739.

- [25] Long Pan, Yi-Tao Liu, Xu-Ming Xie, and Xiao-Dong Zhu, Coordination-Driven Hierarchical Assembly of Silver Nanoparticles on MoS<sub>2</sub> Nanosheets for Improved Lithium Storage, *Chem. Asian J.*, 9, (2014), 1519–1524.
- [26] L. Qi, B. I. Lee, S. Chen, W.D. Samuels, G. J. Exarhos, High-Dielectric-Constant Silver–Epoxy Composites as Embedded Dielectric, *Adv. Mater.*, 17, (2005), 1777 – 1781.
- [27] E. Sumesh, M. S. Bootharaju, A. T. Pradeep, A practical silver nanoparticle-based adsorbent for the removal of Hg<sup>2+</sup> from water, *J. Hazard. Mater.*, 189, (2011), 450 – 457.
- [28] S. Su, C. Zhang, L. Yuwen, J. Chao, X. Zuo, X. Liu, C. Song, C. Fan and L. Wang, Creating SERS hot spots on MoS<sub>2</sub> nanosheets with in-situ grown gold nanoparticles, *ACS Appl. Mater. Interfaces*, 6, (2014), 18735–18741.
- [29] A. J. Cheah, W. S. Chiu, P. S. Khiew, H. Nakajima, T. Saisopa, P. Songsiriritthigul, S. Radiman and M. A. A. Hamid, Facile Synthesis of Ag/MoS<sub>2</sub> Nanocomposite Photocatalyst for Enhanced Visible-Light Driven Hydrogen Gas Evolution, *Catal. Sci. Technol.*, 5, (2015), 4133–4143.
- [30] Sookhakian M, Basirun WJ, Goh BT, Woi PM, Alias Y, Molybdenum Disulfide Nanosheet Decorated with Silver Nanoparticles for Selective Detection of Dopamine, *Colloids and Surfaces B: Biointerfaces*, S0927-7765(18)30940-8, (2018).
- [31] J. Lu, J. H. Lu, H. Liu, B. Liu, L. Gong, E. S. Tok, K. P. Loh and C. H. Sow, Microlandscaping of Au Nanoparticles on Few-Layer MoS<sub>2</sub> Films for Chemical Sensing, *Small*, 11, (2015), 1792–1800.
- [32] P. Joensen, R. Frindt and S. R. Morrison, Single-layer MoS<sub>2</sub>, *Mater. Res. Bull.*, 21, (1986), 457–461.
- [33] L. Yuwen, F. Xu, B. Xue, Z. Luo, Q. Zhang, B. Bao, S. Su, L. Weng, W. Huang and L. Wang, General synthesis of noble metal (Au, Ag, Pd, Pt) nanocrystal modified MoS<sub>2</sub> nanosheets and the enhanced catalytic activity of Pd–MoS<sub>2</sub> for methanol oxidation, *Nanoscale*, 6, (2014), 5762–5769.
- [34] X. Wu, C. Zhou, Y. Dai, H. Zou, D. Sha, J. Ren, Y. Yan and X. Yan, Preparation and characterisation of AgNPs/MoS<sub>2</sub> nanocomposites, *Chalcogenide Letters*, 12(10), (2015), 505 – 509.
- [35] Anjali Rani, Arun Singh Patel, Anirban Chakraborti, Kulvinder Singh and Prianka Sharma, Tailoring Optical and Magnetic Properties of Molybdenum Disulfide Nanosheets by Incorporating Plasmonic Gold Nanoparticles, arXiv:1912.03869 [cond-mat.mtrl-sci], (2020).
- [36] Z. Jiang, Q. Zhang, C. Zong, B.-J. Liu, B. Ren, Z. Xie, and L. Zheng, Cu–Au alloy nanotubes with five-fold twinned structure and their application in surface-enhanced Raman scattering, *Journal of Materials Chemistry* 22, (2012), 18192–18197.
- [37] Jeffrey R. Lince, Hyun I. Kim, Paul M. Adams, Daniel J. Dickrel and Michael T. Dugger. Nanostructural, electrical, and tribological properties of composite Au–MoS<sub>2</sub> coatings, *Thin Solid Films*, 517, (2009), 5516–5522.
- [38] E. Lee & Y.-U. Kwon, Epitaxial Growth of Pd Nanoparticles on Molybdenum Disulfide by Sonochemistry and its Effects on Electrocatalysis, *RSC Adv.*, 6, (2016), 47468–47473.

- [39] H. Kobayashi, M. Yamauchi, H. Kitagawa, Y. Kubota, K. Kato and M. Takata, Hydrogen absorption in the core/shell interface of Pd/Pt nanoparticles, *J. Am.Chem. Soc.*, 130, (2008), 1818–1819.
- [40] J.-H. Jang, J. Kim, Y.-H. Lee, C. Pak and Y.-U. Kwon, Sonochemical synthesis of tungsten carbide-palladium nanocomposites and their electrocatalytic activity for hydrogen oxidation reaction, *Electrochim. Acta*, 55, (2009), 485–490.
- [41] L. Z. Hao, W. Gao, Y. J. Liu, Y. M. Liu, Z. D. Han, Q. Z. Xue and J. Zhu, Self-powered broadband, high-detectivity and ultrafast photodetectors based on Pd-MoS<sub>2</sub>/Si heterojunctions, *Phys. Chem.Chem. Phys.*, 18, (2016), 1131.
- [42] M. L. Tsai, S. H. Su, J. K. Chang, D. S. Tsai, C. H. Chen, C. I. Wu, L. J. Li, L. J. Chen and J. H. He, Monolayer MoS<sub>2</sub> Heterojunction Solar Cells, *ACS Nano*, 2014, 8, (2014), 8317.
- [43] Y. Shi, W. Zhou, A. Y. Lu, W. Fang, Y. H. Lee, A. L. Hsu, S. M. Kim, K. K. Kim, H. Y. Yang, L. J. Li, J. C. Idrobo and J. Kong, van der Waals Epitaxy of MoS<sub>2</sub> Layers Using Graphene As Growth Templates, *Nano Lett.*, 12, (2012), 2784.
- [44] Hyeon Ho Shin, Eunmi Kang, Haeli Park, Taejun Han, Chul-Ho Lee and Dong-Kwon Lim, Pd-nanodot decorated MoS<sub>2</sub> nanosheets as a highly efficient photocatalyst for the visible-lightinduced Suzuki–Miyaura coupling reaction, *J. Mater. Chem. A*, 5, (2017), 24965.
- [45] Y.-S. Chi, H.-P. Lin and C.-Y. Mou, CO oxidation over gold nanocatalyst confined in mesoporous silica, *Appl. Catal., A*, 284, (2005), 199-206.
- [46] W.-H. Ryu, J.-W. Jung, K.-S. Park, S. Kim and I.-D. Kim, Vine-like MoS<sub>2</sub> anode materials self-assembled from 1-D nanofibers for high-capacity sodium rechargeable batteries, *Nanoscale*, 6, (2014), 10975-10981.
- [47] Shao Su, Wenfang Cao, Chi Zhang, Xiaoyan Han, Huan Yu, Dan Zhu, Jie Chao, Chunhai Fanab and Lianhui Wang, improving performance of MoS<sub>2</sub>-based electrochemical sensors by decorating noble metallic nanoparticles on the surface of MoS<sub>2</sub> nanosheet, *RSC Adv.*, 6, (2016), 76614.
- [48] Zongyou Yin, Bo Chen, Michel Bosman, Xiehong Cao, Junze Chen and Bing Zheng Hua Zhang, Au Nanoparticle-Modified MoS<sub>2</sub> Nanosheet-Based Photoelectrochemical Cells for Water Splitting *Nano. Micro small*, (2014).
- [49] J. Kim, S. Byun, A. J. Smith, J. Yu, J. Huang, Enhanced Electrocatalytic Properties of Transition-Metal Dichalcogenides Sheets by Spontaneous Gold Nanoparticle Decoration, *J. Phys. Chem. Lett.*, 4, (2013), 1227-1232.
- [50] Huang, Xiao, Zeng, Zhiyuan, Bao, Shuyu. Wang, Mengfei, Qi, Xiaoying, Fan, Zhanxi & Zhang, Hua., Solution-phase epitaxial growth of noble metal nanostructures on dispersible single-layer Molybdenum Disulfide nanosheets, *Nature communications*, 4, (2013), 1444.
- [51] Sagar H. Patil, Bihag Anothumakkool, Shivaram D. Sathayec and Kashinath R. Patil, Architecturally designed Pt–MoS<sub>2</sub> and Pt–graphene composites for electrocatalytic methanol oxidation, *Phys.Chem.Chem.Phys.*, 17, (2015), 26101.

- [52] Ameena Nazneen, M.I. Khan, M.A. Naeem, M. Atif, Munawar Iqbal, Nafeesah Yaqub, W.A. Farooq, Structural, morphological, optical, and photocatalytic properties of Ag-doped MoS<sub>2</sub> nanoparticles, *Journal of Molecular Structure*, S0022-2860, (20), (2020), 31060-7.
- [53] Haofan Sun, Jie Chao, XiaoleiZuo, Shao Su, XingfenLiu, LihuiYuwen, ChunhaiFanab and Lianhui Wang, Gold nanoparticle-decorated MoS<sub>2</sub> nanosheets for simultaneous detection of ascorbic acid, dopamine and uric acid, *RSC Adv.*, 4, (2014), 27625.
- [54] Cihan Kuru, Chulmin Choi, Alireza Kargar, Duyoung Choi, Young Jin Kim, Chin Hung Liu, Serdar Yavuz, and SunghoJin, MoS<sub>2</sub> Nanosheet–Pd Nanoparticle Composite for Highly Sensitive Room Temperature Detection of Hydrogen, *Adv. Sci.*, 2, (2015), 1500004.
- [55] Sha Li, Ja Kyung Lee, Si Zhou, Mauro Pasta, and Jamie H. Warner, Synthesis of Surface Grown Pt Nanoparticles on Edge-Enriched MoS<sub>2</sub> Porous Thin Films for Enhancing Electrochemical Performance, *Chem. Mater.*, 31, (2019), 387–397.
- [56] G. Eda, H. Yamaguchi, D. Voiry, T. Fujita, M. Chen and M. Chhowalla, Photoluminescence from Chemically Exfoliated MoS<sub>2</sub>, *Nano Lett.*, 11, (2011), 5111-5116.
- [57] B. Visic, R. Dominko, M. K. Gunde, N. Hauptman, S. D. Skapin and M. Remskar, Optical properties of exfoliated MoS<sub>2</sub> coaxial nanotubes - analogues of graphene, *Nanoscale Res. Lett.*, 6, 1. (2011), 662.
- [58] G. Frey, S. Elani, M. Homyonfer, Y. Feldman and R. Tenne, Optical-absorption spectra of inorganic fullerenelike MS<sub>2</sub> (M=Mo, W), *Phys. Rev. B: 663 Condens. Matter*, 57, 6666. (1998), 664.
- [59] A. Slistan-Grijalva, R. Herrera-Urbina, J. F. Rivas-Silva, M. Ávalos-Borja, F. 665 F. Castellón-Barraza and A. Posada-Amarillas, *Mater. Res. Bull.*, 43, (2008), 666-667.
- [60] N. R. Jana, L. Gearheart and C. J. Murphy, Wet chemical synthesis of silver nanorods and nanowires of controllable aspect ratio Electronic supplementary information (ESI) available: UV–VIS spectra of silver nanorods, *Chem. Commun.*, (2001), 617-618.
- [61] Jana, N. R.; Gearheart, L.; Murphy, C. J., Seeding Growth for Size Control of 5–40 nm Diameter Gold Nanoparticles, *Langmuir*, 17 (22), (2001), 6782-6786.
- [62] D. E. Mustafa, T. Yang, Z. Xuan, S. Chen, H. Tu, and A. Zhang, Surface Plasmon Coupling Effect of Gold Nanoparticles with Different Shape and Size on Conventional Surface Plasmon Resonance Signal, *Plasmonics* 5, (2010), 221–231.
- [63] V. Amendola, R. Pilot, M. Frascioni, O. M. Marago, and M. A. Iati, Surface plasmon resonance in gold nanoparticles: a review. *Journal of Physics: Condensed Matter* 29, (2017), 203002.
- [64] A. S. Patel, P. Mishra, P. K. Kanaujia, S. S. Husain, G. V. Prakash, and A. Chakraborti, Investigating resonance energy transfer from protein molecules to van der Waals nanosheets, *RSC Advances* 7, (2017), 26250– 26255.
- [65] Z. Zhang, F. Xu, W. Yang, M. Guo, X. Wang, B. Zhang and J. Tang, A facile one-pot method to high-quality Ag-graphene composite nanosheets for efficient surface-enhanced Raman scattering, *Chem. Commun.*, 47, (2011), 6440.

- [66] T. Teranishi and M. Miyake, Size Control of Palladium Nanoparticles and Their Crystal Structures, *Chem. Mater.*, 10, (1998), 594-600.
- [67] S.-Y. Zhao, S.-H. Chen, S.-Y. Wang, D.-G. Li and H.-Y. Ma, Preparation, Phase Transfer, and Self-Assembled Monolayers of Cubic Pt Nanoparticles, *Langmuir*, 18, (2002), 3315.
- [68] K. F. Mak, C. Lee, J. Hone, J. Shan and T. F. Heinz, Atomically Thin MoS<sub>2</sub>: A New Direct-Gap Semiconductor, *Phys. Rev. Lett.*, 671, (2010), 136805., 671.
- [69] Windom, B.C., W. Sawyer, and D.W. Hahn, A Raman Spectroscopic Study of MoS<sub>2</sub> and MoO<sub>3</sub>: Applications to Tribological Systems, *Tribology Letters*, 42(3), (2011), 301-310.
- [70] Dattatray J. Late, Bin Liu, H. S. S. Ramakrishna Matte, C. N. R. Rao, Vinayak P. Dravid,, Rapid Characterization of Ultrathin Layers of Chalcogenides on SiO<sub>2</sub>/Si Substrates, *Advanced Functional Materials*, 22(9), (2012), 1894-1905.
- [71] Rao, C., U. Maitra, and U.V. Waghmare, Extraordinary attributes of 2-dimensional MoS<sub>2</sub> nanosheets, *Chemical Physics Letters*, 609, (2014), 172-183.
- [72] Lv, R., Robinson JA, Schaak RE, Sun D, Sun Y, Mallouk TE, Terrones M, Transition metal dichalcogenides and beyond: synthesis, properties, and applications of single- and few-layer nanosheets. *Accounts of chemical research*, 48(1), (2014), 56-64.
- [73] Li, H., Qing Zhang, Chin Chong Ray Yap, Beng Kang Tay, Teo Hang Tong Edwin, Aurelien Olivier, Dominique Baillargeat, From Bulk to Monolayer MoS<sub>2</sub>: Evolution of Raman Scattering, *Advanced Functional Materials*, 22(7), (2012), 1385-1390.
- [74] C. Rice, R. J. Young, R. Zan, U. Bangert, D. Wolverson, T. Georgiou, R. Jalil, and K. S. Novoselov, Raman-scattering measurements and first-principles calculations of strain-induced phonon shifts in monolayer MoS<sub>2</sub>, *Physical Review B*, 87(8), (2013), 081307.
- [75] Xin Zhang, Xiao-Fen Qiao, Wei Shi, Jiang-Bin Wu, De-Sheng Jiang and Ping-Heng Tan, Phonon and Raman scattering of two-dimensional transition metal dichalcogenides from monolayer, multilayer to bulk material, *Physical Review B*, 44(9), (2015), 2757-2785.
- [76] Cantalini, C., et al., Springer, 17-25, (2011-2012).
- [77] Geng, X., et al., Pure and stable metallic phase Molybdenum Disulfide nanosheets for hydrogen evolution reaction., *Nature communications*, 7, (2016), 10672.
- [78] S. Su, C. Zhang, L. Yuwen, J. Chao, X. Zuo, X. Liu, C. Song, C. Fan, and L. Wang, Creating SERS Hot Spots on MoS<sub>2</sub> Nanosheets with in Situ Grown Gold Nanoparticles, *ACS applied materials & interfaces* 6, (2014), 18735–18741.
- [79] G. Plechinger, S. Heydrich, J. Eroms, D. Weiss, C. Schüller, and T. Korn, Raman spectroscopy of the interlayer shear mode in few-layer MoS<sub>2</sub> flakes, *Applied Physics Letters* 101, (2012), 101906.
- [80] J. D. Lin, C. Han, F. Wang, R. Wang, D. Xiang, S. Qin, X. Zhang, L. Wang, H. Zhang, A. T. S. Wee and W. Chen, Electron-Doping-Enhanced Trion Formation in Monolayer Molybdenum Disulfide Functionalized with Cesium Carbonate, *ACS Nano*, 8, (2014), 5323.

## High Power Analysis of a Junctionless Field Effect Transistor With High K Spacer and Low Work Function Gate Material

A. Baro\*<sup>1</sup>, K.C.D. Sarma<sup>2</sup>

<sup>1,2</sup>Department of Instrumentation Engineering, Central Institute of Technology Kokrajhar, Kokrajhar,  
INDIA

Email: [anganju1992@gmail.com](mailto:anganju1992@gmail.com)

### ABSTRACT

This paper presents a high power analysis of Junctionless field effect transistor (JLFET) with High K Spacer and Low Work Function Gate Material. The structure consists of Hafnium Oxide (HfO<sub>2</sub>) as spacer. The work function of the gate material is selected in such a way that the device is Normally off in the absence of externally applied gate field. The high K spacer helps in reducing off-state leakage while low work function gate material results reduction of on-state loss making the device suitable for high power applications. Various performance parameters such as off current, on-state resistance etc of the proposed structure are compared with conventional JLFET and Power Metal oxide semiconductor field effect transistor (MOSFET) on Cogenda VisualTCAD 1.8.2 simulation platform. The simulation results shown that the device exhibits lower off current, lower on-state resistance and lower subthreshold swing compared to that of conventional JLFET and Power MOSFET.

**Keywords:** High power, JLFET; Low work function; High K Spacer`

### INTRODUCTION:

Power semiconductor devices are unavoidable part of almost all modern industries. Power MOSFET is one of the most widely used power devices as it possesses very low switching loss and handle very high power. However the on-state resistance of Power MOSFET is comparatively higher which causes a significant increase in on-state loss in small dimensions. A Junctionless Field Effect Transistor (JLFET) exhibits much lower on-state resistance compared to Power MOSFET. But it posses higher off state loss. Therefore a novel technique to reduce the off-state loss while keeping

the on-state loss to a minimum is proposed in the paper. The structure uses a high K spacer and low work function gate material which improves the performance of the device by a fringing field.

### DEVICE STRUCTURE AND SIMULATION:

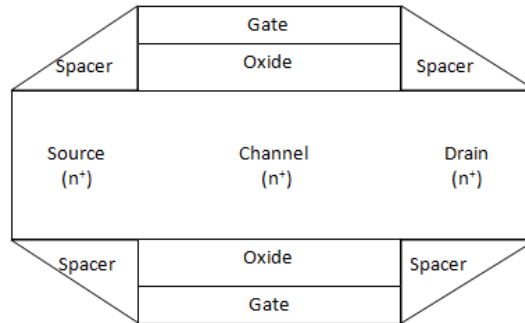


**Figure 1.** Symmetric Double gate JLFET with high K spacer

The simulation work is performed in COGENDA VisualTCAD platform. Carrier statistics used for the study is Fermi-Dirac statistics without impact ionization.

### RESULTS AND DISCUSSIONS

Variations of on current and off current for different values of drain voltages, gate oxide thicknesses, channel thicknesses, doping concentration and gate dielectric materials are shown in table 1 to table 5.

Higher drain voltage results in higher current (both on and off) as it is the biasing voltage and Drain induced barrier lowering effect is more for higher drain voltage.

Thinner gate oxide implies higher gate capacitance and higher gate controllability. Therefore off current is lower while on current is higher for thinner gate oxide.

Thicker channel results in lower channel resistance causing both on and off current to rise. Higher doping concentration results in higher current due to increase in total charge in the channel.

Gate dielectric material with higher dielectric constant results in higher gate capacitance. Therefore off current is lower while on current is higher for a high K dielectric such as  $\text{HfO}_2$ .

From all the tables it can be seen that proposed structure exhibits better characteristics with reduced off current and larger on current because fringing field resulting from the spacer.

**Table1.** On-current and Off-current for various drain voltages

Drain Voltage(V)	Off-current (A)		On Current (A)	
	Proposed Structure	Conventional Structure	Proposed Structure	Conventional Structure
100	$0.57 \times 10^{-6}$	$0.835 \times 10^{-6}$	11.2	8.35
140	$1.04 \times 10^{-6}$	$1.38 \times 10^{-6}$	15.4	10.8
180	$1.17 \times 10^{-6}$	$1.52 \times 10^{-6}$	16.64	11.3

**Table2.** On-current and Off-current for various gate oxide thicknesses

Gate oxide thickness (nm)	Off-current (A)		On Current (A)	
	Proposed Structure	Conventional Structure	Proposed Structure	Conventional Structure
2	$0.57 \times 10^{-6}$	$0.835 \times 10^{-6}$	11.2	8.35
4	$6.15 \times 10^{-6}$	$3.28 \times 10^{-6}$	7.41	6.62
6	$10.72 \times 10^{-6}$	$8.23 \times 10^{-6}$	4.64	3.31

**Table3.** On-current and Off-current for various channel thicknesses

Channel thickness (nm)	Off-current (A)		On Current (A)	
	Proposed Structure	Conventional Structure	Proposed Structure	Conventional Structure
10	$0.57 \times 10^{-6}$	$0.835 \times 10^{-6}$	11.2	8.35
20	$9.3 \times 10^{-6}$	$12.38 \times 10^{-6}$	25.4	15.8
30	$16.7 \times 10^{-6}$	$18.2 \times 10^{-6}$	44.64	21.2

**Table4.** On-current and Off-current for various doping concentration

Doping Concentration ( $/\text{cm}^3$ )	Off-current (A)		On Current (A)	
	Proposed Structure	Conventional Structure	Proposed Structure	Conventional Structure
$10^{19}$	$0.57 \times 10^{-6}$	$0.835 \times 10^{-6}$	11.2	8.35
$10^{18}$	$0.18 \times 10^{-6}$	$0.27 \times 10^{-6}$	9.52	7.6
$10^{17}$	$0.023 \times 10^{-6}$	$0.036 \times 10^{-6}$	7.61	5.3

**Table5.** On-current and Off-current for various gate dielectric

Gate Dielectric	Off-current (A)		On Current (A)	
	Proposed Structure	Conventional Structure	Proposed Structure	Conventional Structure
SiO <sub>2</sub>	0.57x10 <sup>-6</sup>	0.835 x10 <sup>-6</sup>	11.2	8.35
Si <sub>3</sub> N <sub>4</sub>	0.43 x10 <sup>-6</sup>	0.58 x10 <sup>-6</sup>	12.2	9.7
HfO <sub>2</sub>	0.19 x10 <sup>-6</sup>	0.32 x10 <sup>-6</sup>	21.16	13.2

## CONCLUSIONS

High power analysis has been done for a JLFET with high K spacer with low work function gate. Off current and on current of the proposed structure of the proposed structure has been compared with conventional structure. The simulation study shows that the proposed structure exhibits higher on current and lower off current compared to that of conventional structure.

## REFERENCES

1. Lee, C. W., Afzalian, A., Akhavan, N.D., Yan, R., Ferain, I., and Colinge. J.P., Junctionless multigate field effect transistor. *Applied Physics Letters*. **94**(05)(2009) , 053511
2. Colinge J.P., Lee, C.W., Afzalian, A., Dehdashti, N., Yan, R., Ferain, I., Razavi, P., O'Neill, B., Blake, A., White, M., Kelleher, A.M., McCarthy B., and Murphy R. SOI Gated Resistor: CMOS without Junctions. *IEEE International SOI Conference*, Foster City, California, USA : 1-2(2009)
3. Colinge, J. P., Lee, H.W., Afzalian, A., Akhavan, N.D., Yan, R., Ferain, I., Razavi, P., O'Neill, B., Blake, A., White, M., Kelleher, A.M., McCarthy, B., and Murphy, R. Nanowire transistors without junctions. *Nature Nanotechnology*. **5**(2010), 225–229

4. Raskin, J. P., Colinge, J. P., Ferain, I., Kranti, A., Lee, C. W., Dehdashti, N., Yan, R., Razavi, P., and Yu., R. Mobility Improvement in Nanowire Junctionless Transistors by Uniaxial Strain. *Applied Physics Letters*, **97**(4)(2010), 042114
5. Gundapaneni, S., Ganguly, S., and Kottantharayil, A. Enhanced Electrostatic Integrity of Short-Channel Junctionless Transistor With High- $\kappa$  Spacers. *IEEE Electron Device Letters*, **32**(10)(2011), 1325-1327.
6. Lou, H., Zhang, L., Zhu, Y., Lin, X., Yang, S., He, J., and Chan M. A junctionless nanowire transistor with a dual-material gate. *IEEE Transactions on Electron Devices*. **59**(7)(2012), 1829–1836.
7. Baruah, R. K. and Paily, R. A Dual-Material Gate Junctionless Transistor With High- $\kappa$  Spacer for Enhanced Analog Performance. *IEEE Transactions on Electron Devices*. **61**(1)(2014), 123-128
8. Sharma, R., Rathore, R.S., and Rana, A.K., Impact of High- $\kappa$  Spacer on Device Performance of Nanoscale Underlap Fully Depleted SOI MOSFET. *Journal of Circuits, Systems and Computers*. **27**(5)(2018), 1850063
9. Baruah, R. K. and Paily, R. Impact of High- $\kappa$  Spacer on Device Performance of Junctionless transistors. *Journal of Computational Electronics*. **12**(2013), 14-19
10. Raju , V., and Sivasankaran K., Impact of high  $\kappa$  spacer on RF stability performance of double gate junctionless transistor. International Journal of Numerical Modelling: Electronic Networks, Devices and Fields. **31**(08)(2018) <https://doi.org/10.1002/jnm.2481>
11. Goel A., Rewari S., Verma S. and Gupta R.S. High- $\kappa$  Spacer Dual-Metal Gate Stack Underlap Junctionless Gate All Around (HK-DMGS-JGAA) MOSFET for high frequency applications. Microsystem Technologies. **26**(2020), 1697–1705.
12. Chahal N. and Saini G. Analog performance investigation of double gate junctionless transistor using spacer layer engineering. *2017 8th International Conference on Computing, Communication and Networking Technologies (ICCCNT), Delhi, 1-4, (2017) doi: 10.1109/ICCCNT.2017.8204086.*
13. Baro A. and Sarma K.C.D. Study on Electrical Characteristics of Double gate Junctionless Field Effect Transistor With Triangle Shaped Spacer. *International Conference on Computational Performance Evaluation (ComPE)*, Shillong, Meghalaya, India. Jul 2-4, (2020)
14. Sarma K.C.D., and Sharma S. An Approach for Complete 2-D Analytical Potential Modelling of Fully Depleted Symmetric Double Gate Junction Less Transistor. *Journal of Computational Electronics*, Springer, **14**(2015), 717-725

## A Review on Layered Graphene Oxide and Transition Metal Dichalcogenides Material: Synthesis and Application in Memory Devices

Nipom Sekhar Das<sup>1</sup> and Avijit Chowdhury<sup>1\*</sup>

<sup>1</sup>Organic Electronics and Sensor Laboratory, Department of Physics, National Institute of Technology Silchar, Cachar, Assam-788010, India.  
E-mail: [avijitiacs@gmail.com](mailto:avijitiacs@gmail.com)

### ABSTRACT

Two-dimensional (2D) layered materials such as graphene oxide (GO) and transition metal dichalcogenides (TMDs) have drawn growing attention due to their excellent physical and structural properties and have been considered as a promising candidate in photonics, electronic, energy storage, sensing, optoelectronic devices. Here, different synthesis processes of layered materials have been reviewed. Recent progresses of non-volatile memory devices based on these materials with and without polymer have been discussed and trying to focus on memory characteristics such as  $I_{on}/I_{off}$  ratio, switching voltages, endurance, retention which are very important parameter for designing next generation electronic devices.

**Keywords:** Graphene oxide, transition metal dichalcogenide, layered, endurance, retention

### INTRODUCTION:

During the past few years, a wide research is going on in the field of 2D layered materials such as graphene, TMDs etc. Graphene was first introduced as a wonder material with 2D sheet of carbon atoms [1]. Prof A. K. Geim and K.S. Novoselov was awarded Nobel prize for their groundbreaking discovery of graphene [2]. The schematic diagram of graphene has been presented in Fig.1.

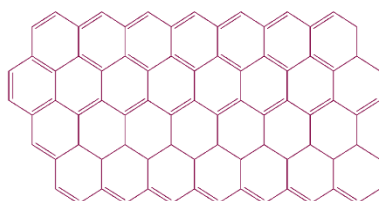


**Figure 1.** Schematic diagram of graphene.

The term graphene emanates from the prefix graph from graphite and the suffix ene from polycyclic aromatic hydrocarbons as for e.g., naphthalene, anthracene etc. It is a two-dimensional layer of  $sp^2$  hybridized carbon atoms with  $\pi$  electrons. Graphene have grabbed increasing attention because of their outstanding physical, chemical and structural characteristics which include high intrinsic strength of 136 GPa, specific area of  $2620 \text{ m}^2/\text{g}$ , Young's modulus of 1 TPa, high electrical and thermal conductivity [3] and have perceived promising applications in various modern technologies such as electronic devices, sensors, energy storage devices etc. [4,5]. Despite of all these properties it has major drawback of low dispersibility in water which limits its applications. Moreover, due to zero band gap in graphene causes major limitations in data storage applications. On the other hand, GO shows increased band gap, improved solubility, and also displays considerable mechanical and electrical properties. To overcome this drawback, oxygen functional groups are introduced on the graphene sheets by chemical oxidation. Oxidation of graphite-to-graphite oxide was discovered by Schafhaeutl and Brodie in 1840 and 1855, respectively [6-8]. The method of synthesizing graphene oxide (GO) had already been developed by Brodie in 1859 where he accomplished a reaction between graphite and  $\text{KClO}_3$  [9]. After that Staudenmaier increased the acidity of the mixture by adding  $\text{H}_2\text{SO}_4$  and chlorate during the whole process in 1898. Later Hummer and Offeman enhanced the procedure by oxidation using  $\text{NaNO}_3$ ,  $\text{KMnO}_4$  and Concentrated  $\text{H}_2\text{SO}_4$  [10]. Hummers' formulated the experimental method where graphite was oxidized by taking  $\text{KMnO}_4$ ,  $\text{NaNO}_3$  in concentrated  $\text{H}_2\text{SO}_4$  in 1958 [11]. It is schematically presented in Fig.2.

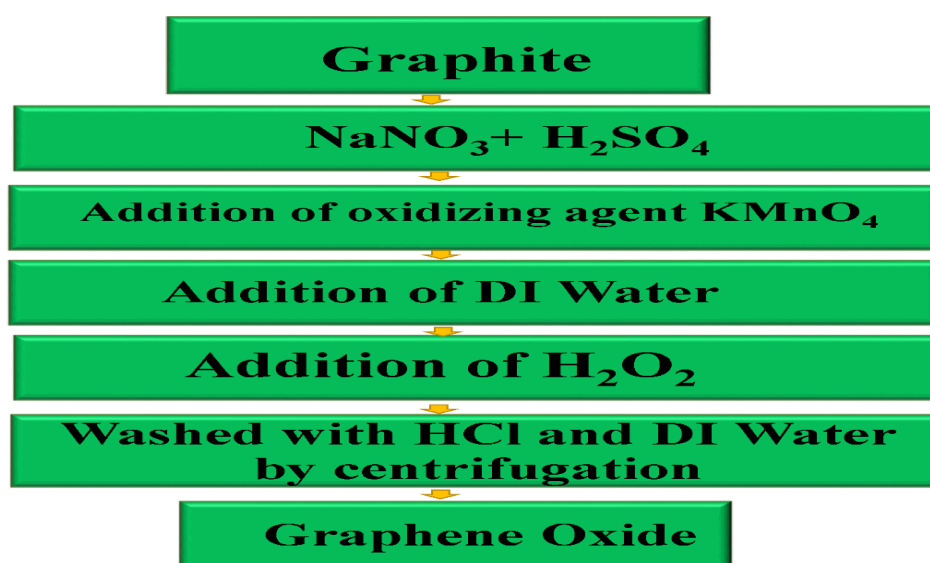
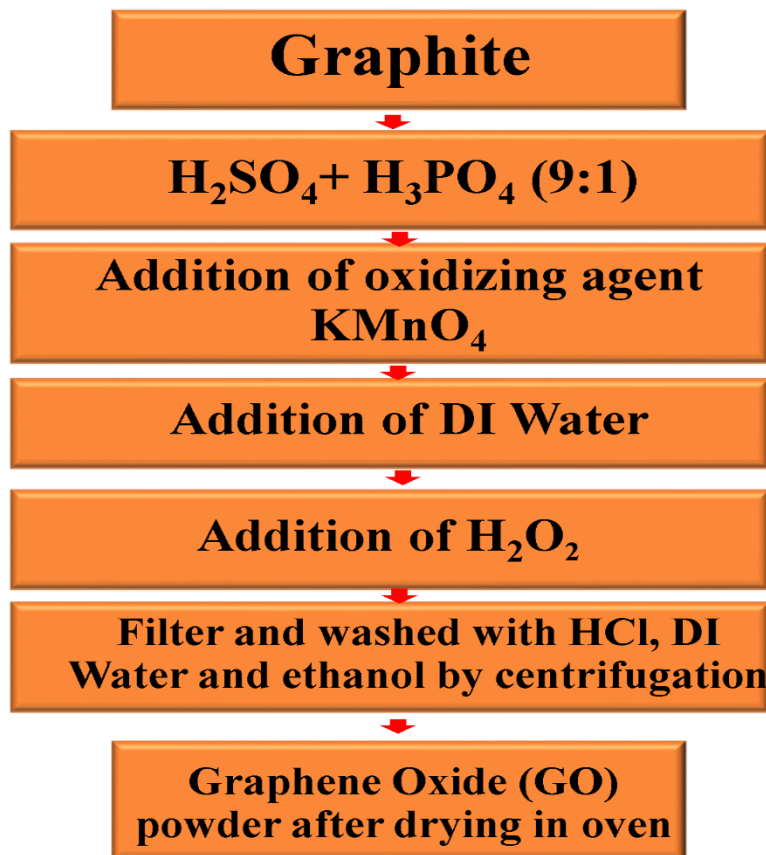


**Figure 2.** Schematic diagram of synthesis of GO by conventional Hummers' method.

GO can be synthesized by ultrasound assisted modified Hummer's method from expanded graphite [12]. This method is highly productive, less energy consuming and time saving. Use of  $\text{NaNO}_3$  emit toxic gases therefore, in improved Hummers' method  $\text{NaNO}_3$  is replaced by  $\text{H}_2\text{SO}_4$  and  $\text{H}_3\text{PO}_4$  which gives the advantages such as equivalent conductivity, emission of no toxic gas, hydrophilic carbon nanomaterials as shown in Fig 3.



GO is a single thick layer of graphite oxide which contains oxygen functional groups such as carboxylic (-COOH), carbonyl (-C=O), hydroxyl (-OH), epoxy (-O-) at the edges and the basal planes respectively [13, 14]. A diagram of graphene oxide is schematically presented in Fig. 4.

**Figure 3.** Schematic diagram of synthesis of GO by improved Hummers' method.

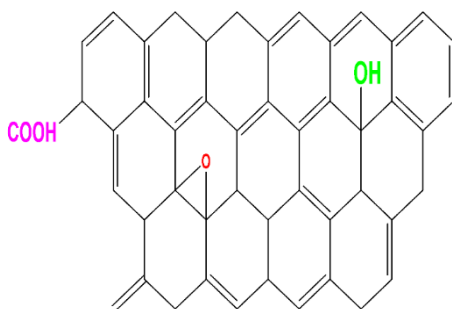


**Figure 4.** Schematic diagram of graphene oxide (GO).

It can be exploited for memory application because of their outstanding electrical and structural properties [15]. Due to the existence of energy gap and defect states in graphene oxide, it becomes an outstanding charge trapping layers in resistive memory devices [16]. Classification of memory is schematically shown in Fig. 5.

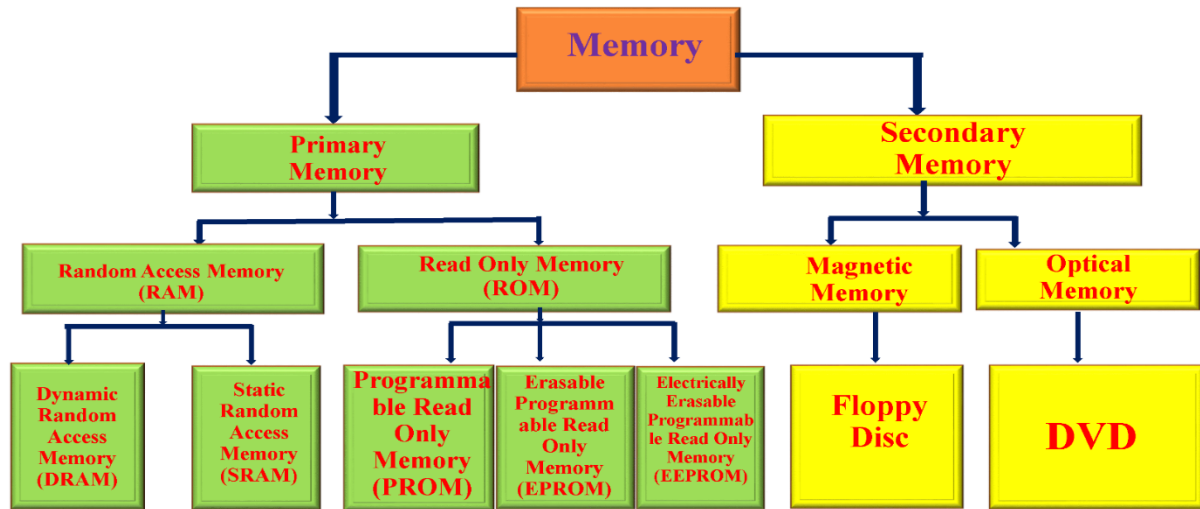


**Figure 5.** Schematic diagram of classification of memory

Alongside, 2D layered transition metal dichalcogenides (TMDs) ( $\text{MX}_2$  where M corresponds to Sn, Mo, W etc. and X corresponds to S, Se etc.) have drawn immense attention due to their distinctive electronic and optical properties [17,18]. Diagram of TMDs is schematically presented in Fig. 6.

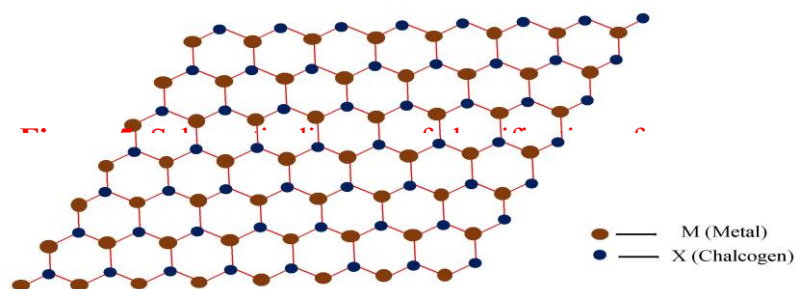


**Figure 6.** Schematic diagram of  $\text{MX}_2$  (Metal dichalcogenide).

Among different TMDs,  $\text{MoS}_2$  is one of the promising 2D layered material after graphene and having direct band gap of about 1.9 eV [19]. In  $\text{MoS}_2$ , Mo layer has been sandwiched between two sulfur layers via van der Waals forces similar to graphite [20] and have potential application

in electronics after conventional silicon. MoS<sub>2</sub> nanostructure can be synthesized through simple hydrothermal method [21] schematically shown in Fig.7.

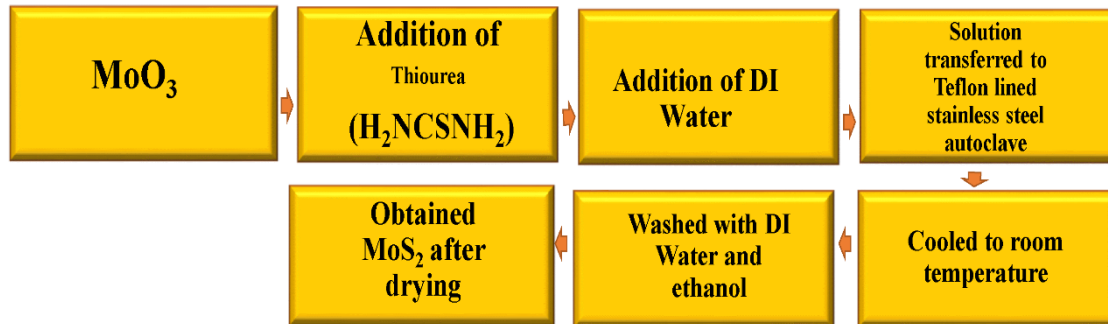


**Figure 7.** Schematic diagram of synthesis of MoS<sub>2</sub>.

Resistive switching in organic/ inorganic nanofillers have drawn promising attention because of their considerable physical and structural characteristics. Recently, carbon-based material particularly GO and TMDs have been under comprehensive investigation due to their broad exploitation in resistive memory devices because of their outstanding charge transport properties. Recently, Jeong *et al.* fabricated the device Al/GOs/Al which showed bipolar resistive switching with retention time more than 10<sup>5</sup> sec and I<sub>on</sub>/I<sub>off</sub> 10<sup>2</sup> [22]. Wu *et al.* fabricated the multistacking layered device PS/SLG/PMMA/SLG/PMMA and observed the tristable resistive memory characteristics with current on/ off (I<sub>on</sub>/I<sub>off</sub>) ratio of about 10<sup>4</sup> [23]. He *et al.* fabricated the Cu/GO/Pt device and observed that the device showed bipolar resistive switching nature with a retention time longer than 10<sup>4</sup> s and I<sub>on</sub>/I<sub>off</sub> about 20 [24]. Liu *et al.* fabricated the device Al/GO-PVK/ITO and the device showed bistable electrical conductivity switching with endurance up to 10<sup>8</sup> [25]. Rehman *et al.* fabricated the device Ag/WS<sub>2</sub>/Ag and observed the bipolar resistive switching behavior with retention 10<sup>5</sup> s and I<sub>on</sub>/I<sub>off</sub> 10<sup>3</sup> [26]. Lee *et al.* fabricated the Al/ WS<sub>2</sub> NSs: PMMA/ITO/PEN device, which exhibited bipolar switching nature and I<sub>on</sub>/I<sub>off</sub> ratio up to 10<sup>4</sup> [27]. Deepak *et al.* fabricated the Al/MoS<sub>2</sub>(PVDF-HFP)/ITO device and the device showed the bipolar resistive switching with I<sub>on</sub>/I<sub>off</sub> 10<sup>4</sup> [28]. Memory device structure is schematically presented in Fig.8.

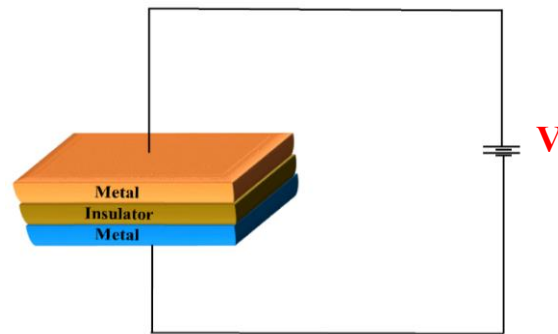


**Figure 8.** Schematic diagram of memory device structure.

## DIFFERENT SYNTHESIS PROCESSES OF 2D LAYERED MATERIALS

Various approaches have been followed over the years for the production of low cost, high quality and highly efficient 2D layered materials. The methods include hydrothermal method, sol gel technique, top-down approach, bottom-up approach etc.

**Hydrothermal Method:** It is one of the very well-known and suitable methods for the synthesis of nanomaterial. In this process the production of nanomaterial can occur in a temperature that ranges from room temperature to very high temperatures. The desirability of the method is its capability to produce crystalline phases that are not steady at the melting point.

It is an efficient method for the synthesis of GO based material which is carried out in high vapour pressure and temperature. Moreover, this method is very environmentally friendly, cost effective. Hydrothermal method can also be regarded as solvothermal method which is performed in a teflon lined stainless steel autoclave and where the temperature ranges from 160° C to 180° C [29-31].

**Sol gel technique:** Sol gel process is a very known method. It is a wet chemical process used for the synthesis of solid materials from small molecules. The sol gel derived inorganic compounds need very low temperature for the synthesis [32].

**Top-down approach:** It involves the breakdown of bulk materials into small nanomaterials schematically shown in Fig. 9 (a). This method implies that the nanostructured materials are synthesized after removing the crystal planes which are present in the substrate. It has the

advantage of large-scale production, moreover, chemical purification is not required in this method. This approach includes liquid phase exfoliation method, micromechanical exfoliation.

Liquid phase exfoliation method is widely used for synthesizing cost effective two-dimensional nanosheet. It is one of the largely acceptable procedure for the large-scale production of few layered 2D nanomaterial which is cost effective [33].

Micromechanical exfoliation is a method for producing low defects, high quality, and thin materials. It is a widely used method that offers high quality 2D nanostructured materials, allowing to study the properties, and outstanding device performances [34].

**Bottom-up approach:** It involves physical or chemical process for constructing larger compounds from basic units' atom by atom, molecule by molecule, schematically shown in Fig. 9(b). It has many advantages such as high accuracy, less wastages etc. Ultra-fine nanoparticles can be produced, but in this method large-scale production is very difficult, and chemical purification is needed. This method includes physical vapour deposition, chemical vapour deposition etc. [35].

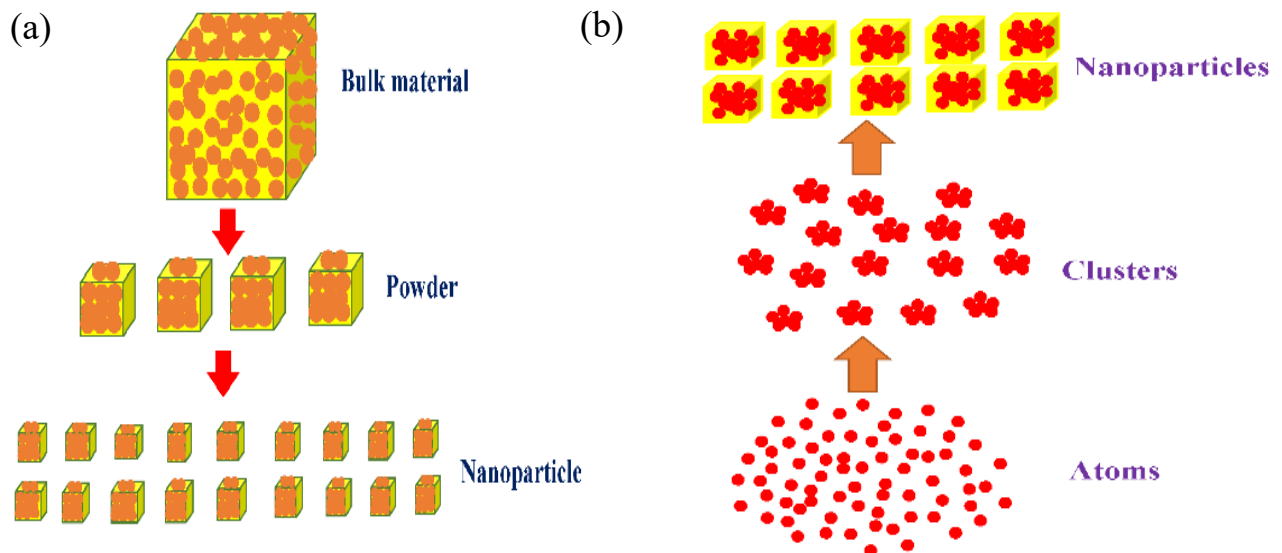


**Figure 9.** Schematic diagram of (a) Top-down approach (b) Bottom-up approach.

## 2D LAYERED MATERIAL BASED NON-VOLATILE MEMORY DEVICES

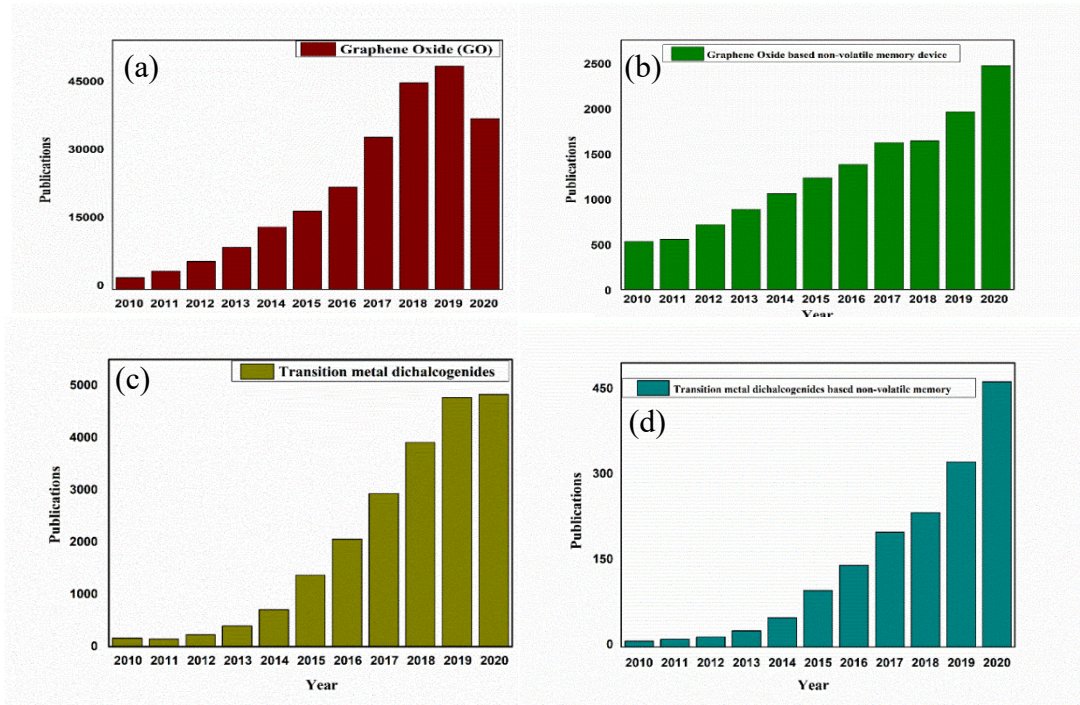


**Figure 10.** Publication vs Year graph of (a) Graphene oxide (GO) nanomaterials (b) GO based non-volatile memory devices (c) Transition metal dichalcogenides (TMDs) (d) TMDs based non-volatile memory devices (Data obtained from Google Scholar).

Fig.10 shows the publications of layered material-based memory devices over the past few years. Functionalized layered nanohybrid materials have been exploited in various applications such as sensor, supercapacitor, and resistive random access memory devices. Recently, researcher have been focussing on the fabrication of memory devices with simple structure and easy fabrication technique. The important parameters for designing high performance memory devices are high density, high  $I_{on}/I_{off}$  ratio, long retention time, good endurance property, reproducibility, and high switching speed. To achieve such memory properties various semiconducting and insulating materials are explored to exhibit the resistive memory properties. Among the different known organic-inorganic layered nanohybrid materials two-dimensional layered carbon-based materials and transition metal dichalcogenides with or without polymeric materials have drawn immense attention because of their outstanding performances in modern electronic devices. Various 2D layered material-based memory devices and their memory characteristics is shown in Table 1.

**Table 1. Two-dimensional layered material-based memory device**

DEVICE STRUCTURE	V <sub>SET</sub> (VOLT)	V <sub>RESET</sub> (VOLT)	I <sub>ON</sub> /I <sub>OFF</sub>	ENDURANCE CYCLES	RETENTION TIME (SEC)	MEMORY EFFECT	PUBLICATION YEAR	REFERENCES
RGO/MOS <sub>2</sub> - PVP/AL	-	-	10 <sup>2</sup>	-	-	THE DEVICE EXHIBITED THE ELECTRICALLY BISTABLE BEHAVIOR.	2012	36
AG/MOS <sub>2</sub> + PVA/AG	-	-	10 <sup>2</sup>	10 <sup>3</sup>	10 <sup>5</sup>	BISTABLE, NON-VOLATILE AND REWRITABLE RESISTIVE SWITCHING BEHAVIOR.	2016	37
RGO/ MOS <sub>2</sub> - P123/ RGO/PET	-	-	10 <sup>2</sup>	-	10 <sup>3</sup>	IT SHOWED THE NON-VOLATILE FLASH	2015	38

						MEMORY DIODE BEHAVIOR.		
RGO/ MOS <sub>2</sub> - ZIF8/ RGO/PET	-	-	10 <sup>4</sup>	-	10 <sup>3</sup>	IT SHOWED THE WRITE-ONCE-READ-MANY-TIMES (WORM) MEMORY CHARACTERISTICS.	2014	39
AL/GOS+P MMA/ITO	-1.87	-	10 <sup>4</sup>	-	10 <sup>4</sup>	THE DEVICE EXHIBITED THE WORM CHARACTERISTICS.	2019	40
ITO/PMMA/ RGO- CDS/PMMA/ AL	-0.48	2.88	10 <sup>6</sup>	10 <sup>3</sup>	10 <sup>4</sup>	THE DEVICE EXHIBITED BIPOLAR RESISTIVE SWITCHING CHARACTERISTICS.	2020	41
ITO/ GRAPHENE -MOS <sub>2</sub> + PMMA/CU	-1.0	1.0	>10 <sup>4</sup>	10 <sup>4</sup>	10 DAY S	THE DEVICE EXHIBITED NON-VOLATILE RRAM.	2018	42

ITO/PS+GO/ AL	-0.80 TO - 1.55	3.7 TO 5.2	$10^3$	$10^4$	$10^5$	THE DEVICE EXHIBITED REWRITABLE, NON- VOLATILE TERNARY MEMORY PROPERTY.	2017	43
------------------	-----------------------	---------------	--------	--------	--------	--	------	----

RRAM: Resistive Random-Access Memory; PS: Polystyrene; PVA: Polyvinyl Alcohol; PVP: Polyvinyl pyrrolidone; P123: Poly (ethylene glycol)- poly (propylene glycol)-poly (ethylene glycol); ZIF8: Zeolitic imidazolate framework; PMMA: Poly (methyl methacrylate).

## CONCLUSION

In summary, different methods have been investigated for the synthesis of low cost, environmentally friendly, high quality and highly efficient two-dimensional layered materials in this review article. Micromechanical exfoliation and liquid phase exfoliation provide the highest material quality and compatible for modern research and large-scale industrial production. Recent progresses of non-volatile resistive memory devices based on various organic/inorganic layered material such as GO, TMDs e.g., MoS<sub>2</sub> are discussed thoroughly. From the review it can be summarized that layered materials hold promising attention as active layers in next generation electronic devices. Different electrical switching behaviors such as current on/off ( $I_{ON}/I_{OFF}$ ) ratio, retention time, switching voltages are investigated here to compare the reliability of the memory devices. Current research on 2D layered materials and their nanocomposites are highly appreciated because of their outstanding physical and electronic properties in non-volatile memory devices.

## REFERENCES

- [1] Boehm, H.-P., Setton, R. and Stumpp, R. Nomenclature and terminology of graphite intercalation compounds. *Pure & Appl. Chem.* **66** (1994), 1893-1901.
- [2] Geim, A. K. and Novoselov, K. S. The rise of graphene. *Nature Materials* **6** (2007), 183-191.

- [3] Alam, S., Sharma, N. and Kumar, L. Synthesis of Graphene Oxide (GO) by Modified Hummers Method and Its Thermal Reduction to Obtain Reduced Graphene Oxide (rGO). *Graphene* **6** (2017), 1-18.
- [4] Inagaki, M., Kim, Y. A. and Endo, M. Graphene: preparation and structural perfection, *J. Mater. Chem.* **21** (2011), 3280-3294.
- [5] Jia, X., Campos-Delgado, J., Terrones, M., Meunier, V. and Dresselhaus, M. S. Graphene edges: a review of their fabrication and characterization. *Nanoscale* **3** (2011), 86–95.
- [6] Fischer, J.E. and Thompson, T.E. Graphite intercalation compounds. *Phys. Today* **31** (1978), 36.
- [7] Brodie, B. C. On the Atomic Weight of Graphite. *Philosophical Transactions of the Royal Society of London* **149** (1859), 249–259.
- [8] Hamwi, A. and Marchand, V. Some chemical and electrochemical properties of graphite oxide. *J. Phys. Chem Solids* **57** (1996), 867–872.
- [9] Dreyer, D. R., Park, S., Bielawski, C. W. and Ruoff, R.S. The chemistry of graphene oxide. *Chem. Soc. Rev.* **39** (2010), 228–240.
- [10] Paulchamy, B. Arthi, G., BD, Lignesh. A Simple Approach to Stepwise Synthesis of Graphene Oxide Nanomaterial. *Journal of Nanomedicine & Nanotechnology* **6** (2015).
- [11] Hummers, W. S. and Offeman, R. E. Preparation of graphitic oxide. *Journal of the American Chemical Society* **80** (1958), 1339–1339.
- [12] Yang, H., Li, H., Zhai, J., Sun, L. and Yu, H. Simple Synthesis of Graphene Oxide Using Ultrasonic Cleaner from Expanded Graphite. *Industrial & Engineering Chemistry Research* **53** (2014), 17878–17883.
- [13] Lu, N., Yin, D., Li, Z. and Yang, J. Structure of Graphene Oxide: Thermodynamics versus Kinetics. *J. Phys. Chem. C* **115** (2011), 11991–11995.
- [14] Biswal, S., Bhaskaram, D. S. and Govindaraj, G. Graphene oxide: Structure and temperature dependent magnetic characterization. *Materials Research Express* **5** (2018), 086104.
- [15] Pradhan, S. K., Xiao, B., Mishra, S., Killam, A. and Pradhan, A. K. Resistive switching behavior of reduced graphene oxide memory cells for low power nonvolatile device application. *Scientific Reports* **6** (2016), 26763.
- [16] Li, L., Tunable Memristic Characteristics Based on Graphene Oxide Charge-Trap Memory. *Micromachines* **10** (2019), 151.
- [17] Seifert, G., Terrones, H., Terrones, M. and Frauenheim, T. Novel NbS<sub>2</sub> metallic nanotubes. *Solid state communications* **115** (2000). 635-638.
- [18] Kociak, M., Stephan, O., Henrard, L., Charbois, V., Rothschild, A., Tenne, R. and Colliex, C. Experimental Evidence of Surface-Plasmon Coupling in Anisotropic Hollow Nanoparticles. *Physical Review Letters* **87** (2001), 075501.

- [19] Splendiani, A., Sun, L., Zhang, Y., Li, T., Kim, J., Chim, C.-Y., Galli, G. and Wang, F. Emerging Photoluminescence in Monolayer MoS<sub>2</sub>. *Nano Letters* **10** (2010), 1271–1275.
- [20] Fan, L.-Q., Liu, G.-J., Zhang, C.-Y., Wu, J.-H. and Wei, Y.-L. Facile one-step hydrothermal preparation of molybdenum disulfide/carbon composite for use in supercapacitor. *International Journal of Hydrogen Energy* **40** (2015), 10150–10157.
- [21] Wang, X., Ding, J., Yao, S., Wu, X., Feng, Q., Wang, Z. and Geng, B. High supercapacitor and adsorption behaviors of flower-like MoS<sub>2</sub> nanostructures. *J. Mater. Chem. A* **2** (2014), 15958–15963.
- [22] Jeong, H. Y., Kim, J. Y., Kim, J. W., Hwang, J. O., Kim, J.-E., Lee, J. Y., Yoon, T. H., Cho, B. J., Kim, S. O. and Ruoff, R. S. Graphene Oxide Thin Films for Flexible Nonvolatile Memory Applications. *Nano Lett.* **10** (2010), 4381–4386.
- [23] Wu, C., Li, F. and Guo, T. Efficient tristable resistive memory based on single layer graphene/insulating polymer multi-stacking layer. *Appl. Phys. Lett.* **104** (2014), 183105.
- [24] He, C. L., Zhuge, F., Zhou, X. F., Li, M., Zhou, G. C., Liu, Y. W., Wang, J. Z., Chen, B., Su, W. J., Liu, Z. P., Wu, Y. H., Cui, P. and Li, R.-W. Nonvolatile resistive switching in graphene oxide thin films. *Appl. Phys. Lett.* **95** (2009), 232101.
- [25] Liu, G., Zhuang, X., Chen, Y., Zhang, B., Zhu, J., Zhu, C.-X., Neoh, K.-G. and Kang, E.-T. Bistable electrical switching and electronic memory effect in a solution-processable graphene oxide-donor polymer complex. *Appl. Phys. Lett.* **95** (2009), 253301.
- [26] Rehman, M. M., Siddiqui, G. U., Doh, Yang H. and Choi, K. H. Highly Flexible and Electroforming Free Resistive Switching Behavior of Tungsten Disulfide Flakes Fabricated through Advanced Printing Technology. *Semiconductor Science and Technology* **32** (2017).
- [27] Lee, J. H., Wu, C., Sung, S., An, H. and Kim, T. W. Highly flexible and stable resistive switching devices based on WS<sub>2</sub> nanosheets: poly (methyl methacrylate) nanocomposites. *Scientific Reports* **9** (2019), 19316.
- [28] Deepak, Deb, R., Nair, M. G., Halder, S., Sharma, A.L. and Mohapatra, S. R. Liquid Phase Exfoliation of MoS<sub>2</sub> Nano-sheets and Observation of Resistive Switching Memory in MoS<sub>2</sub> Nano-sheets-PVDF-HFP Composite Films. *Materials Today: Proceedings* **18** (2019), 5447–5453.
- [29] Xu, X., Shen, J., Li, N. and Ye, M. Facile synthesis of reduced graphene oxide/CoWO<sub>4</sub> nanocomposites with enhanced electrochemical performances for supercapacitors. *Electrochimica Acta* **150** (2014), 23–34.
- [30] Peng, Y., Meng, Z., Zhong, C., Lu, J., Yu, W., Jia, Y. B. and Qian, Y. Hydrothermal Synthesis and Characterization of Single-Molecular-Layer MoS<sub>2</sub> and MoSe<sub>2</sub>. *Chemistry Letters* **30** (2001), 772–773.
- [31] Hashim, N., Muda, Z., Hussein, M. Z., Isa, I. M., Mohamed, A., Kamari, A., Bakar, S. A., Mamat, M. and Jaafar, A.M. a brief review on recent graphene oxide-based material nanocomposites: Synthesis and Applications. *J. Mater. Environ. Sci.* **7** (2016) 3225-3243.

- [32] Zheng, C., Zheng, Y., Chen, W. and Wei, L. Encapsulation of graphene oxide/metal hybrids in nanostructured sol-gel silica ORMOSIL matrices and its applications in optical limiting. *Optics & Laser Technology* **68** (2015), 52–59.
- [33] Coleman, J. N., Lotya, M., O'Neill, A., Bergin, S. D., King, P. J., Khan, U., Young, K., Gaucher, A., De, S., Smith, R. J., Shvets, I. V., Arora, S. K., Stanton, G., Kim, H.-Y., Lee, K., Kim, G. T., Duesberg, G. S., Hallam, T., Boland, J. J., Wang, J. J., Donegan, J. F., Grunlan, J. C., Moriarty, G., Shmeliov, A., Nicholls, R. J., Perkins, J. M., Grieveson, E. M., Theuwissen, K., McComb, D. W., Nellist, P. D. and Nicolosi, V. Two-Dimensional Nanosheets Produced by Liquid Exfoliation of Layered Materials. *Science* **331** (2011), 568–571.
- [34] Radisavljevic, B., Whitwick, M. B. and Kis, A. Integrated Circuits and Logic Operations Based on Single-Layer MoS<sub>2</sub>. *ACS Nano* **5** (2011), 9934-9938.
- [35] Sun, J., Li, X., Guo, W., Zhao, M., Fan, X., Dong, Y., Xu, C., Deng, J. and Fu, Y. Synthesis Methods of Two-Dimensional MoS<sub>2</sub>: A Brief Review. *Crystals* **7** (2017), 198.
- [36] Yin, Z., Zeng, Z., Liu, J., He, Q., Chen, P. and Zhang, H. Memory Devices Using a Mixture of MoS<sub>2</sub> and Graphene Oxide as the Active Layer. *Small* **9** (2013), 727–731.
- [37] Rehman, M. M., Siddiqui, G. U., Gul, J. Z., Kim, S.-W., Lim, J. H. and Choi, K. H. Resistive Switching in All-Printed, Flexible and Hybrid MoS<sub>2</sub>-PVA Nanocomposite based Memristive Device Fabricated by Reverse Offset. *Scientific Reports* **6** (2016), 36195.
- [38] Tan, C., Qi, X., Liu, Z., Zhao, F., Li, H., Huang, X., Shi, L., Zheng, B., Zhang, X., Xie, L., Tang, Z., Huang, W. and Zhang, H. Self-Assembled Chiral Nanofibers from Ultrathin Low-Dimensional Nanomaterials. *Journal of the American Chemical Society* **137** (2015), 1565–1571.
- [39] Huang, X., Zheng, B., Liu, Z., Tan, C., Liu, J., Chen, B., Li, H., Chen, J., Zhang, X., Fan, Z., Zhang, W., Guo, Z., Huo, F., Yang, Y., Xie, L.-H., Huang, W. and Zhang, H. Coating Two-Dimensional Nanomaterials with Metal–Organic Frameworks. *ACS Nano* **8** (2014), 8695–8701.
- [40] Gogoi, K. K. and Chowdhury, A. Electric field induced tunable memristive characteristics of exfoliated graphene oxide embedded polymer nanocomposites. *J. Appl. Phys.* **126** (2019), 025501.
- [41] Gogoi, K. K. and Chowdhury, A. Performance improvement of organic resistive memories by exploiting synergistic layered nanohybrid dispersed polymer composites. *J. Appl. Phys.* **127** (2020), 065501.
- [42] Bhattacharjee, S., Das, U., Sarkar, P. K. and Roy, A. Stable charge retention in graphene-MoS<sub>2</sub> assemblies for resistive switching effect in ultra-thin super-flexible organic memory devices. *Organic Electronics* **58** (2018), 145-152.
- [43] Sun, Y., Wen, D., Bai, X., Lu, J. and Ai, C. Ternary Resistance Switching Memory Behavior Based on Graphene Oxide Embedded in a Polystyrene Polymer Layer. *Scientific Reports* **7** (2017), 3938.

## Estimation of Radon Exhalation Rate in Soil Samples of Oil Field Area of Tinsukia District of Assam and its Possible Correlation with Radium Content in Soil Using Can Technique Method

Sonali Dutta<sup>1</sup>, Hiranya Kr. Sarma<sup>2</sup> Ranjan Kr. Kakati<sup>3</sup>

<sup>1</sup>Department of Physics, Assam Down Town University, Guwahati, Assam, India

<sup>2</sup>Principal, Suren Das College Hajo, Kamrup, Assam, India

<sup>3</sup>Director, Students' Welfare, Gauhati University, Assam, India

**Email:** *sonaliphysics1@gmail.com*

### ABSTRACT

Radon activities and radon exhalation rates have been measured in soil samples collected from different locations of oil field area of Tinsukia District (Digboi) of Assam, India. 'Can Technique' using LR115 (type II) detectors, has been used for the estimation of radium concentration & radon exhalation rate. Radium concentration observed for soil samples has been found to be varying from 1.33 Bq/Kg to 1.6 Bq/Kg. The Radon exhalation rate in these samples has been found to be varying from 0.834 to 0.998 mBqm<sup>-2</sup> h<sup>-1</sup>. A positive correlations with ( $R^2 = 0.99$ ) have been found between radon exhalation rate and radium concentration in the samples for the investigated area. The obtained results indicate normal levels of indoor radon concentration and effective radium content in all locations of the studied area. Life threats to the dwellings in the particular area. In the importance of a study of radon has been recognized globally. So we have taken up a study to compare the radon data with respect to our present study. Institutions like EPA, WHO, ICRP and many more world recognized organizations have taken up the study of radon and its importance. So, a qualitative analysis and comparison is highly essential in context to world concern.

**Keywords:** Can technique, radon exhalation, emanation, effective radium content

### INTRODUCTION:

Radon is produced in the soil due to the presence of <sup>238</sup>U and is transported to atmosphere by turbulent diffusion (J.E.Tanner). Once formed by the decay of the parent <sup>226</sup>Ra, the <sup>222</sup>Rn atoms are free to diffuse through the interstices between mineral or soil particles where they become a minor constituent of soil. The processes effective in transporting <sup>222</sup>Rn from soil to the surface are related directly to the size and configuration of the space occupied by the soil gas. Radon

concentrations in soil pores (J.Porstendorfer) at depth are dependent directly upon the radium content of the soil, emanating power for radium and soil moisture content. Exhalation of  $^{222}\text{Rn}$ , a radioactive inert gas, is associated with the presence of  $^{226}\text{Ra}$  and its ultimate precursor uranium in the earth crust. Although these elements occur in virtually all types of rocks and soils, their concentration varies with specific sites and geological formation of materials. The rate at which radon escapes or emanates from solid into the surrounding air is known as radon exhalation rate of the solid. This may be measured by either per unit mass or per unit surface area of the solid. Measurement of radon exhalation rate of soils and rocks are helpful to study radon health hazards. Radon exhalation is the amount of radon (radon activity) as obtained from a given layer (geological material on the surface/surface exposure) mainly the outer thinner part of the crust. On the other hand, emanation depends on the nature of uranium and/or thorium. Radon enters into buildings through the soil or building materials. So radon exhalation rate from the soil or building material is an important parameter for estimating local environmental radon level. On the basis of epidemiological studies it has been established that the enhanced levels of indoor radon in dwellings can cause health hazards and may cause serious diseases like lung cancer in human beings ( F.Bichichi, R.W.Field). A number of studies of exhalation rates of radon/thoron from soil and building materials are available which are same as observed by (F.W.Wilkening,M.Folkerts,Singh, R.Prasad). Therefore, it is also necessary to check the correlation between the radium concentration and radon exhalation rate of the source material. In the present study we have applied solid state nuclear track detectors (LR-115,TYPE II) for the analysis of radium and radon exhalation rate measurements in the soil samples taken from wide range of areas of oil field areas of Assam, India.

## MATERIALS & METHODS

The ‘Can technique’ is used for the measurement of radium and radon exhalation rates in some soil samples collected from different study areas. The dried samples collected from different places are finely powdered and sieved through a 200 mesh sieve. The fine powder (250g) of samples from each site is placed in different glass bottles and sealed with thin polyethylene sheets for 30 days so as to attain the equilibrium. After one month, LR-115 (type II) plastic track detectors are fixed on the lower side of cork lids, which are then gently pressed against the polyethylene sheets on the glass bottles (acting as emanation chambers) as shown in Fig1. so that

the equilibrium is not disturbed or there is minimum possible disturbance, if any. The bottles are then sealed and left as such for 90 days so that the detectors can record tracks produced by the decay of radon. The exposed detectors are etched in 2.5N, NaOH solution at  $(60 \pm 1)^{\circ}\text{C}$  for 90 minutes. The tracks are counted using an (Olympus) optical microscope at 400X magnification.

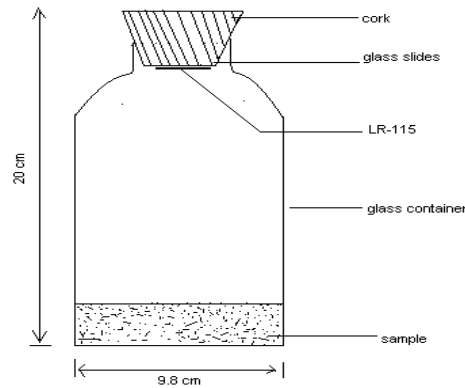


Fig 1: The Can technique used for the study of radium content and radon exhalation rate of soil samples

The track density  $\rho$  (tracks.cm<sup>-2</sup>) so obtained was converted into the units of (Bq m<sup>-3</sup>) of radon concentration  $C_{Rn}$  using the following equation (F.Saad, H.A.Hend, &N.A. Hussein;M.A. Ayman & A.Ali; I.Tayseer & M.A.Ayman):

$$C_{Rn} = \rho / kt \quad \dots\dots\dots(1)$$

where  $t$  is the exposure time of distributed LR-115 detector in (days) and  $k$  is the calibration factor tracks of CR-39 in (tracks.cm<sup>-2</sup>. day<sup>-1</sup>/Bqm<sup>-3</sup>) (F.Saad; M.A.Ayman &A. Ali; I.Tayseer & M.A.Ayman) The effective radium content  $C_{Ra}$  (Bq/Kg) can be calculated from the relation

$$C_{Ra} = \rho hA /kT M \quad \dots\dots\dots (2)$$

where  $\rho$ .is the counted track density (tracks.cm<sup>-2</sup>),  $h$  is the distance between the detector and the top of the sample (m),  $A$  is the area of cross section of the can (m<sup>2</sup>),  $K$  is the calibration factor of the detector,  $M$  is the mass of the sample (Kg) and  $T_e$  is The effective exposure time (in hour) which can be determined using the following equation.

$$T_e = T - (1 - e^{-\lambda RnT}) / \lambda \dots\dots\dots (3)$$

where T is the exposure time, and  $\lambda_{Rn}$  the decay constant for radon. The radon exhalation rate in terms of area,  $E_A$  ( $mBqm^{-2} h^{-1}$ ) can be calculated from the (F.Saad, M.A. Ayman &A. Ali; I.Tayseer & M.A.Ayman):

$$E_A = C_{Rn} V\lambda / A[T + 1/\lambda (e^{-\lambda T} - 1) \dots\dots\dots(4)$$

Where A, V,  $\lambda$  and T are the area of the can in ( $m^2$ ), the effective volume of the can in ( $m^3$ ), decay constant for radon in ( $h^{-1}$ ), and the exposure time in hours, respectively. The radon exhalation rates in terms of mass,  $E_M$  ( $mBqm^{-2} h^{-1}$ ) can be calculated by the following formula

$$E_M = C_{Rn} V\lambda / M[T + 1/\lambda (e^{-\lambda T} - 1) \dots\dots\dots(5)$$

Where M is the mass of the sample (250 gm)

The risk of lung cancer from domestic exposure due to radon and its daughters can be computed directly from the equivalent effective dose. The annual effective dose, D ( $mSvy^{-1}$ ) was computed from the integrated radon concentration using the following formula (Gupta, Mahur, Sonkawade, & Verma, 2010):

$$D = C_{Rn} 0.4 \times 3.88 \times 7000 / 170 \ 3700 \dots\dots\dots (6)$$

Where D and  $C_{Rn}$  are the annual effective dose in ( $mSvy^{-1}$ ) and the integrated radon concentration in ( $Bq.m^{-3}$ ) respectively. The equilibrium factor and the ICRP conversion factor (ICRP, 1993) are 0.4 and 3.88 mSv.WLM, respectively. 7000 is the number of hours per year, and 170 is the number of hours per working month

## RESULTS & DISCUSSION

Table 1 represents the activity concentrations of indoor Radon-222, effective Radium content ( $Bq/kg$ ) and radon exhalation rate ( $mBqm^{-2} h^{-1}$ ) were measured at different locations in oil field areas of Digboi, Assam. The soil samples are collected from different locations near oil industry within the range 2 – 4 Kms. The values of radium content at Digboi varies from 1.33  $Bq/Kg$  to 1.6  $Bq/Kg$  and radon exhalation rate varies from 29.37  $mBqm^{-2}h^{-1}$  to 31.18  $mBqm^{-2}h^{-1}$ . From these data, a good positive correlation have been observed between radium content and radon exhalation rate in soil samples. The results show that there is a variation in radon exhalation rate from one location to other which depends on the geological formation. The variation in values

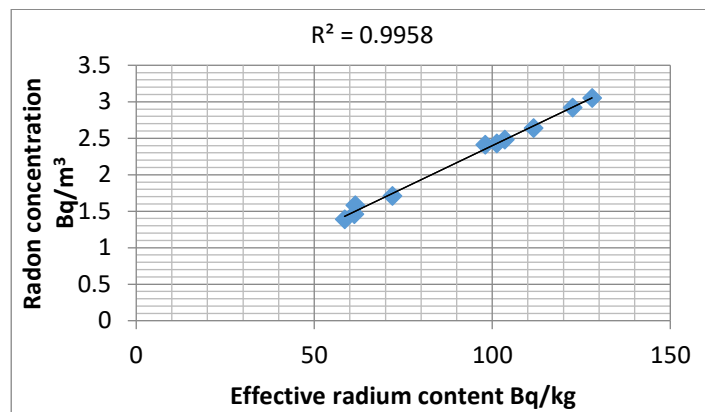
of radon exhalation rate may be due to the differences in radium content (T.V.Ramachandran and M.C.Subba Ramu) and porosity (M.Folkerts) of the soil. The values of effective radium content are less than the permissible value of  $370 \text{ Bq kg}^{-1}$  as recommended by Organization for Economic Cooperation and Development (OECD 1979). Hence, the result shows that these study areas are safe as far as the health hazards of radium are concerned.

Table1: Values of Radon Exhalation Rates and Radium Content in Soil Samples Collected From Different areas of Digboi

Location	GPS locations	Track Density (Tracks $\text{cm}^{-2}$ )	Radon Concentration ( $\text{Bq m}^{-3}$ )	Radium content $\text{Bq/ kg}$	Mean $\text{Bq/ kg}$	Radon exhalation rates in terms of area ( $E_A$ ) in $\text{mBqm}^{-2}\text{h}^{-1}$	Mean $E_A$ in $\text{mBq m}^{-2} \text{h}^{-1}$	Radon exhalation rates in terms of mass, ( $E_M$ ) $\text{mBqm}^{-2} \text{h}^{-1}$	Mean $E_M$ $\text{mBq m}^{-2} \text{h}^{-1}$
Digboi	<b>27°23'41.0"N &amp; 95°36'10.6"E</b>	210	95.23	1.33	1.43 ± 0.07	29.37	31.71 ± 0.03	0.834	0.898 ± 0.06
	<b>27°23'40.6"N &amp; 95°36'14.8"E</b>	220	99.97	1.39		30.76		0.871	
	<b>27°23'40.9"N &amp; 95°36'11.2"E</b>	222	100.68	1.41		31.04		0.879	
	<b>27°24'17.7"N</b>	250	113.37	1.58		34.96		0.990	

<b>&amp;95°36′ 14.4′E</b>						
<b>27°36′18 .3′N &amp;95°31′ 16.5′E</b>	215	97.50	1.36		30.06	0.852
<b>27°36′15 .4′N &amp;95°36′ 17.2′E</b>	223	103.4 0	1.44		31.89	0.903
<b>27°36′14 .16′N &amp;95°37′ 03.1′E</b>	230	104.3 0	1.46		32.16	0.911
<b>26° 90′14.5″ N &amp;94°72′ 10.6′E</b>	252	114.2 8	1.6		35.24	0.998
<b>26°90′41 .0′N &amp;94°66′ 16.1′E</b>	218	98.86	1.38		30.48	0.864
<b>26°90′11</b>	223	101.1	1.41		31.18	0.883

Fig2: Co-relation co-efficient between radium content and rad. Exhalation rate in area at Digbo



### CONCLUDING OBSERVATIONS:

Based on the results obtained in this study the following concluding observations may be drawn as follows:

1. With increase of radium content of soil samples the radon exhalation rate also increases in the studied locations.
2. The average values of effective radium content at the locations of the studied area are lower than the OECD recommended value.
3. A good positive correlation have been observed between effective radium content with radon exhalation rate of soil samples.

### ACKNOWLEDGEMENT

I express my sincere gratefulness and profound sense of gratitude to Dr. Hiranya Kr. Sarma, Principal, Hajo Suren Das College, Hajo, Kamrup(M) for their inspiring guidance throughout the course of the present work. I express my heartfelt thanks to my co-guide Dr. Ranjan Kr. Kakati Sir for his encouraging attitudes and best wishes during the course of this work. I extend my thanks to department of Physics, Assam Down Town University for providing necessary laboratory facilities during the course of my research work. I express my heartfelt thanks to my colleagues for their encouraging attitudes and best wishes during the course of this work. I offer my sincere thanks to Dr. Subir Sarkar Sir, for extending his help in the computational work. I am

highly indebted to my all the family members and specially thanks to my husband Mr. Diganta Baruah for supporting and encouraging me during the course of the work.

## REFERENCES

- [1] Ali, A. 2001. Macroeconomic variables as common pervasive risk factors and the empirical content of the Arbitrage Pricing Theory. *Journal of Empirical finance*, 5(3): 221–240.
- [2] Basu, S. 1997. The Investment Performance of Common Stocks in Relation to their Price to Earnings Ratio: A Test of the Efficient Markets Hypothesis. *Journal of Finance*, 33(3): 663-682.
- [3] Bhatti, U. and Hanif. M. 2010. Validity of Capital Assets Pricing Model. Evidence from KSE-Pakistan. *European Journal of Economics, Finance and Administrative Science*, 3 (20).
- [4] Subha Ramu M.C, Shaikh A.N., Muraleedharan T.S. and Ramachandran T.V. (1993). Measurement of indoor radon levels in India using SSNTD; Need for standardization. *Proceeding of the 7th NCPT conference, Jodhpur*, 181-190.
- [5] Jha G, (1987), Development of a passive  $^{222}\text{Rn}$  dosimeter for application in radiation protection and uranium exploration, Ph D. thesis, University of Mumbai.
- [6] Durrani S. A. and Bull R.K. (1998), *Solid State Nuclear Track Detection, Principles, Methods and Application*, International Series in Natural Philosophy, III, 169, Pergamon press, Oxford.
- [7] Jojo P.J. (1993), study of radon and its progeny using etched track detectors and micro analysis of uranium, Ph D. thesis, Aligarh Muslim University, Aligarh 123.
- [8] Maya Y.S., Eappen K.P., Nambi K.S.V. (1998), Parametric Methodology for inhalation dosimetry due to a mixed field of Radon and Thoron using passive detectors, in 12th National Symposium on Radiation Physics, Jodhpur, January 28-30.
- [9] Homer J.B and Miles J.C.H (1986), The effects of heat and humidity before, during and after exposure on the response of PADC (CR-39)
- [10] Dwivedi K.K, Mishra R, Tripathy S.P., Kulshreshtha A, Singh D, Srivastava A, Deka P, Bhattacharjee B, Ramachandran T.V, Nambi K.S.V. (2001), Simultaneous determination of radon, thoron and their progeny in dwellings. *Radiation Measurements*, 33, 7-11.
- [11] ICRP (1993), Protection against Radon-222 at home and at work. ICRP publication 65, *Annals of the ICRP*, 23(2).
- [12] Alter M.W. and Price P.B. (1972). Radon detection using track registration material, U.S. Patent 3, 665, 194.
- [13] Abu-Jarad, F (1988). Application of nuclear track detectors for radon related measurements. *Nuclear Tracks and Radiation Measurement*, 15 (1-4), 525.

- [14] Somogyi, G (1990). The environmental behaviour of radium, Technical reports series no. 310, vol.1, IAEA, Vienna, 229-256.
- [15] Khan, A.J., Prasad, R., & Tyagi, R.K. (1992). Measurement of radon exhalation rate from some building materials. Nuclear Tracks and Radiation Measurements, 20, 609-10.
- [16] Singh S., Sharma D.K, Dhar S, Kumar A., (2007), Uranium, Radium and Radon Measurements in the Environs of Nurpur Area, Himachal Himalayas, India, Environ, Monit. Assess 128,301.
- [17] Azam A., Naqvi A.H. & Srivastava D.S. (1995). Radium concentration and radon exhalation measurement using LR-115 type-II plastic track detectors. Nuclear Geophysics 9 (6), 653-657.
- [18] Abu-Jarad, F (1988). Application of nuclear track detectors for radon related measurements. Nuclear Tracks and Radiation Measurement, 15 (1-4), 525.
- [19] Khan, A.J., Prasad, R., & Tyagi, R.K. (1992). Measurement of radon exhalation rate from some building materials. Nuclear Tracks and Radiation Measurements, 20, 609.
- [20] United Nations Scientific Committee on the Effect of Atomic Radiation. Report to the General Assembly, Annex B: Exposures from Natural Radiation Sources, United Nations, New York; 2000.
- [21] International Commission on Radiological Protection. Protection Against Radon-222 at home and at Work. ICRP Publication 65. Annals of the ICRP 23(2). Oxford: Pergamon Press; 1993. †
- [22] ICRP. Recommendations of the International Commission for Radiological Protection. Vol. 37. New York: ICRP Publication; 2007. p. 103.
- [23].Abu-Jarad F, Fremlin JH, Bull R. A study of radon emitted from building materials using plastic alpha-track detectors. Phys Med Biol 1980;25:683-94
- [24] United Nations. Sources, Effects and Risks of Ionizing Radiation. United Nations Scientific Committee on the Effects of Atomic Radiation, 1988 Report to the General Assembly, with annexes. United Nations, New York: United Nations Sales Publication E.88.IX.7; 1988.
- [25] Henshaw DL, Eatough JP, Richardson RB. Radon as a causative factor in induction of myeloid leukaemia and other cancers. Lancet 1990;335:1008-12
- [26] Abdelzaher M. Seasonal variation of radon level and radon effective doses in the Catacomb of Kom EI-Shuqafa Alexandria, Egypt. Pramana J Phys 2011;77:749-57.

## **Effect of Endophytic Fungus *Fusarium oxysporum* on Crystallographic Properties of PdO: Nanoparticles Synthesis, Characterization and Evaluation of Anti-oxidant Activity**

Sk Najrul Islam, Syed Mohd Adnan Naqvi, Sadia Parveen and Absar Ahmad\*

Interdisciplinary Nanotechnology Centre (INC), Faculty of Engineering and Technology,  
Aligarh Muslim University, AMU, Aligarh 202002, India

\*Email: aahmad786in@gmail.com

### **ABSTRACT**

In recent times, semiconductor transition metal-oxide nanoparticles have gained a lot of attention because of their unique physio-chemical properties which mainly depend on size, shape, crystallographic phase and routes of synthesis. Palladium Oxide Nanoparticles (PdO NPs) belonging to the platinum group metal oxide possesses potential application in catalytic conversion of organic molecules and gas sensing application. Different methods have been reported for the synthesis and low-pressure phase transition of PdO NPs. Herein we report a simple endophytic fungus *Fusarium oxysporum* assisted novel approach for the biofabrication of face-centered cubic PdO NPs (f-PdO NPs) from tetragonal PdO (t-PdO) powder. The change in crystallographic properties under fungal stress was confirmed by XRD analysis while TEM images show biotransformed PdO NPs of average particles of size 6-8 nm. FTIR spectrum confirmed the presence of capping protein which made PdO NPs water dispersible with very high shelf-life. Anti-oxidant activity and optical band gap energy (1.9 eV) have also been estimated using UV-VIS-NIR spectrophotometry.

**Keywords:** Anti-oxidant activity, crystallographic phase transition, Endophytic, *Fusarium oxysporum*, PdO NPs.

### **INTRODUCTION:**

The increased multidisciplinary applications of nano-size materials and their unique properties have drawn researchers toward the field of nanotechnology research. Although different methods have been employed for the fabrication of nanomaterials, biological routes of nanoparticle synthesis using plants and micro-organisms have gained much more attention as they provide highly stable, naturally protein-capped nanoparticles with very high shelf-life. A range of nanoparticles like metal, metal oxide, metal chalcogenide, quantum dots and biomineral

nanoparticles have been successfully synthesized using biological routes and some of them are in use in commercial and industrial products. Various types of biofabricated nanoparticles with different physiochemical properties have also been reported by our group [1-5]. These novel physicochemical properties mainly depend on particle size, chemical composition, surface-to-volume ratio, morphology and crystalline structure of NPs. It was also known that the thermodynamic stability of NPs is highly dependent on their crystallographic phase. High-temperature annealing methods for the phase transition of barium titanate NPs, Fe<sub>2</sub>O<sub>3</sub> NPs and TiO<sub>2</sub> NPs have been reported previously [5-8]. Fungus base phase, size and shape transformation of TiO<sub>2</sub> were also reported by our group [9]. Arora K., Sandil D. et al studied the effect of a low-pressure hydrogen environment on crystallographic properties of PdO nanoparticles [10].

Antioxidants are substances that inhibit the production of reactive oxygen species or reduce oxidative stress by scavenging free radicals. Reactive oxygen species which are the byproduct of metabolic processes cause serious diseases including Alzheimer's disease, Parkinson's disease, Cancer, etc [11]. As many antioxidant exhibits anticancer activity, the antioxidant activity of different metal and metal oxides nanoparticles were evaluated [12-14]. It was also established that ultra-sonication enhances the antioxidant activity of metal oxide nanoparticles by increasing reaction feasibility [15].

Palladium oxide nanoparticles, a transition metal oxide, belong to the platinum oxide group has been widely used in organic reaction catalysis [16-18], formic acid oxidation [19] and gas sensing applications [20]. DNA binding properties of PdO NPs and anticancer activity of many palladium complexes have also been studied as palladium complexes show structural similarity with platinum-based drugs [21]. As PdO NPs become an important candidate for selective catalysis of various organic reactions, various methods have been reported for the synthesis of PdO NPs from the precursor salt of palladium [22-26]. Herein we have investigated the effect of fungal stress on t- PdO powder and evaluated the antioxidant activity of biotransformed f-PdO nanoparticles.

## **MATERIALS & METHODS**

### **Isolation, purification and maintenance of endophytic fungus *Fusarium oxysporum***

The endophytic fungus *Fusarium oxysporum* was isolated from the plant parts such as leaves. Then isolated and purified strains of *Fusarium oxysporum* were transferred on potato dextrose agar (PDA) slants and these slants were incubated in B.O.D incubator at 25°C. After 96 h incubation of the freshly prepared slant, fungal mycelia were inoculated from stock PDA slant to 500 ml Erlenmeyer flask containing 100 ml of MGYM medium which is composed of 0.3% Malt extract, 1% Glucose, 0.3% Yeast extract and 0.1% Peptone. The mycelia-containing MGYM medium was then placed on a rotary shaker (200 rpm) at 25°C and it was kept under systematic review. After 96 h of fermentation at pH 7, the fungal biomass was separated from the culture broth by centrifugation (7000 rpm) which was performed at 15°C for 20 min. The obtained biomass was then washed thrice with sterile distilled water. All the processes were performed under sterile conditions.

### **Investigation of fungal stress on t-PdO powder and f-PdO NPs formation**

The investigation of the stress of fungus *Fusarium oxysporum* on t-PdO powder was accomplished by adding 20 gram of fungal biomass in a 500 ml Erlenmeyer flask having 100 ml aqueous suspension of 0.1% t-PdO powder. The reaction mixture was then kept on a rotary shaker (200 rpm) at 25°C and was monitored for 96 h. After 96 h, the reaction product was filtered out by using a simple filtration method. The filtrate solution containing f-PdO NPs was then lyophilized to powder for further characterization and investigation.

## **CHARACTERIZATION**

### **UV-Vis- NIR Spectroscopy**

After completion of reaction, the aliquots of biotransformed f-PdO NPs (3.5 ml) was subjected to double beam Cary 5000 UV-Vis-NIR spectrophotometer (Agilent, USA) for the measurement of optical absorption and band gap. The spectrum was recorded at a resolution of 1 nm and wavelength range of 350-500 nm.

### **Transmission electron microscopy (TEM)**

TEM images of biotransformed f-PdO NPs were captured by transmission electron microscopy (JEM-JEOL, JAPAN) operated at the magnification of 100,000X to explore the shape, size and particle size distribution of nanoparticles. For TEM analysis, the biotransformed f-PdO NPs

were loaded onto the carbon coated copper grids by drop casting. These grid was also used for the recording of Selected Area Electron Diffraction (SAED) pattern at an angular magnification of 0.001 nm per degree.

### **X-ray diffraction (XRD)**

XRD (Rigaku, Tokyo, Japan) measurement was carried out to investigate the effect of fungal stress on crystallographic properties of PdO powders and establish the crystallographic structure of f-PdO NPs. XRD patterns of both t-PdO powder and lyophilized f-PdO NPs were recorded in the  $2\theta$  range of  $20-80^\circ$  with a step size of  $0.04^\circ$  and a time of 5 seconds per step at 40 kV voltage and a current of 30 mA.

### **Fourier transform infrared spectroscopy (FTIR)**

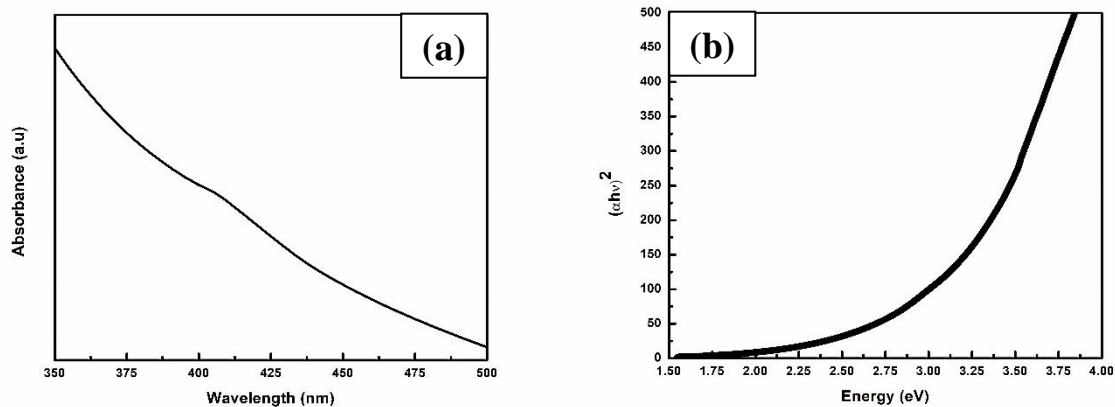
The FTIR spectrum of t-PdO powder and f-PdO NPs were recorded using Perkin Elmer (USA) Fourier transform infrared spectrophotometer to examine the characteristic metal-oxide bond vibration and confirm the presence of capping biomolecules (proteins) onto the surface of nanoparticles. For FTIR study, thin pellets of KBr containing nanoparticles were analyzed while a pure KBr pellet was used for background scan.

### **Antioxidant activity evaluation**

Antioxidant activity of biofabricated f-PdO NPs was evaluated using 2,2-Diphenyl-1-picrylhydrazyl (DPPH) radical scavenging assay [27]. To execute the experiment, 50 ml methanolic solution (0.01 mM) of DPPH and different concentration (0.05 mg/ml, 0.1 mg/ml, 0.15 mg/ml, 0.2 mg/ml, 0.25mg/ml) of aqueous test solution of f-PdO NPs were prepared while aqueous solution of ascorbic acid with 0.05 mg/ml concentration was used as control. 1 ml of each NPs solution and standard solution were added with 3 ml of DPPH solution separately. The obtained mixtures were then incubated for 10 min at room temperature. The antioxidant activity of f-PdO NPs was evaluated by measuring the absorbance of all mixtures at 513 nm against methanol as blank.

## RESULTS & DISCUSSION

UV-Vis-NIR spectrum of biotransformed f-PdO NPs was recorded in the wavelength range 350-500 nm (Fig. 1a.) and the appeared absorption band at 407 nm confirms the existence of PdO NPs [23]. Using UV-Vis-NIR data direct bandgap energy was estimated from tauc plot (Fig. 1b.) as 1.9 eV which is approximately the same as the reported band gap energy 1.8 eV for PdO NPs

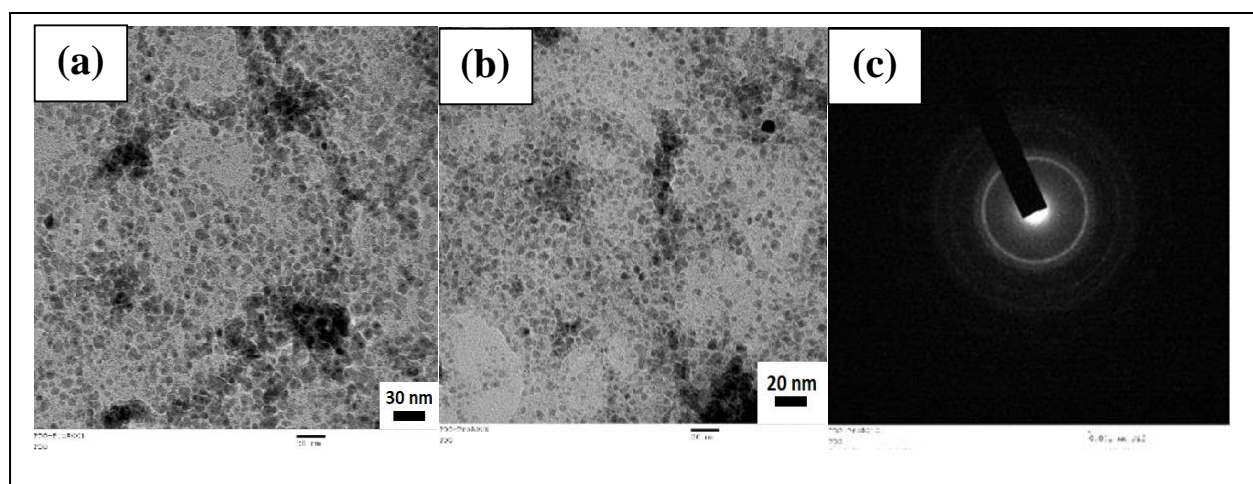


[10].

**Figure 1.** (a) UV-Visible spectrum of an aqueous solution of f-PdO NPs. (b) Optical band gap estimation using Tauc plot.

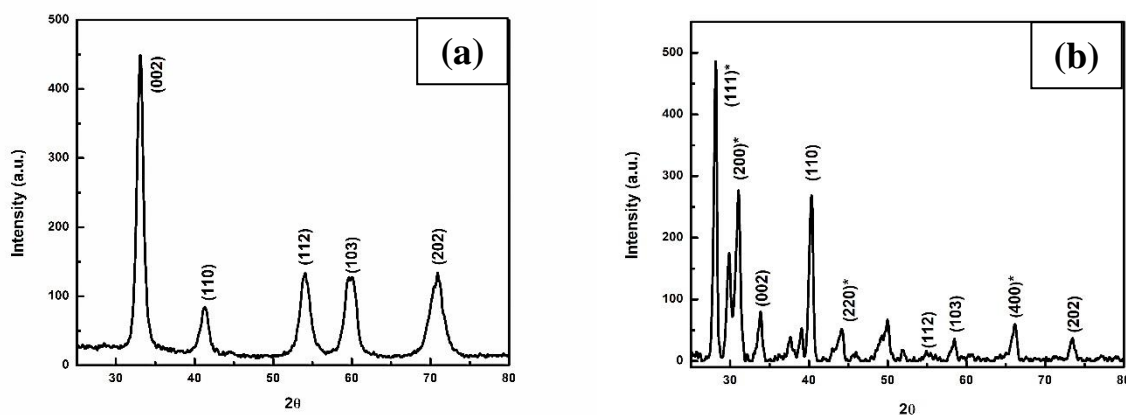
**Figure 2.** (a,b) TEM images and (c) SAED pattern of biofabricated f-PdO NPs.

Fig. 2a. and Fig. 2b. shows the TEM images of biotransformed f-PdO NPs. These TEM images indicate the formation of f-PdO NPs having an average particle size of 6-8 nm. Selected Area



Electron Diffraction (SAED) pattern (Fig. 2c) was also captured during TEM analysis which confirmed the crystalline nature of biotransformed f-PdO NPs.

XRD diffraction pattern of PdO, before (Fig. 3a.) and after (Fig. 3b.) treatment with fungus *Fusarium oxysporum*, was recorded to investigate the effect of fungus stress on the crystallography phase. Diffraction peak appeared (Fig. 3a.) at  $2\theta$  angle of  $33.82^\circ$ ,  $40.47^\circ$ ,  $54.7^\circ$ ,  $59.16^\circ$  and  $73.12^\circ$  correspond to the planes (002), (110), (112), (103) and (202) ensure the tetragonal phase of precursor PdO powder (JCPDS file No. 043- 1024) [10],[28]. After biotransformation of t-PdO powder, the relative intensity of the peak at  $40.47^\circ$  (110) get increased and four new diffraction peaks were indexed (Fig. 3b.) at  $28.03^\circ$  (111),  $31.25^\circ$  (200),  $44.78^\circ$  (220) and  $66.17^\circ$  (400) which confirm the PdO nanoparticles with a face-centered cubic structure having lattice parameters  $5.642\text{\AA}$  (JCPDS file No. 046-1211) [22]. The increased intensity of the diffraction peak and newly appeared peaks established the biotransformation of the crystallographic phase during nanoparticles formation.



**Figure 3.** XRD pattern of (a) t-PdO powder and (b) biotransformed f-PdO NPs.

The FTIR spectrum of t-PdO powder and biotransformed f-PdO NPs was recorded in the wavenumber range of  $400\text{--}2000\text{ cm}^{-1}$  at room temperature (Fig. 4.). The recorded spectrum of control t-PdO powder shows two characteristic absorption peak at  $590$  and  $650\text{ cm}^{-1}$  correspond to stretching vibration of Pd-O bond [21]. In case of f-PdO NPs, these absorption bands were shifted towards lower wavenumber ( $545$  and  $614\text{ cm}^{-1}$ ) along with two new additional peaks were appeared at  $1554\text{ cm}^{-1}$  (N-H bending, amide II), and  $1645\text{ cm}^{-1}$  (N-C=O stretching, amide I). The change in peak positions and newly appeared amide bands demonstrated that the biofabricated f-PdO NPs were capped by protein molecules [24, 29].

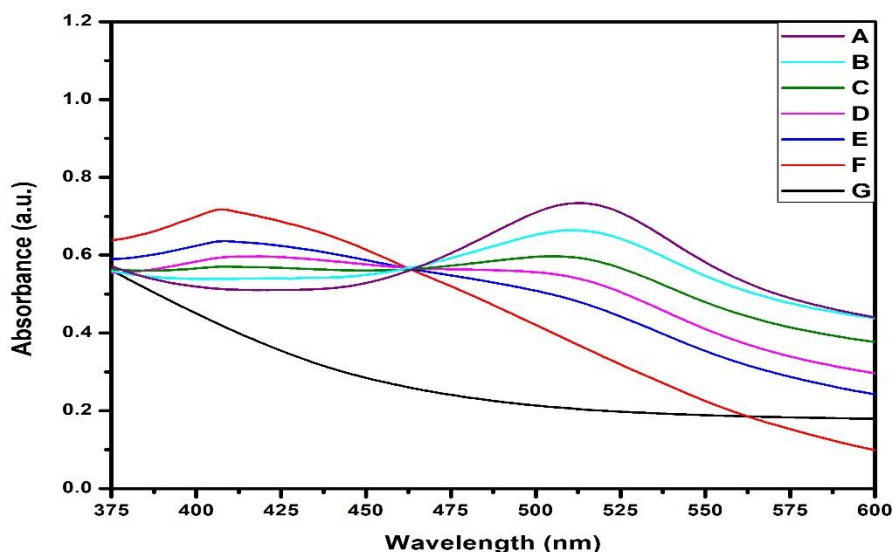


**Figure 4.** FTIR spectra of t-PdO powder and f-PdO nanoparticles

Antioxidant activity of biotransformed, protein-capped f-PdO NPs was performed where ascorbic acid was used as a positive control. The UV-VIS absorption study (Fig. 5.) shows the DPPH radical scavenging activity of biotransformed f-PdO NPs. The absorption peak appeared at 514 nm correspond to DPPH decreases with increasing concentration of f-PdO NPs while the absorption at 407 nm associated with f-PdO NPs increases. The change in color and the gradual decrease in absorption maxima at 514 nm with increasing concentration of f-PdO NPs indicates its good potential to act as an antioxidant agent.

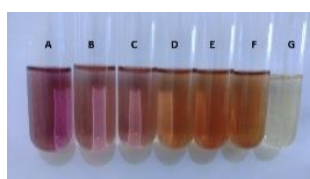


**Figure 5.** UV-VIS absorption spectra of (A) Pure DPPH, (B-F) DPPH with increasing concentration of t-PdO NPs, (G) DPPH with ascorbic acid.

## Conclusion

At the flourishing time of green nanoscience and nanotechnology, crystallographic phase transitions of different materials are being carried out using harsh chemicals and extreme heating conditions. However, we have developed a simple fungus-based green approach to obtain f-PdO NPs with an average particle size of 6-8 nm from t-PdO powder. The biosynthesized NPs were characterized by well-recognized techniques and antioxidant activity has been investigated using

DPPH radical scavenging assay. The experimental result demonstrated significant antioxidant activity of biotransformed f-PdO NPs.

### Acknowledgments

We acknowledge the Department of Biotechnology (DBT), Government of India, for setting up a Centre of Excellence (COE, BT/PR1-3584/COE/34/29/2015) at Interdisciplinary Nanotechnology Centre (INC), Aligarh Muslim University, AMU, Aligarh, UP-202002, India. We thank Mr. Ashraf Ali Khan and Mr. Alim Kazmi of INC for their technical assistance.

### REFERENCES

- [1] Shankar, S. S., Rai, A., Ahmad, A. and Sastry, M. Rapid synthesis of Au, Ag, and bimetallic Au core-Ag shell nanoparticles using Neem (*Azadirachta indica*) leaf broth. *Journal of Colloid and Interface Science*, **275** (2004), 496–502.
- [2] Ahmad, A., Mukherjee, P., Mandal, D., Senapati, S., Khan, M. I., Kumar, R. and Sastry, M. Enzyme mediated extracellular synthesis of CdS nanoparticles by the fungus, *Fusarium oxysporum*. *Journal of the American Chemical Society*, **124** (2002), 12108–12109.
- [3] Rautaray, D., Sanyal, A., Adyanthaya, S. D., Ahmad, A. and Sastry, M. Biological synthesis of strontium carbonate crystals using the fungus *Fusarium oxysporum*. *Langmuir*, **20** (2004), 6827–6833.
- [4] Islam, S.N., Naqvi, S.M.A., Parveen, S and Ahmad, A. Application of mycogenic silver/silver oxide nanoparticles in electrochemical glucose sensing; alongside their catalytic and antimicrobial activity. *3 Biotech* **11** (2021), 342.
- [5] Bharde, A., Rautaray, D., Bansal, V., Ahmad, A., Sarkar, I., Yusuf, S. M., Sanyal, M. and Sastry, M. Extracellular biosynthesis of magnetite using fungi. *Small*, **2** (2006), 135–141.
- [6] Hoshina, T., Kakemoto, H., Tsurumi, T., Wada, S. and Yashima, M. Size and temperature induced phase transition behaviors of barium titanate nanoparticles. *Journal of Applied Physics*, **99** (2006), 1–9.
- [7] Jafari, A., Farjami Shayesteh, S., Salouti, M. and Boustani, K. Effect of annealing temperature on magnetic phase transition in Fe<sub>3</sub>O<sub>4</sub> nanoparticles. *Journal of Magnetism and Magnetic Materials*, **379** (2015), 305–312.
- [8] Pal, M., Serrano, J. G., Santiago, P. and Pal, U. Size-controlled synthesis of spherical TiO<sub>2</sub> nanoparticles: Morphology, crystallization, and phase transition. *Journal of Physical Chemistry C*, **111** (2007), 96–102.
- [9] Khan, S. A. and Ahmad, A. Phase, size and shape transformation by fungal biotransformation of bulk TiO<sub>2</sub>. *Chemical Engineering Journal*, **230** (2013), 367–371.
- [10] Arora, K., Sandil, D., Sharma, G., Srivastava, S. and Puri, N. K. Effect of low pressure hydrogen environment on crystallographic properties of PdO nanoparticles. *International Journal of Hydrogen Energy*, **41** (2016), 22155–22161.
- [11] Tetey, C. O. and Shin, H. M. Evaluation of the antioxidant and cytotoxic activities of zinc oxide nanoparticles synthesized using *scutellaria baicalensis* root. *Scientific African*, **6** (2019), e00157.

- [12] Chahardoli, A., Karimi, N., Ma, X. and Qalekhani, F. Effects of engineered aluminum and nickel oxide nanoparticles on the growth and antioxidant defense systems of *Nigella arvensis* L. *Scientific Reports*, **10** (2020), 1–11.
- [13] Liu, Q., Liu, H., Yuan, Z., Wei, D. and Ye, Y. Evaluation of antioxidant activity of chrysanthemum extracts and tea beverages by gold nanoparticles-based assay. *Colloids and Surfaces B: Biointerfaces*. **92** (2012), 348-352.
- [14] Dhall, A. and Self, W. Cerium oxide nanoparticles: A brief review of their synthesis methods and biomedical applications. *Antioxidants*, **7** (2018), 1–13.
- [15] Saikia, J. P., Paul, S., Konwar, B. K. and Samdarshi, S. K. Ultrasonication: Enhances the antioxidant activity of metal oxide nanoparticles. *Colloids and Surfaces B: Biointerfaces*, **79** (2010), 521–523.
- [16] Kumar, P., Ray, S., Das, T., Gage, S. H., Nandi, M., Richards, R. M. and Biswas, P. Microporous and Mesoporous Materials Palladium oxide nanoparticles intercalated mesoporous silica for solvent free acceptorless dehydrogenation reactions of alcohols. *Microporous and Mesoporous Materials*, **284** (2019), 186–197.
- [17] Muniz-Miranda, M., Zoppi, A., Muniz-Miranda, F. and Calisi, N. Palladium oxide nanoparticles: Preparation, characterization and catalytic activity evaluation. *Coatings*, **10** (2020), 207.
- [18] Krishnaveni, T., M. V. Kaveri, M. V., and Kadirvelu, K. The first PdO nanoparticles catalyzed one pot synthesis of propargylamine through A3-coupling aldehyde, alkyne and amine. *New J. Chem.* (2021). <https://doi.org/10.1039/D1NJ02994K>.
- [19] Li, Z., Song, J., Lee, D. C., Abdelhafiz, A., Xiao, Z., Hou, Z., Liao, S., DeGlee, B., Liu, M., Zeng, J., and Alamgir, F.M. Mono-disperse PdO nanoparticles prepared via microwave-assisted thermo-hydrolyzation with unexpectedly high activity for formic acid oxidation, *Electrochimica Acta*, **329** (2020), 135166.
- [20] Samoylov, A. M., Ryabtsev, S. V., Popov, V. N. and Badica, P. Palladium (II) Oxide Nanostructures as Promising Materials for Gas Sensors. *Novel Nanomaterials - Synthesis and Applications*. (2018).
- [21] Sorinezami, Z., Mansouri-Torshizi, H., Aminzadeh, M., Ghahghaei, A., Jamgohari, N. and Heidari Majd, M. Synthesis of new ultrasonic-assisted palladium oxide nanoparticles: an in vitro evaluation on cytotoxicity and DNA/BSA binding properties. *Journal of Biomolecular Structure and Dynamics*, **37** (2019), 4238–4250.
- [22] Wang, K., Huang, T., Liu, H., Zhao, Y., Liu, H. and Sun, C. Size control synthesis of palladium oxide nanoparticles by microwave irradiation. *Colloids and Surfaces A: Physicochemical and Engineering Aspects*, **325** (2008), 21–25.
- [23] Kumar, C. S. S. R., Modrow, H. and Hormes, J. Characterisation of sonochemically produced PdO nanoparticles by X-ray absorption near edge structure spectroscopy. *Particle and Particle Systems Characterization*, **19** (2002), 336–341.
- [24] Shargh, A. Y., Sayadi, M. H., and Heidari, A. Green Biosynthesis of Palladium Oxide Nanoparticles Using *Dictyota indica* Seaweed and its application for adsorption. *Journal of Water and Environmental Nanotechnology*. **3** (4), 337–347.
- [25] Ismail, E., Khenfouch, M., Dhlamini, M., Dube, S. and Maaza, M. Green palladium and palladium oxide nanoparticles synthesized via *Aspalathus linearis* natural extract. *Journal of Alloys and Compounds*, **695** (2017), 3632–3638.
- [26] Téllez, V. C., Portillo, M. C., Santiesteban, H. J., Castillo, M. P., Santiago, A. C., Mora-Ramírez, M. A., Coyotecatl, H. A., and Moreno, O. P. Green synthesis of palladium mixed with PdO nanoparticles by chemical bath deposition, *Optical Materials*, **112** (2021), 110747.

- [27] College, M. M., and Ambala, M. in Vitro Antimicrobial and Antioxidant Activity of Ginkgo Biloba Bark Extract. *International Research Journal of Pharmacy*, **3** (2012), 116–119.
- [28] Mayedwa, N., Mongwaketsi, N., Khamlich, S., Kaviyarasu, K., Matinise, N. and Maaza, M. (2018). Green synthesis of nickel oxide, palladium and palladium oxide synthesized via *Aspalathus linearis* natural extracts: physical properties & mechanism of formation. *Applied Surface Science* **446** (2018), 266-272.
- [29] Islam, S.K.N., Naqvi, S.M.A., Parveen, S. *et al.* Endophytic fungus-assisted biosynthesis, characterization and solar photocatalytic activity evaluation of nitrogen-doped  $\text{Co}_3\text{O}_4$  nanoparticles. *Appl Nanosci* **11**, 1651–1659 (2021). <https://doi.org/10.1007/s13204-021-01824-5>

## BEST POSTER PRESENTATION AWARD

*Paper Code: EMNSD-2020/PP/04*

**Title: Effect of Fe Substitution on the Magnetic Properties of  $MnCo_2O_4$**

**Corresponding Author: Junmoni Barman**

Department of Physics, Rajiv Gandhi University, Arunachal Pradesh-791112, India

*Paper Code: EMNSD-2020/PP/29*

**Title: Recycling of E-Waste Derived Printed Circuit Boards**

**Corresponding Author: Anuj Thukral**

CSIR-National Physical Laboratory, Dr. K. S. Krishnan Marg, Pusa, New Delhi-110012, India



# International Conference on Evolving Materials and Nanotechnology for Sustainable Development



(Online Mode)

Organised By:

Department of Physics,  
Central Institute of Technology Kokrajhar,  
Deemed to be University (under MHRD, Govt. of India),  
Kokrajhar, BTR, Assam-783370, India.

Date: 15-16 December 2020 (Tuesday & Wednesday)  
Venue: Online Mode via CISCO WebEx / Google Meet

## EMNSD-2020 Conference:

Evolving materials especially synthesis of the green materials bring tremendous changes in the line of sustainable development. Nanotechnology has the diverse applications in areas of energy, drug delivery, biotechnology, food technology, devices, and many others, and the benefit goes to the entire society directly. For this reason, the investment of evolving materials towards nanotechnology has been increasing day by day worldwide in Research and Development sectors. Believe that such conference will encourage the collaborative exchange of thought in international level among faculty as well as research scholar so that can enjoy the global exposure to get the momentum for carrying their individual research work.

### Themes:

- Physical Science
- Material Science
- Green Synthesis
- Renewable Materials and Energy
- Waste Materials & Management
- Nanoscience & Nanotechnology
- Food Engineering & Biotechnology
- Agricultural Science & Environmental Science
- Green Building and Sustainable Habitat
- Design for Sustainability

### Paper Details:

The abstract with maximum of 200 words in single A4 size page should be submitted to [emnsd20@cit.ac.in](mailto:emnsd20@cit.ac.in) by 12 December, 2020. The decision for the acceptance/rejection will be final by the organizing committee. Accepted papers will be published in the proceedings E-Book with ISBN.

### Format -

- All Font type: Times New Roman.
- Title: size 14 and Bold; Author: size 11, underline of the presenting author.
- Affiliation with address and email id: size 10.
- The abstract text : size 12 .

### Resource Persons:

#### Prof. Madan K Bhattacharyya

Dept. of Agronomy,  
Iowa State University, Ames, Iowa, USA.



#### Prof. Absar Ahmad

Director, Interdisciplinary Nanotechnology  
Centre (INC), Aligarh Muslim University,  
Aligarh, Uttar Pradesh, India.



#### Dr. Chris Holland

Senior Lecturer,  
Dept. of Materials Science & Engineering,  
The University of Sheffield, UK.



#### Dr. Indrani Banerjee

Associate Professor and Dean,  
School of Nano Sciences ,  
Central University of Gujarat,  
Gandhinagar, Gujarat, India.



#### Prof. Hiranya K Nath

Dept. of Economics and  
Intl. Business, Sam Houston State  
University, Texas, Houston, USA.



#### Dr. Logudurai Radhakrishnan

Associate Professor & Head,  
Dept. of Chemistry, Madanapalle Institute  
of Technology & Science, Madanapalle,  
Andhra Pradesh, India.



#### Dr. Bharat Baruah

Associate Professor, Dept. of Chemistry,  
Kennesaw State University, Atlanta, USA.



#### Dr. Pranjal Kalita

Associate Professor, Dept. of Chemistry,  
CIT Kokrajhar, Assam, India.



### Chief Patron



Prof. Deb Kumar Chakrabarti,  
Director,  
CITK.

### Patron



Ms. Chaitali Brahma,  
Registrar,  
CITK.

### Convener



Dr. Manasi Buzar Baruah,  
Assistant Professor,  
Dept. of Physics, CITK.

### Advisory Committee:

Prof. Madan Bhattacharyya, ISU, USA.  
Dr. Chris Holland, UOS, UK.  
Prof. Hiranya K Nath, SHSU, USA.  
Prof. Absar Ahmad, AMU, India.  
Dr. Indrani Banerjee, CUG, India.  
Prof. Tapan Kumar Maity, CITK, India.  
Prof. Hemanta Kumar Kalita, CITK, India.  
Dr. Avik Mukherjee, CITK, India.  
Dr. Bichitra Nanda Parida, CITK, India.  
Dr. Pranjal Kalita, CITK, India.

### Organising Committee:

Dr. Rajib Lochan Hota, Asso. Prof., CITK.  
Dr. Sandeep Kumar Srivastava, Asso. Prof., CITK.  
Mr. Mahananda Brahma, Asst. Prof., CITK.  
Dr. Bhaskar Saha, Asst. Prof., CITK.  
Mr. Sanjib Narzary, Asst. Prof., CITK.  
Dr. Anamika Deka Kalita, Asst. Prof., CITK.  
Dr. Sahalad Borgoyary, Asst. Prof., CITK.  
Dr. Gunajit Sarma, Asst. Prof., CITK.  
Dr. Santosh Kumar, Asst. Prof., CITK.  
Mr. Bikramjit Choudhury, Asst. Prof., CITK.  
Mr. Jeet Dutta, Asst. Prof., CITK.  
Dr. Kaushik Dev Sharma, Asst. Prof., CITK.  
Mr. Ranjan Patowary, Asst. Prof., CITK.  
Mr. Yendrebam Suresh Singh, Asst. Prof., CITK.

### Technical Committee:

Mr. Biswajit Paul, LIA, CITK.  
Mr. Bipin Brahma, Network Admn (i/c), CITK.  
Mr. Nayan Moni Barman, JTS, Dept. of CSE, CITK.  
Mr. Rituparna Bora, JTS, Dept. of MCD, CITK.

### Members:

Mr. Sanjib Baglari, PhD Scholar, CITK.  
Mr. Riu Riu Wary, PhD Scholar, CITK.  
Mr. Dulu Brahma, PhD Scholar, CITK.

**Central Institute of Technology Kokrajhar (CITK)** is a Deemed-to-be-University of de-novo category under the Ministry of Education of the Government of India, established in 2006. The Institute imparts education in engineering and design through its doctoral, postgraduate, undergraduate and diploma programs. Located in Kokrajhar in the Bodoland Territorial Region of Assam in the North Eastern part of India, the Institute is mandated to fuel all-round development of the region by providing requisite technological and vocational skill-based training, and to contribute to the country's economic growth.



### Registration Details:

- <https://forms.gle/W9NZU5bEbLpYur7K6>
- Payment Details: Axis Bank, Account name: EMNSD-2020 A/C: 920020068978450, IFSC: UTIB0001781, MICR :783211302  
Address: Axis Bank Ltd, J. D. Road, Ward no.5, Kokrajhar, Assam-783370, India.
- Last date for registration: 12 December 2020
- Fee: Indian- INR1000 & International-50USD,

### Contact:

Website: [www.emnsdconference.in/www.cit.ac.in](http://www.emnsdconference.in/www.cit.ac.in)  
Email: [emnsd20@cit.ac.in](mailto:emnsd20@cit.ac.in)  
Phone: +91- 9435120216/  
+91- 8447294108





International Conference on  
**Evolving Materials and Nanotechnology for Sustainable Development**



(Online Mode)  
Organised By:

Department of Physics,  
Central Institute of Technology Kokrajhar,  
Deemed to be University (under MHRD, Govt. of India),  
Kokrajhar, BTR, Assam-783370, India.

**PROGRAMME**

**DAY 1, 15 December 2020, TUESDAY**

TIME	
	<b>9:30-1.00 PM (Day 1, 1<sup>st</sup> Session)</b> Session Co-ordinator: Dr. Anamika Kalita Deka
9.30-10.00AM	<b><u>INAUGURATION</u></b> <b>Convener Speech:</b> Dr. Manasi Buzar Baruah, Asstt. Professor, Dept. of Physics, CITK <b>Welcome Speech:</b> Ms. Chiatali Bramha, Registrar, CITK <b>Welcome Speech and Opening of e-Abstract Volume:</b> Prof. Debkumar Chakrabarti, Director, CITK Photo Session
10.00-10.45AM	<b><u>KEYNOTE SPEAKER</u></b> <b>Prof. Madan K Bhattacharyya</b> Department of Agronomy, Iowa State University, Ames, Iowa, USA <b>Title: Genetic modification of a soybean gene for enhancing broad-spectrum disease and pest resistance in soybean</b> Department of Agronomy, Iowa State University, Ames, Iowa, USA
10.45-11:15AM	<b><u>INVITED SPEAKER</u></b> <b>Prof. Hiranya K Nath</b> Department of Economics International Business, Sam Houston University, Texas, USA <b>Title: Information and Communications Technology (ICT) and Economy</b>
11:30-12.00 NOON	<b><u>INVITED SPEAKER</u></b> <b>Dr. Indrani Banerjee</b> Associate Professor and Dean, School of Nano Sciences, Central University of Gujarat, Gandhinagar, Gujarat, India <b>Title: Structure Function Relation of Microwave Synthesized Muga Silk Nanoparticles</b>

<b>ORAL PRESENTATION (Day 1, 1<sup>st</sup> Session)</b>	
<b>Chairman: Dr. Indrani Banerjee</b> <b>Associate Professor and Dean, School of Nano Sciences,</b> <b>Central University of Gujarat, Gandhinagar, Gujarat, India</b>	
<b>OP1</b> <b>12.00-12.10PM</b>	Challenge and Success In Synthesis Of Quadruple Perovskites At Ambient Condition <b>Ariful Haque</b> Department of Chemistry, Visva-Bharati university, Santiniketan, Pin – 731235, India
<b>OP27</b> <b>12.10-12.20PM</b>	Optical and Electrical Properties of CuO Nanoparticles Synthesized Using Citrus Maxima Peels <b>Sanjib Baglari</b> Department of Physics, Birjhora Mahavidyalaya, Bongaigaon, Assam:783380, India
<b>OP3</b> <b>12.20-12.30PM</b>	Waste Sesamum indicum Plant: An Efficient Heterogeneous Catalyst for Biodiesel Production <b>Sanjay Basumatary</b> Department of Chemistry, Bodoland University, Kokrajhar-783370, Assam, India
<b>OP4</b> <b>12.30-12.40PM</b>	All-optical Binary to Quaternary Radix Converter using SOA-PRS <b>Ashif Raja</b> COSOD, Department of Physics, Kazi Nazrul University, Asansol-713340, West Bengal, India
<b>OP5</b> <b>12.40-12.50PM</b>	A study on Iron Oxide ( $\gamma$ -Fe <sub>2</sub> O <sub>3</sub> ) Nanoparticles synthesised using precipitation method and its possible applications <b>Bandana Gogoi</b> Department of Physics, D.N.Govt College, Itanagar-791113, Arunachal Pradesh, India
<b>OP6</b> <b>12.50-1.00PM</b>	Plasmon Resonances in Interacting Ni Nanoparticles Embedded in Dielectric <b>Jayanta Kumar Majhi</b> Post Graduate Department of Physics, Banowarilal Bhalotia College, Asansol – 713303, West Bengal
<b>1.00-2.00 PM</b>	<b>LUNCH BREAK:</b>

	<p style="text-align: center;"><b>POSTER SESSION: 2.00-3.30PM</b></p> <p><b>Group 1: PP1-PP16: Google Meet Link: <a href="https://meet.google.com/giw-ncsv-okg">https://meet.google.com/giw-ncsv-okg</a></b></p> <p><b>Group 2: PP17-33: Google Meet Link: <a href="https://meet.google.com/cpb-trxe-cft">https://meet.google.com/cpb-trxe-cft</a></b></p>
	<p style="text-align: center;"><b>(Day1, Session 2, 3.30-6.00 PM)</b></p> <p style="text-align: center;"><b>Co-ordinator: Dr. Sahalad Borgoyary &amp; Mr. Bikramjit Choudhury</b></p>
<p><b>3.30-4.00PM</b></p>	<p style="text-align: center;"><b><u>INVITED SPEAKER</u></b>  <b>Dr. Chris Holland</b>  <b>Senior Lecturer</b>  <b>Department of Material Science &amp; Engineering</b>  <b>The University of Sheffield, S. Yorks, UK</b></p> <p style="text-align: center;"><b>Title: Sustainable Polymer Processing Inspired by Silk</b></p>
	<p style="text-align: center;"><b><u>ORAL PRESENTATION</u></b></p> <p style="text-align: center;"><b>Chairman: Dr. Chris Holland</b>  <b>Senior Lecturer</b>  <b>Department of Material Science &amp; Engineering,</b>  <b>The University of Sheffield, S. Yorks, UK</b></p>
<p><b>OP7</b>  <b>4.00-4.10PM</b></p>	<p>Biocompatible Nanocarrier For Effective Delivery Of Antimicrobial To Agricultural Crop</p> <p><b>Gunjan Harshadkumar Vyas</b></p> <p>School of Nano Sciences, Central University of Gujarat, Gandhinagar, India.</p>
<p><b>OP8</b>  <b>4.10-4.20PM</b></p>	<p>Preparation of carotenoid Loaded BSA Nanoparticle Stabilized by Biosurfactant</p> <p><b>Jyoti Jaiswal</b></p> <p>School of Nano Sciences, Central University of Gujarat, Gandhinagar 382030, India.</p>
<p><b>OP9</b>  <b>4.200-4.30PM</b></p>	<p>Microstructure and Abnormal Coalescence Behavior of Ion Beam Sputter Deposited Silver and Gold Thin Films</p> <p><b>Rajeeb Brahma</b></p> <p>Department of Physics, Bodoland University, Kokrajhar, BTAD, Assam – 783370, India.</p>

<b>OP12</b> <b>4.30-4.40PM</b>	Study on Electrical Characteristics of Normally On Junctionless Field Effect Transistor <b>Angshumala Talukdar</b> Department of Instrumentation Engineering Central Institute of Technology Kokrajhar, Kokrajhar, India.
<b>OP16</b> <b>4.40-4.50PM</b>	Investigation of the Spin Speed Variation on the Performance of PEDOT:PSS/Si Hybrid Solar Cells <b>Avritti Srivastava</b> CSIR-National Physical Laboratory, New Delhi-110012, India
<b>OP25</b> <b>4.50-5.00PM</b>	Application of Musa paradisiaca derived ashes as heterogeneous base catalyst for Cross-Aldol reactions at room temperature <b>Dulu Brahma</b> Department of Chemistry, Central Institute of Technology Kokrajhar (Deemed to be University, MHRD, Govt. of India), Kokrajhar-783370, Assam, India.
<b>5.00-5.30PM</b>	<p style="text-align: center;"><b><u>INVITED SPEAKER</u></b></p> <p style="text-align: center;"><b>Dr. Bharat Baruah</b></p> <p style="text-align: center;">Department of Chemistry and Biochemistry, Kennesaw State University, GA, 30144, USA</p> <p style="text-align: center;"><b>Title: Fabrication of Flexible Transparent Wood Infiltrating Natural Polymer</b></p>

**DAY 2, 16 December 2020, WEDNESDAY**

<b>10:00-1.00PM (Day 2, 1<sup>st</sup> Session)</b>	
Co-ordinators: Mr. Mahananda Brahma & Mr. Sanjib Narzary; Mr. Bipin Brahma	
<b>10:00-10:45AM</b>	<b><u>KEYNOTE SPEAKER</u></b>  <b>Prof. Absar Ahmed</b>  Director, Interdisciplinary Nanotechnology Centre (INC), Aligarh Muslim University, Aligargh, Uttar Pradesh, India.  <b>Title: Green Fabrication of Nanomaterials, and their applications in healthcare, agriculture, environment, energy and life sciences</b>
<b>10:45-11:15AM</b>	<b><u>INVITED SPEAKER</u></b>  <b>Dr. Pranjal Kalita</b>  Associate professor, Department of Chemistry, CIT Kokrajhar, Assam, India  <b>Title: Recovery of Waste into Value-Added Compounds</b>
<b><u>ORAL PRESENTATION (Day2, Session 1, 11.15AM-1.00PM)</u></b>	
<b>Chairman: Dr. Pranjal Kalita</b> Associate Professor, Department of Chemistry, CIT Kokrajhar, Assam, India	
<b>OP10</b> <b>11:15-11:25AM</b>	Synthesis and Ultrasound-assisted Extraction of Polyhydroxybutyrate (PHB) from Invasive Weeds <b>Sushobhan Pradhan</b> School of Chemical Engineering, Oklahoma State University, Stillwater, Oklahoma, USA.
<b>OP11</b> <b>11:25-11:35AM</b>	Biodiesel production from waste cooking oil using a novel heterogeneous catalyst based on calcium oxide nanoparticles <b>Gaurav Singh</b> St. Peter's Engineering College, Hyderabad, India.
<b>OP13</b> <b>11:35-11:45AM</b>	Depletion Width Determination of Double gate Junctionless Field Effect Transistor With Triangle Shaped Spacer <b>Anjanmani Baro</b> Department of Instrumentation Engineering, Central Institute of Technology Kokrajhar, Kokrajhar, India

<p><b>OP14</b> 11:45- 11:55AM</p>	<p>Tera-Hertz Optical Asymmetric Demultiplexer(TOAD) using quantum dot Semiconductor Optical Amplifier</p> <p><b>Kousik Mukherjee</b></p> <p>Physics Department, B B College, Asansol, West Bengal, India</p>
<p><b>OP15</b> 11:55- 12:05PM</p>	<p>Effect of Annealing Temperature on the Structural and Optical Properties of ZnO Nanoparticles Synthesised by Colloidal Route</p> <p><b>Premshila Kumari</b></p> <p>CSIR-National Physical Laboratory (NPL), New Delhi-12, India</p>
<p><b>OP22</b> 12:05- 12:15PM</p>	<p>Design of a Power Inverter Using Solar Cell As A Source Of Charger</p> <p><b>HEMEN CH MEDHI</b></p> <p>Department of Electronics, St. Edmund's College, Shillong-793003, India</p>
<p><b>OP17</b> 12:15- 12:25PM</p>	<p>Hydrogen Adsorption on TMMg<sub>3</sub>(TM=Ni, Pd, Pt) Clusters: First Principles Study</p> <p><b>Bishwajit Boruah</b></p> <p>Department of Physics, Dibrugarh University, Dibrugarh, Assam, India-786004</p>
<p><b>OP18</b> 12:25- 12:35PM</p>	<p>Effect of the Ligands PPIA and TOPO on the spectroscopic behaviour of Sm<sup>3+</sup> ions in sol-gel silica matrix</p> <p><b>Navaneeta Rajkonwar</b></p> <p>Department of Physics, Dibrugarh University, Assam, India</p>
<p><b>OP19</b> 12:35- 12:45PM</p>	<p>Mg-doped ZnO Nanomaterial: An efficient sunlight driven photocatalyst</p> <p><b>Riu Riu Wary</b></p> <p>Department of Physics, Central Institute of Technology Kokrajhar (Deemed to be University, MHRD, Govt. of India), Assam.</p>
<p><b>OP20</b> 12:45- 12:55PM</p>	<p>Direct Synthesis of Co<sub>3</sub>O<sub>4</sub> Nanomaterials by Carbonate Precursor</p> <p><b>Arnab Kanti Giri</b></p> <p>Department of Chemistry, Karim City College, Jamshedpur, Jharkhand, India.</p>
<p><b>1.00- 2.00PM</b></p>	<p style="text-align: center;"><b>LUNCH BREAK</b></p>

	<p style="text-align: center;"><b><u>(Day2, Session 2, 2.30-5.00PM)</u></b></p> <p style="text-align: center;">Coordinators: Dr. Kaushik Chandra Dev Sarma &amp; Bikramjeet Choudhury; Biswajit Paul and Nayanmani Barman</p>
<p><b>2.00- 2.30PM</b></p>	<p style="text-align: center;"><b><u>INVITED SPEAKER</u></b></p> <p style="text-align: center;"><b>Dr. Logudurai Radhakrishnan</b> Associate Professor &amp; Head, Department of Chemistry, Madanapalle Institute of Technology &amp; Science, Madanapalle, Andrapradesh, India</p> <p style="text-align: center;"><b>Title: Electrochemical Investigation of Nano-porous Gold Electrodes in presence of Biofouling Solutions</b></p>
	<p style="text-align: center;"><b><u>ORAL PRESENTATION</u></b></p> <p style="text-align: center;"><b>Chairman: Dr. Logudurai Radhakrishnan</b> Associate Professor, &amp; Head, Department of Chemistry, Madanapalle Institute of Technology &amp; Science, Madanapalle, Andrapradesh, India</p>
<p><b>OP21 2.30P- 2.40PM</b></p>	<p>Orientational Order, Optical and Dielectric Properties of Liquid Crystals containing Bicyclohexane Rigid Core</p> <p><b>S. Mondal</b> Department of Physics, Siliguri Institute of Technology, Siliguri, West Bengal-734009, India.</p>
<p><b>OP23 2.40P- 2.50PM</b></p>	<p>Comparison of Polyvinyl Alcohol Capped Chemically Synthesized CdS and CdZnS Nanostructured Films</p> <p><b>Prince Kumar Mochahari</b> Department of Physics, Bodoland University, Kokrajhar, India</p>
<p><b>OP24 2.50P- 3.00PM</b></p>	<p>Application of Nanofluids for heat transfer processes</p> <p><b>Monisha Mridha Mandal</b> University School of Chemical Technology, Guru Gobind Singh Indraprastha University, New Delhi</p>
<p><b>OP26 3.00P- 3.10PM</b></p>	<p>Structural Evaluation of Muga silk protein by experimental and computational approach</p> <p><b>Prithvi Asapur</b> Central University of Gujarat, Ahmedabad, Gujarat, India</p>

<b>OP2</b> <b>3.10P-</b> <b>3.20PM</b>	Chromeno[2,3-b] indoles as ultra-high Stokes shift luminescent materials <b>Basanta Kumar Rajbongshi</b> Department of Chemistry, Cotton University, Panbazar, Guwahati – 781001, Assam, India.
<b>OP28</b> <b>3.20P-</b> <b>3.30PM</b>	Nanoparticle analysis using Digital Image Processing <b>Minakshi Gogoi</b> Dept. Of CSE, Girijananda Chowdhury Institute of Management and Technology, Guwahati-17, Assam, India
<b>OP29</b> <b>3.30P-</b> <b>3.40PM</b>	TL Dating of Potsherds from Tumu Ching, Manipur, India <b>Sheikh, M.R</b> Lilong Haoreibi College, Manipur, India.
<b>OP30</b> <b>3.40P-</b> <b>3.50PM</b>	Design And Simulation Of Non-metallic And Flexible Broadband Metamaterial Absorber For X-band Applications <b>Dipangkar Borah</b> Department of Physics, B. N. College, Dhubri, Assam, India.
<b>4.00-</b> <b>Onwards</b>	<b>Valedictory</b> <b>Vote of Thanks</b>

### **Cisco Webex Software for EMNSD-2020 Conference Links**

**EMNSD 2020, Day 1 Hosted by Webmaster CIT Kokrajhar**

<https://citkokrajhar.webex.com/citkokrajhar/j.php?MTID=m5f00f3e0f5307148dd2d43326e677722>

**Tuesday, Dec 15, 2020 8:00 am | 12 hours | (UTC+05:30) Chennai, Kolkata, Mumbai, New Delhi**

**Meeting number: 176 678 6589**

**Password: EMNSD2020D1**

**EMNSD 2020, Day 2, Hosted by Webmaster CIT Kokrajhar**

<https://citkokrajhar.webex.com/citkokrajhar/j.php?MTID=mf0d9afd623058ac3f73c35a4e4556b87>

**Wednesday, Dec 16, 2020 8:00 am | 12 hours | (UTC+05:30) Chennai, Kolkata, Mumbai, New Delhi**

**Meeting number: 176 003 8282**

**Password: EMNSD2020D2**



## FEW GLIMPSES OF THE CONFERENCE



Gunjan Vyas	Gaurav Singh	Payal Saha	Prkrthi A N
Bidhu Bhushan Bra...	Manasi Buzar Baruah	prince kumar Moch...	sudem borgayary

- DK 🗨️ Dr. Pranjal Kalita  
Me
- WK 🗨️ Webmaster CIT Kokrajhar  
Host
- CS 🗨️ Chris Holland The Universit  
Cohost
- AR 🗨️ Ashif Raja
- BG 🗨️ Bandana Gogoi
- BB 🗨️ Bharat Baruah
- BB 🗨️ Bidhu Bhushan Brahma
- DB 🗨️ Dulu Brahma
- GS 🗨️ Gaurav Singh
- GV 🗨️ Gunjan Vyas



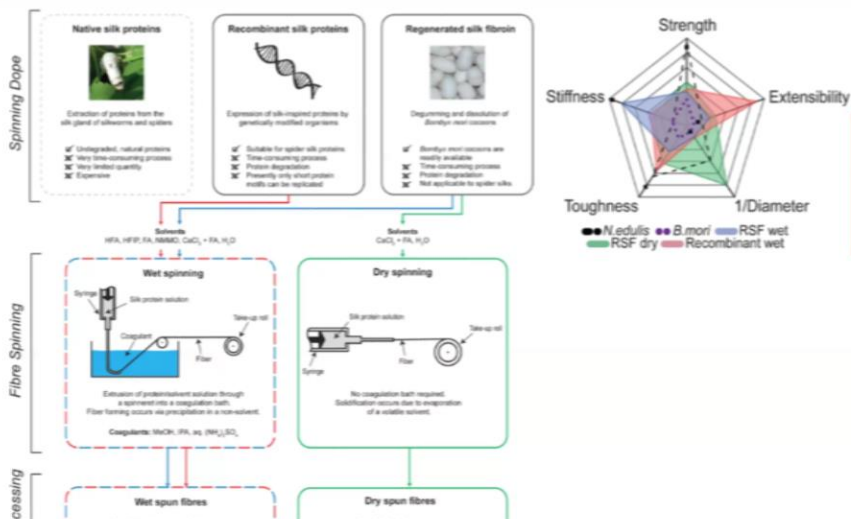
Layout

Participants (25)

Search

- DK Dr. Pranjal Kalita Me
- WK Webmaster CIT Kokrajhar Host
- CS Chris Holland The Universit
- AT Angshumala Talukdar
- AT Angshumala Talukdar
- BB Bidhu Bhushan Brahma
- BB Bishwajit Boruah
- BP Biswajit Paul
- DG Dr. Arnab Kanti Giri
- DB Dulu Brahma

## Current Challenge: Processing to take advantage of self assembly



Understanding natural spinning reveals fibroin's self assembly mechanisms, and the process variables we can use to control them



Speaking: Chris Holland The Universit...



Participants (34)

Chat

from Bikramjit Choudhury to Everyone: 3:59  
very interesting session sir

Send to: Everyone

Enter chat message here



## About the Conference,



Evolving materials especially synthesis of the green materials bring tremendous changes in the line of sustainable development. Nanotechnology has the diverse applications in areas of energy, drug delivery, biotechnology, foodtechnology, devices, and many others, and the benefit goes to the entire society directly. For this reason, the investment of evolving materials towards nanotechnology has been increasing day by day worldwide in Research and Development sectors. Believe that such conference will encourage the collaborative exchange of thought in international level among faculty as well as research scholar so that can enjoy the global exposure to get the momentum for carrying their individual research work.



## About the CIT Kokrajhar

Central Institute of Technology Kokrajhar (CITK) is a Deemed-to-be-University of de-novo category under the Ministry of Education of the Government of India, established in 2006. The Institute imparts education in engineering and design through its doctoral, postgraduate, undergraduate and diploma programs. Located in Kokrajhar in the Bodoland Territorial Region of Assam in the North Eastern part of India, the Institute is mandated to fuel all-round development of the region by providing requisite technological and vocational skill-based training, and to contribute to the country's economic growth.



EMNSD 2020

**Publisher**  
CITK Publication

ISBN- 978-93-5426-643-0

